Diagnostics and characterization of beam halo at the KEK Accelerator Test Facility

Renjun Yang

université PARIS-SACLAY

NNT : 2018SACLS261

Thèse de doctorat

UNIVERSITÉ PARIS SUD
Comprendre le monde, construire l'avenir

Diagnostics and characterization of beam halo at the KEK Accelerator Test Facility

Thèse de doctorat de l'Université Paris-Saclay
préparée à l'Université Paris-Sud

École doctorale n°576 Particules, Hadrons, Énergie, Noyau, Instrumentation, Imagerie, Cosmos et Simulation (PHENIICS)

École Doctorale PHENIICS Doctoral School

spécialité de doctorat : physique des accélérateurs

Thèse présentée et soutenue à Orsay, le 5 Octobre 2018, par

Renjun YANG

Composition du Jury :

Achille STOCCHI Professeur, LAL	Président
Pantaleo RAIMONDI Physicien Sénior, ESRF	Rapporteur
Helmut BURKHARDT Physicien Sénior, CERN	Rapporteur
Ryutaro NAGAOKA Physicien Sénior, Synchrotron SOLEIL	Examinateur
Takashi NAITO Professeur associé, KEK	Examinateur
Philip BAMBADE Directeur de recherche, LAL	Directeur de thèse

Laboratoire de l'Accélérateur Linéaire n° LAL-18-018

I would like to dedicate this thesis to my loving parents ...

Résumé

Aux futurs collisionneurs linéaires et circulaires, la présence d'un halo autour du faisceau est susceptible de fortement limiter les performances, et peut également activer, voire endommager, les composants de l'accélérateur. Le halo doit par conséquent est contrôlé par un système de collimateurs efficace. Pour évaluer l'impact sur les expériences de physique des particules ainsi que les efficacités de collimation, une bonne compréhension des mécanismes physiques générateurs de halo est essentielle, pour par exemple prédire les distributions de probabilité de manière fiable. Pour ce faire, une investigation systématique ont été menée à l'Accelerator Test Facility (ATF) du KEK dans le cadre de cette thèse, d'abord à travers une analyse théorique des principales sources de halo dans ATF, puis moyennant le développement et l'implémentation de diagnostiques dédiés aux mesures du halo, dont les résultat sont ensuite présentés et comparés aux prédictions théoriques.

Le halo produit par la diffusion des particules du faisceau sur les noyaux des molécules du gaz résiduel dans la chambre à vide (« Beam Gas Scattering » - BGS) est d'abord estimé analytiquement, avec certaines approximations, puis moyennant une simulation Monte-Carlo. Un nombre considérable de particules de halo BGS est prédit, ainsi qu'une dépendance dans la pression de gaz résiduel. Pour étudier la possible formation d'un halo par le mécanisme de diffusion intra-paquet à grand angle dit de « Touschek » en présence d'une dispersion optique résiduelle, le taux de cette diffusion a été estimé en fonction de plusieurs paramètres faisceau pertinents. Une simulation Monte-Carlo de la diffusion intra-faisceau à petit angle (IBS) et de « Touschek » est aussi en cours de développement.

Pour tester les prédictions théoriques, les performances d'un détecteur de halo déjà existant basé sur un capteur diamant ont été améliorées moyennant une technique de repondération qui a permis d'en augmenter la gamme dynamique jusqu'à 10^5. Afin de disposer d'un instrument complémentaire pour mesurer le halo, un moniteur YAG/OTR a aussi été conçu, construit et installé dans la ligne d'extraction d'ATF. Il a pu être montré que la gamme dynamique et la résolution de ce moniteur YAG-OTR sont, respectivement, autour de 10^5 et inférieure à 10 μm.

Grâce aux diagnostiques développés pour mesurer le halo du faisceau d'ATF, les distributions transverses et en énergie ont pu être étudiées. L'accord satisfaisant obtenu entre les prédictions théoriques et les mesures, ainsi qu'une dépendance importante dans la pression de gaz résiduel, ont permis de montrer que la distribution verticale du halo est dominée par le mécanisme BGS. Par contre, la distribution horizontale est bien supérieure aux prédictions BGS, et est par ailleurs

asymétrique. L'asymétrie observée peut être en partie reliée à la qualité du champ de l'élément pulsé servant à l'extraction du faisceau d'ATF, ainsi qu'à certaines aberrations dans le transport optique. La distribution de probabilité du halo en fonction de l'énergie a par ailleurs pu être mesurée, grâce à une technique nouvelle d'ajustement de la dispersion optique dans le plan vertical, et a été trouvée compatible qualitativement avec le mécanisme de diffusion « Touschek ». Un scénario plausible de génération du halo dans le plan horizontal a ainsi pu être suggéré.

Mots-clés : Halo du faisceau, diffusion du faisceau sur le gaz résiduel, diffusion « Touschek », capteur diamant, moniteur YAG/OTR, queue de distribution en énergie

Abstract

At future linear and circular colliders, beam halo can strongly limit machine performances, cause as well component damage and activation, and should, therefore, be controlled by an efficient collimation system. To evaluate the impact on particle physics experiments and collimation efficiencies, a clear understanding of beam halo formation mechanisms is essential, e.g., to predict halo distribution reliably. For this purpose, systematic investigations have been carried out at the Accelerator Test Facility (ATF) of KEK. In this dissertation, the theoretical analysis of the primary halo sources at ATF and the development of dedicated halo diagnostics are presented. Measurements of beam halo at ATF are also described and compared with the theoretical predictions.

Beam halo arising from Beam-Gas Scattering (BGS) in the damping ring was firstly estimated through analytical approximations and a Monte Carlo simulation. A considerable amount of halo particles generated by BGS and the corresponding vacuum dependence have been predicted. To explore the probability of beam halo formation from Touschek scattering in the presence of dispersion, the Touschek scattering rate was estimated with respect to relevant beam parameters. Furthermore, a Monte Carlo simulation of Intra-Beam Scattering (IBS) and Touschek scattering is under development.

To probe the theoretical predictions, the performance of an already existing diamond sensor detector was optimized via a data rescaling technique to increase the dynamic range to 1×10^5. For a complementary diagnostics of beam halo, a YAG/OTR monitor was also designed and installed in the extraction section of ATF2. The dynamic range and resolution of the YAG/OTR monitor have been shown to be around 1×10^5 and less than 10 μm, respectively.

Thanks to the halo monitors developed at ATF2, the transverse halo and momentum tail have been studied. Satisfactory agreement between numerical predictions and measurements as well as a significant vacuum dependence indicate that the BGS process dominates the vertical halo. On the other hand, the horizontal halo appeared to be higher than the prediction from BGS, and moreover asymmetric. The observed asymmetry was shown to be related to the quality of the extraction kicker field and optical aberration. Finally, the momentum tail was for the first time observed by implementing a novel scheme of vertical dispersion adjustment and was found to be qualitatively consistent with the presence of Touschek scattering. A possible scenario for horizontal beam halo formation from Touschek scattering was also suggested.

Keywords: Beam halo, beam gas scattering, Touschek scattering, diamond sensor detector, YAG/OTR monitor, momentum tail

Acknowledgements

Great appreciation to those who have contributed to this thesis!

First and foremost, I would like sincerely thank my supervisor P. Bambade, who has guided me with great patience and constant support during my PhD research. I benefited enormously from his profound knowledge and rich experience. It would have been impossible to accomplish this thesis without his support and encouragement.

I would like to express my heartfelt gratitude to the ATF collaboration and to the staff and engineers of ATF. Special thanks to T. Naito for our fruitful collaboration on the development of the YAG/OTR monitor, discussions on the ATF damping ring tuning and the great support on halo experiments. I am also grateful to A. Aryshev, M. Bergamaschi, S. Wallon, K. Tama, S. Mazzoni, R. Kieffer and T. Lefevre for their invaluable support and help on the YAG/OTR monitor. Great thanks to K. Kubo, T. Okugi, N. Terunuma and S. Kuroda for their help on beam dynamics and experiments. Many thanks to all my colleagues on ATF, A. Faus-Golfe, D. Bett, N. Blaskovic Kraljevic, P. Burrows, V. Cilento, N. Fuster-Martinez, P. Korysko, E. Marin, Y. Morikawa, R. Ramjiawan, T. Tauchi, G. White et al., for many useful discussion and help.

Special thanks to V. Kubytskyi and S. Liu for teaching me the operation of the DS detector. I am very much indebted to K. Oide, D. Zhou, M. Kikuchi and S. Bai for their support and help with SAD simulations. I would also like to thank Y. Papaphilippou, R. Nagaoka, A. Vivoli and S. Papadopoulou for discussions and advice on the simulation of intra-beam scattering and Touschek scattering.

I would like as well to sincerely thank the referees P. Raimondi and H. Burkhardt for reading my thesis. Many thanks to A. Stocchi and R. Nagaoka for being the members of my thesis committee.

Many thanks to the Département Accélérateurs of LAL, for hosting me and for giving me the chance to work on this exciting project. I would like to thank every single person in the accelerator department, especially R. Chehab, W. Kaabi, H. Guler, I. Chaikovska, M. El Khaldi, C. Bruni, S. Chancé, N. Delerue, N. El Kamchi and J. Cayla, M. Biagini, C. Rimbault, A. Gamelin, C. Pang, K. Wang and Y. Han.

Thanks to X. Li, Z. Chen, D. El Khechen, L. Garolfi, P. Ding, Z. Hu, P. Li, Z. Li and J. Wang for their friendship, unconditional help and encouragement.

I gratefully acknowledge the financial support from the Chinese Scholarship Council.

Table of contents

Chapter 1

Introduction

1.1 Future linear colliders

Since the 1960s, high energy accelerators have played essential roles in the field of the particle physics [1–3]. The Large Hadron Collider (LHC), for instance, the world's largest (circumference 27 km) and highest energy (14 TeV, center-of-mass energy) accelerator with a record luminosity of 2.06×10^{34} cm^{-2}s^{-1} [4, 5], has been continuously devoted to the production and investigation of new particles, discovering the Higgs boson, probing its properties [6] and exploring the unsolved problems beyond the Standard Model [7–10]. At the energy frontier of experimental particle physics, high energy colliders have been among the most powerful tools to discover new particles and verify the theoretical models for new physics. The great discoveries of the subatomic particles thanks to the development of accelerators and colliders contain: the Xi or "cascade" baryon discovered at Brookhaven National Laboratory in 1964 [11], the partons observed at the Stanford Linear Collider (SLC) in 1969 [12, 13], the J/Ψ meson demonstrating the existence of the charm quark discovered at the Stanford Positron Electron Accelerating Ring (SPEAR) in 1974 [14, 15], the tau lepton discovered at SPEAR in 1975 [16], the upsilon meson demonstrating the existence of the bottom quark at the Fermilab Proton Center Laboratory in 1977 [17], the indirect observation of the evidence of gluons at the Positron Elektron Tandem Ring Anlage (PETRA) in 1979 [18], the W and Z bosons found at the CERN Proton-Antiproton collider in 1983, the top quark discovered at the Fermilab Tevatron in 1995 [19] and, again, the Higgs boson discovered at LHC in 2012 [10]. Until now, all the elementary particles predicted by the Standard Model have been discovered or confirmed, as shown in Fig. 1.1.

However, it is believed that the Standard model is an effective theory valid only up to some energy scale. Beyond this scale, some new physics is expected that can't be well explained in the context of the Standard Model. Unsolved fundamental questions in particle physics include the origin of mass, the properties of gravity, dark matter and dark energy, the asymmetry between matter and anti-matter, etc. To explain these questions, many theories have been proposed,

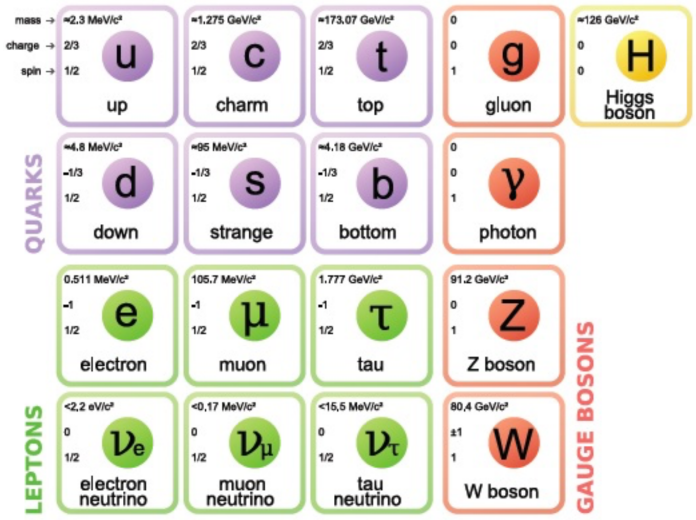

Fig. 1.1 The elementary particles in the Standard Model. Taken from Ref. [20]

e.g., string theories, supersymmetry and extra dimensions. What's more, the experimental observations at particle colliders have also made great progress.

Beyond the colliders in operation, e.g., LHC, Relativistic Heavy Ion Collider (RHIC) and SuperKEKB [21], several ambitious future colliders have been proposed including the International Linear Collider (ILC), the Compact Linear Collider (CLIC), the Future Circular Collider (FCC), the Circular Electron-Positron Collider (CEPC) and so on [22–25]. Compared with a hadron machine, a lepton collider has a significant advantage in the precise measurement of the interaction between elementary particles with well-defined initial conditions. Moreover, collisions between leptons do not involve the strong-force and can therefore provide a cleaner background environment which is favoured by the particle physicists. For the precise measurements of the physical properties of elementary particles, such as the top quark or the Higgs boson, as well as the further yet to be discovered weakly interacting particles, a lepton collider has definitely some important advantages. In the framework of lepton colliders, there are two categories: the electron-positron collider and the muon collider. Although the muon collider is normally featured by the higher cross section of the generation of Higgs boson and negligible synchrotron radiation and Bremsstrahlung, the production, acceleration and storage of muons are still critical challenges. On the other hand, an electron-positron collider is more feasible in the aspects of the technology and cost.

There are two approaches for developing electron-positron colliders, the linear collider and the circular collider. Even though the tunnel of a circular collider can in principle be re-used for an upgraded or completely new machine, as the case of the Large Electron-Positron Collider (LEP) which was followed by the LHC, the maximum energy of a circular electron-positron collider is limited by the enormous energy losses due to the synchrotron radiation, which scale like the energy to the fourth power. In contrast, linear electron-positron colliders avoid this

problem and are thought to be a favorable and efficient technology for detailed measurements of Higgs boson properties and the exploration of many related unsolved fundamental questions in particle physics. For a linear collider, the precisely tunable energy from 91 GeV to 1 TeV [26] with luminosities higher than 10^{34} cm^{-2}s^{-1} is required to achieve the required flexibility and precision to tackle these physics questions. Higgs production cross sections are shown as a function of center of mass energy in Fig. 1.2

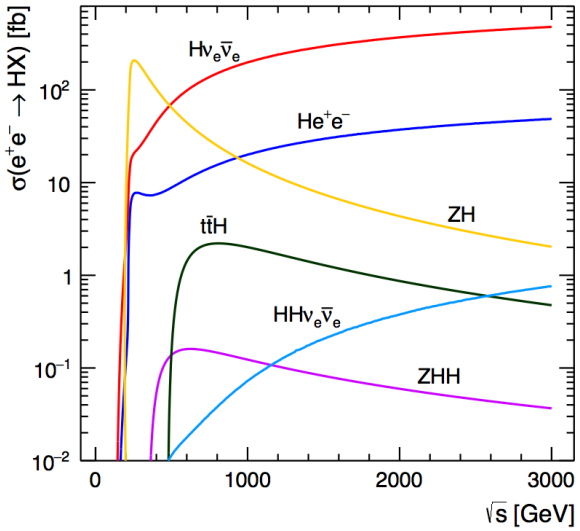

Fig. 1.2 Cross sections for Higgs production at an electron-positron collider. Taken from Ref. [27]

Regarding the accelerator part of a linear collider, the most important challenges are to achieve stable and economically affordable high gradient acceleration and high luminosity in the range of $10^{34} - 10^{35}$ cm^{-2}s^{-1}. For a Gaussian beam distribution, the luminosity of a linear collider can be expressed as [28]

$$\mathcal{L} = \frac{N^2 n_b f_{\text{rep}}}{2\pi\sigma_x^*\sigma_y^*}\mathcal{F} \tag{1.1}$$

where N is the number of particles per bunch, n_b the number of bunches per bunch train, f_{rep} the repetition rate, σ_x^* and σ_y^* the horizontal and vertical rms beam sizes at the Interaction Point (IP), respectively, and $\mathcal{F}$ the reduction factor due to the beam-beam [29–31] and hourglass effects [30, 32]. To achieve an extremely high luminosity, it is essential to focus the beam to ultra-small sizes at the IP with low beam emittances and ultra-low beta functions.

In general, a linear collider mainly consists of the electron and positron sources, the damping rings, the main linacs, the Beam Delivery Systems (BDS) and the detector. Particles from the sources are bunched, pre-accelerated and then injected into the damping ring with an energy of the order of GeV. In the damping rings, beam emittances can be damped to very small values within a short storage time (< 1 s) and then, in the main linacs, the beam energy is boosted to the desired value. Finally, the beam is focused down to hundreds of nanometers horizontally and a few nanometers vertically at the IP in the Final Focus System (FFS), which is the last part of the

BDS [33]. Besides, important beam diagnostics and collimation are also performed in the BDS. To obtain a high luminosity, i.e., low emittance beam and low β-function at the IP, the damping ring and the final focus system are of great importance.

Currently, two linear collider projects are under discussion: the ILC in Japan and the CLIC led by CERN. Both are pursued by large international collaborations of institutes and universities all over the world.

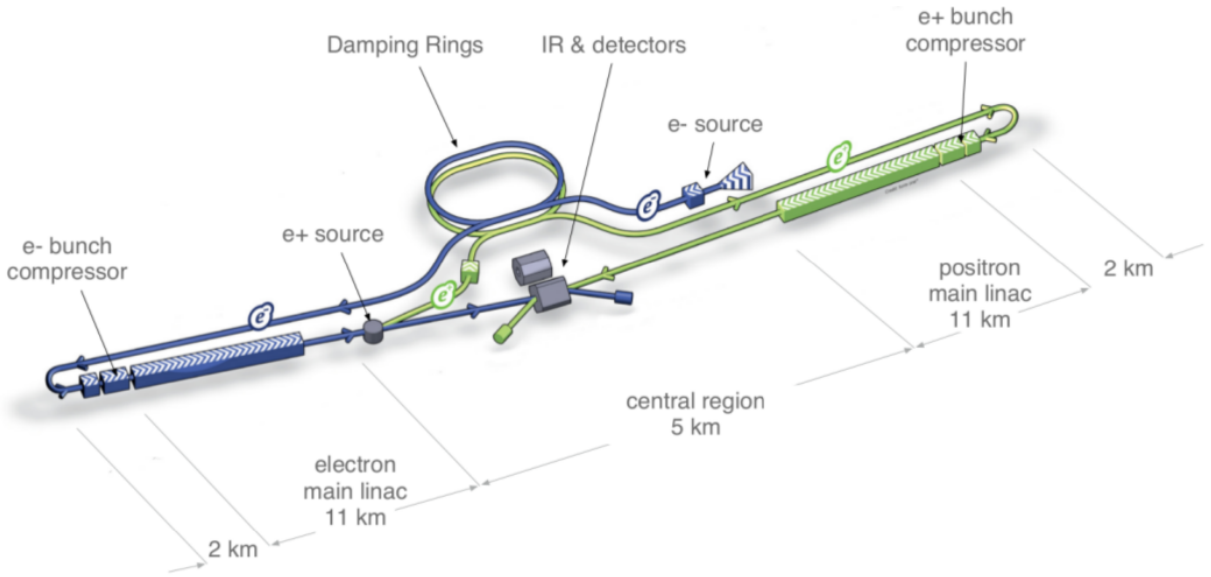

Fig. 1.3 Schematic of the ILC project. Taken from Ref. [27]

The ILC has a nominal center of mass energy of 250 GeV with the potential to be upgraded to 500 GeV [22]. The accelerator section of ILC contains the polarized electron and positron sources, two damping rings, each 3.2 km long and operating at 5 GeV, for the electrons and positrons, respectively, transport beam lines from the damping rings to the 11 km long main linacs and the 2.2 km long beam delivery systems, as shown in Fig. 1.3. In the main linac, the beam is accelerated based on the SuperConducting Radio-Frequency (SCRF) technology, with an accelerating gradient of 31.5 MV/m using the 9-cell SCRF niobium cavities [34]. Such a SC accelerating scheme has been demonstrated at the European XFEL at DESY and the present effort is devoted to reduce costs. To validate the low emittance damping ring technology and the compact final focus scheme, the Accelerator Test Facility (ATF&ATF2) has been constructed and opreated at KEK [35, 36].

The CLIC project has an initial phase of operation at 380 GeV followed by two possible stages at 1.5 TeV and 3 TeV [23] (see Fig. 1.4). Comparing to the ILC, CLIC will use an accelerating gradient of 72 MV/m (for the first stage), based on the innovative two-beam acceleration scheme [37, 38]. The feasibility of this advanced two-beam acceleration scheme has been addressed at the CLIC Test Facility (CTF3) at CERN [39, 40]. Besides, the demonstration of the CLIC final focus system is also being carried out at ATF2 [41–43]. Detailed description of the CLIC project could be found in Ref. [23].

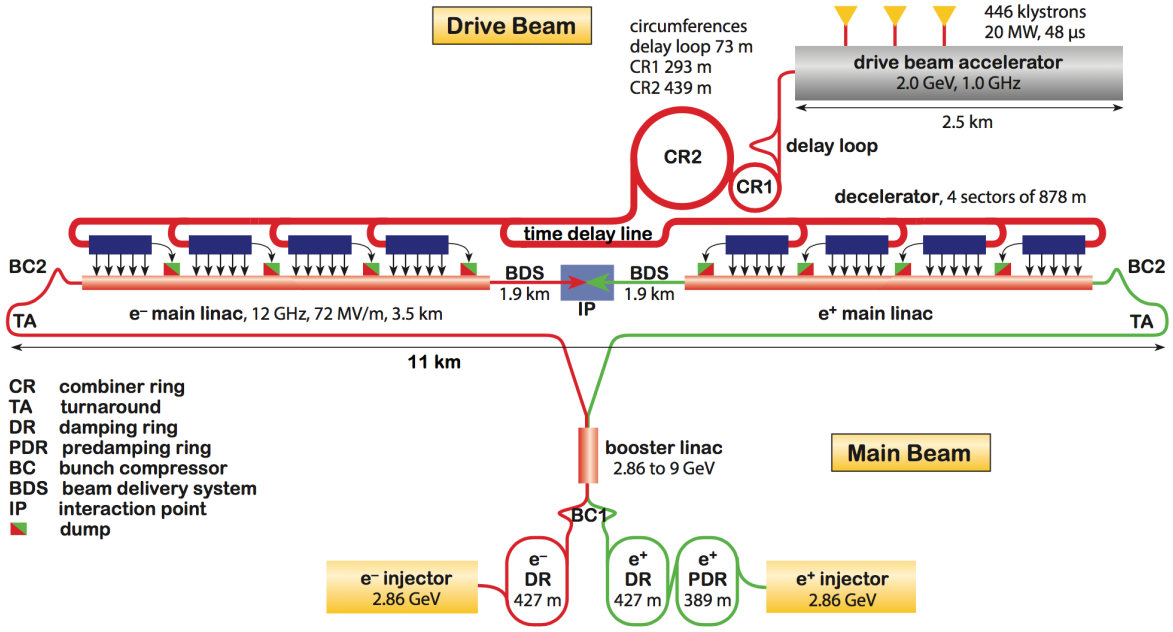

Fig. 1.4 Schematic of CLIC 380 GeV machine. Taken from Ref. [44]

In the ILC and CLIC BDS, a collimation system is always needed in order to reduce the background by removing the halo particles with large betatron amplitudes or large momentum deviations [45]. Also, the collimation system can provide a necessary protection for the downstream components in case of a sub-system failure.

A sufficient collimation system must fulfill many specific requirements [46, 47]: high cleaning efficiency, high mechanical robustness and low wakefield (impedance) effect [48]. To meet the above requirements, a conventional collimation system, consisting of spoilers and absorbers downstream, is usually considered [49]. Besides, some innovative halo collimation concepts have been proposed and demonstrated [50–52]. No matter which kind of collimator scheme is applied, an accurate modeling of beam halo (betatron and momentum halo) based on an existing machine is doubtless of critical importance. As pointed out in Ref. [53], a serious issue in the design of a robust collimation system is the lack of a precise model of the beam halo. For the linear collider, the primary mechanisms of beam halo formation can be typically summarized in several categories:

- Physical particle processes, including elastic beam-gas scattering [54], beam-gas Bremsstrahlung [55], Touschek scattering [56], scattering off thermal photons [57] and beam-beam interaction [58]
- Optical related mechanisms, for instance, mismatch [59, 60], misalignment [61, 62], dispersion [63], non-linearity [64] and resonance [65]
- Other processes, including wakefields [66], dark current [67] and secondary emission [68]

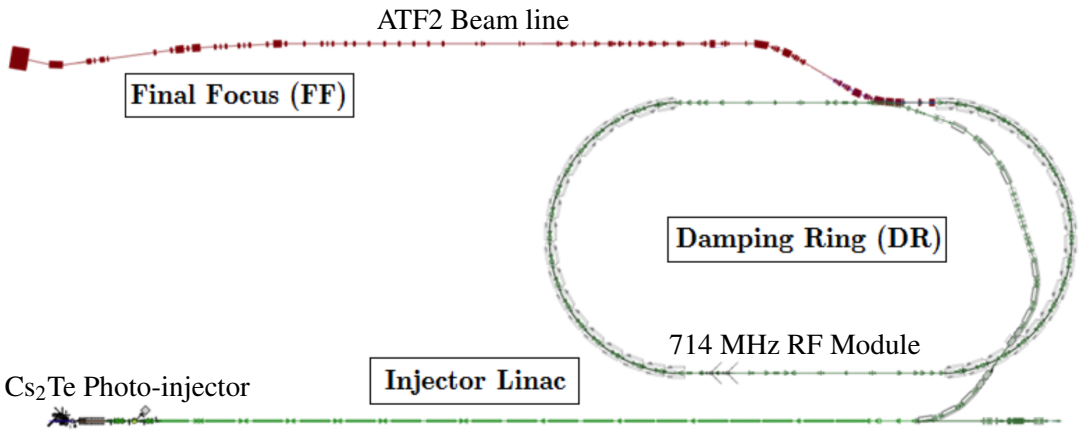

Fig. 1.5 Schematic of ATF accelerator complex. Notice that the old extraction line has been replaced by a new extended extraction line: ATF2.

1.2 Accelerator Test Facility at KEK

The Accelerator Test Facility at KEK has been construted to study the feasibility of producing the low-emittance beam required at a linear collider as well as supply a high-quality beam for the R&D activivities on beam instrumentation and control technologies needed at linear colliders. It contains an electron source based on a Cs_2Te photo-cathode RF gun, a 1.3 GeV injector linac, a Damping Ring (DR), and an extraction line, in which the ATF2 beam line was later built [69] (see Fig. 1.5).

The ATF DR is a race-track type storage ring with a circumference of 138.6 m. In the arc sections, there are 36 FOBO cells, where B represents the combined-function bending magnet. Such bending magnets can provide a horizontally defocusing field and reduce the horizontal dispersion function in arc sections. The phase advances per FOBO cell are $\pi/2<\nu_x<5\pi/6$ and $\pi/6<\nu_y<\pi/3$, horizontally and vertically, respectively, and can be adjusted using two independent quadrupoles in the cell [36]. A RF cavity operated at a frequency of 714 MHz and a cavity-gap voltage around 300 kV has been integrated to compensate the energy loss due to synchrotron radiation. The critical parameters of the ATF DR, as well as those of the ILC and CLIC DR, are outlined in Tab. 1.1.

The smallest vertical emittance of 4 pm, $\gamma\varepsilon_y = 1.1 \times 10^{-8}$ m, was achieved at low beam intensity around 1×10^9 e/bunch [73, 74]. Tuning of the low-emittance beam was realized through iterating a series of corrections: the Closed-Orbit Distortion (COD) correction, vertical COD correction + vertical dispersion correction, and *xy* coupling correction. Thanks to such well-developed tuning techniques, the vertical emittance can be typically be maintained at the level of 12 pm, about 1% of the horizontal emittance, during the daily operation at ATF.

To address the feasibility of focusing the electron beam to a small beam size (tens of nanometers), vertically, and provide beam orbit stabilization at the nanometer (nm) level at the IP, a prototype FFS based on the local chromaticity correction principle [75] has been constructed

Table 1.1 Lattice parameters of the ATF damping ring, the ILC damping ring in the low-power mode (5 Hz) and the CLIC damping ring [27, 36, 70–72].

	ATF DR	ILC DR	CLIC DR	
		5 Hz mode	2 GHz	1 GHz
Energy [GeV]	1.3	5	2.86	
Particles/bunch [10^{10}]	<2	2	0.41	
Number of bunches	<10	1312	312	156
Repetation rate [Hz]	3.12	5	50	
Circumference [m]	138.6	3238	427.5	
Momentum compaction factor	2.14×10^{-3}	3.3×10^{-4}	1.3×10^{-4}	
Damping time (x/y/s) [ms]	17/27/20	24/24/12	2/2/1	
Storage time [ms]	200	100	20	
Normalized natural horizontal emittance [μm]	2.8	57	53.9	
Natural energy spread	5.6×10^{-4}	0.1%	0.1%	
Natural chromaticity (ξ_x/ξ_y)	29.6/20.6	-51.3/-43.3	-18.99/-22.85	
Natural bunch length [mm]	5.3	6.02	1.6	1.8
Energy loss per turn [MeV]	0.044	4.5	4.0	
RF frequency [GHz]	0.714	0.65	2	1
Total RF voltage [MV]	0.28-0.33	14	10	
Lattice type	FOBO	FODO	TME (arc) FODO (straight)	

at ATF. This extensive extraction line is the so-called ATF2. As an energy-scaled version of the compact final focusing optics for the ILC, ATF2 consists of an extraction section for dispersion and coupling correction, a β-matching section and a Final Focus (FF) section to demagnify the transverse beam optics at the IP [76]. The schematic of the ATF2 beam line and the corresponding betatron and dispersion functions are presented in Fig. 1.6.

In front of the FF section, the beam is first extracted from the ATF damping ring through a pulsed kicker magnet, followed by three successive septum magnets, and then enters a "dogleg" type inflector, as shown in Fig. 1.7. The optics in the inflector consists of a "pseudo-I" transformation ($\Delta u_x=\pi/2$ and $R_{21} \neq 0$) between the kicker magnet and the second kicker "KEX2"[1]. The maximum horizontal dispersion in the inflector does not exceed 600 mm at the QF1X and QF6X quadrupoles, close to which two additional skew quadrupoles (QS1X, QS2X) have been installed for dispersion correction and coupling correction. After the inflector, an ILC-style coupling correction module, consisting of four skew quadrupoles QK1–QK4, enables the orthonormal correction of all transverse couplings [78]. The multi-OTR system, composed of four OTR monitors, is then used to provide fast single-shot emittance measurements, as well as the xy tilt imaging before and after coupling correction [79]. After the diagnostic section, six bipolar

[1]The second kicker KEX2, paired to the first kicker with a goal of achieving a partial cancellation of the corresponding jitter was later replaced by a regular dipole [77].

quadrupoles (QM16–QM11) are used for optics matching (beta functions) between the extraction section and FF section.

The FFS of ATF2 is based on the local chromaticity correction scheme, which can compensate the chromaticity and other optical aberrations locally, using as few elements as possible. The final doublet (QD0 and QF1) focus the beam at the IP and the predominant chromaticity generated by this strong final doublet is cancelled thanks to the two sextupoles (SD0 and SF1), placed adjacent to the final doublet ,and the three dipoles (B1FF, B2FF and B5FF) upstream to generate the necessary horizontal dispersion [81–83]. The accompanying second-order dispersion is canceled by additional chromaticity generated upstream. Three additional sextupoles (SD4, SF5 and SF6) plus an appropriate adjustment of the optical transfer matrices further compensate higher order geometric and chromogeometric aberrations generated in the FFS system, as shown in Fig. 1.8. Notice that the phase advance between sextupoles and the IP is $(n+\frac{1}{2})\pi$. To loosen the tolerance to multipole field errors and to enable second-order aberration corrections, four skew sextupoles (SK1–SK4) have also been installed in the FF section. However, tuning of the small beam size is still extremely complicated in the real machine because of both expected and unexpected imperfections, e.g., the wakefield, beam jitters, misalignments and ground motion.

To measure a beam size less than a hundred nanometers with enough accuracy, a *Shintake* monitor [84–86] has been installed at the IP. Two paths of a laser are focused at the IP to form a vertically-orientated interference fringe pattern. The phase of the interference pattern is scanned by adjusting the path length of one incident laser beams relative to the electron beam, as shown in Fig. 1.9 (a). The beam size is then inferred from the modulation depth (M_d) in the rate of photons resulting from the Compton scattering of the beam electrons, as collected by a photon detector consisting of a CsI(Tl) calorimeter. The relation between the vertical beam size and the modulation depth can be expressed as [78]

$$\sigma_y = \frac{d}{2\pi}\sqrt{2\log\left(\frac{C|\cos\theta|}{M_d}\right)} \tag{1.2}$$

with

$$d = \frac{\lambda}{2\sin(\theta/2)}$$

where d is the fringe pitch, θ the crossing angle, C the reduction factor and λ the laser wavelength. The reduction factor represents the contrast reduction of the laser fringe pattern from the laser profile distortion, mismatching in the laser overlap and other possible sources. The *Shintake* monitor can be operated in three modes, by adjusting the crossing angle: 2°– 8° mode, 30° mode and 174° mode. It can cover a beam size from several microns down to a minimum of 20 nm by switching the operational mode remotely, as shown in Fig. 1.9 (b).

The modulation depth can also be significantly reduced due to background photons at the Post-IP, which is considered as a systematic error of the modulation measurement. The undesired background predominantly comes from halo particles lost in the final doublet and bending

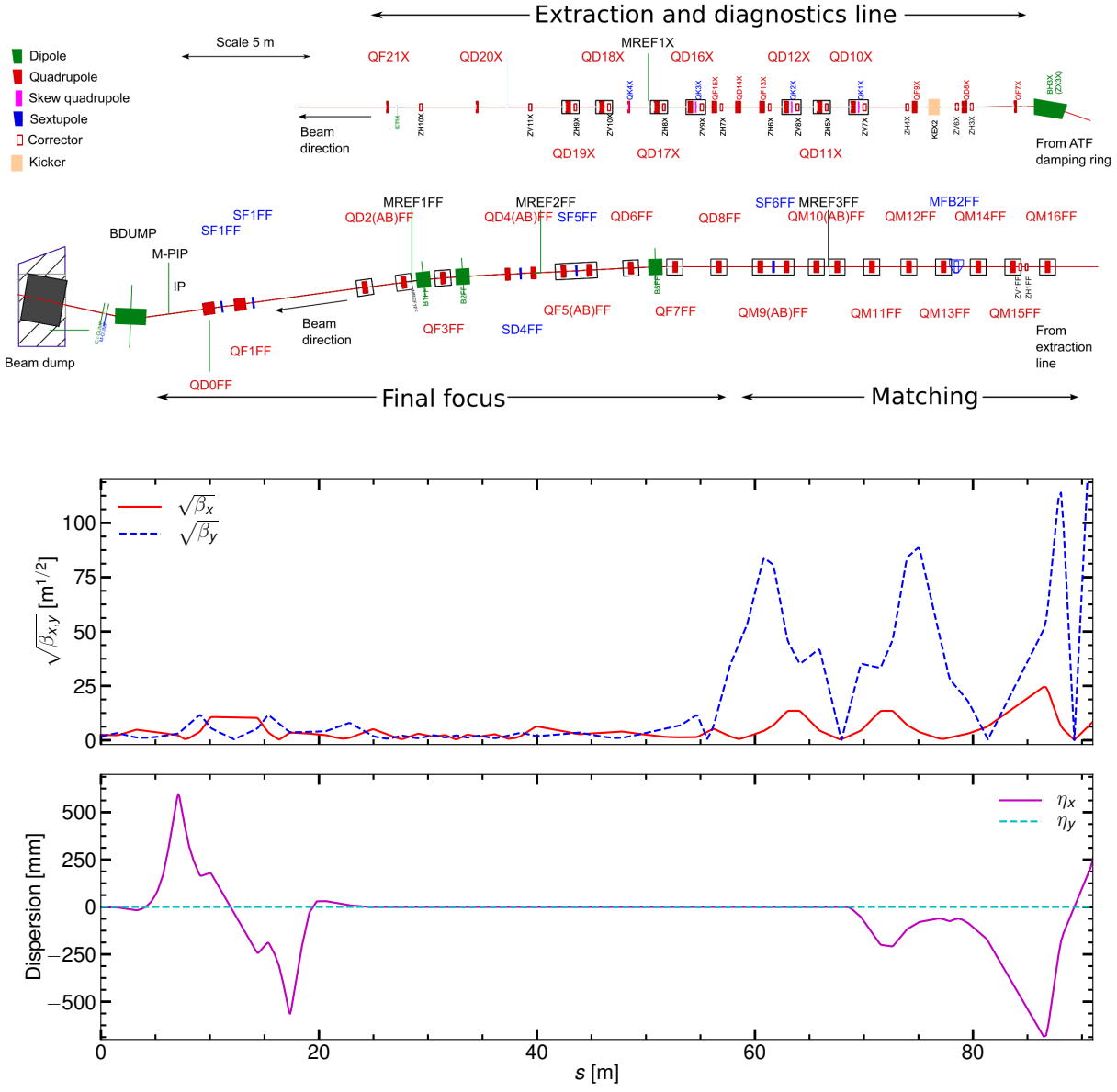

Fig. 1.6 Upper: Schematic of the extraction line, β-matching section and the final focus section of ATF2 (from the ending of the inflector). Taken from Ref. [80]. Bottom: beta functions and dispersion functions of ATF2 for the $10\beta_x^* 1\beta_y^*$ optics.

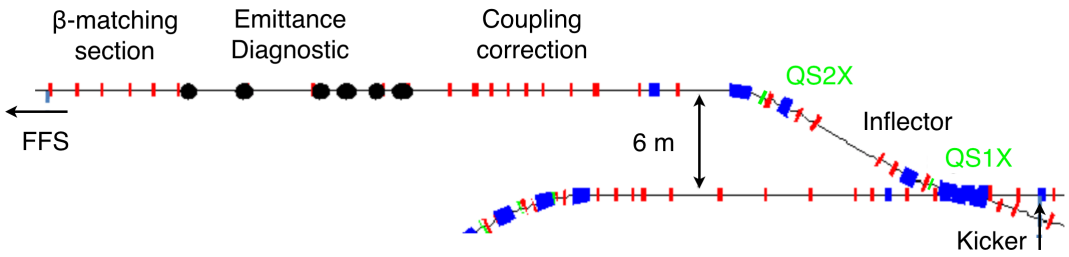

Fig. 1.7 Schematic of the ATF2 extraction section and β-matching section.

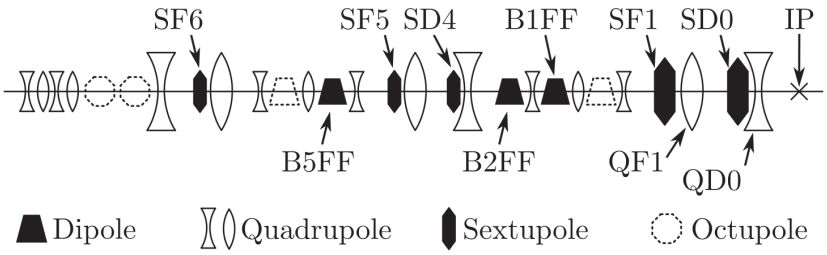

Fig. 1.8 Schematic of the ATF2 FFS. Taken from Ref. [80]

magnet behind the IP. To suppress the background, cone-shape collimators have been placed in front of the photon detector [85]. Moreover, a vertical collimator has been installed in the FF section to remove the vertical betatron halo. Measurements of the modulation depth as a function of the collimator aperture indicate a considerable influence of the background induced by particles lost near the IP, as shown in Fig. 1.10. In terms of small size tuning and measurement, it is definitely crucial to have a reliable beam halo model at ATF2 and establish an efficient collimation system.

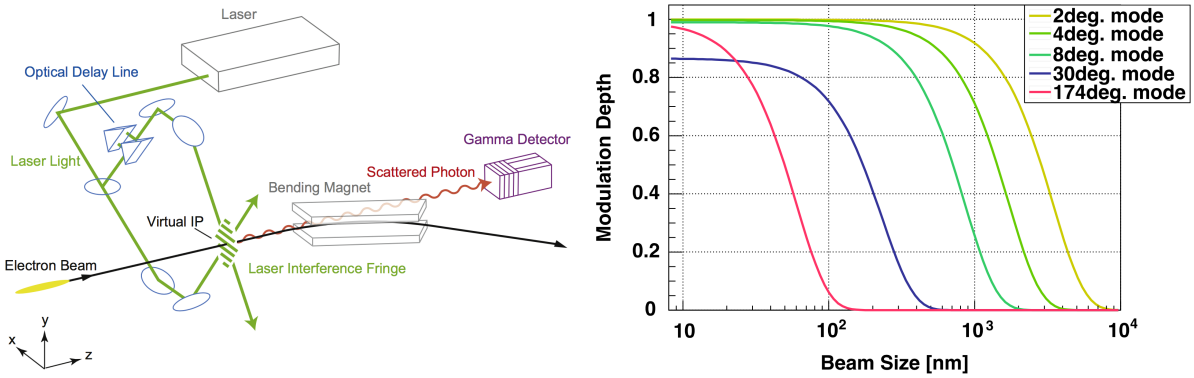

(a) (b)

Fig. 1.9 Schematic of the *Shintake* monitor at ATF (a) and the relation between beam size and modulation depth in different modes (b). Figures are taken from Ref. [86].

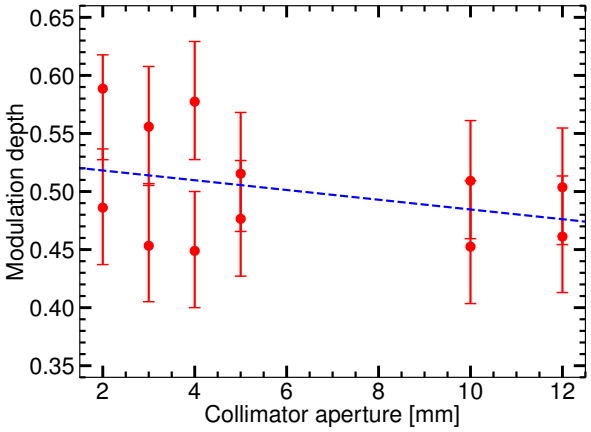

Fig. 1.10 Dependence of the modulation depth on collimator aperture. Notice that the *Shintake* monitor is in 30° mode and the beam intensity is stablized at 7×10^9 e/pulse. The figure is reproduced from Ref. [87]

1.3 Halo diagnostics

The issue of beam halo commonly exists in all accelerators but a general definition of "halo" is complicated because it should be with respect to the requirements of each specific machine, including its required beam physics investigations. In the workshop on Beam Halo Dynamics, Diagnostics, and Collimation (HALO'03), a common statement was given, i.e., "... a general definition of 'beam halo' could not be given, because of the very different requirements in different machines, and because of the differing perspectives of instrumentation specialists and accelerator physicists... from the diagnostic point of view, one thing is certainly clear – by definition halo is low density and therefore difficult to measure..." [88]. In some literature, the beam profile is therefore divided into three parts referring to beam center: beam core, beam tail and beam halo. However, the difference between tail and halo is typically ambiguous. As a consequence, in this dissertation, "halo" stands for both tail and halo parts if there is no additional specification.

Diagnostics of beam halo are of great importance for the mitigation of halo particles through the optimization of machine conditions and an efficient collimation system. Typically, halo diagnostics can be classified into three categories [89]: 1) direct measurements of halo and its evolution, e.g., Wire Scanners (WS) [90, 91], optical methods based monitors [92–96] and diamond detectors [97, 98]; 2) measurements of the effects of halo particles, e.g., beam loss monitor [55]; 3) diagnostics of machine condition stimulated halo particles, e.g., the tune measurement system [99]. Different from the ordinary beam profile measurements, diagnostics of beam halo require a dynamic range of at least 10^5 for the simultaneous measurement of beam core and beam halo, in order to appropriately probe the theoretical predictions [100, 68]. In this section, an overview of various kinds of halo monitors in the above categories, developed in the past decades, is presented.

For the direct detection of halo particles, a primary example is the WS. To ensure a satisfactory dynamic range, several upgraded versions of the WS have been reported, e.g., the halo scraper/wire scanner [90, 101], the wire scanner with the varying Photomultiplier Tube (PMT) voltage [102] and the vibrating wire scanner [103–106]. The scraper/wire scanner uses a thin wire to measure beam core and a paddle type structure (scraper) to measure beam tail/halo. The scraper data is then normalized to the wire core data by matching two sets of data in the overlapping regions. A dynamic range of around 10^5 can be achieved via the combination of wire scanner and halo scraper [107]. Besides, to extend the dynamic range of the WS, diagnostics of core and halo particles could be performed with varying PMT voltage and then by normalizing core and halo distributions in the overlaps between measurements. Experiments at ATF2 have demonstrated a dynamic range of 10^4 in this method [102]. Using multiple wires of different diameters, an extremely high dynamic range of 10^8 has been achieved after applying a coincidence technique at the Continuous Electron Beam Accelerator Facility (CEBAF) [108], as shown in Fig. 1.11. In their case, four PMTs were placed around the beam (top, bottom, left and right) to count the Cerenkov or scintillation light from halo particles striking the quartz window and the scintillator+quartz window.

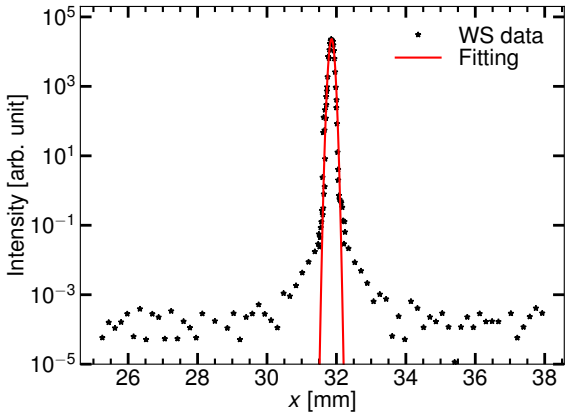

Fig. 1.11 Horizontal beam profile by combining data of the 25 μm and 1 mm Iron (Fe) wires. Figure is reproduced from Ref. [108]

In addition to the conventional WS measuring the beam profile by counting the secondary radiation due to particles going through the wire, a vibrating wire scanner has been proposed and proved to have a dynamic range over 10^5. The principle of the vibrating wire scanner can be summarized as: the interaction between beam and wire heats the wire and results in a temperature increase. As a result, the frequency of the natural oscillation of the wire is changed, and the beam profile information can be obtained from that change, using the analytic expressions [105]

$$\Delta f = -0.25 \frac{f_0 E \alpha_s T_{\mathrm{m}}}{\sigma} \tag{1.3}$$

with

$$f_0 = \frac{1}{2l}\sqrt{\sigma/\rho}\left(1+\frac{d}{2l}\sqrt{E/\sigma}\right) \tag{1.4}$$

where f_0 is the frequency of the first harmonic of the wire oscillations, E the modulus of elasticity, α_s the coefficient of thermal expansion, T_m the temperature change due to the incident particles with respect to the temperature of the environment, σ the stress of the wire for a length of l, ρ the density of the wire material and d the diameter of the wire. The natural oscillation is excited by the interaction of an alternating current through the wire immersed in a permanent magnetic field. An advanced design of such a vibrating wire scanner employs two mechanically coupled wires. One acts as the vibrating wire to measure the strain of the other wire (target wire) which interacts with the halo particles [106], as shown in Fig. 1.12 (a). The dynamic range of this improved vibrating wire scanner is around 10^5, as shown in Fig. 1.12 (b).

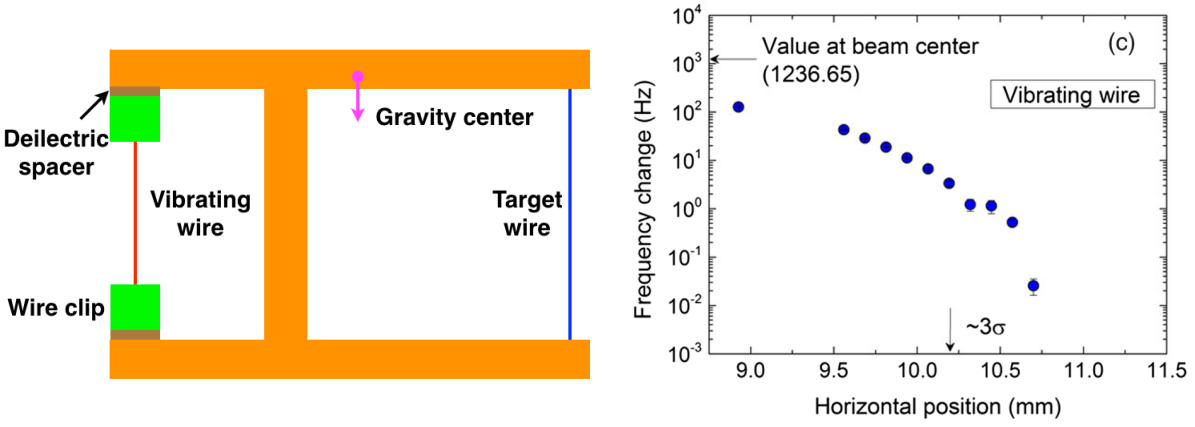

Fig. 1.12 Schematic of the desgin of two mechanically coupled wires (a) and the halo distribution measured by this vibrating wire scanner (b). Figures are reproduced/taken from Ref. [106]

Halo measurements through optical methods are usually hampered by the dynamic range of the camera sensor (typically, 16 bit) and the "blooming" effect, i.e., the enhancement of the actual halo distribution due to scattered/coupled light from the bright core. To overcome these limitations, several remarkable methods have been developed, for instance, data acquisition using a cooled Charge Injection Device (CID) [96], observation using a coronagraph [109, 110], a masking method based on a Digital Micromirror-array Device (DMD) [94] and a combination of OTR and fluorescence screens [111].

The commercial CID has an excellent dynamic range exceeding 10^6 thanks to its capacity for non-destructive pixel readout, i.e., the photon-generated charge may be transferred in each individually addressable pixel and provide a signal without destroying the charge signal [112]. Light detection with a CID camera has been demonstrated at CTF3 using a pulsed diode light source to approach the Optical Transision Radiation (OTR) light from the electron beam [96]. Measurements using an 8-bit CCD camera, a PMT set up and a CID camera (SpectraCAM$^{\mathrm{TM}}$84)

indicate that the highest dynamic range ($> 10^5$) is achieved with the CID camera [93], as shown in Fig. 1.13. However, the poor radiation hardness and the high price of CID camera might limit its applications in accelerator beam diagnostics.

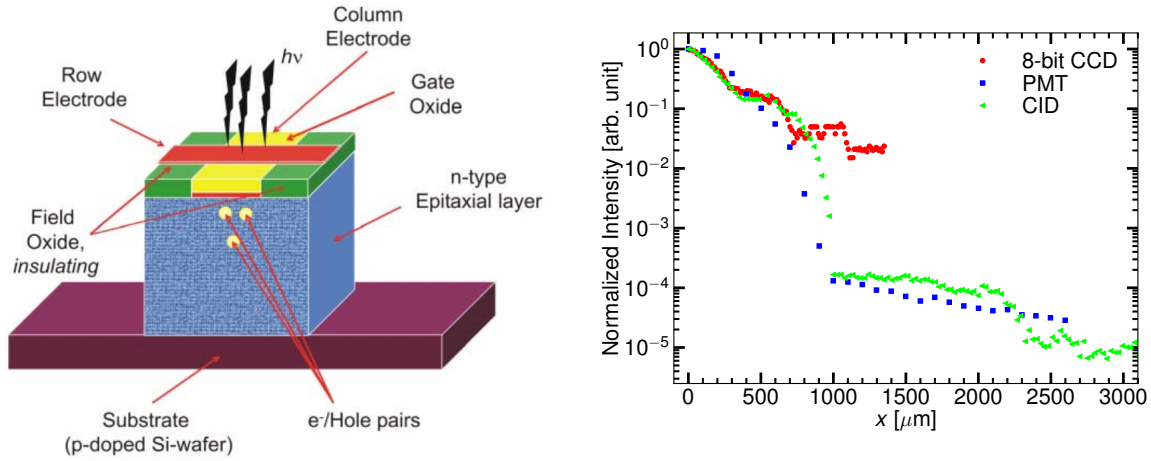

(a) (b)

Fig. 1.13 Schematic of the pixel configuration of the CID imager (a) and the intensity distributions measured by an 8-bit CCD camera, a set of PMT and a CID camera at CTF3. Figures are taken/reproduced from Ref. [93]

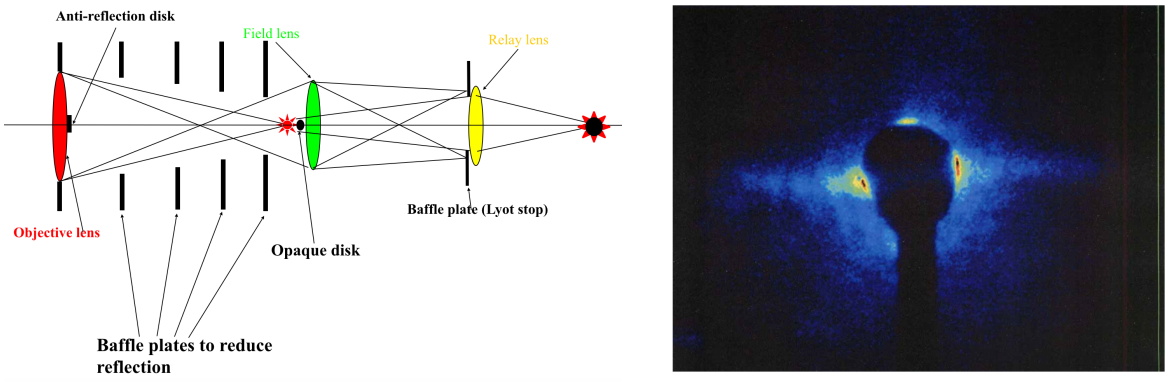

(a) (b)

Fig. 1.14 Layout of the optical system of a coronagraph (a) and an example of the beam halo observed using the coronagraph at the PF storage ring (b). Figures are taken from Ref. [113]

Motivated by the coronagraph to observe the corona of the sun via artificial eclipse, halo diagnostics based on the concept of coronagraph have been developed. The observing system with a coronagraph is merged in a synchrotron radiation beam profile monitor to allow the non-invasive diagnostics of beam core and beam halo. To suppress the light from the beam core, an opaque disk is placed in the image plane to filter out the glare of the beam image. Besides, a re-diffraction system with a mask (Lyot stop) is inserted before the objective lens to eliminate

the diffraction finger, as shown in Fig. 1.14 (a). A signal to background ratio of 1.7×10^6 has been achieved with a well-polished objective lens at the Photon Factory (PF) [113]. An example of the halo image with the opaque disk is shown in Fig. 1.14 (b).

An alternative technique to suppress the light scattered or diffracted from the bright core is to generate a "core block" using the DMD array. Each pixel of the DMD array can be individually controlled and rotated about its diagonal, which makes the DMD become a programmable spatial filter (see Fig. 1.15 (a)). This filtering function leads to a significant improvement of the dynamic range (up to 10^5) as demonstrated at the University of Maryland Electron Ring (UMER) and the JLAB 100 MeV Energy Recovery Linac with an 8-bit CCD camera [114], as shown in Fig. 1.15. What's more, an optical observation system based on a DMD can produce a core block with arbitrary shape and size, and is, therefore, suitable for any incoherent radiation source, for example, OTR light and fluorescence light.

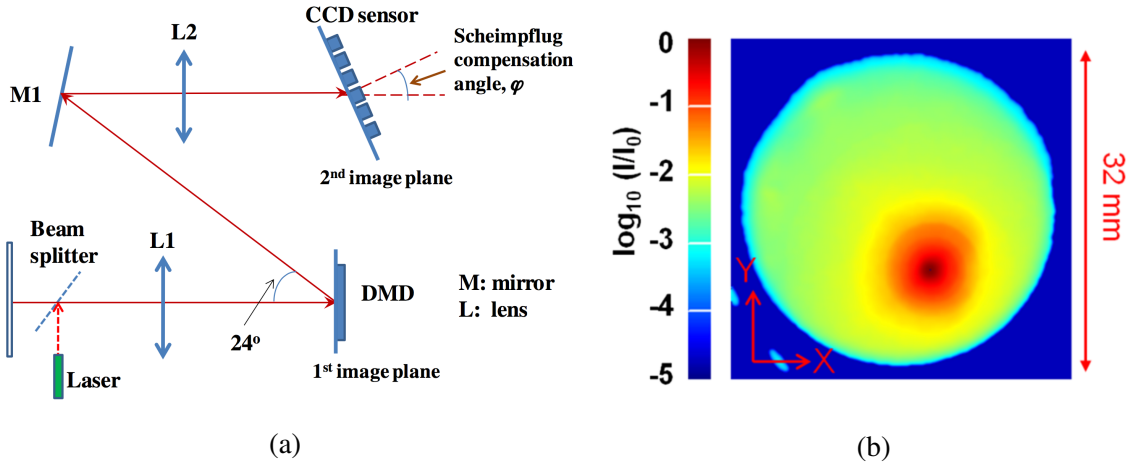

(a) (b)

Fig. 1.15 Schematic of the optical imaging system with a DMD (a) and an example of the reconstructed 2D beam profile given by a DMD based halo monitor at the UMER (b). Figures are taken from Ref. [94]

Besides, an OTR screen with a hole bored in the center has been used to measure both beam core and beam halo at the ELSA linac [115, 116]. The beam is steered towards the hole to make most of the core particles pass through, and only halo particles hit the screen. Hence, the influence from the bright core is suppressed. The dynamic range based on this scheme has been demonstrated to be about 10^4 [115], mainly restricted by the low photon production of the OTR screen. To handle this issue, measurements of beam core and beam halo using OTR and fluorescence screens, respectively, have been carried out at J-PARC [111]. By combining the OTR and fluorescence images with respect to the light yield abilities of two screens, a dynamic range of 10^6 has been achieved for the projected 1D beam distribution, as shown in Fig. 1.16.

Thanks to the excellent radiation hardness, heat resistance and small leakage current, the diamond-based beam profile monitors have been used in several machines, e.g., LHC [117], SPring-8 Angstrom Compact free electron LAser (SACLA) [97, 98] and KEK-ATF [118]. The dynamic range of the diamond-based monitor is typically around 10^4 limited by the pick-up

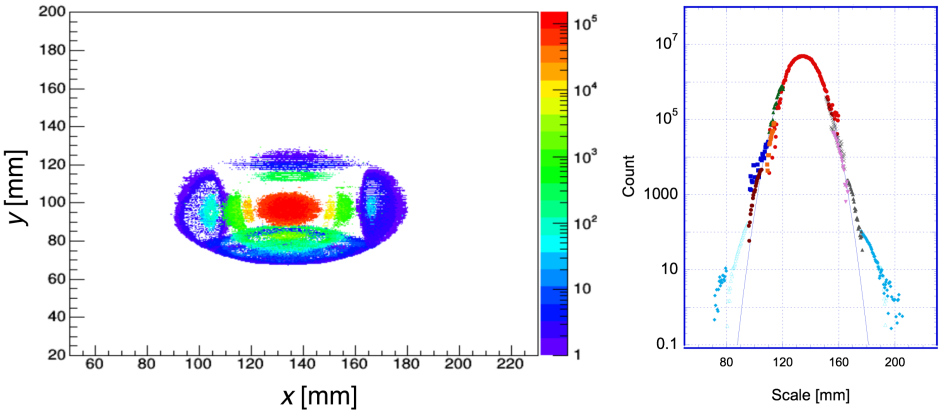

(a) (b)

Fig. 1.16 Examples of a 2D beam profile (a) and its projection in the horizontal plane (b) acquired by the OTR/fluorescence screens at J-PARC. Figures are taken from Ref. [111]

signal (induction current) and the charge-collection saturation. The diamond-based beam halo monitor at SACLA, for example, employed the Chemical Vapor Deposition (CVD) diamond to monitor halo particles and provide information to protect undulator permanent magnets, as shown in Fig. 1.17 (a). The dynamic range of the improved detector reaches 10^4 after adopting the RF fingers and the necessary shielding of the electronic circuit using a microstrip line structure to reduce the pick-up signal [98], as shown in Fig. 1.17 (b).

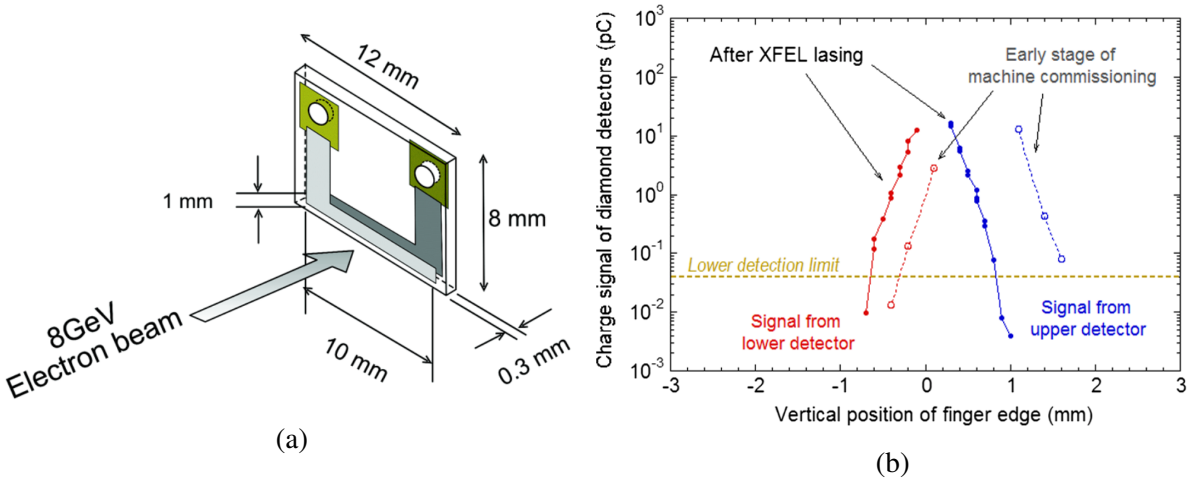

(a) (b)

Fig. 1.17 Schematic of the diamond-based detector at SACLA (a), and the charge collection versus the vertical position of the finger edge (distance from beam center) before and after the lasing of the free-electron laser (b). Notice that only the bottom of the diamond sensor, 10 mm$\times$1 mm$\times$ 0.3 mm dimension, is active. Figures are taken from Ref. [98]

Besides, tail/halo scanning with the collimator jaw has been proposed at LEP. The loss rate, which is proportional to the population of halo particles, for different collimator apertures is recorded by a PIN-diode-type beam loss monitor attached to the collimator, as shown in Fig. 1.18 (a). Measurements of horizontal beam halo indicate a dynamic range about 10^4,

as shown in Fig. 1.18 (b). Unfortunately, it is not easily possible to measure the beam core distribution with this technique.

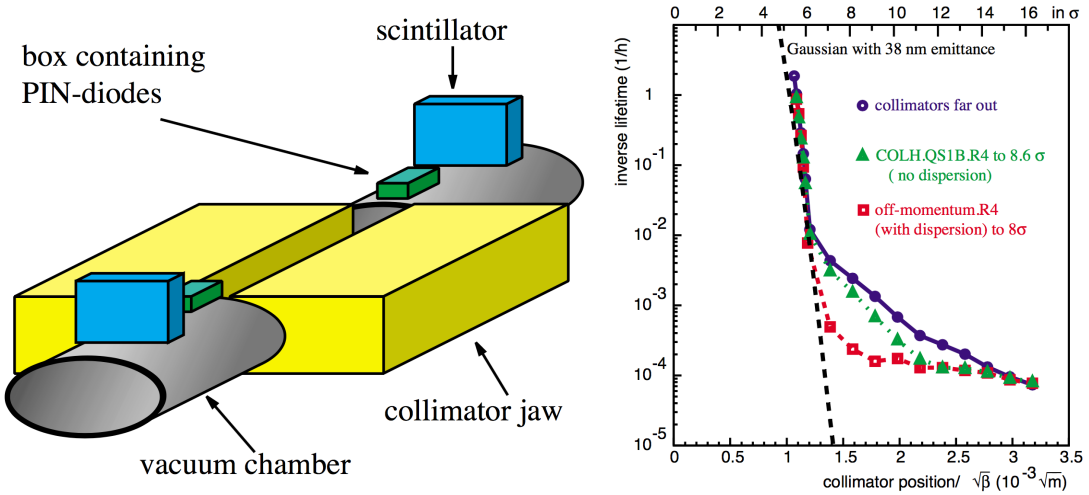

(a) (b)

Fig. 1.18 A collimator with PIN-diode-type loss monitors and scintillators on both sides (a) and the measured horizontal beam halo distribution at LEP (b). Figures are taken from Ref. [55]

Non-invasive diagnostics can supply on-line measurements of beam halo while maintaining stable beam operation. Devices developed for non-destructive halo monitoring include the coronagraph, the Ionization beam Profile Monitor (IPM) [119–121], the ultra-thin gas jet monitor [122], the scattered electron based monitor [123] and so on. The IPM typically consists of electrodes to generate external electric fields, magnets to generate a deflecting magnetic field and Microchannel Plates (MCPs) for the detection of the produced ions and electrons. Ions and electrons generated due to interactions between beam and gas atoms are deflected in the electric/magnetic field and projected on the MCPs, as shown in Fig. 1.19 (a). However, the dynamic range for beam distributions reconstructed from the MCP signal does not exceed 10^3 for most IPMs. The ultra-thin gas jet beam profile monitor, which works similar to the wire scanner but is non-interceptive, has been proposed for CLIC. The configuration of a thin gas jet monitor is like that of the IPM, but the scattering rate can be enhanced using a dense gas jet, as shown in Fig. 1.19 (b). Finally, beam halo observation using the scattered electrons from the interaction between ions and electron beams in an electron lens has been proposed at RHIC [123]. The feasibility and dynamic range of halo diagnostics with these last two monitors are expected to be demonstrated soon.

In conclusion, various methods have been developed to enable a sufficient dynamic range, typically over 10^5, for beam halo studies. These methods need to overcome two main issues: the probing of few particles with an adequate signal-noise ratio and the capability to simultaneously measure beam core and beam halo. A common feature of all the measurements is the relatively complex diagnostic system and data analysis. Some diagnostics could image the whole beam profile while some devices are dedicated to beam halo measurement. However, for the investiga-

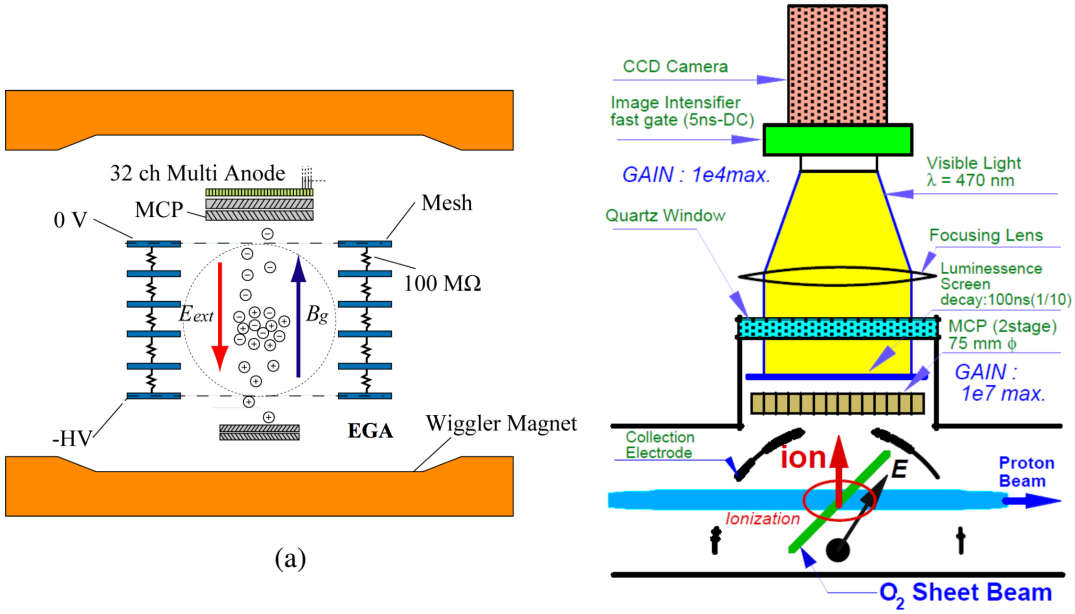

Fig. 1.19 Schematics of an IPM at J-PARC (a) and a gas jet scanner at Cockcroft Institute (b).

tion of halo dynamics, a valid and precise measurement of beam halo plus the information of the beam core are always desirable. For the future high repetition and high energy machines, non-invasive diagnostics of beam halo would be tremendously advantageous.

1.4 Halo studies at ATF

Explorations of the halo distribution and its generation have been sustained for many years at ATF. Previous investigations, including the theoretical estimations and experimental measurements, have indicated a significant halo at the extraction line. Furthermore, a preliminary parameterization of the halo distribution has been obtained based on these measurements.

Theoretically, an approximation to the halo distribution from stochastic processes has been given firstly by K. Hirata and adapted to the ATF damping ring in 1992 [124]. Meanwhile, T. Raubenheimer has also derived analytical approximations for the beam profile distortion in the presence of elastic beam-gas scattering and intra-beam scattering [125]. These theoretical models predicted a considerable beam halo resulting from elastic beam-gas scattering in the damping ring (see Chap. 2 for the details). Moreover, D. Wang has tried to extend Hirata's model more generally for elastic/inelastic beam-gas scattering or intra-beam scattering [126]. Unfortunately, the above theoretical approximations have not been entirely validated through systematic experimental measurements.

Experimental study of beam halo at ATF/ATF2 were much delayed because of the lack of a high dynamic-range halo monitor. In 2005, the first beam halo measurement at ATF was

performed using the wire scanners in the original extraction line [127]. With a dynamic range of about 10^4, the systematic measurements enabled defining a realistic beam halo model, based on the parameterization

$$f(x) = \Lambda(x/\sigma_x)^{-3.5}, \qquad x > 3\sigma_x$$
$$f(y) = \begin{cases} \Lambda(y/\sigma_y)^{-3.5}, & 3\sigma_y < y \leq 6\sigma_y \\ \frac{3.7\Lambda}{22}(y/\sigma_y)^{-2.5}, & y > 6\sigma_y \end{cases} \tag{1.5}$$

where Λ is a factor related to the beam intensity, and σ_x and σ_y are the horizontal and vertical beam sizes, respectively. The measured profile has a clear Gaussian beam core with an exponential beam tail/halo, as shown in Fig. 1.20 (a).

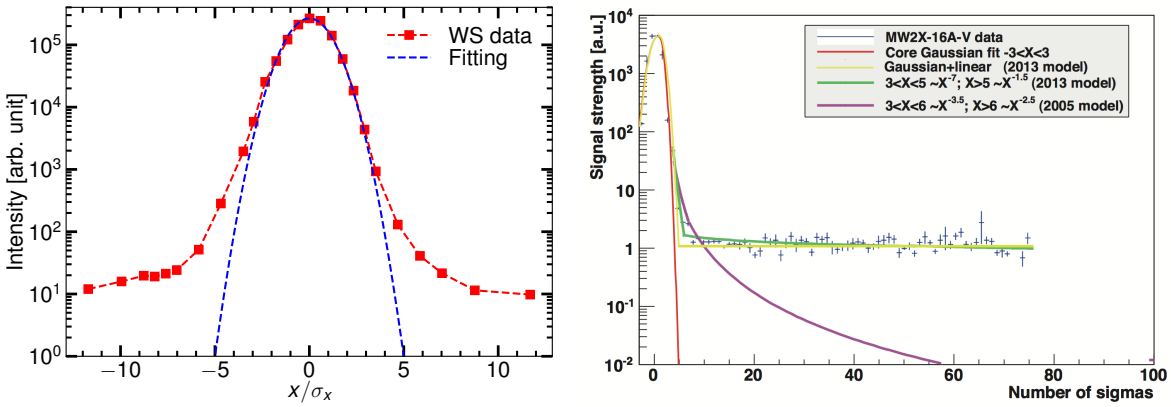

(a) (b)

Fig. 1.20 Examples of beam halo measured by the WS at ATF. (a): the horizontal beam profile at the old extraction line, reproduced from Ref. [127]; (b): the vertical beam profile at the Post-IP, taken from Ref. [102].

After, the old extraction line and the wire scanners were removed, and another wire scanner was installed after the virtual IP of ATF2, to allow transverse beam profile measurements reflecting the beam angular divergence at the IP. Recently, beam core and beam halo have been scanned with varying voltages for the PMT. Then, the readout was corrected taking into account the resulting different PMT gains [102]. The dynamic range of these measurements is around 10^4, limited by the sensitivity of the PMT as well as unwanted background noise presented at the Post-IP location, as shown in Fig. 1.20 (b).

To probe the halo particles and the Compton recoil electrons, a set of *in-vacuum* single crystal Chemical Vapor Deposition (sCVD) Diamond Sensor (DS) detectors have been installed at ATF2 (behind the WS) [128]. A linear dynamic range around 10^4 has been demonstrated for these DS detectors. Cuts of the transverse beam profile due to a tight beam pipe and the vacuum dependence of vertical and horizontal halo have been observed using these DS detectors [118]. Details and further investigations are presented in Chap. 3.

Additionally, halo observation using Cerium-doped Yttrium Aluminium Garnet(Ce:YAG) screen, which has a high photon yield and radiation hardness, were also successfully pursued at ATF [129]. To reduce the blooming effect, two vertical YAG pads with a 1 mm center slit were attached on a support, as shown in Fig. 1.21 (a). When performing beam halo measurements, core particles pass through the slit without hitting the scintillator and the influence from the brilliant beam core can be significantly reduced. The preliminary experimental measurements, using an 8-bit CCD camera, show clearly the vacuum dependence of the vertical beam halo and confirm that such a YAG monitor is adequate for halo diagnostics, as shown in Fig. 1.21 (b).

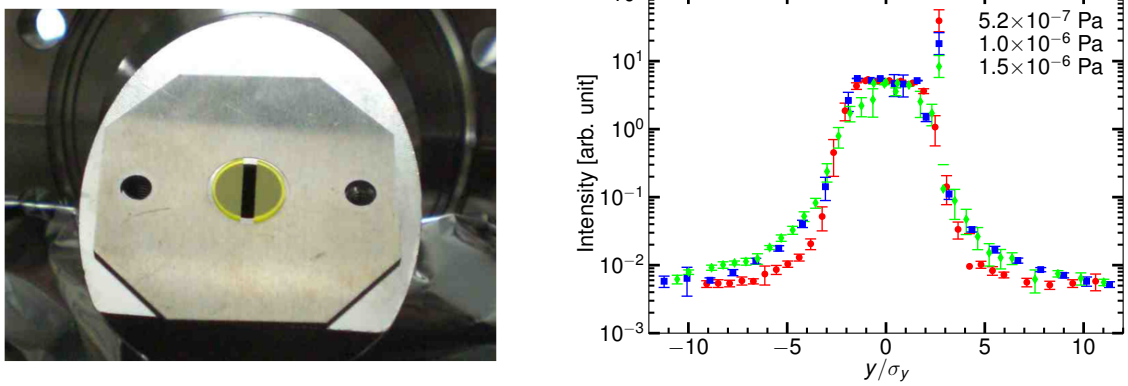

(a) (b)

Fig. 1.21 Two vertical YAG screens attached on the support with a 1 mm slit in the center [129] (a) and the observed vacuum dependence of the vertical beam halo (b). One can see the "flat" beam core, which is mainly caused by the saturation of the 8-bit CCD camera.

Significant efforts were devoted to beam halo investigations at ATF. However, a precise model for the beam halo distribution or a clear understanding of the beam halo formation were not yet achieved. As essential complement to the evaluations based on analytical approximations, systematic simulations of beam distortion in the presence of elastic/inelastic beam-gas scattering and intra-beam scattering are essential. Regarding the halo diagnostic, further improvements of the DS detector and upgrading of the YAG monitor were needed to meet the required dynamic range of at least 10^5. Motivated by these aspects, numerical predictions of beam halo formation, development of more advanced halo diagnostics, and careful measurements of the transverse beam halo and momentum tail of the ATF beam have been carried out and are presented in this dissertation.

Chapter 2

Theoretical studies of beam halo formation at ATF

2.1 Transverse motion

Betatron motion describes the transverse motion around a closed orbit. Typically, the amplitude of betatron motion is small and Hill's equation can govern the linear betatron motion

$$y'' + K_y(s)y = 0 \tag{2.1}$$

where y and y' represent either the horizontal or the vertical phase space coordinates, $K_y(s)$ is the focusing function satisfying the periodic condition $K_y(s+L) = K_y(s)$ with L the length of a periodic structure. Using the Floquet transformation, the general solution of Hill's equation can be given by [130]

$$y(s) = aw(s)\mathrm{e}^{-i\psi(s)} \tag{2.2}$$

where a is a constant, $w(s)$ and $\psi(s)$ are the amplitude and phase functions, respectively. The betatron amplitude equation and betatron phase equation are in the form of

$$\begin{aligned} w'' + K(s)w - 1/w^3 &= 0 \\ \psi' &= 1/w^3 \end{aligned} \tag{2.3}$$

The transformation matrix from s_1 to s_2 is then expressed as

$$M(s_2|s_1) = \begin{pmatrix} \frac{w_2}{w_1}\cos\psi - w_2 w_1' \sin\psi & w_1 w_2 \sin\psi \\ -\frac{1+w_1 w_1' w_2 w_2'}{w_1 w_2}\sin\psi - \left(\frac{w_1'}{w_2} - \frac{w_2'}{w_1}\right)\cos\psi & \frac{w_1}{w_2}\cos\psi + w_1 w_2' \sin\psi \end{pmatrix} \tag{2.4}$$

where $\psi = \psi(s_2) - \psi(s_1)$ is the betatron phase advance. Let $s_2 - s_1 = L$, the periodic boundary conditions are $w_1 = w_2 = w$, $w_1' = w_2' = w'$ and $\psi(s+L) - \psi(s) = \Phi$. Typically, the transfer matrix $\boldsymbol{M}$ has a common expression in the form of the Courant-Snyder parameters (Twiss parameters), i.e., α, β and γ [131]

$$\boldsymbol{M} = \begin{pmatrix} \cos\Phi + \alpha\sin\Phi & \beta\sin\Phi \\ -\gamma\sin\Phi & \cos\Phi - \alpha\sin\Phi \end{pmatrix} \tag{2.5}$$

Equating Eq. (2.4) and Eq. (2.5), we obtain the expressions of Twiss parameters as

$$\begin{aligned} \beta &= w^2 \\ \alpha &= -\frac{d\beta}{2ds} \\ \gamma &= \frac{1+\alpha^2}{\beta} \end{aligned} \tag{2.6}$$

where $\beta(s)$ is the betatron amplitude function representing the amplitude of the betatron motion and $\alpha(s)$ is related to the slope of the betatron amplitude function. The solutions of Hill's equation are then given by

$$\begin{aligned} y(s) &= a\sqrt{\beta(s)}\cos(\psi(s) + \psi_0) \\ y'(s) &= -a\sqrt{\beta(s)}(\alpha\cos(\psi(s) + \psi_0) + \sin(\psi(s) + \psi_0)) \end{aligned} \tag{2.7}$$

The transfer matrix from s_1 to s_2 can be further derived as

$$\begin{aligned} M(s_2|s_1) &= \begin{pmatrix} \sqrt{\frac{\beta_2}{\beta_1}}(\cos\psi + \alpha_1\sin\psi) & \sqrt{\beta_1\beta_2}\sin\psi \\ -\frac{1+\alpha_1\alpha_2}{\sqrt{\beta_1\beta_2}}\sin\psi + \frac{\alpha_1-\alpha_2}{\sqrt{\beta_1\beta_2}}\cos\psi & \sqrt{\frac{\beta_1}{\beta_2}}(\cos\psi - \alpha_2\sin\psi) \end{pmatrix} \\ &= \boldsymbol{B}(s_2)\begin{pmatrix} \cos\psi & \sin\psi \\ -\sin\psi & \cos\psi \end{pmatrix}\boldsymbol{B}^{-1}(s_1) \end{aligned} \tag{2.8}$$

and

$$\boldsymbol{B}(s) = \begin{pmatrix} \sqrt{\beta(s)} & 0 \\ -\frac{\alpha(s)}{\sqrt{\beta(s)}} & \frac{1}{\sqrt{\beta(s)}} \end{pmatrix} \tag{2.9}$$

where $\boldsymbol{B}(s)$ is the betatron amplitude matrix. Notice that the linear betatron motion reduces to a pure rotation after the normalization using the betatron amplitude matrix. From Eq. (2.7), an invariant for the betatron motion can be defined by [130]

$$H_y = \gamma y^2 + 2\alpha y y' + \beta y'^2 \tag{2.10}$$

The area of the ellipse enclosed by the trace of the particle motion is constant and equal to $\pi\varepsilon$, where ε is often incorrectly called "emittance". Furthermore, we introduce the action-angle variables (J_y, ψ) to simplify the analysis of particle motion. The action J_y is defined as

$$J_y = \frac{1}{2\beta}[y^2 + (\alpha y + \beta y')^2] \tag{2.11}$$

and ψ is the phase factor, equal to the phase advance. It is apparent that the Courant-Snyder invariant is twice the betatron action, $H_y = 2J_y$. As shown in the later section, the Courant-Snyder invariant and betatron action will be frequently used for analytical estimations of the perturbations from field errors, synchrotron radiation and collective effects [132–134]. The betatron oscillation of a particle in terms of the betatron action J_y becomes

$$\begin{aligned} y(s) &= \sqrt{2J_y\beta(s)}\cos(\psi(s)+\psi_0) \\ y'(s) &= -\sqrt{\frac{2J_y}{\beta}}[\sin(\psi(s)+\psi_0) + \alpha\cos(\psi(s)+\psi_0)] \end{aligned} \tag{2.12}$$

For a particle "travelling" along the beam line, the shape of the phase-space ellipse keeps varying but the area occupied by the ellipse is constant. The average of the betatron action of particles in the bunched beam gives the rms emittance $\varepsilon_{\mathrm{rms}}$. Concerning a normalized distribution of the particles, $\int \rho(y,y')dydy' = 1$, the rms emittance is defined as

$$\begin{aligned} \varepsilon_{\mathrm{rms}} &= \langle J_y \rangle \\ &= \sqrt{\sigma_y^2\sigma_{y'}^2 - \sigma_{yy'}^2} \end{aligned} \tag{2.13}$$

with

$$\begin{aligned} \sigma_y^2 &= \int (y - \langle y \rangle)^2 \rho(y,y')dydy' \\ \sigma_{y'}^2 &= \int (y' - \langle y' \rangle)^2 \rho(y,y')dydy' \\ \sigma_{yy'} &= \int (y - \langle y \rangle)(y' - \langle y' \rangle)\rho(y,y')dydy' \end{aligned} \tag{2.14}$$

where σ_y and $\sigma_{y'}$ are the rms beam size and the rms divergence, respectively, $\sigma_{yy'}$ the correlation between y and y', $\langle y \rangle = \int y\rho(y,y')dydy'$ and $\langle y' \rangle = \int y'\rho(y,y')dydy'$. With the Liouville theorem, the rms emittance is a constant during the beam transport. The rms beam size and rms beam divergence can be expressed as $\sigma_y = \sqrt{\varepsilon_{\mathrm{rms}}\beta(s)}$ and $\sigma_{y'} = \sqrt{\varepsilon_{\mathrm{rms}}\gamma(s)}$, respectively, as shown in Fig. 2.1. The variation of the rms emittance due to synchrotron radiation and beam instabilities will be presented in the following section.

The off-momentum particle has an off-momentum closed orbit around the reference orbit. This off-momentum orbit is proportional to the fractional momentum deviation in the first-order

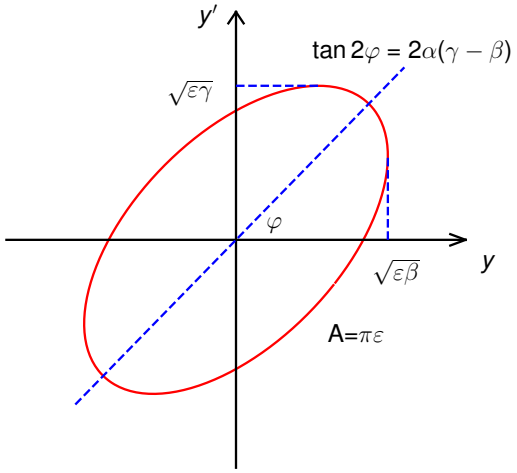

Fig. 2.1 The ellipse with $\varepsilon = \varepsilon_{\rm rms}$ in the phase space. α, β and γ are the Twiss parameters. The rms beam size and the rms divergence are $\sqrt{\varepsilon\beta}$ and $\sqrt{\varepsilon\gamma}$.

approximation. To characterize this difference, we define the dispersion function as the derivative of the off-momentum orbit with respect to the fractional momentum deviation. The coordinates of a particle in the phase space are then expressed as

$$\begin{aligned} y(s) =& y_\beta(s) + \eta_y(s)\delta \\ y'(s) =& y'_\beta(s) + \eta'_y(s)\delta \end{aligned} \tag{2.15}$$

where $y_\beta(s)$ denotes the betatron amplitude, $\eta_y(s)$ the dispersion function, $\eta'_y = d\eta_y/ds$ and $\delta = \Delta p/p_0$ the momentum deviation. The dispersion function arises whenever there is a non-zero dipole component. It can be propagated along the beam line, similar to the transformation of the Twiss parameters. The 3×3 transfer matrix of dispersion function from s_1 to s_2 can be expressed as

$$\begin{pmatrix} \eta_y(s_2) \\ \eta'_y(s_2) \\ 1 \end{pmatrix} = \begin{pmatrix} M(s_2|s_1) & \vec{f} \\ 0 & 1 \end{pmatrix} \begin{pmatrix} \eta_y(s_1) \\ \eta'_y(s_1) \\ 1 \end{pmatrix} \tag{2.16}$$

where $M(s_2|s_1)$ is the transfer matrix of the betatron motion, $\vec{f}$ represents the particular solutions. In the presence of a non-zero dispersion, the path length of the off-momentum closed orbit and the revolution time are longer than those of the reference particle for beam energies above the transition energy. Moreover, momentum fluctuations arising for instance from the emission of the synchrotron radiation photons or from intra-beam scattering can get coupled into the transverse planes through non-zero dispersion. This is a part of the effect responsible for the finite transverse emittances of the beams in a storage ring. In the beam transport system/section of a storage ring or a linear machine, the dispersion has to be properly matched by applying the dispersion suppression units or the achromatic modules. This is extremely important for

modern low-emittance storage rings and the circular colliders. A large dispersion in a specific section, on the other hand, allows the diagnostic of the energy spectrum via the measurement of the transverse distribution [135]. Similar to the Courant-Snyder invariant, we can define the dispersion $\mathcal{H}_y$-function as

$$\mathcal{H}_y = \frac{1}{\beta}[\eta_y^2 + (\alpha\eta_y + \beta\eta_y')^2] \tag{2.17}$$

The $\mathcal{H}_y$-function is an invariant in the dipole-free region and satisfies the homogeneous equation of betatron motion. Moreover, the dispersion action J_η can also be defined in the normalized dispersion phase space and satisfies $J_\eta = \mathcal{H}_y/2$.

Beyond the dispersion function, the chromatic aberrations due to momentum errors also play an important role in transverse beam dynamic. Such kinds of chromatic effects are analogous to that of the corresponding magnet field error. The respective quadrupole gradient errors ΔK_x and ΔK_y can be approximated (to the first order) by

$$\begin{aligned} \Delta K_x &= \Big[-\frac{2}{\rho^2} + K(s)\Big]\delta + O(\delta^2) \approx -K_x\delta \\ \Delta K_y &= -K(s)\delta + O(\delta^2) \approx -K_y\delta \end{aligned} \tag{2.18}$$

In a circular machine, the chromaticity is defined as the variation of the betatron tune with respect to the momentum deviation. First, we define the betatron tune as the number of betatron oscillation over one revolution, that is

$$v_{x,y} = \frac{1}{2\pi}\oint_{\mathrm{c}} \frac{ds}{\beta(s)} \tag{2.19}$$

And, the betatron tune shift due to the chromatic effect is given by

$$\Delta v_{x,y} = \frac{1}{4\pi}\oint \beta_{x,y}\Delta K_{x,y} ds \tag{2.20}$$

Then, the chromaticities $\xi_{x,y}$ are defined as

$$\xi_{x,y} = \frac{d(\Delta v_{x,y})}{d\delta} \tag{2.21}$$

The chromaticity determined by the focusing terms (quadrupole) is called the natural chromaticity. It is by convention always negative, i.e., less effective focusing for particles with larger momenta. For the chromaticity correction, sets of sextupoles in the dispersive region are used. These sextupoles can provide a focusing force with respect to the momentum deviation in the presence of off-momentum orbits. Notice that sextupoles also induce additional non-linearity which might affect the dynamic aperture [36, 136].

In a transport beam line, the chromaticity changes the focusing length of quadrupoles and enlarges the beam size. The respective characterization of chromaticity is different from that in

a ring. In a final focus system, for instance, the change of focus length with respect to particle energy is called the chromaticity of the final focus. It can be coumputed by [53]

$$\xi_y = \frac{L^*}{\beta_y^*} = -\frac{1}{\beta_y^*}\int ds K_q(s) R_{34}^2(s) \tag{2.22}$$

where R_{34} is the (3, 4) term of the transfer matrix and $K_q = K_0(1-\delta)$ is the normalized focus strength of the quadrupole. Moreover, there are other aberrations disturbing the beam delivery and causing beam instability. Taking into account all the non-linear elements, the transformation of particle coordinates can be further expressed in a general formalism [137, 138]

$$\vec{X}_i(s_2) = \sum_{j=1}^{6} \boldsymbol{R}_{ij}(s_2|s_1)\vec{X}_j(s_1) + \sum_{j=1}^{6}\sum_{k=1}^{6} \boldsymbol{T}_{ijk}(s_2|s_1)\vec{X}_j(s_1)\vec{X}_k(s_1) + \cdots \tag{2.23}$$

where $\vec{X} = (x, x', y, y', \beta c\Delta t, \delta)^T$, the 2×2 diagonal matrices with the indices of 1, 2 and 3, 4 are the horizontal and vertical transfer matrix, R_{13}, R_{14}, R_{23} and R_{24} terms represent the betatron cross-plane coupling, and R_{i6} (i =1, 2, 3, 4) the dispersion function related terms. The longitudinal motion in the frame $(\beta c\Delta t, \delta)$ is described by 2×2 diagonal matrices with (5, 6) indices. T_{126} and T_{346} represent the linear chromaticities, T_{166} is the second order dispersion and other terms of the $\boldsymbol{T}$ matrix are additional aberrations.

2.2 Synchrotron motion

For the discussion of the synchrotron motion in a circular machine, the momentum compaction factor and the phase-slip factor have to be defined. With a non-zero dispersion function, the closed orbit for an off-momentum particle is different from the reference orbit. This path length difference can be expressed as

$$\Delta C = \delta \oint \frac{\eta_x(s)}{\rho} ds \tag{2.24}$$

To be simple, we assume the vertical dispersion is small, $\eta_y(s) \approx 0$. Dependence of the circumference on the momentum deviation can be described by the momentum compaction factor α_c, which is given by

$$\alpha_c = \frac{1}{C}\frac{d\Delta C}{d\delta} \tag{2.25}$$

It is apparent that the revolution period, $T = C/\beta c$, depends on the momentum deviation. Consequently, the off-momentum particle has a different arriving time and energy gain at the accelerating field (RF cavity).

$$\frac{\Delta T}{T_0} = (\alpha_c - \frac{1}{\gamma^2})\delta = \eta_c \delta \tag{2.26}$$

and

$$\eta_c = \alpha_c - \frac{1}{\gamma^2} = \frac{1}{\gamma_t^2} - \frac{1}{\gamma^2} \tag{2.27}$$

where η_c is the phase-slip factor and γ_t is the transition energy. Below the transition energy, a particle with $\delta > 0$ has a shorter revolution period than that of the synchronous particle. Above the transition energy, it is the opposite, with the particles appearing to have a "negative" mass[1]. Usually, the beam energy is above the transition energy in electron/positron storage rings, e.g., the ATF damping ring, $\alpha_c \approx 0.0021$, $\gamma \gg \gamma_t$.

In a synchrotron or a storage ring, the accelerating section consists of one or several RF cavities supplying an accelerating voltage of

$$V = V_0 \sin(\phi_s + \omega_{\rm rf} T) \tag{2.28}$$

where V_0 is the amplitude of the RF voltage, ϕ_s the synchrotron phase, $\omega_{\rm rf} = h\omega_0$ the angular frequency of the RF cavity with h the harmonic number and ω_0 the angular revolution frequency. Here, we have ignored the higher-order harmonic components of the RF cavity. Using the phase and momentum deviation (ϕ, δ) as the longitudinal phase space coordinates and the time t as the argument, equations of motion are in the form of

$$\begin{aligned} \frac{d\delta}{dt} &= \frac{eV\omega_0}{2\pi\beta^2 E}[\sin\phi - \sin\phi_s] \\ \frac{d\phi}{dt} &= h\omega_0\eta\delta \end{aligned} \tag{2.29}$$

where $\beta = \sqrt{1-1/\gamma^2}$ and $\eta = -\Delta\omega/(\omega_0\delta)$. Assuming a weak acceleration or the case of a beam stored in a ring, the motion can be approximated in terms of an adiabatic synchrotron motion. The trace of a particle in the phase space can be described by

$$\delta^2 + \frac{eV}{\pi\beta^2 Eh\eta}[\cos\phi - \cos\phi_0 + \phi\sin\phi_s - \phi_0\sin\phi_s] = 0 \tag{2.30}$$

where we assume the trace passes through the point (ϕ_0, 0). Remarkably, there are two points (ϕ_s, 0) and ($\pi - \phi_s$, 0) where $\dot{\phi} = 0$ and $\dot{\delta} = 0$. The former is called the stable point, around which the particle performs stable small-amplitude oscillations. The latter is the unstable point beyond which the motion becomes unstable and the particle will get lost. The trace at the border of the stable and unstable regions defines the separatrix (RF bucket). The bucket height or the maximum momentum height is given by

$$\delta_{\rm max} = \sqrt{-\frac{eV}{\pi\beta^2 Eh\eta}[1 + \cos(\pi - \phi_s) - (\pi - \phi_s)\sin(\pi - \phi_s)]} \tag{2.31}$$

[1] In a medium energy synchrotron, e.g., the PS at CERN, the particle energy can be boosted across the transition energy. The synchrotron phase then has to shift from ϕ_s to $\pi - \phi_s$ within a short time [130, 139, 140].

Particles with a large momentum deviation exceeding the bucket height, caused by the beam gas Bremsstrahlung, Touschek scattering or synchrotron radiation, will get lost in the beam line and result in beam current decay.

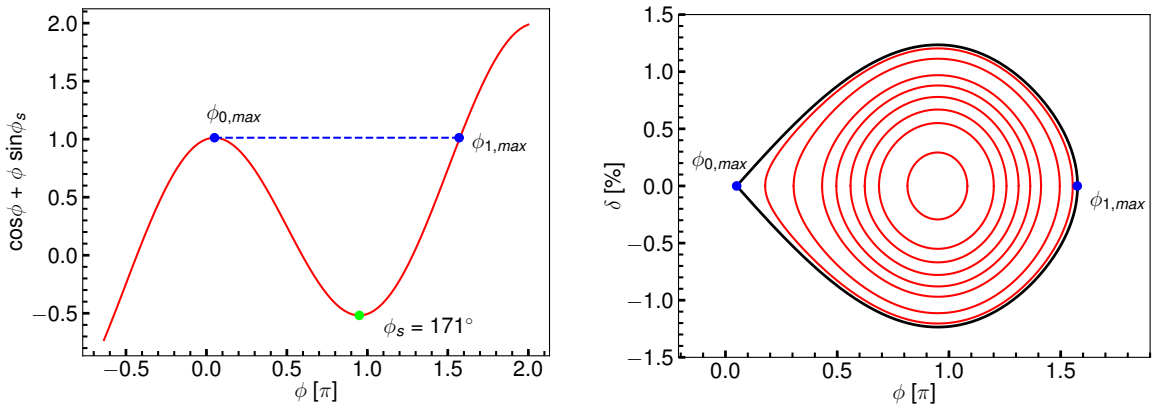

(a) (b)

Fig. 2.2 Evolution of the $\cos\phi + \phi\sin\phi_s$ term in Eq. (2.30) (a) and phase-space diagram for particles above the transition energy with the synchrotron phase $\phi_s = 171^\circ$ (b). $\phi_{0,\max} = \pi - \phi_s$ and $\phi_{1,\max}$ define the maximum stable phases. The black line denotes the separatrix.

Particles inside the separatrix execute quasi-harmonic motion. For small-amplitude oscillations of particles around the stable point, the motion is similar as the transverse betatron motion, while for large-amplitude motion it will be much more complicated. Typically, synchrotron motion is slow and a Taylor series can expand the accelerating voltage at $\phi = \phi_s$. The phase equation can be derived to be

$$\ddot{\varphi} + \Omega^2\varphi = 0 \tag{2.32}$$

where $\varphi = \phi - \phi_s$ and Ω is the small-amplitude synchrotron tune

$$\Omega^2 = -\frac{eVh\eta\cos\phi_s}{2\pi E\beta^2} \tag{2.33}$$

The synchrotron tune is defined as $\nu_s^2 = -eVh\eta/2\pi E\beta^2$ and is equal to the small-amplitude synchrotron tune if $\cos\phi_s = 1$ [141]. The stability condition for the synchrotron motion is $\eta_c\cos\phi_s < 0$ which means the synchrotron phase should be: $\phi_s \in (0,\ \pi/2)$ for $\gamma < \gamma_t$ and $\phi_s \in (\pi/2, \pi)$ for $\gamma > \gamma_t$. Solutions of Eq. (2.32) are given by

$$\begin{aligned} \varphi &= \hat{\phi}\cos(\Omega t + \chi) \\ \delta &= -\frac{\Omega}{h\eta_c}\hat{\phi}\sin(\Omega t + \chi) \end{aligned} \tag{2.34}$$

where $\hat{\phi}$ is the maximum phase difference. With the coordinates (φ, δ), it is difficult to obtain a similar expression as for the transverse betatron motion[2]. However, an action for the longitudinal small-amplitude oscillation can be defined as

$$J_s = \frac{1}{2}\left(\beta_L \varphi^2 + \frac{1}{\beta_L}\delta^2\right) \tag{2.35}$$

where $\beta_L = \frac{\Omega}{\hbar\eta}$. The area enclosed by the ellipse in the phase space is $2\pi J_s$ and particles oscillate on this ellipse with a angular frequency $\Omega\omega_0$.

For the large-amplitude oscillation, the trace of a particle in the phase space characterized by Eq. (2.30) is not anymore a standard ellipse but with a periodic distortion. Moreover, the synchrotron tune may diffuse for particles with large synchrotron amplitude such that particles will spread out in the longitudinal phase space and result in a dilution of the particle distribution.

2.3 Equilibrium beam distribution in a storage ring

2.3.1 Radiation damping and quantum excitation

The instantaneous power of synchrotron radiation from a relativistic particle of energy E is [130]

$$P_r = \frac{1}{2\pi} e^2 c^3 C_r E^2 B^2 \tag{2.36}$$

where c is the velocity of light in the vacuum, $C_r = \frac{4\pi r_e}{3 m_e c^2} = 8.85 \times 10^{-5}$ m·GeV^{-3} and B is the transverse magnetic field strength. In an isomagnetic ring, the average radiation power emitted by an electron is given by[3]

$$\langle P_r \rangle = \frac{c C_r E^4}{2\pi R \rho} \tag{2.37}$$

where R is the average radius of the ring and ρ is the bending radius. The radiation energy spectrum is continuous with a critical photon energy u_c

$$\begin{aligned} I(\omega) &= \frac{P_r}{\omega_c} S\left(\frac{\omega}{\omega_c}\right) \\ u_c &= \hbar\omega_c = 0.665 E^2 B \quad [\mathrm{GeV}\cdot\mathrm{T}] \end{aligned} \tag{2.38}$$

[2]With the coordinates $(\Delta t, \delta)$, the small-amplitude motion can be described similarly to the betatron motion by means of a longitudinal betatron amplitude function $\beta_s = \frac{2\pi e V_0 c^2 \cos\phi_s}{h\beta\eta\lambda^2(cp_0)}$.

[3]We consider only the radiation in bending magnet and ignore for the moment the radiation in quadrupole.

with

$$S\left(\frac{\omega}{\omega_c}\right) = \frac{9\sqrt{3}}{8\pi}\left(\frac{\omega}{\omega_c}\right)\int_{\omega/\omega_c}^{\infty} K_{5/3}(\varsigma)d\varsigma$$
$$\omega_c = \frac{3\gamma^2 c}{2\rho} \tag{2.39}$$

The radiation flux increases with frequency as $(\omega/\omega_c)^{3/2}$ for $\omega \ll \omega_c$, reaches its maximum near ω_c, and drops exponentially for $\omega \gg \omega_c$, as shown in Fig. 2.3. In the orbital plane, the high-frequency photons are in an angular cone $1/\gamma$ and the low-frequency photons have large angles with respect to the beam direction. The emitted photons are linearly polarized in the orbital plane and elliptically polarized away from the orbital plane [142]. This polarized high-frequency light collimated in the forward direction offers a powerful tool to investigate the atomic and molecular properties of materials [143, 144], opening the era of the modern synchrotron radiation light source.

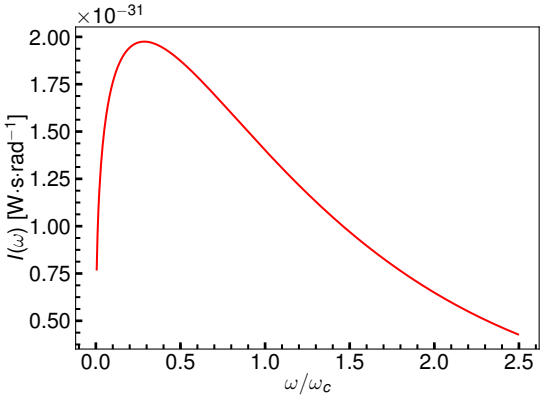

Fig. 2.3 Synchrotron radiation power spectrum of electron (ATF beam).

Synchrotron radiation is a quantum process with discrete photon emissions of energy $\hbar\omega$. The photon emission follows a Gaussian probability distribution function with respect to the momenta. The mean photon energies are

$$\langle u \rangle = \frac{8}{15\sqrt{3}}u_c$$
$$\langle u^2 \rangle = \frac{11}{27}u_c^2 \tag{2.40}$$

In the presence of synchrotron radiation, the longitudinal motion is determined by both synchrotron motion and radiation energy loss. The mapping equation over one revolution period

is given by

$$\begin{aligned} \delta_{i+1} &= \delta_i + \frac{E_g}{E} - \frac{U_0}{E} \\ t_{i+1} &= t_i - \delta_{i+1} T_0 \alpha_c \end{aligned} \tag{2.41}$$

where E_g is the energy gain from the longitudinal electrical field of the RF cavity, U_0 the synchrotron radiation energy loss per revolution, T_0 the revolution period and α_c the momentum compaction factor. Since the radiated power per revolution is proportional to E^2, $U_0 = \oint \langle P_r \rangle ds \propto E^2$, the high energy particle loses more energy and the amplitude of the synchrotron motion will be damped with a damping coefficient defined as

$$\alpha_s = \frac{1}{2T_0}\frac{dU_0}{dE} = \frac{U_0}{2T_0 E}(2+\mathcal{D}) \tag{2.42}$$

where $\mathcal{D}$ is the damping partition number[145]

$$\mathcal{D} = \begin{cases} \frac{\alpha_c R}{\rho}, & \text{separate-function dipoles} \\ 2 - \frac{\alpha_c R}{\rho}, & \text{combined-function dipoles} \end{cases} \tag{2.43}$$

In the case of the ATF damping ring, the filamentation and damping of beam injected from linac is predicted using Eq. (2.41), as shown in Fig. 2.4.

When a particle emits a photon, the momentum of the particle will have a small perturbation $\Delta\vec{p}$ parallel to the forward direction. In this process, coordinates in the transverse phase space, as well as the particle trajectory, do not change. However, the particle will later gain energy from the RF cavity and the vertical momentum will decrease by an amount of $\Delta y = -y' \frac{u}{E}$ while the instantaneous position does not change simultaneously. As a result, the vertical action is reduced by

$$\begin{aligned} \delta(2J_y) = &-\frac{2U_0}{E}[-2J_y\alpha\cos(\phi_s+\phi)(\alpha\cos(\phi_s+\phi)+\sin(\phi_s+\phi)) \\ &+2J_y(\alpha^2\cos^2(\phi_s+\phi)+2\alpha\cos(\phi_s+\phi)\sin(\phi_s+\phi)+\sin^2(\phi_s+\phi))] \end{aligned} \tag{2.44}$$

where α is the vertical Twiss parameter. Averaging over all particles, the time evolution of the vertical action is in the form of

$$\frac{d(2J_y)}{dt} = -\frac{2J_y U_0}{T_0 E} \tag{2.45}$$

which indicates a damping effect for the vertical motion. In terms of the amplitude of the vertical betatron motion, the damping coefficient is given by

$$\alpha_y = \frac{U_0}{2T_0 E} \tag{2.46}$$

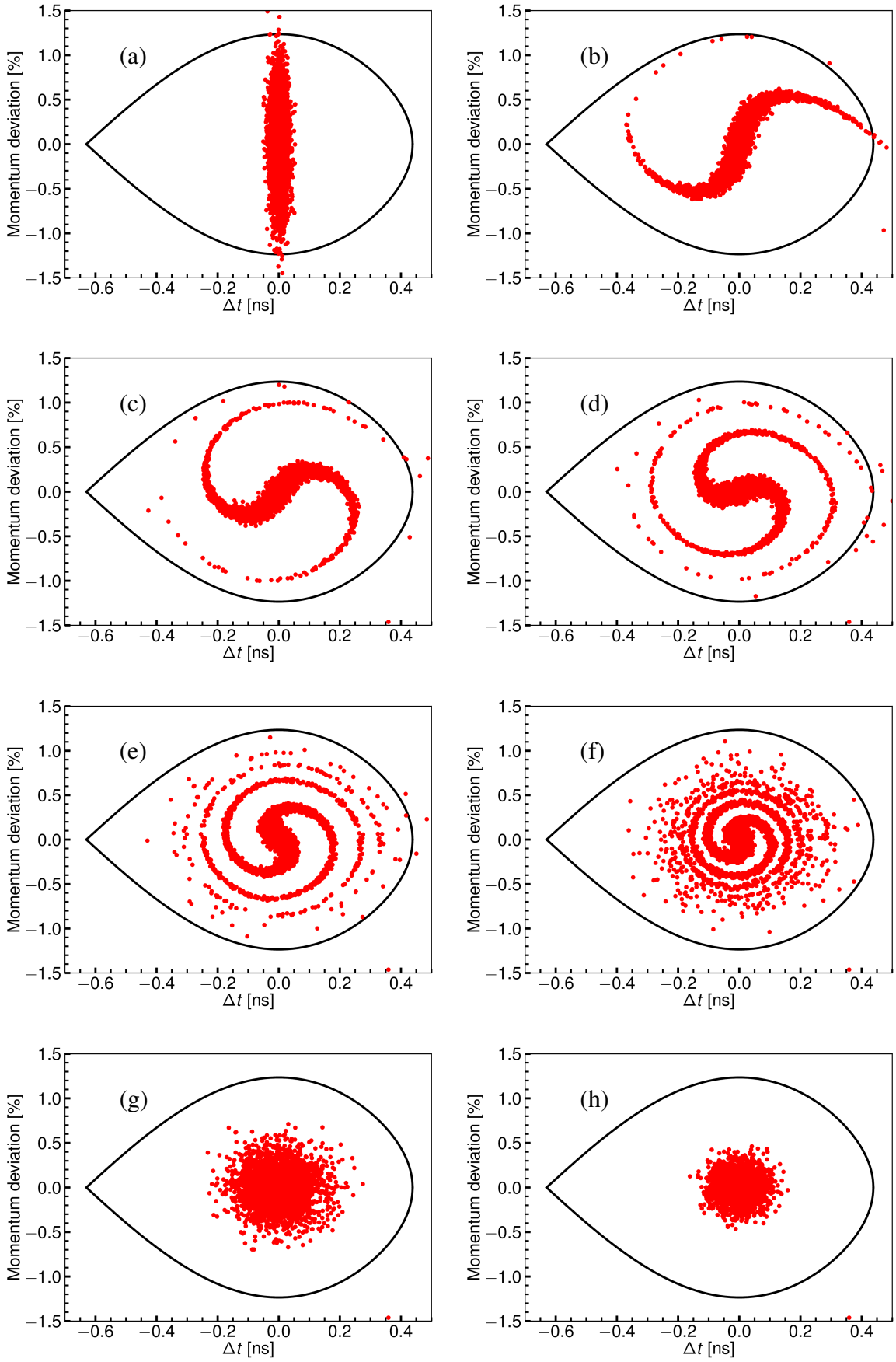

Fig. 2.4 Filamentation and damping of the longitudinal phase space distribution after beam being injected into the ATF damping ring for 0, 20, 50, 100, 200, 500, 1000 and 2000 turns (a) – (h).

In the horizontal plane, the betatron motion in the presence of synchrotron radiation is determined by: damping of the betatron oscillation at the RF cavity and an increase of betatron amplitude due to the discrete photon energy in terms of non-zero horizontal dispersion. The variation of the horizontal action is

$$\frac{d(2J_x)}{dt} = -(1-\mathcal{D})\frac{2J_xU_0}{T_0E} \tag{2.47}$$

and the horizontal damping coefficient is then given by

$$\alpha_x = -(1-\mathcal{D})\frac{U_0}{2T_0E} \tag{2.48}$$

Notice that the nominal vertical and horizontal damping coefficients are half of those for the vertical and horizontal actions, respectively. From the definition of α_x, α_y and α_s, we can deduce that the damping rate can be shortened by increasing the radiation power per revolution (e.g., with a damping wiggler) and adjusting the damping partition number $\mathcal{D}$ by means of a Robinson wiggler [130]. On the other hand, the photon emission is discontinuous which excites perturbations to the energy oscillations. The competition between radiation damping and quantum excitation, as well as other diffusive processes, dominates the beam dynamics in a storage ring and determines the equilibrium parameters as a balance between the two. The synchrotron radiation process is similar to random noise and result in equilibrium beam distribution functions which are Gaussians, consistent with the central limit theorem [146].

2.3.2 Equilibrium beam distribution

To compute the equilibrium distribution function, we follow the derivation introduced in Ref. [142] by solving the Fokker-Planck equation in the presence of stochastic processes. For large, statistically significant numbers of particles with a slowly varying density distribution in phase space, we use the density distribution function $\vec{\psi}(\vec{x},t)$ to characterize its evolution in time. Here, we use x, x' to represent coordinates in the 2D phase space. To be simple, we would like to restrict our discussion to the 2D normalized coordinates (u,u'), defined as

$$\begin{aligned} u &= x/\sqrt{\beta_x} \\ u' &= du/d\psi = \frac{1}{\sqrt{\beta_x}}(\alpha_x x + \beta_x x') \end{aligned} \tag{2.49}$$

where β_x and α_x are Twiss parameters and ψ is the phase advance. Taking into account the radiation damping and quantum excitation, the Fokker-Planck equation in the normalized frame can be expressed as

$$\frac{\partial\psi}{\partial t} + f_u\frac{\partial\psi}{\partial u} + g_u\frac{\partial\psi}{\partial u'} = 2\alpha_u\psi + D_\varepsilon\frac{\partial^2\psi}{\partial u^2} + D_\pi\frac{\partial^2\psi}{\partial u'^2} \tag{2.50}$$

where f_u and g_u are the changes of u and u' in the interval $t \to t + \Delta t$

$$\begin{aligned} f_u &= \frac{du}{dt} \\ g_u &= \frac{du'}{dt} \end{aligned} \tag{2.51}$$

D_ε and D_π are diffusion coefficients with respect to the instantaneous statistical change of u and u', and α_u is the damping coefficient

$$\alpha_u = -\frac{1}{2}\left(\frac{\partial f_u}{\partial u} + \frac{\partial g_u}{\partial u'}\right) \tag{2.52}$$

In the presence of damping effects, Eq. (2.50) has a unique stationary solution. In the action-angle frame (r, θ) with $r^2 = u^2 + u'^2$ and $\phi \in [0, 2\pi)$, the Fokker-Planck equation can be expressed as

$$\frac{\partial \psi}{\partial t} = 2\alpha_u \psi + \left(\alpha_u r + \frac{D}{r}\right)\frac{\partial \psi}{\partial r} + D\frac{\partial^2 \psi}{\partial r^2} \tag{2.53}$$

where $D = (D_\varepsilon + D_\pi)/2$. The stationary distribution function satisfying the above differential equation is in the form of

$$\psi(r,t) = \sum_{n>0} C_n G_n(r) \propto \exp\left(-\frac{\alpha_u}{2D} r^2\right) \tag{2.54}$$

After the normalization, we obtain a Gaussian distribution function

$$\begin{aligned} \psi(r) &= \frac{1}{\sqrt{2\pi}\sigma_r} e^{-\frac{r^2}{2\sigma_r^2}} \\ \sigma_r &= \sqrt{D/\alpha_u} \end{aligned} \tag{2.55}$$

In the physical phase space (x, x'), the density distributions are described by

$$\psi(x,x') = \frac{\beta_x}{2\pi\sigma_x^2} \exp\left[-\frac{x^2 + (\alpha_x x + \beta_x x')^2}{2\sigma_x^2}\right] \tag{2.56}$$

$$\psi(x) = \frac{1}{\sqrt{2\pi}\sigma_x} \exp\left(-\frac{x^2}{2\sigma_x^2}\right) \tag{2.57}$$

$$\psi(x') = \frac{1}{\sqrt{2\pi}\sigma_{x'}} \exp\left(-\frac{x'^2}{2\sigma_{x'}^2}\right) \tag{2.58}$$

where $\sigma_x = \sqrt{\beta_x}\sqrt{D_x/\alpha_x}$ and $\sigma'_x = \sqrt{\gamma_x}\sqrt{D_x/\alpha_x}$ are the equilibrium beam size and divergence, respectively, D_x the horizontal diffusion coefficient and α_x the horizontal damping rate. Eq. (2.55)–Eq. (2.56) are also valid for the vertical distribution.

Regarding the synchrotron motion, the stationary distribution can be given using a similar method as that applied for the transverse motion. Distribution functions in the (δ, t) coordinate

system are given by

$$\begin{aligned}\psi(\delta) &= \frac{1}{\sqrt{2\pi}\sigma_\delta}\exp\Big(-\frac{\delta^2}{2\sigma_\delta^2}\Big)\\ \psi(t) &= \frac{1}{\sqrt{2\pi}\sigma_t}\exp\Big(-\frac{t^2}{2\sigma_t^2}\Big)\end{aligned} \tag{2.59}$$

with

$$\begin{aligned}\sigma_\delta &= \sqrt{\tau_\varepsilon D_\varepsilon}\\ \sigma_t &= \frac{|\alpha_c|}{\Omega_s}\sqrt{\tau_\varepsilon D_\varepsilon}\end{aligned} \tag{2.60}$$

where $\tau_\varepsilon = 1/\alpha_\varepsilon$ is the longitudinal damping time, D_ε the diffusion coefficient, α_c the momentum compaction factor and Ω_s the synchrotron oscillation frequency, that is

$$\Omega_s^2 = \frac{2\pi c\alpha_c eV_0\cos\phi_s}{\lambda^2 h\beta^2 p_0} \tag{2.61}$$

where λ is the wavelength of the RF field. Here, we have preliminarily shown that the distribution for each degree of freedom in the 6D phase space is Gaussian. However, to determine the true equilibrium beam size and distribution, the knowledge of the practical lattice and storage ring configuration is further required.

2.3.3 Equilibrium emittance

The diffusion coefficient of particle oscillations due to emissions of energy E_γ is

$$D_x = \frac{1}{2E_0}\langle \mathcal{N}\langle E_\gamma^2\rangle \mathcal{H}_x\rangle \tag{2.62}$$

where $\langle ...\rangle$ denotes the average over the ring, E_0 the beam energy, $\mathcal{N}$ the number of photons emitted per unit time and $\mathcal{H}_x = \beta_x\eta_x'^2 + 2\alpha_x\eta_x\eta_x' + \gamma_x\eta_x^2$ the dispersion invariant. Let's say the synchrotron radiation is only at the bending magnet, and the radiation at other elements, e.g., wigglers and quadrupoles, is treated as additional perturbation. The diffusion coefficient can then be further expressed as

$$D_x = \frac{55}{48\sqrt{3}}\frac{\langle P_\gamma\hbar\omega_c\mathcal{H}_x\rangle}{E_0^2} \tag{2.63}$$

where P_γ is the instantaneous power of the photon emission and $\hbar\omega_c$ is the photon energy.

The damping rate in the three degrees of freedom is typically in the form of

$$\alpha_i = \mathcal{J}_i\alpha_0 = \mathcal{J}_i\frac{P_\gamma}{2E_0} \tag{2.64}$$

where $\mathcal{J}_i$ $(i = x, y, \varepsilon)$ is the damping partition number which satisfies the Robinson theorem

$$\mathcal{J}_x + \mathcal{J}_y + \mathcal{J}_\varepsilon = 4 \tag{2.65}$$

Then, the horizontal equilibrium emittance becomes

$$\varepsilon_x = \sigma_x^2/\beta_x = \frac{\langle \mathcal{N}\langle E_\gamma^2\rangle \mathcal{H}_x\rangle}{2E_0\mathcal{J}_x\langle P_\gamma\rangle\beta_x} \tag{2.66}$$

Using the expression of the synchrotron radiation power in Eq. (2.37), the horizontal beam emittance can be further simplified as

$$\varepsilon_x = C_q\gamma^2\frac{\langle \mathcal{H}_x/|\rho^3|\rangle}{J_x\langle 1/\rho^2\rangle} \tag{2.67}$$

where C_q is the quantum excitation constant:

$$C_q = \frac{55}{32\sqrt{3}}\frac{\hbar c}{m_0c^2} \tag{2.68}$$

The vertical emittance is mainly determined by residual dispersion in the vertical plane and xy betatron coupling, both of which mainly arise from imperfections, and therefore we can express the vertical equilibrium emittance as

$$\varepsilon_y = \sigma_y^2/\beta_y = C_q\gamma^2\frac{\langle \mathcal{H}_y/|\rho^3|\rangle}{\mathcal{J}_y\langle 1/\rho^2\rangle} + \frac{\kappa}{1+\kappa}\varepsilon_x \tag{2.69}$$

where $\mathcal{H}_y$ is the vertical dispersion invariant and κ is the coupling coefficient. In the longitudinal plane, the equilibrium energy spread and bunch length in time could also be derived as

$$\sigma_\delta^2 = C_q\gamma^2\frac{\langle|1/\rho^3|\rangle}{\mathcal{J}_\varepsilon\langle 1/\rho^2\rangle} \qquad \text{and} \qquad \sigma_\tau^2 = \frac{\alpha_c^2}{\Omega_s^2}\sigma_\delta^2 \tag{2.70}$$

Furthermore, we introduce the synchrotron radiation integrals:

$$\begin{aligned}
I_1 &= \int \frac{\eta_x}{\rho}ds \\
I_2 &= \int \frac{1}{\rho^2}ds \\
I_3 &= \int \frac{1}{|\rho^3|}ds \\
I_4 &= \int \frac{\eta_x}{\rho}(\frac{1}{\rho} + 2k_1)ds, \quad k_1 = \frac{1}{(B\rho)}\frac{\partial B_y}{\partial x} \\
I_5 &= \int \frac{\mathcal{H}_x}{|\rho^3|}ds
\end{aligned} \tag{2.71}$$

Expressions of the equilibrium beam size and emittance in terms of the synchrotron radiation integrals are

$$\begin{aligned}
\alpha_c &= \frac{I_1}{C_0} \\
\mathcal{J}_x &= 1 - \frac{I_4}{I_2}, \quad \mathcal{J}_y = 1, \quad \mathcal{J}_\varepsilon = 2 + \frac{I_4}{I_2} \\
\varepsilon_x &= C_q \gamma^2 \frac{I_5}{I_2 - I_4} \\
\sigma_\delta^2 &= C_q \gamma^2 \frac{I_3}{2I_2 + I_4} \\
\sigma_\tau &= \frac{\alpha_c}{\omega_s} \sigma_\delta
\end{aligned} \tag{2.72}$$

However, these formulas in the form of radiation integrals provide only a rough approximation of the equilibrium beam distribution. For a more complicated lattice with system errors, which is the case of most modern low-emittance storage ring, the equilibrium emittances could be computed with the help of numerical codes based on different algebraic methods, e.g., the radiation integral in the normal mode[134], Chao's method[147] and the "envelop" method[148].

2.4 Evaluation of beam halo from beam-gas scattering

2.4.1 Coulomb scattering between particles and nuclei of gas atoms

The interactions between a particle and an atom of the residual gas are of two principal categories: the elastic scattering and the inelastic scattering. In the former case, the particle is deflected transversely due to the electrical field of the nucleus of the residual gas atom. In the latter case, the momentum of the particle is reduced through photon emission due to the interaction with the nucleus or electron of an atom. Both could result in particle loss when exceeding either the physical aperture or the dynamic aperture, which determines a vacuum lifetime.

The elastic scattering between a particle and the point-like nucleus of a residual gas atom can be characterized in terms of Rutherford scattering with the screening effect. Within the small angle approximation, the cross section for Rutherford scattering is given by [149]

$$\frac{d\sigma}{d\Omega} = \left(\frac{2Ze^2}{\gamma m_e c^2}\right)^2 \frac{1}{\theta^4} \tag{2.73}$$

where θ is the deflection angle with respect to the forward direction. Corrections are needed for two extreme cases, ultra-small scattering angles where the screening effect from the surrounding electrons of the nucleus is dominant, and large scattering angles where the influence of the finite size of the nucleus has to be taken into account. The modified expression of the cross section

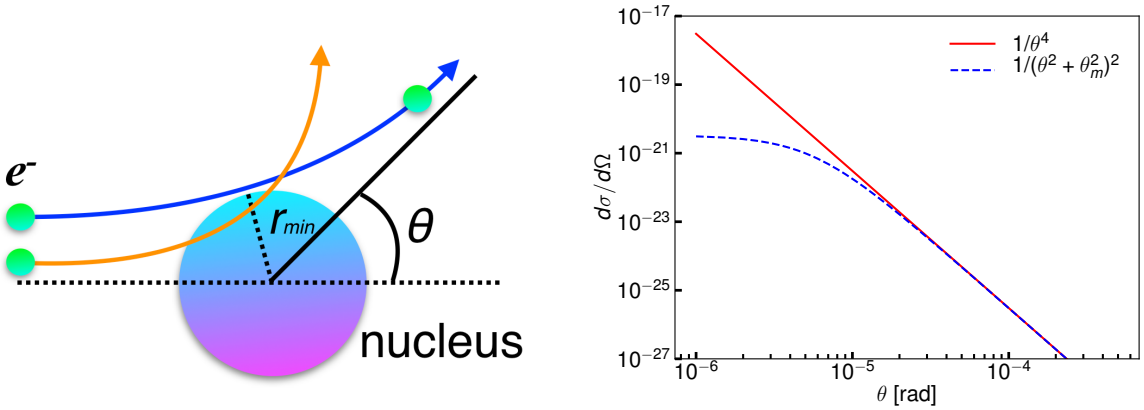

(a) (b)

Fig. 2.5 Schematic of the elastic scattering for an electron passing the nucleus of a gas atom (a) and a comparison of the cross section with/without screening effect (b).

becomes[150]

$$\begin{aligned}\frac{d\sigma}{d\Omega} &= \left(\frac{2Ze^2}{\gamma m_e c^2}\right)^2 \frac{1}{(\theta^2+\theta_m^2)^2} \\ &= \left(\frac{2Zr_e}{\gamma}\right)^2 \frac{1}{(\theta^2+\theta_m^2)^2}\end{aligned} \tag{2.74}$$

where Z is the charge multiplicity of the particle, $\theta_m = Z^{1/3}\alpha/\gamma$ the minimum angle due to the screening effect and $r_e = e^2/m_e c^2$ the classical electron radius. The total cross section with a scattering angle less than $\theta_{\max}$ is

$$\sigma = \frac{4\pi Z^2 r_e^2}{\gamma^2}\left(\frac{1}{\theta_m^2} + \frac{1}{\theta_m^2+\theta_{\max}^2}\right) \tag{2.75}$$

The inelastic scattering contains two processes: the Bremsstrahlung scattering where a photon is emitted and the excitation of an atom where the incident particle's momentum is transferred to the electron of an atom. The cross sections for the two types of scattering are

$$\begin{aligned}\left.\frac{d\sigma}{du}\right|_1 &= \frac{4\alpha_0 Z^2 r_e^2}{u}\left[\left(\frac{4}{3}(1-\frac{u}{E})+\frac{u^2}{E^2}\right)\left(\frac{\varphi_1(0)}{4}-\frac{\log Z}{3}\right)+\frac{1}{9}(1-\frac{u}{E})\right] \\ \left.\frac{d\sigma}{du}\right|_2 &= \frac{4\alpha_0 Z r_e^2}{u}\left[\left(\frac{4}{3}(1-\frac{u}{E})+\frac{u^2}{E^2}\right)\left(\frac{\psi_1(0)}{4}-\frac{2\log Z}{3}\right)+\frac{1}{9}(1-\frac{u}{E})\right]\end{aligned} \tag{2.76}$$

where u is the momentum transfer, α_0 the fine structure constant, $\varphi_1(0)$ and $\psi_1(0)$ are the screening functions. The total cross section of the inelastic scattering is approximated as

$$\sigma \approx 4\alpha r_e^2\left[\mathcal{C}\left(\frac{4}{3}\log(E/u_m)-\frac{5}{6}\right)+\frac{1}{9}(Z^2+Z)(\log(E/u_m)-1)\right] \tag{2.77}$$

with

$$\mathcal{C} = Z^2 \ln\left(\frac{183}{Z^{1/3}}\right) + Z \ln\left(\frac{1194}{Z^{2/3}}\right) \tag{2.78}$$

where u_m is the lower limit of the momentum transformation ($u_m \ll E$).

2.4.2 Theoretical estimation

We follow the approach developed by K. Hirata [124] for the description of particle redistribution in the presence of stochastic processes. The transverse motion in a ring or transport beam line can be perturbed by stochastic processes such as synchrotron radiation, BGS or IBS. It can be described by the diffusion equation

$$\frac{d\vec{x}}{ds} = -[H(\vec{x},s),\vec{x}] + \xi(\vec{x},s) \tag{2.79}$$

where $\vec{x}$ is the 6D phase space coordinate, $H(\vec{x},s)$ the Hamiltonian representing the symplectic part of the motion and $\xi(\vec{x},s)$ contains the diffusion effects. The solution to the equation of motion can be expressed in terms of a linear map plus the integrated perturbation of the stochastic process

$$\vec{x}(s) = M(s,s_0)\vec{x}_0 + \int_{s_0}^{s} M(s,s')\tilde{\xi}(s)ds' \tag{2.80}$$

with

$$M(s,s_0) = M_0 \exp[\int_{s_0}^{s} [s\tilde{H}(s'') - D(s'')]ds''] \tag{2.81}$$

where M_0 is the symplectic matrix representing the linear transformation, $\tilde{H}$ a symmetric 6×6 matrix and D the damping matrix which contains the radiation damping [148]. Here we describe only the transverse motion (in the horizontal plane for example) and we consider only the betatron motion, radiation damping, quantum excitation and diffusion from BGS, ignoring betatron coupling. In normalized coordinates $u = x/\sqrt{\beta}$ and $u' = du/d\phi$, Eq. (2.80) can be written as

$$\vec{u}(s) = R(s,s_0)\vec{u}(s_0)\exp(-\frac{\alpha}{c}\int_{s_0}^{s} ds) + \delta\vec{u} \tag{2.82}$$

where $\vec{u} = (u,u')^T$, $R(s,s_0)$ represents a pure rotation, α is the damping rate and $\delta\vec{u}$ the perturbation, expressed as

$$R(s,s_0) = \begin{pmatrix} \cos(\Delta\phi) & \sin(\Delta\phi) \\ -\sin(\Delta\phi) & \cos(\Delta\phi) \end{pmatrix} \tag{2.83}$$

$$\delta\vec{u} = R(s,s_0)\begin{pmatrix} 0 \\ \sqrt{\beta}\theta_x \end{pmatrix}\exp(-\tfrac{\alpha}{c}\textstyle\int_{s_0}^{s} ds) \tag{2.84}$$

where $\Delta\phi = \int_{s_0}^{s} \frac{ds}{\beta(s)}$ is the phase advance, β the betatron function, θ_x the transverse kick angle at s_0 and c the velocity of light in the vacuum. We can further specify the perturbation term in

Eq. (2.82) in terms of the transformation in presence of radiation damping, diffusion due to the quantum excitation, $\delta\vec{u}_{qe}$, and the external perturbation due to BGS, $\delta\vec{u}_{ex}$

$$\vec{u}(s) = R(s,s_0)\vec{u}(s_0)\exp(-\frac{\alpha}{c}\int_{s_0}^{s} ds) + \delta\vec{u}_{qe} + \delta\vec{u}_{ex} \tag{2.85}$$

The stationary distribution is determined by the integral of all stochastic processes. Since particle distributions under the influence of radiation damping and quantum excitation have been well understood, it is convenient to express the distribution function $\psi(u)$ as

$$\psi(u) = \frac{1}{2\pi}\int e^{i\omega u}\tilde{\psi}_t(\omega)\tilde{\psi}_f(\omega)d\omega \tag{2.86}$$

where $\tilde{\psi}_t(\omega)$ is the characteristic function in the presence of radiation damping and quantum excitation

$$\tilde{\psi}_t(\omega) = \exp(-\omega^2\sigma_t^2/2) \tag{2.87}$$

and σ_t is the beam size in absence of external perturbation. The characteristic function $\tilde{\psi}_f(\omega)$ has been derived in Ref. [124] and Ref. [125], thanks to Campbell's theorem [151]. Here, we use the formalism in Ref. [124] where the stochastic perturbation is treated over many betatron oscillation periods. Approximating β by its average value over the ring, $\bar{\beta}$, the characteristic function $\tilde{\psi}_f(\omega)$ can be written as

$$\tilde{\psi}_f(\omega) = \exp(\frac{N_s}{\alpha}\hat{f}(\omega\sqrt{\bar{\beta}})) \tag{2.88}$$

where

$$\hat{f}(\tilde{\omega}) = \frac{2}{\pi}\int_0^1 d\zeta\frac{\Re[\tilde{f}(\tilde{\omega}\zeta)]-1}{\zeta}\cos^{-1}\zeta \tag{2.89}$$

and

$$\tilde{f}(\tilde{\omega}) = \int d\theta_x f(\theta_x)\cos(\tilde{\omega}\theta_x) \tag{2.90}$$

The factor N_s is the scattering rate of a test particle, $\Re[\tilde{f}(\tilde{\omega}\zeta)]$ the real part of $\tilde{f}(\tilde{\omega}\zeta)$ and $f(\theta_x)$ is the probability distribution for a deflection angle θ_x. The final distribution function can be expressed as

$$\psi(u) = \frac{1}{2\pi}\int_{-\infty}^{\infty} e^{i\omega u}\exp(-\frac{\omega^2\sigma_t^2}{2} + \frac{N}{\alpha}\hat{f}(\omega\sqrt{\bar{\beta}}))d\omega \tag{2.91}$$

This characteristic function is an even function, so only the cosine part remains after performing the integration

$$\psi(u) = \frac{1}{\pi}\int_0^{\infty}\cos(\omega u)\exp(-\frac{\omega^2\sigma_t^2}{2} + \frac{N}{\alpha}\hat{f}(\omega\sqrt{\bar{\beta}}))d\omega \tag{2.92}$$

The transverse distribution in x can be described by

$$\psi(x_i) = \frac{1}{\pi}\int_0^\infty \cos(\omega x_i)\exp(-\frac{\omega^2\sigma_{x_i}^2}{2} + \frac{N}{\alpha}\hat{f}(\omega\sqrt{\bar{\beta}\beta_i}))d\omega \tag{2.93}$$

where x_i is the horizontal coordinate at position i, σ_{x_i} the equilibrium horizontal beam size in presence of radiation damping and quantum excitation, and β_i is the beta function at the observation point.

To obtain the numerical form of the distribution function $\psi(u)$ or $\psi(x)$, we have to first evaluate $\tilde{f}(\tilde{\omega})$ in the presence of BGS. Treating BGS as the classical Rutherford scattering process and considering the screening effect, the cross section in the CGS system of units is given by

$$\frac{d\sigma}{d\Omega} = (\frac{2Zr_e}{\gamma})^2\frac{1}{(\theta^2+\theta_m^2)^2} \tag{2.94}$$

Subsequently, the transverse deflection angle θ can be further specified as

$$\theta^2 = \theta_x^2 + \theta_y^2 \tag{2.95}$$

Note that $\theta_x \in [-\theta_{x,\max}, \theta_{x,\max}]$ and the same for θ_y. The differential $d\sigma/d\theta_x$ can be obtained by integration of Eq. (2.94) over the vertical deflection angle θ_y.

$$\begin{aligned}\frac{d\sigma}{d\theta_x} &= \int \frac{d\sigma}{d\Omega}d\theta_y \\ &= \Big(\frac{2Zr_e}{\gamma}\Big)^2\int\frac{d\theta_y}{(\theta_x^2+\theta_y^2+\theta_m^2)^2} \\ &= \Big(\frac{2Zr_e}{\gamma}\Big)^2\Big[\frac{\theta_y}{2(\theta_x^2+\theta_m^2)(\theta_x^2+\theta_y^2+\theta_m^2)} + \frac{\arctan(\theta_y/\sqrt{\theta_x^2+\theta_m^2})}{2(\theta_x^2+\theta_m^2)^{3/2}}\Big]\Big|_{-\theta_{y,\max}}^{\theta_{y,\max}}\end{aligned} \tag{2.96}$$

where $\theta_{y,\max}$ is the maximum scattering angle in the y direction. If we assume$\theta_{y,\max} \gg \sqrt{\theta_x^2+\theta_m^2}$, Eq. (2.96) can be approximated by

$$\frac{d\sigma}{d\theta_x} \approx \frac{\pi}{2}(\frac{2Zr_e}{\gamma})^2\frac{1}{(\theta_x^2+\theta_m^2)^{3/2}} \tag{2.97}$$

Then the total cross section σ_{tot}, the probability function $f(\theta_x)$ and the scattering rate N become

$$\sigma_{tot} = \int_{-\theta_{x,\max}}^{\theta_{x,\max}}\frac{d\sigma}{d\theta_x}d\theta_x = \frac{4\pi Z^2 r_e^2}{\gamma^2\theta_m^2} \tag{2.98}$$

$$f(\theta_x) = \frac{1}{\sigma_{tot}}\frac{d\sigma}{d\theta_x} = \frac{\theta_m^2}{2(\theta_x^2+\theta_m^2)^{3/2}} \tag{2.99}$$

$$N = \rho_v\sigma_{tot}c \tag{2.100}$$

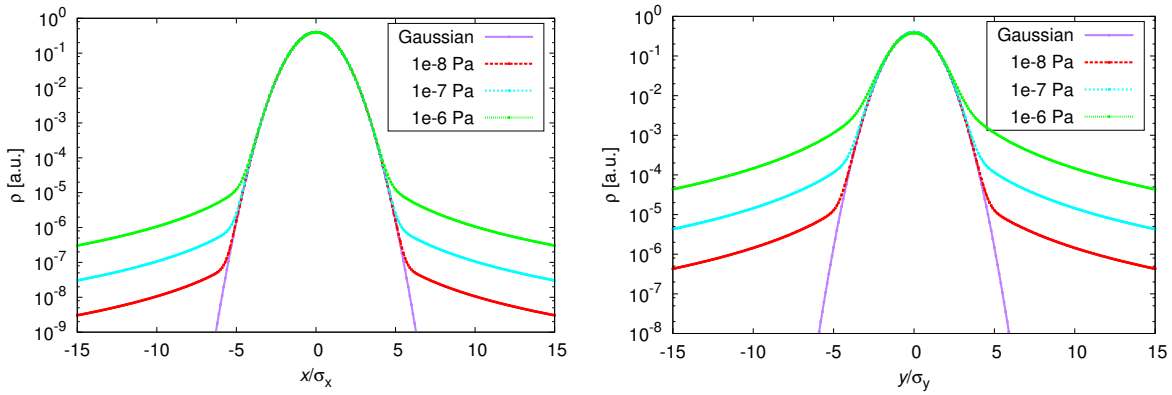

(a) (b)

Fig. 2.6 Horizontal and vertical normalized beam profiles in the presence of radiation damping, quantum excitation and the elastic BGS.

where ρ_v is the volume density of the residual gas atoms. Following the derivation in Ref. [124], functions $\tilde{f}(\tilde{\omega})$ and $\hat{f}(\tilde{\omega})$ are finally expressed as

$$\begin{aligned} \tilde{f}(\tilde{\omega}) &= \tilde{\omega} K_1(\tilde{\omega}) \\ \hat{f}(\tilde{\omega}) &= \frac{2}{\pi} \int_0^1 d\zeta \frac{\tilde{\omega}\zeta K_1(\tilde{\omega}\zeta) - 1}{\zeta} \cos^{-1}\zeta \end{aligned} \tag{2.101}$$

where K_1 is the modified Bessel function of first order. Estimates of the beam profile using Eq. (2.93) for the ATF damping ring are shown in Fig. 2.6. Here, we assume horizontal and vertical damping times of 20 ms and 27 ms, and averaged betatron amplitude functions of 4.3 m and 4.6 m, vertically and horizontally, respectively. Besides, the residual gas is considered to have $Z = \sqrt{50}$ and two atoms per molecule, to approximate air or CO.

2.4.3 Monte Carlo simulation

To clarify the analytical estimation of the beam profile distortion in the presence of BGS, tracking of the scattered particle in presence of radiation damping and quantum excitation was considered. Generation and tracking of core particles and scattered particles were performed through a script developed in SAD [152], a program used for optical matching and Closed-Orbit Distortion (COD) correction during beam operation. The equilibrium vertical emittance ε_y is mainly determined by the residual vertical dispersion η_y and cross-plane betatron coupling, both of which strongly depend on the magnet alignment errors and the resulting COD [36, 153]. The vertical emittance can be modeled by introducing random vertical displacements to quadrupoles and sextupoles (20μm, rms), and rotations of quadrupoles (2 mrad, rms). The equilibrium emittance ε_y obtained in this way for various seeds ranges from 5 pm to 30 pm. Alternatively, the actual COD measured by Beam Position Monitors (BPMs) can be modeled by local orbit bumps using steering magnets,

as shown in Fig. 2.7. Obtained equilibrium emittances are 12 pm and 1.2 nm, vertically and horizontally, respectively, for a realistic COD. The latter can better represent the realistic orbit and beam parameters, and is therefore used in our BGS simulations. The emittances and beam sizes considered here and in the following are evaluated by Gaussian fits to the beam core distributions.

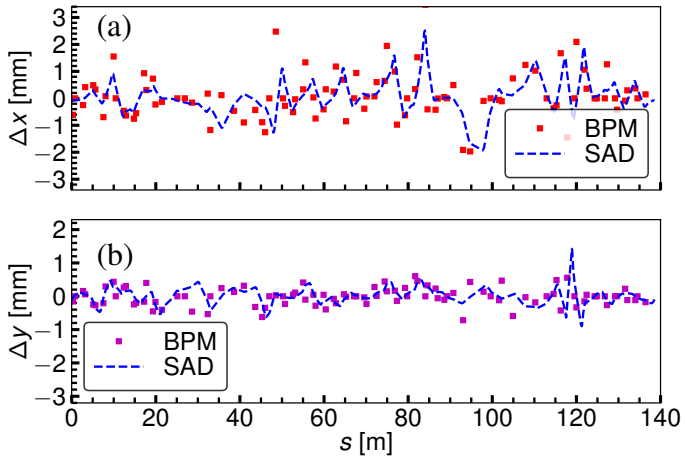

Fig. 2.7 Horizontal (a) and vertical (b) COD measured by BPMs in January 2017 and approached by local-orbit bumps.

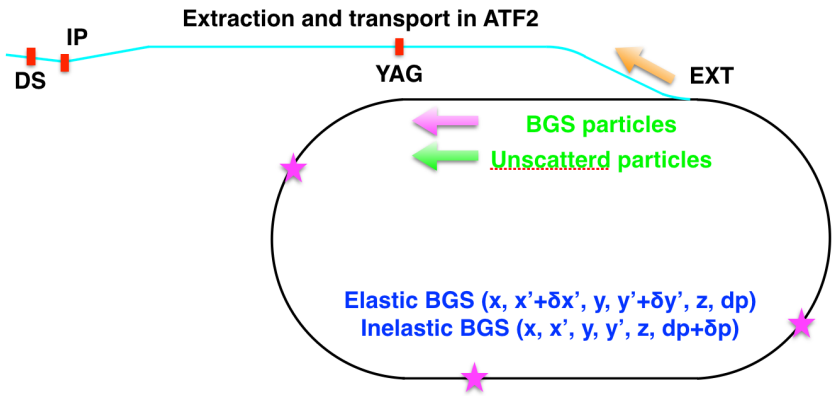

Fig. 2.8 Schematic of the simulation of BGS in the ATF damping ring.

Tracking of both scattered and non-scattered particles is performed element by element utilizing the beam parameters at injection, as sketched in Fig. 2.8. The simulation of scattered particles is performed as follows [154]. First, in each turn, the number of scattering events and their perturbations are generated randomly according to the residual gas pressure and the cross section. Second, perturbations in the 6D phase space of particles are implemented at random longitudinal positions to simulate particle scattering. The location of particle scattering is approximated to be at the closest element, which determines the local Twiss parameters and orbit. Third, the scattered particles in the present turn are transported to the observation point (at

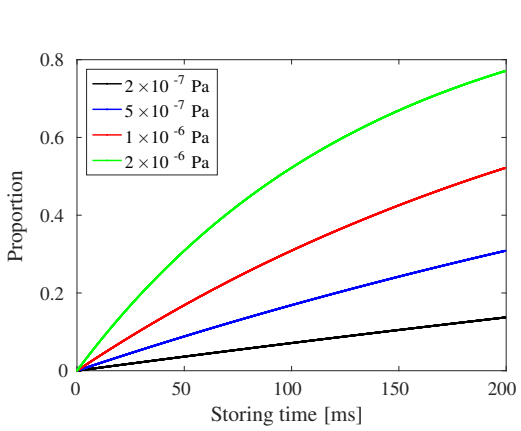

(a)

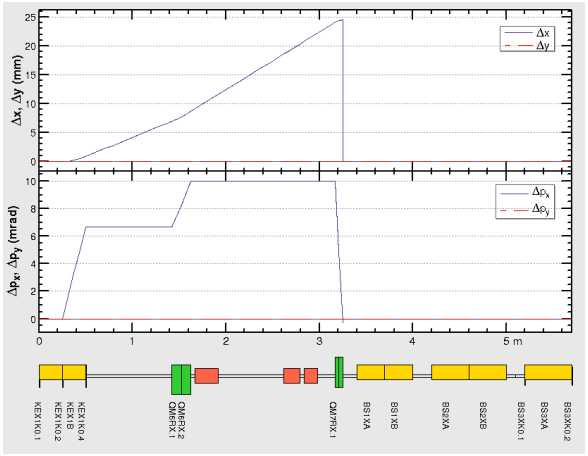

(b)

Fig. 2.9 Percentage of the scattered particles as a function of gas pressure and storage time (a). The orbit distortion in the extraction region (b). The red blocks represent the septum magnets.

the location of the extraction kicker), to be combined with the scattered particles accumulated from the previous turns. The above process is then repeated until beam extraction. In addition, the possibility of multi-BGS, which is highly probable for a high gas pressure and a long storage time, has been taken into account. The percentage of the scattered particles depends on both the vacuum pressure and the storage time, as shown in Fig. 2.9 (a).

To estimate the beam profile in ATF2, stored particles are extracted and transported to diagnostic devices. Initial Twiss parameters of the ATF2 lattice are well matched with the damping ring lattice at the extraction kicker. Orbit distortion of the extracted beam in the kicker-septum region can be represented by a coordinate transformation, as shown in Fig. 2.9 (b).

Benchmarking of Monte Carlo simulations

Estimates of the vacuum lifetime τ_v, which depends directly on the gas pressure, supply benchmarks for the simulations. The vacuum lifetime can be determined in two methods: analytical evaluation according to the acceptance and cross section, and through tracking simulation. Here, we say that the vacuum lifetime is driven by the elastic and inelastic BGS.

The elastic scattering between a particle and atomic nucleus of the residual gas induces a transverse kick θ to the particle. The amplitude of the betatron motion will be enlarged and result in beam loss due to finite physical aperture if the deflection angle is large enough. The transverse offset of the particle is increased by

$$\Delta x = \theta_i \sqrt{\beta_1 \beta_2} \sin(\psi_2 - \psi_1) \tag{2.102}$$

where θ_i is the scattering angle, β_2, β_1 the betatron amplitude functions at an arbitrary location and the location of scattering, and ψ_2, ψ_1 the phases of the betatron oscillations at these two

locations. The minimum deflection angle for particles to go beyond the physical aperture is given by

$$\theta_c = \frac{A/2}{\sqrt{\beta_{\max}\beta_i}} \tag{2.103}$$

where A is the physical aperture. For a random scattering event along the beam line, θ_c could be represented by its average over the ring $\bar{\beta}$. The minimum deflection angle resulting in particle loss is expressed as

$$\theta_c = \mathrm{Min}\Big(\frac{A_x/2}{\sqrt{\beta_{x,\max}\bar{\beta}_x}}, \frac{A_y/2}{\sqrt{\beta_{y,\max}\bar{\beta}_y}}\Big) \tag{2.104}$$

Adapting the cross section of elastic BGS derived in Eq. (2.74), the total cross section of the large angle elastic BGS events can be expressed as

$$\sigma_1 = \frac{4\pi Z^2 r_e^2}{\gamma^2}\Big(\frac{1}{\theta_c^2} - \frac{1}{\theta_{\max}^2}\Big) \tag{2.105}$$

Lifetime resulting from the elastic BGS is defined as

$$\frac{1}{\tau_1} = -\frac{1}{N}\frac{dN}{dt} = \rho_v \cdot \sigma_1 \cdot \beta c \tag{2.106}$$

where N is the number of particles per bunch and ρ_v the volume density of the residual gas atoms.

For the beam-gas Bremsstrahlung and the scattering off electrons of the residual gas atoms, the total cross section depends on the dynamic aperture and the physical aperture and is characterized by Eq. (2.77). The minimum momentum determined by the momentum acceptance is expressed as

$$u_{m1} = E\sqrt{\frac{2U_0}{\pi\alpha_c kE}\big(\sqrt{V^2-1} - \arccos(1/V)\big)} \tag{2.107}$$

where U_0 is the energy loss per revolution, α_c the momentum compression factor and V the RF voltage. Besides, the maximum acceptance of the instantaneous orbit, which is mainly determined by the physical aperture, sets an additional limitation to the minimum momentum

$$u_{m2} = \frac{A_x/2}{\eta_x}E \tag{2.108}$$

where we assume the amplitude of vertical betatron oscillations is much smaller than that of horizontal ones. Then, the vacuum lifetime due to inelastic BGS becomes

$$\frac{1}{\tau_2} = -\frac{1}{N}\frac{dN}{dt} = \rho_v \cdot \sigma_{\mathrm{inel}}(u_{m1}, u_{m2}) \cdot \beta c \tag{2.109}$$

The total vacuum lifetime is given by

$$\frac{1}{\tau_v} = \frac{1}{\tau_1} + \frac{1}{\tau_2} \tag{2.110}$$

We assume Z = $\sqrt{50}$ and two atoms per molecule, which approximates air or CO [124], to represent the residual gas. For an average gas pressure of 1×10^{-6} Pa, the calculated value of τ_v is 83 minutes [155]. Meanwhile, the simulated value is 87 minutes using the equilibrium beam parameters and realistic physical apertures. Simulation of vacuum lifetime follows a similar procedure as that described above. The vacuum lifetime mainly depends on the elastic BGS process and particle loss in the straight section where the betatron amplitude function is large. Meanwhile, the inelastically scattered particles are mainly lost at the entrance of two arc sections where the horizontal dispersion becomes large, as shown in Fig. 2.10.

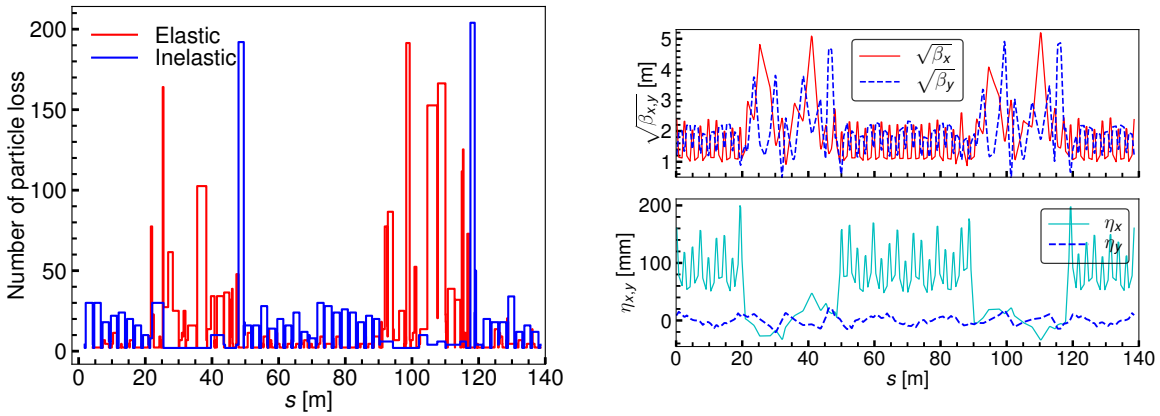

(a) (b)

Fig. 2.10 Loss map of the elastic and inelastic BGS particles in the ATF damping ring (a) and the corresponding betatron amplitude function and dispersion (b) in the presence of a realistic COD.

Assuming Touschek scattering and elastic BGS dominate the beam lifetime, the time dependence of the beam intensity can be described by

$$n(t) = 1 - \alpha \int_0^t dt' P(t') n(t') - \frac{1}{\tau_{Tous}(\kappa)} \int_0^t n^2(t') dt' \tag{2.111}$$

where $n(t) = N(t)/N_0$ is the normalized beam intensity, $\alpha = 1/(\tau_v P)$ a coefficient related to the vacuum lifetime τ_v and gas pressure P, and τ_{Tous} is the Touschek lifetime. The decay of the beam current and the variation of the average gas pressure are shown in Fig. 2.11 for different vertical emittances. The coefficient α is measured as around 1000 $\mathrm{Pa}^{-1}\cdot\mathrm{s}^{-1}$, and $\tau_v \approx 16$ minutes, as determined by fitting the current decay with Eq. (2.111). Such a reduction in the experimentally measured vacuum lifetime has also been reported in Ref. [156] and Ref. [157], which suggest the probable beam loss channels: 1) existence of a larger horizontal beam halo induced by

other mechanisms; 2) reduction of the dynamic aperture due to sextupole components at the entrance/exit of the combined function bending magnets.

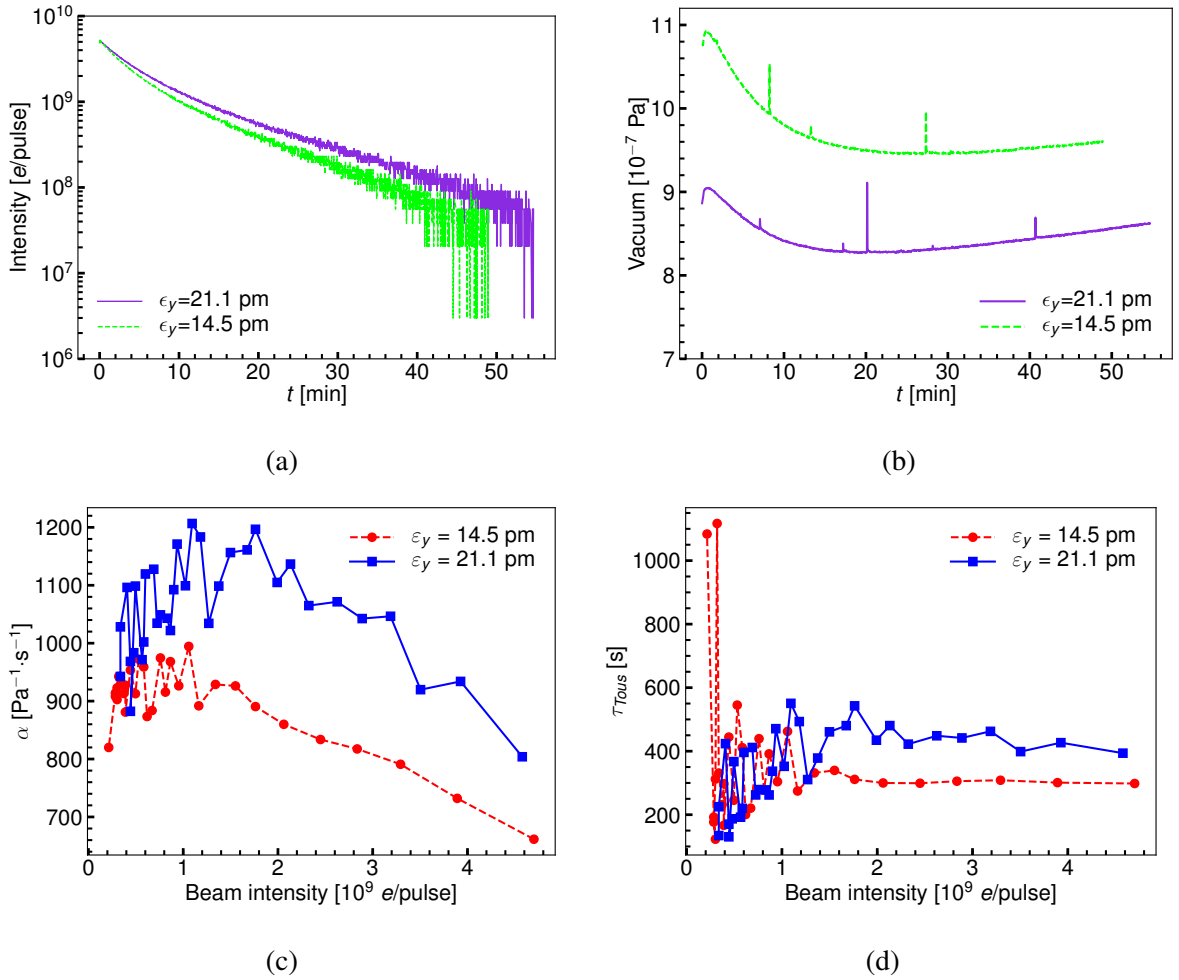

Fig. 2.11 Evolution of the average gas pressure (a) and current decay of the stored beam (b) in the ATF damping ring. The fitting factor α and the Touschek lifetime as a function of beam intensity (c, d).

Evolution of beam profile from BGS

The cross section of elastic BGS is inversely proportional to θ^2 and therefore the large-angle events are infrequent. Thus, we set an upper bound on the scattering angle at $100\theta_m$, which is much larger than the rms divergence of core particles. Note that the minimum angle θ_m for the ATF beam is 5.5 μrad. To acquire sufficient statistics, the number of accumulated particle scattering events can be as many as 2×10^7. The simulations indicate that at least twice the damping time is essential to reach the equilibrium distribution in the ATF damping ring. For the typical vacuum level of 5×10^{-7} Pa, satisfactory agreement between the analytical calculation using Eq. (2.93) and the simulation is observed (see Fig. 2.12), where the distribution is normalized to the core beam size. After such a normalization, the horizontal tail/halo appears

lower than the vertical halo by around two orders of magnitude, due to the flat aspect ratio of the ATF beam, the horizontal beam size being typically ten times larger than the vertical.

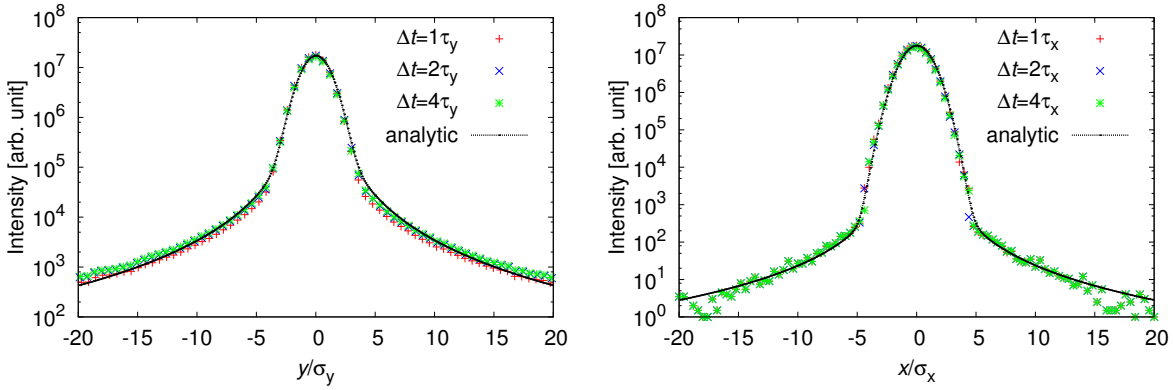

(a) (b)

Fig. 2.12 Comparison of the vertical (a) and horizontal (b) beam distortion between analytic approximation and simulation. A tracking time of more than two damping times is essential before reaching an equilibrium.

In the analytic calculation, while radiation damping and quantum excitation have been considered to reach a quasi equilibrium, the distribution function contains no assumption whether or not equilibrium has been reached, and Eq. (2.93) can in principle also be used for calculations of the profiles during the damping process. Subsequently, beam profiles predicted analytically and by simulation were compared at different times, showing a reasonable qualitative agreement, see Fig. 2.13.

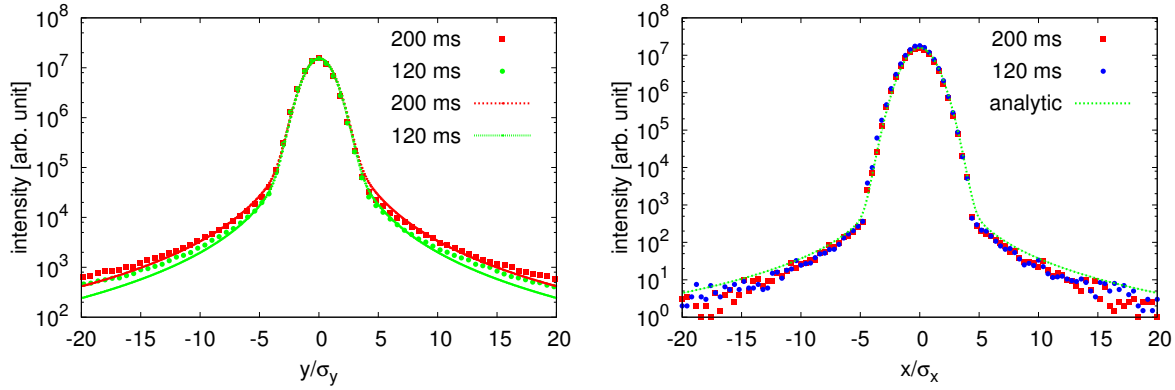

(a) (b)

Fig. 2.13 Beam profiles visualized at different moments, vertically (a, symbol: simulation and line: analytic calculation) and horizontally (b, with ε_x in equilibrium).

The probability of BGS depends on the density of residual molecules, and therefore, the beam halo can increase for a higher vacuum pressure in the ring. Presently, the average gas pressure obtained in the normal operation is 2×10^{-7} Pa, which can be adjusted by turning off some of

the Sputter Ion Pumps (SIPs). Simulations have been performed for three different pressure levels which were achieved in operation. Significant increases of the beam tail/halo can be observed for higher vacuum pressure, as shown in Fig. 2.14. The vacuum dependence, together with the distribution predicted by simulation, indicates a convenient method to determine if BGS dominates beam halo or not.

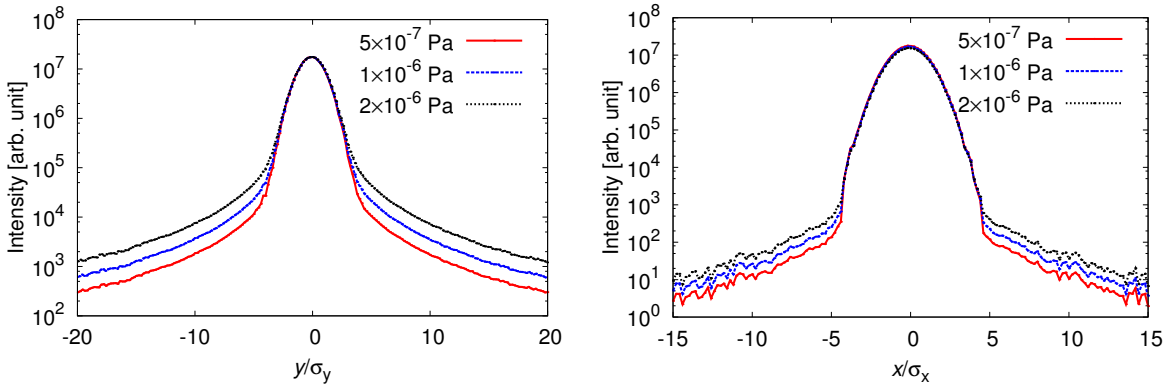

(a) (b)

Fig. 2.14 Dependence of vertical (a) and horizontal (b) beam profiles on vacuum pressure.

Beam halo from BGS mainly depends on the accumulated effect of the stochastic transverse kicks, whereas equilibrium emittance determines beam size (beam core). Therefore, different behaviors of core and halo parts of beam profile in the presence of different equilibrium emittances are expected. In the physical coordinate system, the beam core is broadened for an increased initial emittance, while the halo distribution is not affected. An enhancement of beam tail/halo as a function of emittance is however observed in the normalized coordinate, see Fig. 2.15. Here, only the evolution with varying ε_y is considered since ε_y is ultra small (pm level), and halo from BGS is more significant in the vertical plane. If BGS dominates the vertical halo formation, the correlation between emittance and beam tail/halo could supply an alternative method for vertical ultra-small emittance measurement, without a knowledge of the β function or scanning the betatron phase.

Large-angle scattering events are rare but can induce large betatron oscillation amplitudes, which drive particles into the halo region. Small-angle scattering events have a higher probability and will act analogously to quantum excitation. They can dilute the core particle distribution and cause emittance growth.

For normal vacuum pressures ($10^{-7} \sim 10^{-6}$ Pa) at ATF, vertical emittance dilution is evaluated concerning the beam distribution function derived in Sec. 2.4.2 and using Monte Carlo simulation. We assume that the worst vacuum pressure is 5×10^{-6} Pa and the equilibrium vertical emittance (without BGS and IBS) is 12.8 pm. This value is increased to 18.4 pm and 18.9 pm, as predicted by the analytic approximation and Monte Carlo simulation, respectively (see Fig. 2.16).

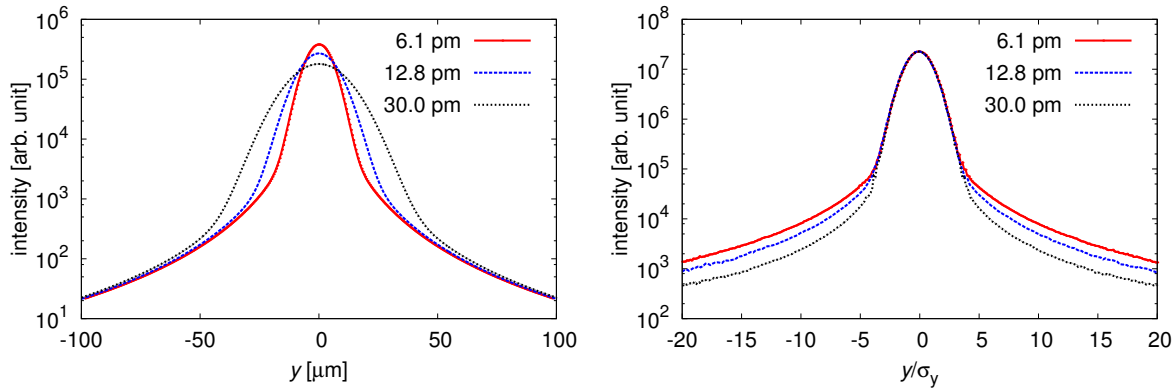

(a) (b)

Fig. 2.15 Vertical beam profile with different emittances, in the physical frame (a) and the normalized coordinate (b). The averaged gas pressure is assumed to be 1×10^{-6} Pa.

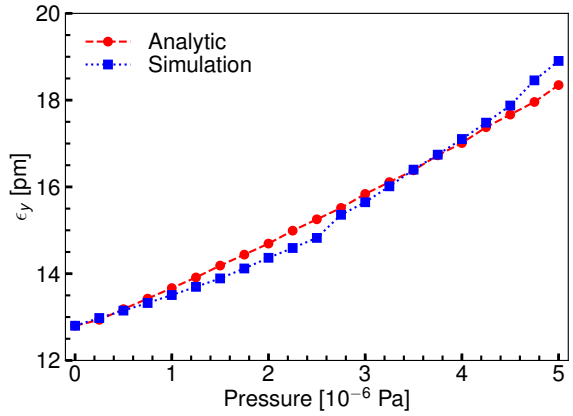

Fig. 2.16 Emittance growth as a function of vacuum pressure predicted by analytic calculation and Monte Carlo simulation.

2.5 Halo/tail induced by Touschek scattering

Coulomb scattering of charged particles inside a bunch causes the momentum exchange between the transverse and longitudinal motion. The multiple small-angle Coulomb scattering, called Intra-Beam Scattering (IBS) [158], causes diffusion of the particle distribution and leads to the emittance growth which is of critical importance for the state-of-art low-emittance storage rings. The large angle Coulomb scattering, named Touschek scattering [159], can transfer transverse momentum to the longitudinal, which can be boosted by a Lorentz factor γ for the relativistic beam. The dispersed particles will get lost if the momentum deviation after collision exceeds the momentum acceptance or the transverse acceptance in the dispersive regions. The IBS is a multiple scattering process leading to the beam diffusion and dilution of the emittances. The Touschek effect, however, is a single scattering which may result in particle loss and beam intensity decay. Analytical estimation of Touschek scattering is best done considering only the

transfer of horizontal momenta to longitudinal momenta [160]. For the small-angle scattering, on the other hand, we normally assume the momentum transfer is comparable with the natural momentum spread.

The theoretical analysis of IBS and Touschek scattering have been described in many publications [158, 161–168]. The basic IBS theory established by Piwinski and developed by other authors gives a detailed description of the kinematics of the interaction process involved in multiple Coulomb scattering in a storage ring [158]. Then, J. Bjorken and S. Mtingwa (BM) proposed an approximation based on the scattering matrix formalism from quantum electrodynamics which is suitable for strong-focusing machines [162]. Both approximations consider the two-body collision for a Gaussian, uncoupled beam. The result of the BM theory is typically thought to be more general and then was followed by K. Kubo and K. Oide who derived a formalism for an arbitrary coupling [167], which has been implemented in the computer code SAD. The early Touschek theory has been investigated as soon as the Touschek effect was first observed in the ADA storage ring [159]. Le Duff derived the formalism considering the transfer of horizontal momentum to the longitudinal motion in the presence of dispersion [161]. Using the same method as that in the IBS theory, Piwinski has developed a theory to estimate the Touschek scattering rate and Touschek lifetime, which treats the transfer of the transverse momentum to the longitudinal motion considering the transverse betatron oscillation, dispersion and the evolution of the beam envelope [160]. Piwinski's theory is basic and easy to grasp and therefore is used in the later discussion of two-body Coulomb scattering for the relativistic beam. Emittance growth from IBS diffusion is calculated in SAD based on Kubo's theory and verified using a Monte-Carlo simulation.

The Touschek scattering theory focuses on the particle loss due to significant momentum deviation but not the diffusion of beam distributions. Therefore the scattering rate of large momentum transfer is highly weighted without considering later transverse and longitudinal motion in the presence of synchrotron radiation. However, our interest is mainly on the Coulomb scattering which induces the "large" momentum deviations with particles still stable (within the RF bucket in the longitudinal phase space).

2.5.1 Momentum change from Coulomb scattering

The momenta of particles before collision in the laboratory (LAB) coordinate system (s, x, y) are given by

$$\vec{p}_{1,2} = \begin{pmatrix} p_{s1,2} \\ p_{x1,2} \\ p_{y1,2} \end{pmatrix}_{\hat{s},\hat{x},\hat{y}} \tag{2.112}$$

where $\hat{s}$, $\hat{x}$ and $\hat{y}$ represent the longitudinal, horizontal and vertical unit vector parallel to the s, x and y coordinate axes. We then define a new coordinate system in the LAB frame with the unit

vectors ($\hat{u}$, $\hat{v}$, $\hat{w}$) which satisfies

$$\hat{u} = \frac{\vec{p}_1 + \vec{p}_2}{|\vec{p}_1 + \vec{p}_2|}, \quad \hat{v} = \frac{\vec{p}_1 \times \vec{p}_2}{|\vec{p}_1 \times \vec{p}_2|}, \quad \hat{w} = \hat{u} \times \hat{v} \tag{2.113}$$

and the momenta becomes

$$\vec{p}_{1,2} = p_{1,2} \begin{pmatrix} \cos\chi_{1,2} \\ 0 \\ \pm\sin\chi_{1,2} \end{pmatrix}_{\hat{u},\hat{v},\hat{w}} \tag{2.114}$$

where $\chi_{1,2}$ is the angle between $\vec{p}_{1,2}$ and $\hat{u}$, as sketched in Fig. 2.17 (a). Applying a Lorentz transformation parallel to $\hat{u}$, we obtain the expression of the momenta in the center-of-mass (COM) coordinate system ($\tilde{u}$, $\tilde{v}$, $\tilde{w}$) as

$$\vec{\tilde{p}}_{1,2} = p_{1,2} \begin{pmatrix} \gamma_t(\cos\chi_{1,2} - \frac{\beta_t}{\beta_{1,2}}) \\ 0 \\ \pm\sin\chi_{1,2} \end{pmatrix}_{\hat{\tilde{u}},\hat{\tilde{v}},\hat{\tilde{w}}} = \begin{pmatrix} \bar{p}_s \\ 0 \\ \pm p_\perp \end{pmatrix}_{\hat{\tilde{u}},\hat{\tilde{v}},\hat{\tilde{w}}} \tag{2.115}$$

where β_t is the relative velocity of the ($\tilde{u}$, $\tilde{v}$, $\tilde{w}$) coordinate system and $\beta_{1,2}$ are the relative

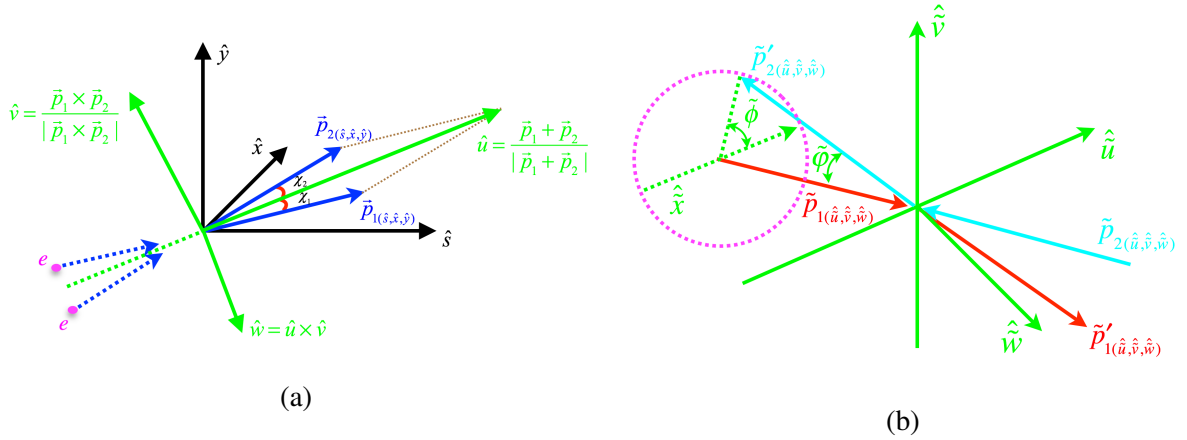

Fig. 2.17 Definition of (u, v, w) coordinate system in the laboratory frame (a) and the schematic of Coulomb scattering in ($\tilde{u}$, $\tilde{v}$, $\tilde{w}$) coordinate system (b). Notices the dotted circle in the right figure is in parallel to the $\tilde{u}\tilde{w}$ plane. We assumed that the two colliding particles have the same spatial coordinate.

velocities of the two particles in the laboratory frame.

$$\beta_t = \frac{|\vec{p}_1 + \vec{p}_2|c}{E_1 + E_2} = \frac{\beta_1\gamma_1\cos\chi_1 + \beta_2\gamma_2\cos\chi_2}{\gamma_1 + \gamma_2} \tag{2.116}$$

and the Lorentz factor of the transformation is

$$\gamma_t^2 = \frac{1}{1-\beta_t^2} \approx \frac{\gamma^2}{1+\beta^2\gamma^2\chi^2} \tag{2.117}$$

Moreover, the particle energy in the COM frame is given by

$$\tilde{E}_{1,2} = \frac{E_1 + E_2}{2\gamma_t} \tag{2.118}$$

In the COM frame, the Coulomb scattering changes the direction of the momenta but not the absolute values. Then, we define two angles $\tilde{\varphi}$ and $\tilde{\phi}$, where $\tilde{\varphi}$ is the polar angle between the momentum $\vec{\tilde{p}}'_1$ and the $\tilde{v}$-axis and $\tilde{\phi}$ is the azimuthal angle in the $\tilde{v}\tilde{x}$ plane, the axis $\tilde{x}$ is perpendicular to $\vec{\tilde{p}}_1$ in the $\tilde{u}\tilde{w}$ plane, as shown in Fig. 2.17. The momenta after collision become

$$\vec{\tilde{p}}'_{1,2} = \pm \begin{pmatrix} \bar{p}_s \cos\tilde{\varphi} + p_\perp \sin\tilde{\varphi}\cos\tilde{\phi} \\ |\tilde{p}_{1,2}| \sin\tilde{\varphi}\sin\tilde{\phi} \\ p_\perp \cos\tilde{\varphi} - \bar{p}_s \sin\tilde{\varphi}\cos\tilde{\phi} \end{pmatrix}_{\hat{\tilde{u}},\hat{\tilde{v}},\hat{\tilde{w}}} \tag{2.119}$$

Transferring to the LAB frame by the inverse Lorentz transformation, we obtain

$$\begin{aligned} \vec{p}'_{1,2} &= \pm \begin{pmatrix} \gamma_t (p'_{\tilde{u}1,2} + v_t \tilde{E}/c^2) \\ p'_{\tilde{v}1,2} \\ p'_{\tilde{w}1,2} \end{pmatrix}_{\hat{u},\hat{v},\hat{w}} \\ &= \pm \begin{pmatrix} \gamma_t (\bar{p}_s \cos\tilde{\varphi} + p_\perp \sin\tilde{\varphi}\cos\tilde{\phi}) + \frac{\gamma_t v_t \tilde{E}}{c^2} \\ |\tilde{p}_{1,2}| \sin\tilde{\varphi}\sin\tilde{\phi} \\ p_\perp \cos\tilde{\varphi} - \bar{p}_s \sin\tilde{\varphi}\cos\tilde{\phi} \end{pmatrix}_{\hat{u},\hat{v},\hat{w}} \end{aligned} \tag{2.120}$$

Concerning the definitions of $\bar{p}_s$ and $p_\perp$ in Eq. (2.115), the momenta after collision are further expressed as

$$\vec{p}'_{1,2} = \pm p_{1,2} \begin{pmatrix} \gamma_t [\gamma_t (\cos\chi_{1,2} - \beta_t/\beta_{1,2}) \cos\tilde{\varphi} + \sin\chi \sin\tilde{\varphi}\cos\tilde{\phi}] + \frac{\gamma_t \beta_t \tilde{E}}{c p_{1,2}} \\ \sqrt{\gamma_t^2 (\cos\chi_{1,2} - \beta_t/\beta_{1,2})^2 + \sin^2\chi} \sin\tilde{\varphi}\sin\tilde{\phi} \\ \sin\chi\cos\tilde{\varphi} - \gamma_t (\cos\chi_{1,2} - \beta_t/\beta_{1,2}) \sin\tilde{\varphi}\cos\tilde{\phi} \end{pmatrix}_{\hat{u},\hat{v},\hat{w}} \tag{2.121}$$

The change of momentum in the (u, v, w) coordinate system is

$$\vec{p}'_{1,2} - \vec{p}_{1,2} = \pm p_{1,2} \begin{pmatrix} \gamma_t [\gamma_t (\cos\chi_{1,2} - \beta_t/\beta_{1,2}) \cos\tilde{\varphi} + \sin\chi \sin\tilde{\varphi}\cos\tilde{\phi}] - \gamma_t \bar{p}_s / p_{1,2} \\ \sqrt{\gamma_t^2 (\cos\chi_{1,2} - \beta_t/\beta_{1,2})^2 + \sin^2\chi} \sin\tilde{\varphi}\sin\tilde{\phi} \\ \sin\chi(\cos\tilde{\varphi} - 1) - \gamma_t (\cos\chi_{1,2} - \beta_t/\beta_{1,2}) \sin\tilde{\varphi}\cos\tilde{\phi} \end{pmatrix}_{\hat{u},\hat{v},\hat{w}} \tag{2.122}$$

We assume the transverse momentum is small, that is $p_{s1,2} \approx p_{1,2}$, $p_{x1,2}^2 \ll 1$, $p_{y1,2}^2 \ll 1$ and $\sin\chi \approx \chi \ll 1$. Concerning the relations of $\vec{p}_1$ and $\vec{p}_2$ in the LAB frame

$$\begin{aligned} \vec{p}_1 \vec{p}_2 &= p_1 p_2 \cos(\chi_1 + \chi_2) \\ p_1 \sin\chi_1 &= p_2 \sin\chi_2 \end{aligned} \tag{2.123}$$

we obtain

$$\frac{(p_{x1}-p_{x2})}{p^2}+\frac{(p_{y1}-p_{y2})}{p^2}=4\chi^2 \tag{2.124}$$

Following Piwinski's derivation [158, 160], we define[4]

$$\begin{aligned}&\xi=\frac{p_1-p_2}{\gamma p},\quad \theta=\frac{p_{x1}-p_{x2}}{p},\quad \zeta=\frac{p_{y1}-p_{y2}}{p}\\ &4\chi^2=\theta^2+\zeta^2,\quad \rho^2=\xi^2(1+\gamma^2\chi^2)+4\chi^2\end{aligned} \tag{2.125}$$

where p is the mean momentum (of all the particles). Then, Eq. (2.115) is simplified to

$$\vec{\tilde{p}}_{1,2}=\pm\frac{p}{2}\begin{pmatrix}\xi\sqrt{1+\gamma^2\chi^2}\\ 0\\ 2\chi\end{pmatrix} \tag{2.126}$$

which indicates $\bar{p}_s=\frac{p}{2}\xi\sqrt{1+\gamma^2\chi^2}$. And, Eq. (2.122) can be further expressed as

$$\vec{p}'_{1,2}-\vec{p}_{1,2}=\pm\frac{p}{2}\begin{pmatrix}\gamma[\xi\cos\tilde{\varphi}+2\chi\sin\tilde{\varphi}\cos\tilde{\phi}]-\xi\gamma\\ \rho\sin\tilde{\varphi}\cos\tilde{\phi}\\ 2\chi(\cos\tilde{\varphi}-1)-\xi\sin\tilde{\varphi}\cos\tilde{\phi}\end{pmatrix}_{\hat{u},\hat{v},\hat{w}} \tag{2.127}$$

Note that, for convenience's sake, we assume $|p_1|\approx|p_2|\approx p$ and $\gamma\approx\gamma_t\sqrt{1+\gamma^2\chi^2}$. The momentum change in (s, x, y) coordinate system is then given by

$$\begin{aligned}\frac{\Delta\vec{p}_{1,2}}{p}&=\begin{pmatrix}1&0&0\\ 0&\zeta/2\chi&\theta/2\chi\\ 0&-\theta/2\chi&\zeta/2\chi\end{pmatrix}\cdot\left(\frac{\vec{p}'_{1,2}-\vec{p}_{1,2}}{p}\right)_{\hat{u},\hat{v},\hat{w}}\\ &=\pm\frac{1}{2}\begin{pmatrix}\gamma[\xi(\cos\tilde{\varphi}-1)+2\chi\sin\tilde{\varphi}\cos\tilde{\phi}]\\ \frac{\zeta}{2\chi}\rho\sin\tilde{\varphi}\sin\tilde{\phi}+\frac{\theta}{2\chi}[2\chi(\cos\tilde{\varphi}-1)-\xi\sin\tilde{\varphi}\cos\tilde{\phi}]\\ -\frac{\theta}{2\chi}\rho\sin\tilde{\varphi}\sin\tilde{\phi}+\frac{\zeta}{2\chi}[2\chi(\cos\tilde{\varphi}-1)-\xi\sin\tilde{\varphi}\cos\tilde{\phi}]\end{pmatrix}_{\hat{s},\hat{x},\hat{y}}\end{aligned} \tag{2.128}$$

For the Touscheck scattering which induces a large momentum deviation larger than the rms momentum deviation, we further assume that the initial longitudinal projection is small in the ($\tilde{u}$, $\tilde{v}$, $\tilde{w}$) coordinate system

$$\xi\sqrt{1+\gamma^2\chi^2}\ll 2\chi \tag{2.129}$$

[4] In Ref. [158], $\gamma\chi\ll 1$ is adapted for the discussion of small angle collision and $\rho^2=\xi^2+4\chi^2$.

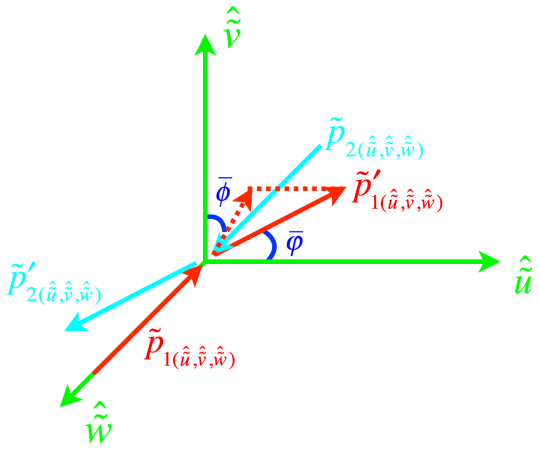

Fig. 2.18 Schematic of momenta transfer from the transverse plane to the longitudinal direction in the COM frame.

and the momenta are approximated as

$$\vec{\tilde{p}}_{1,2} = \begin{pmatrix} 0 \\ 0 \\ \pm p_\perp \end{pmatrix}_{\hat{\tilde{u}},\hat{\tilde{v}},\hat{\tilde{w}}} = \pm\frac{p}{2}\begin{pmatrix} 0 \\ 0 \\ 2\chi \end{pmatrix}_{\hat{\tilde{u}},\hat{\tilde{v}},\hat{\tilde{w}}} \tag{2.130}$$

The relative velocity of the ($\tilde{u}$, $\tilde{v}$, $\tilde{w}$) coordinate system is given by

$$\beta_t = \beta\cos\chi \tag{2.131}$$

where β is a function of the mean momenta p. The Touschek effect concerns mainly the amount of transverse momentum coupled into the longitudinal direction. Therefore, we define two angles: the polar angle $\bar{\varphi}$ between $\vec{p}'_{1,2}$ and $\tilde{u}$-axis, and the azimuthal angle $\bar{\phi}$ between the projection of $\vec{p}'_{1,2}$ on the $\tilde{u}\tilde{w}$ plane and the $\tilde{v}$-axis, as shown in Fig. 2.18. With such definitions, the calculation of the cross section, as well as the magnitude of the momentum transfered into the longitudinal direction, becomes easier. The momenta after a large angle collision in the COM frame become

$$\vec{\tilde{p}}'_{1,2} = p\chi\begin{pmatrix} \cos\bar{\varphi} \\ \sin\bar{\varphi}\cos\bar{\phi} \\ \sin\bar{\varphi}\sin\bar{\phi} \end{pmatrix}_{\hat{\tilde{u}},\hat{\tilde{v}},\hat{\tilde{w}}} \tag{2.132}$$

In the (u, v, w) coordinate system, the momenta of particles after collision are

$$\vec{p}'_{1,2} = \begin{pmatrix} p\chi\cos\bar{\varphi}\gamma_t + \gamma_t\beta_t\tilde{E}/c \\ p\chi\sin\bar{\varphi}\cos\bar{\phi} \\ p\chi\sin\bar{\varphi}\sin\bar{\phi} \end{pmatrix}_{\hat{u},\hat{v},\hat{w}} \tag{2.133}$$

Then, the momentum change due to a two-body collision is

$$\vec{p}'_{1,2} - \vec{p}_{1,2} = p\chi \begin{pmatrix} \gamma_t \cos\bar{\varphi} \\ \sin\bar{\varphi}\cos\bar{\phi} \\ \sin\bar{\varphi}\sin\bar{\phi} - 1 \end{pmatrix}_{\hat{u},\hat{v},\hat{w}} \tag{2.134}$$

Finally, we get the momentum change in the (s, x, y) coordinate system as

$$\frac{\Delta\vec{p}_{1,2}}{p} = \begin{pmatrix} \chi\gamma_t\cos\bar{\varphi} \\ \frac{\zeta}{2\chi}\sin\bar{\varphi}\cos\bar{\phi} + \frac{\theta}{2\chi}(\sin\bar{\varphi}\sin\bar{\phi} - 1) \\ -\frac{\theta}{2\chi}\sin\bar{\varphi}\cos\bar{\phi} + \frac{\zeta}{2\chi}(\sin\bar{\varphi}\sin\bar{\phi} - 1) \end{pmatrix}_{\hat{s},\hat{x},\hat{y}} \tag{2.135}$$

where $\bar{\varphi} \in (0, \bar{\varphi}_m)$[5] and $\bar{\phi} \in (0, 2\pi)$. $\bar{\varphi}_m$ depends on the momentum acceptance:

$$\bar{\varphi}_m = \cos^{-1}(\delta_m/\gamma_t\chi) \tag{2.136}$$

In a dispersive region ($\eta_x \neq 0, \eta_y = 0$), perturbations to the kinetic invariant are

$$\begin{aligned} \delta(2J_x) =& -2[\gamma_x x_\beta \eta_x + \alpha_x x_\beta \eta'_x + x'_\beta \tilde{\eta}_x]\frac{\delta p}{p} + \frac{\eta_x^2 + \tilde{\eta}_x^2}{\beta_x}\left(\frac{\delta p}{p}\right)^2 \\ &+ 2(x'_\beta + \frac{\alpha_x}{\beta_x}x_\beta)\frac{\delta p_x}{p} + \left(\frac{\delta p_x}{p}\right)^2 - \frac{2\tilde{\eta}_x}{\beta_x}\frac{\delta p_x}{p}\frac{\delta p}{p} \\ \delta(2J_y) =& \beta_y\left(\frac{\delta p_y}{p}\right)^2 + 2(\alpha_y y_\beta + \beta y'_\beta)\left(\frac{\delta p_y}{p}\right) \\ \delta(2J_s) =& \frac{h\eta_c}{\Omega_s}\left[2\frac{\delta p}{p}\frac{\Delta p}{p} + \left(\frac{\delta p}{p}\right)^2\right] \end{aligned} \tag{2.137}$$

In the presence of the non-zero horizontal dispersion and zero xy coupling, the vertical invariant is only affected via the transverse heating while the horizontal invariant $2J_x$ could be enlarged due to the transverse heating and the diffusion coupled through the horizontal $\mathcal{H}_x$ function. In fact, the transverse heating is the analogue of the transverse kicks due to the synchrotron radiation emitted at a small angle to the forward direction. Typically, the enlargement of the invariant of the betatron motion from this opening angle of the radiation is extremely small.

2.5.2 Emittance growth due to intra beam scattering

The dilution of the equilibrium emittance from IBS can be estimated employing various self-consistent methods. First, we try to introduce the fundamental process of the analytical calculation following the method developed by K. Kubo.

[5] $\bar{\varphi} \in (\pi - \bar{\varphi}_m, \pi)$ for the second particle.

In SAD, the equilibrium parameters are extracted in the context of the beam-envelope formalism [148, 152]. IBS, as well as quantum excitation, are treated as a momentum diffusion process, which can be described by the diffusion equation in Eq. (2.79). The 6×6 beam-envelope matrix is in the form of

$$\boldsymbol{R}(s) = \boldsymbol{M}(s,s_0)\boldsymbol{R}(s_0)\boldsymbol{M}^T(s,s_0) + \bar{\boldsymbol{B}}(s,s_0) \tag{2.138}$$

where $\boldsymbol{M}(s,s_0)$ is the transfer matrix, and $\bar{\boldsymbol{B}}(s,s_0)$ represents the integrated diffusions

$$\bar{\boldsymbol{B}}(s,s_)) = \int_{s_0}^{s} \boldsymbol{M}(s,s_0)\boldsymbol{B}(s_0)\boldsymbol{M}^T(s,s_0) \tag{2.139}$$

where $\boldsymbol{B}$ is the diffusion matrix in the presence of quantum excitation[6] and IBS diffusion. The diffusion matrix for IBS can be evaluated from the rate of the momentum diffusion, which is a function of bunch charge and beam emittances. The momentum diffusion rate is in the form of [167]

$$\frac{\Delta\langle p_i p_j\rangle}{\Delta t} = \sum_{k=1}^{3} \boldsymbol{R}_{ik}\boldsymbol{R}_{jk}\frac{\Delta\langle w_k^2\rangle}{\Delta t} \tag{2.140}$$

where $\boldsymbol{R}$ is an orthogonal matrix and w is the "normal momentum". $\Delta\langle w_k^2\rangle/\Delta t$ can be understood as the heating of the temperature in the direction of k. The heating term is relevant to the temperature difference between the two directions.

$$\frac{\Delta\langle w_k^2\rangle}{\Delta t} = c_I(g_i + g_j - 2g_k) \tag{2.141}$$

where

$$c_I = \frac{r_e^2 N(\log)}{4\pi\gamma^3\varepsilon_1\varepsilon_2\varepsilon_3} \tag{2.142}$$

and

$$\begin{aligned}
g_1 &= \int_0^{\pi/2} \frac{2u_1\sin^2\psi\cos\psi}{\sqrt{(\sin^2\psi + \frac{u_1}{u_2}\cos^2\psi)(\sin^2\psi + \frac{u_1}{u_3}\cos^2\psi)}} \\
g_2 &= \int_0^{\pi/2} \frac{2u_2\sin^2\psi\cos\psi}{\sqrt{(\sin^2\psi + \frac{u_2}{u_1}\cos^2\psi)(\sin^2\psi + \frac{u_2}{u_3}\cos^2\psi)}} \\
g_3 &= \int_0^{\pi/2} \frac{2u_3\sin^2\psi\cos\psi}{\sqrt{(\sin^2\psi + \frac{u_3}{u_1}\cos^2\psi)(\sin^2\psi + \frac{u_3}{u_2}\cos^2\psi)}}
\end{aligned} \tag{2.143}$$

[6] The diffusion matrix for quantum excitation can be found in Ref. [148]

where N is the number of particles, (log) the Coulomb logarithm, $\varepsilon_1, \varepsilon_2, \varepsilon_3$ the emittances in the normal mode and u_1, u_2, u_3 the terms along the diagonal of the diagonalization matrix $\boldsymbol{G}$

$$\boldsymbol{G} = \boldsymbol{RFR} = \begin{pmatrix} u_1 & 0 & 0 \\ 0 & u_2 & 0 \\ 0 & 0 & u_3 \end{pmatrix} \tag{2.144}$$

where $\boldsymbol{F}$ is the local average of the momentum matrix and $\boldsymbol{R}$ the orthogonal matrix, the same as that in Eq. (2.140). We do not aim to reproduce the whole complicated derivation of the diffusion rate from the small-angle collisions. However, we note that the derivation is under the assumption of Gaussian beam distributions in 6D phase space, that is

$$\rho(x,\rho) = \frac{N}{\Gamma} e^{-S(x,p)} \tag{2.145}$$

with

$$\begin{aligned} S(x,p) &= \sum_{i,j=1}^{3} \left(\frac{1}{2} A_{ij} \delta p_i \delta p_j + B_{ij} \delta p_i \delta p_j + \frac{1}{2} C_{ij} \delta x_i \delta x_j \right) \\ \Gamma &= \int e^{-S(x,p)} d^3x d^3p \end{aligned} \tag{2.146}$$

where $\delta\vec{p}$ and $\delta\vec{x}$ are the momentum and displacement with respect to the beam energy and the reference orbit, respectively, and $e^{-S(x,p)}$ represents a Gaussian phase space distribution.

The Coulomb logarithm (log), in a COM coordinate system, is defined as[7]

$$\begin{aligned} (\log) &= \frac{1}{2} \int_{\cos\theta_{\max}}^{\cos\theta_{\min}} \frac{d(\cos\theta)}{1-\cos\theta} \\ &= \log\left(\frac{b_{\min}}{b_{\max}} \right) \end{aligned} \tag{2.147}$$

where θ is the scattering angle (assuming classical Rutherford scattering) and b is the impact parameter. The values of $b_{\min}$ and $b_{\max}$ are given by

$$\begin{aligned} b_{\min} &= \max\left(\frac{\sqrt{2} m \alpha_0}{\langle \delta p^2 \rangle}, \sqrt{\frac{1}{\pi \langle\rho\rangle \max(\tau_1, \tau_2, \tau_3)}} \right) \\ b_{\max} &= \min(\langle\rho\rangle^3, \sqrt{\nu_1}, \sqrt{\nu_2}, \sqrt{\nu_3}) \end{aligned} \tag{2.148}$$

where m is the electron mass, α_0 the fine-structure constant, $\langle\rho\rangle$ the mean particle density, $\tau_{1,2,3}$ the damping time in the COM frame and $\nu_{1,2,3}$ the eigenvalues of the spatial beam matrix.

[7]The value of the Coulomb logarithm is fixed at 20 in Ref. [162]. Ref. [169] gives another expression of the logarithm and the corresponding criteria to compute it.

On the other hand, the predictions of the emittance growth, as well as the potential momentum tail from Coulomb scattering, requires more precise tracking simulation. The Zenkevich IBS Monte Carlo simulation method by means of a binary collision model (BCM) provides a convenient routine [170]. The BCM stimulates the collision between two macro-particles in the same cell with a scattering angle relevant to the time step Δt. After collision, the change of momenta and invariant is adapted following the formalism derived by Piwinski. A. Vivoli has developed a tracking code "Software for Intra-beam scattering and Radiation Effects" (SIRE) taking into account radiation damping, quantum excitation and IBS based on the BCM [171, 172]. We have added some modification into SIRE in order to adapt it to our purpose of emittance growth predictions and momentum tail simulation. In this section, our discussion of particle tracking and IBS diffusion is concentrated on our modified SIRE code.

To be simple, we ignore the non-linear beam dynamic in the element-by-element particle tracking. Linear beam transport between two elements is governed by the new invariants H_x, H_y and H_s

$$\begin{aligned} H_x &= \beta_x x_\beta'^2 + 2\alpha_x x_\beta x_\beta' + \gamma_x x_\beta^2 \\ H_y &= \beta_y y_\beta'^2 + 2\alpha_y y_\beta y_\beta' + \gamma_y y_\beta^2 \\ H_s &= \delta^2 + \frac{1}{\Omega_s^2} z^2 \end{aligned} \tag{2.149}$$

where $\Omega_s = \frac{\eta_c C}{2\pi \nu_s}$ and $z = \beta c \Delta t$ is the longitudinal position deviation. Horizontal and vertical phase advances are generated randomly at each element taking into account the local Twiss parameters. As a result, the single particle dynamics cannot be studied in the present SIRE code. The Twiss parameters are imported from an external piece of software, e.g., MAD-X or SAD, using the self-defined functions. The one-turn mapping equation including the perturbation from radiation damping and quantum excitation is computed and applied each turn. Considering the average energy loss per revolution due to synchrotron radiation, the one-turn mapping equation for the energy deviation is in the form of

$$\delta_{j+1} = \delta_j + \frac{E_g}{E} - \frac{U_0}{E} \tag{2.150}$$

where j denotes the j-th turn and the high-order harmonics of the RF-cavity has been ignored. In the presence of radiation damping and quantum excitation, the one-turn mapping equation for synchrotron motion (above the transition energy) is given by

$$\begin{aligned} \delta p_{i+1}' &= \delta p_{i+1} e^{-2T_0/\tau_s} + \sigma_{p,\mathrm{eq}} \sqrt{4T_0/\tau_s} \cdot h_i \\ z_{i+1} &= z_i - \delta p_{i+1}' T_0 \alpha_c c \end{aligned} \tag{2.151}$$

and the one-turn map of the horizontal motion (x, x') is

$$\begin{aligned} J_{x,i+1} &= J_{x,i} e^{-2T_0/\tau_x} \\ x_{i+1} &= x_i + \sqrt{\varepsilon_{x,\mathrm{eq}} \beta_x (1 - e^{-2T_0/\tau_x})} \cdot h_i \\ x'_{i+1} &= x'_i + \sqrt{\varepsilon_{x,\mathrm{eq}} \beta_x (1 - e^{-2T_0/\tau_x})} (1 - \alpha_x)/\beta_x \cdot h_i \end{aligned} \tag{2.152}$$

where T_0 is the revolution period, $\tau_{s,x,y}$ the longitudinal/horizontal/vertical damping time, $\sigma_{p,eq}$ the natural equilibrium energy spread, h_i a random number following the Gaussian distribution function with unit standard deviation, $\varepsilon_{x,\mathrm{eq}}$ the natural horizontal emittance and α_x, β_x the Twiss parameters. The mapping equation for the vertical motion is in the same form as Eq. (2.152). The one-turn map of the radiation damping and quantum excitation is applied at the location of the RF cavity.

The kernel of the IBS simulation employs the Zenkevich-Bolshakov approach based on the macro-particle algorithm BCM. The BCM resolves the continuous IBS process through a discrete step "mapping" in the phase space. The change of momenta (invariants) in a discrete time step Δt, which is sufficiently small with respect to the IBS growth time, depends on the initial state of the local particle spatial distribution. The primary stages in the BCM could be summarized as follows:

1. Divide the spatial space into $h \times l \times w$ cells and group the macro-particles at each cell with respect to its spatial coordinates;
2. Determine particle pairs ready for binary collision in a cell. For an odd number of particle in a cell, a pair of three particles is considered;
3. Calculate the Coulomb scattering angle according to the local particle density in a cell;
4. Apply the momentum changes using Eq. (2.128) and update particle invariants after collision;

The first two steps are sketched in Fig. 2.19. In step 3, the scattering angle is generated randomly following the normalized distribution with a variance of [173]

$$\langle \frac{\tilde{\varphi}^2}{2} \rangle = \begin{cases} 2\pi r_e^2 \tilde{\rho}_v \tilde{\Delta t} (\log)/\tilde{\beta}^3, & \text{2-particle pair} \\ \pi r_e^2 \tilde{\rho}_v \tilde{\Delta t} (\log)/\tilde{\beta}^3, & \text{3-particle pair} \end{cases} \tag{2.153}$$

where $\tilde{\rho}_v$ is the particle density in the COM frame, $\tilde{\Delta t}$ the time period between two adjacent elements in the COM frame and $\tilde{\beta}$ the velocity of the COM coordinate system. The Coulomb logarithm in the COM frame is given by

$$(\log) = \log\Big(\frac{2\tilde{\beta}^2 \tilde{b}_{\max}}{r_e}\Big) \tag{2.154}$$

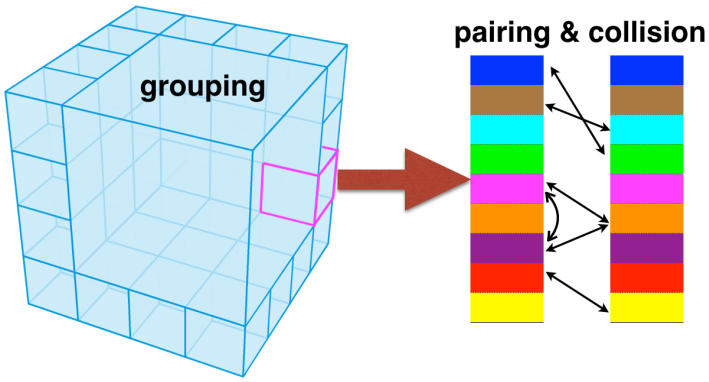

Fig. 2.19 Schematic of the determination of particles in cell and particle pairs in a cell

where $b_{\max}$ is the maximum impact parameter which gives a cut-off angle for $\tilde{\varphi}$. As suggested in Ref. [158] and Ref. [167], $b_{\max}$ can be half of the beam height or else determined using Eq. (2.148). In fact, the choice of $b_{\max}$ is ambiguous and we follow the suggestions in Ref. [167] for the theoretical estimation, similar to the equilibrium-emittance calculation in SAD.

In the case of the ATF damping ring, the Twiss parameters imported into SIRE are from a lattice with residual COD and non-zero vertical dispersion which give a natural vertical emittance around 12 pm. To speed up the simulation, the number of elements in the ATF lattice has been shortened from around 880 to 250. Decreasing of the number of elements has a feeble influence on the prediction of emittance dilution from IBS, as has been checked by simulations. The initial beam parameters, e.g., emittances, energy spread and bunch length, take the values in the absence of IBS. The number of macro-particles per bunch is 2×10^4 in the single-bunch mode. Particles are allocated to $100 \times 100 \times 100$ cells at each element. The (log) factor is evaluated corresponding to the (vertical) beam size at each element. An average of the (log) factor for the simulation is 10–15 which is in good agreement with the analytical estimations in Ref. [167], as shown in Fig. 2.20. At the same time, the time dependence of the emittances suggests that the IBS rise time is less than 40 ms (with the vertical rise time being longer than the longitudinal and horizontal ones).

Furthermore, the emittance growth from IBS has been estimated through analytical formulas developed by K. Kubo and built in to SAD, and also using Monte Carlo simulation. Figure 2.21 shows the comparison of the emittance growth and "equilibrium" distributions. The emittance growth predicted by the two methods are in good agreement for beam intensities from 5×10^8–1×10^{10} e/pulse. Moreover, the Gaussian shape of the beam profile is preserved under the action of IBS diffusion. The scattering angle is drawn from a normalized distribution function dedicated to the small-angle Coulomb interaction. Consequently, there is no significant tail arising from these collision processes. This result validates the assumption of Gaussian beam core distributions in the phase space with coordinates $(x, x', y, y', z, \delta)$. It is of great important for the further numerical evaluations of large-angle Coulomb scattering.

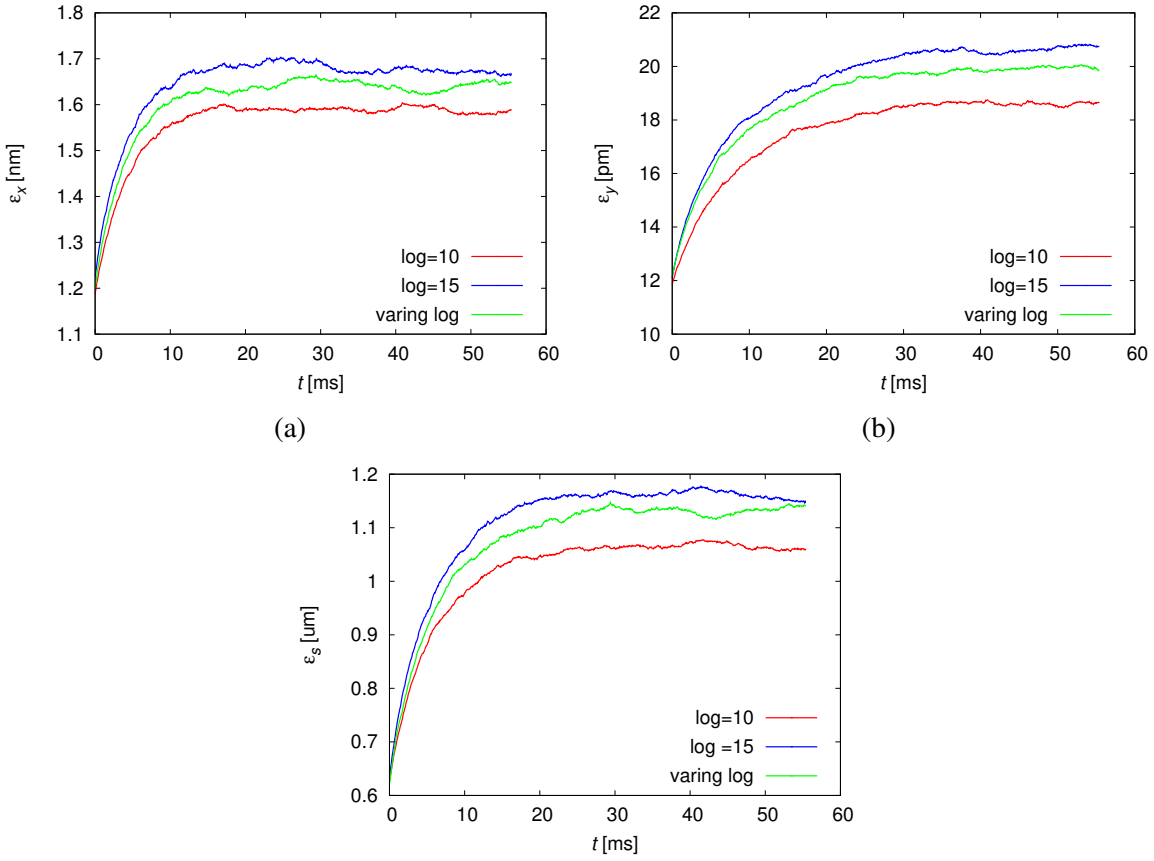

Fig. 2.20 Prediction of emittance growth in SIRE code for 3 different (log) factors. Beam intensity is set to 1×10^{10} e/pulse.

2.5.3 Momentum tail resulted from large-angle Coulomb scattering

Momentum deviation from large-angle Coulomb scattering can be evaluated in two ways: a preliminary estimation of the scattering rate which characterizes the advent of large momentum deviation particles and Monte Carlo simulation of the generation and evolution of these particles.

The calculation of the scattering rate of the large-angle events adapts the method given by Piwinski, which is suitable for an arbitrary ratio of beam height to beam width and takes into account the variation of the beam envelops. For collisions resulting in a momentum deviation within the momentum acceptance, transfer of momentum from the transverse plane to the longitudinal motion follows the same formalism as that for Touschek scattering. The probability of Coulomb scattering in the $(\tilde{u}, \tilde{v}, \tilde{w})$ coordinate system is represented by the Moller scattering cross section [174]

$$\frac{d\tilde{\sigma}}{d\tilde{\Omega}} = \frac{r_e^2}{4\tilde{\gamma}}\left[\left(1+\frac{1}{\tilde{\beta}^2}\right)^2\left(\frac{4}{\sin^4\tilde{\Phi}}+\frac{3}{\sin^2\tilde{\Phi}}\right)+\frac{4}{\sin^2\tilde{\Phi}}+1\right] \tag{2.155}$$

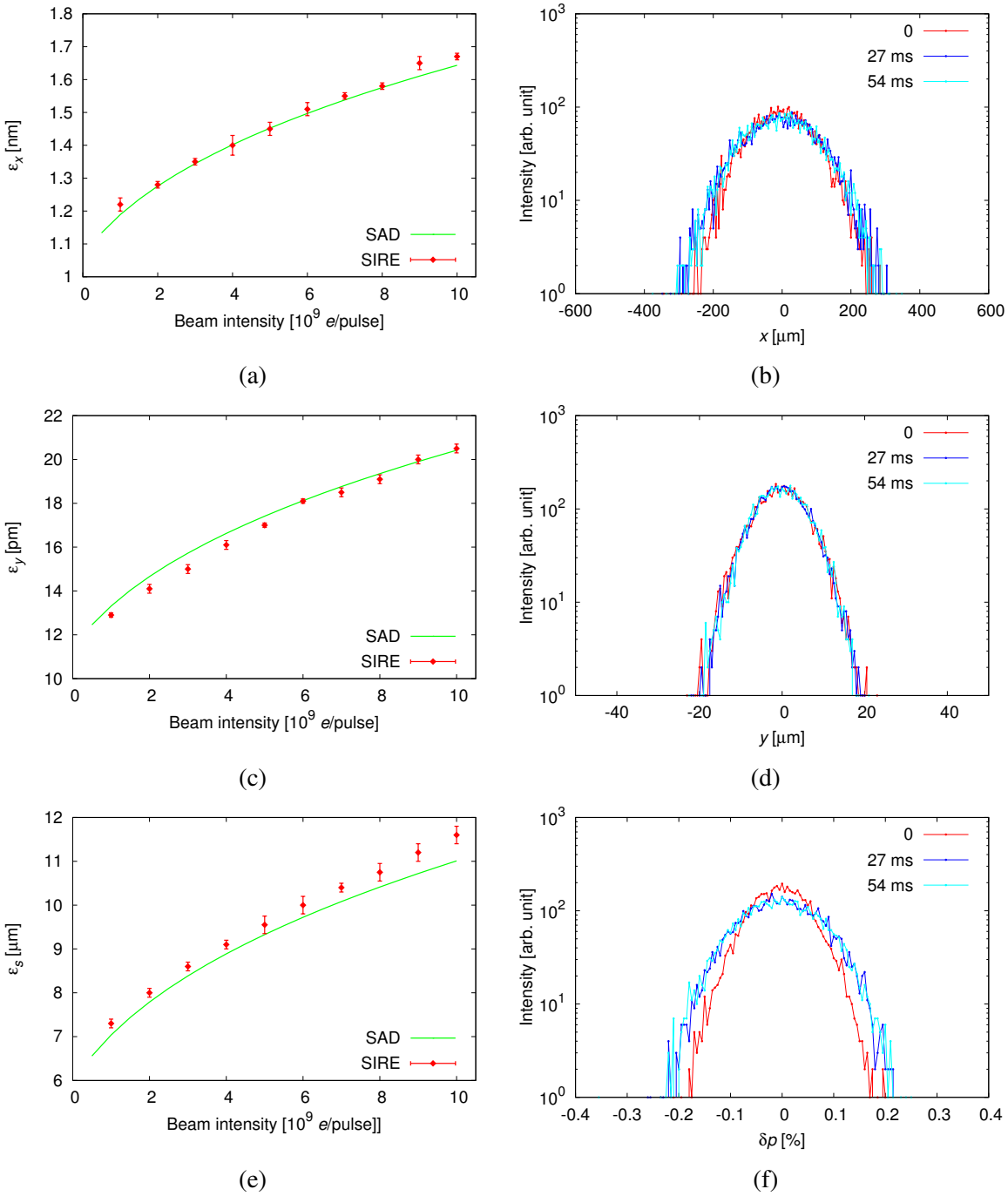

Fig. 2.21 Intensity dependence of the horizontal, vertical and longitudinal emittances and the evolution of beam profiles in the presence of radiation damping, quantum excitation and IBS. The beam profile estimations shown here are for a beam intensity of 6×10^9 e/pulse.

where $\tilde{\gamma} = \gamma/\gamma_t$, $\tilde{\Phi}$ is the angle between the momenta $\vec{\tilde{p}}_1$ and $\vec{\tilde{p}}'_1$. Relative velocity $\tilde{\beta}$ is defined as

$$\tilde{\beta}^2 = \frac{\tilde{p}^2 c^2}{\tilde{E}^2} = \frac{\beta^2\gamma^2\chi^2}{1+\beta^2\gamma^2\chi^2} \tag{2.156}$$

Notice that the relation between $\tilde{\Phi}$, $\bar{\varphi}$ and $\bar{\phi}$ follows

$$\tilde{p}'_{\tilde{w}1,2} = \tilde{p}_{1,2}\cos\tilde{\Phi} = \tilde{p}_{1,2}\sin\bar{\varphi}\cos\bar{\phi} \tag{2.157}$$

Using Eq. (2.136), Eq. (2.156) and Eq. (2.157), the total cross section in the COM frame is given by [160]

$$\begin{aligned}\tilde{\sigma} =& \frac{r_e^2}{4\tilde{\gamma}}\int_0^{\bar{\varphi}_m}\int_0^{2\pi}\Big[\Big(1+\frac{1}{\tilde{\beta}^2}\Big)^2\Big(\frac{4}{\sin^4\tilde{\Phi}}+\frac{3}{\sin^2\tilde{\Phi}}\Big)+\frac{4}{\sin^2\tilde{\Phi}}+1\Big]\sin\bar{\varphi}d\bar{\phi}d\bar{\varphi}\\ =& \frac{\pi r_e^2\gamma_t^2}{2\gamma^2}\Big[\Big(3-\frac{2}{\tilde{\beta}^2}-\frac{1}{\tilde{\beta}^4}\Big)\log\Big(\frac{\gamma_t\chi}{\delta_m}\Big)+\Big(1+\frac{1}{\tilde{\beta}^2}\Big)^2\frac{\gamma_t^2\chi^2-\delta_m^2}{\delta_m^2}-\frac{\delta_m^2}{\gamma_t\chi}+1\Big]\end{aligned} \tag{2.158}$$

which is a function of the minimum momentum deviation δ_m and the transverse momentum χ in the COM frame. The total cross section is then transformed into the rest coordinate system by

$$\sigma = \frac{\tilde{\sigma}}{\gamma_t} \tag{2.159}$$

In the case of the ATF damping ring, where we assume $\delta_m = 1.2\%$, the cross section reaches a maximum near χ =6 μrad and then decreases for larger χ, as shown in Fig. 2.22 (a).

We obtain the scattering rate, which is an integral over all the particles, as

$$\Big(\frac{dN_{\rm sc}}{dt}\Big) = 2\beta c\int\rho_v^2\sigma\sin\chi dV \tag{2.160}$$

where ρ_v is the particle density given by

$$\rho_v^2 = N_e^2 f_s(\delta_1,z_1)f_s(\delta_2,z_2)f_\perp(x_{\beta1},x'_{\beta1},y_{\beta1},y'_{\beta1})f_\perp(x_{\beta2},x'_{\beta2},y_{\beta2},y'_{\beta2}) \tag{2.161}$$

with

$$f_s(\delta,z) = \frac{1}{2\pi\sigma_\delta\sigma_z}\exp\Big[-\frac{\delta^2}{2\sigma_\delta^2}-\frac{z^2}{2\sigma_z^2}\Big] \tag{2.162}$$

$$f_\perp(x_\beta,x'_\beta,y_\beta,y'_\beta) = \frac{\beta_x\beta_y}{4\pi^2\sigma_{x\beta}^2\sigma_{y\beta}^2}\exp\Big[-\frac{x_\beta^2+\tilde{x}_\beta^2}{2\sigma_{x\beta}^2}-\frac{y_\beta^2+\tilde{y}_\beta^2}{2\sigma_{y\beta}}\Big] \tag{2.163}$$

where $\tilde{x}_\beta = \alpha_x x_\beta + \beta_x x'_\beta$, and $\sigma_\delta, \sigma_z, \sigma_{x\beta}$ and $\sigma_{y\beta}$ are rms beam sizes. Following the derivation

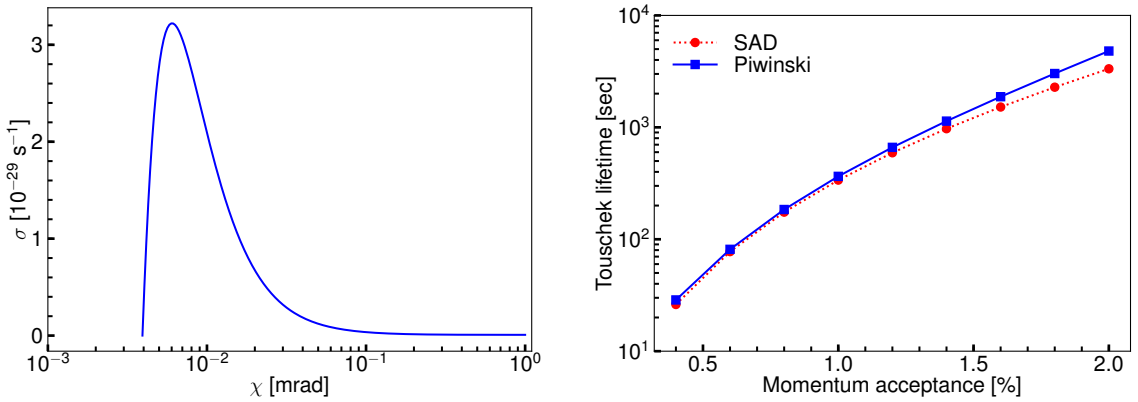

(a) (b)

Fig. 2.22 Evaluation of large-angle scattering for the ATF damping ring: (a) dependence of the total cross section on the χ for a momentum acceptance of 1.2 %; (b) Touschek lifetime estimated using Pinwinski formulas and SAD where only the momentum acceptance was considered.

in Ref. [160], the integration can be further expressed as

$$\left(\frac{dN_{\rm sc}}{dt}\right) = \frac{r_e^2 c\beta_x\beta_y\sigma_h N_e^2}{8\sqrt{\pi}\gamma^4\sigma_{x\beta}^2\sigma_{y\beta}^2\sigma_\delta\sigma_z} \int_{\tau_m}^{\infty}\left[\left(2+\frac{1}{\tau}\right)^2\left(\frac{\tau/\tau_m}{1+\tau}-1\right)+1-\frac{\sqrt{1+\tau}}{\sqrt{\tau/\tau_m}}-\frac{1}{2\tau}\left(4+\frac{1}{\tau}\right)\log\left(\frac{\tau/\tau_m}{1+\tau}\right)\right]e^{-B_1\tau}I_0(B_2\tau)\frac{\sqrt{\tau}d\tau}{\sqrt{1+\tau}} \tag{2.164}$$

and

$$\begin{aligned}
\frac{1}{\sigma_h^2} &= \frac{2}{\sigma_\delta^2}+\frac{\eta_x^2+\tilde{\eta}_x^2}{\sigma_{x\beta}^2}+\frac{\eta_y^2+\tilde{\eta}_y^2}{\sigma_{y\beta}^2} \\
B_1 &= \frac{\beta_x^2}{2\beta^2\gamma^2\sigma_{x\beta}^2}\left(1-\frac{\sigma_h^2\tilde{\eta}_x^2}{\sigma_{x\beta}^2}\right)+\frac{\beta_y^2}{2\beta^2\gamma^2\sigma_{y\beta}^2}\left(1-\frac{\sigma_h^2\tilde{\eta}_y^2}{\sigma_{y\beta}}\right) \\
B_2 &= B_1^2-\frac{\beta_x^2\beta_y^2\sigma_h^2}{\beta^4\gamma^4\sigma_{x\beta}^4\sigma_{y\beta}^4\sigma_\delta^2}\left(\sigma_x^2\sigma_z^2-\sigma_\delta^4\eta_x^2\eta_y^2\right)
\end{aligned} \tag{2.165}$$

where I_0 is the modified Bessel function of the first kind and $\tau_m = \beta^2\delta_m^2$ gives the lower limit of the integration. It is apparent that Eq. (2.164) describes the rate of large-angle scattering events which could induce momentum deviations larger than δ_m. In the case of $\delta_m = \delta_{\rm acc}$, where $\delta_{\rm acc}$ is the momentum acceptance, the Touschek lifetime has the definition of

$$\frac{1}{\tau_{\rm Tous}} = \frac{1}{N_e}\left(\frac{dN_{\rm sc}}{dt}\right)_{\delta_m=\delta_{\rm acc}} \tag{2.166}$$

For a beam intensity of 3×10^9 e/pulse, the Touschek lifetime as a function of the momentum acceptance has been evaluated using Eq. (2.164)–Eq. (2.166), as shown in Fig. 2.22 (b). The numerical estimations define a Touschek lifetime around 330 s which is of the same magnitude as the experimental measurements [157, 175].

The growth rate of particles with a momentum deviation of $\delta_{m1} < |\delta| < \delta_{m2}$ is given by

$$R(\delta_{m1}, \delta_{m2}) = \left(\frac{dN_{\rm sc}}{dt}\right)_{\delta_{m1}} - \left(\frac{dN_{\rm sc}}{dt}\right)_{\delta_{m2}} \tag{2.167}$$

Assuming the excited momentum deviation is from $5\sigma_\delta$ to $\delta_{\rm acc}$, the growth rate, in other words, the scattering rate as a function of resulting momentum deviation, has been calculated and is shown in Fig. 2.23.

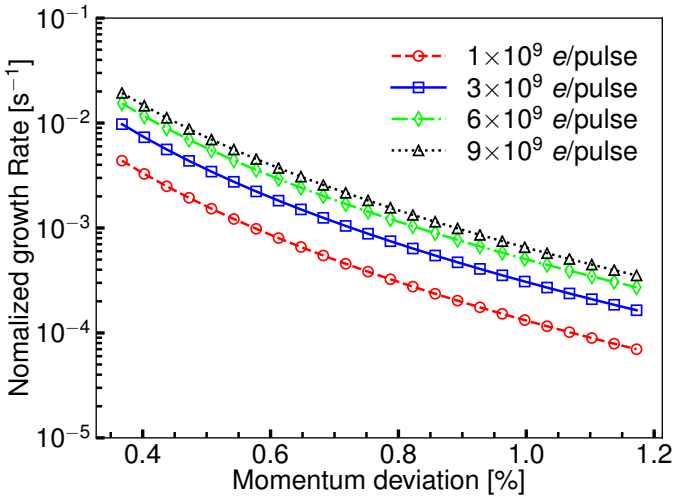

Fig. 2.23 The growth rate of large momentum deviations for different beam intensities. The growth rate has been normalized to the beam intensity.

The growth rate of the "potential" momentum tail from Coulomb scattering depends on the beam intensity, transverse beam sizes, energy spread and bunch length. To define an effective method to experimentally characterize a potential momentum tail at ATF, we estimated the growth rate of the excited momentum deviation as a function of the vertical emittance and beam intensity. Assuming a beam intensity of 3×10^9 e/pulse and taking into account the interplay of beam emittances, the scattering rate is reduced by 32 % for a vertical emittance growth from 8 pm to 44 pm, as shown in Fig. 2.24 (a). For a natural vertical emittance of 12 pm in the presence of a realistic COD achieved by local orbit bumps, the dependence of the growth rate of the large momentum deviation particles on the beam intensity has been evaluated. The growth rate does not increase proportionally to the square of the beam intensity because of the emittance dilution due to IBS diffusion. Normalizing the growth rate to the respective beam intensity, the normalized growth rate blows up faster for lower beam intensity, as shown in Fig. 2.24 (b).

Comparing with the dependence on the vertical emittance, the intensity dependence is more significant and can be further used to characterize the observed the momentum distribution.

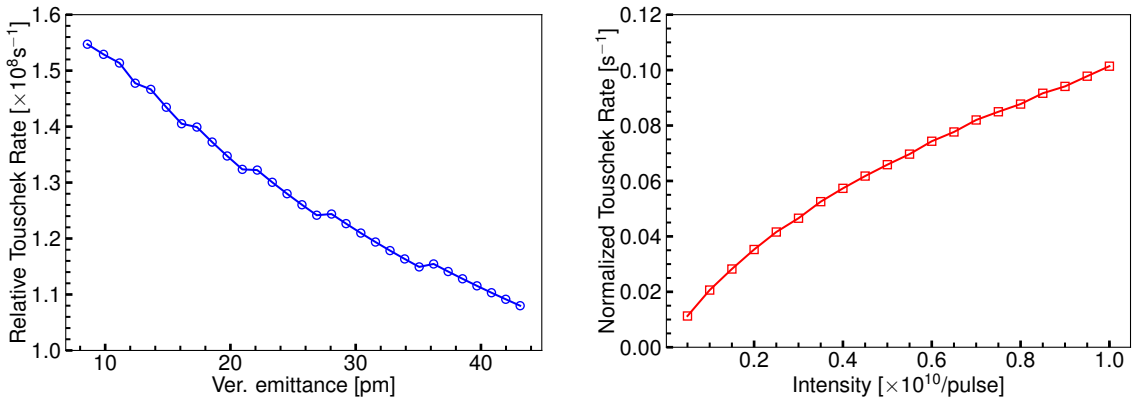

(a) (b)

Fig. 2.24 Dependence of the normalized growth rate of momentum deviations ranging from $5\sigma_\delta$ to δ_{acc} on the vertical emittance and beam intensity. The vertical emittance is controlled by adjusting the *xy* coupling, artificially.

The generation and evolution of a momentum tail can be predicted through Monte Carlo simulation in SIRE. Moreover, bunch lengthening from potential well distortion is comparable with the increment resulting from IBS diffusion and can further reduce the large-angle scattering rate. These aspects are currently under investigation using the Monte Carlo simulation. To probe the prediction of momentum tail, no matter where is it comes from, experimental measurements are the most important. For precise measurements of beam halo and momentum tail, two kinds of instrumentations have been developed and presented in Chapter 3. Then, measurements and characterization of beam halo and momentum tails are described in Chapter 4.

Chapter 3

Experimental setup for halo diagnostics

Several kinds of beam halo diagnostics have been installed at ATF2, e.g., the WS and the DS detector, but the desired effective dynamic range (10^5) was unfortunately not fully met. To enable probing the theoretical predictions of beam halo, we have optimized the performance of the present DS detector. Furthermore, to acquire fast and complementary measurements upstream of the final focus section of ATF2, an OTR/YAG monitor has also been developed.

3.1 Optimization of the *in-vacuum* DS detector

3.1.1 Present state of the DS detector

To probe the halo particles and the Compton recoil electrons, two sets of DS detector have been constructed and installed at the Post-IP in 2014. Each diamond sensor is 500 μm thick, with the metallization arranged in four strips, two broad ones with dimensions of 1.5×4 mm^2 and two narrow ones of 0.1×4 mm^2. All the strips are biased at –400 V by a programmable power supply in order to collect the electron-hole pairs which are generated due to the ionization when particles hit the diamond crystal [176]. To suppress the high-frequency noise on the supplied bias voltage and to provide a sufficient reserve of charge for the largest signals, a low pass filter together with charging capacitors are mounted on the backside of the Printed Circuit Board (PCB) (see Fig. 3.1). The diamond strips are connected to an oscilloscope (Agilent 6104) with long coaxial cables ($\sim$25 m) and 50 Ω resistors converting the current signal to voltage output. The sampling rate of the Aligent oscilloscope is 4 GSample/s with an analog bandwidth of 1 GHz. To keep the amplitude of the signal within the range of the oscilloscope, four –30 dB attenuators are used when measuring the beam core.

Analogous to the WS, the vertical and horizontal distributions are obtained through one-dimensional (1D) scans of the DS detector across the beam. Since the length of the DS strip (4 mm) is comparable to the transverse beam size, an offset between the DS and the beam center in the perpendicular plane will reduce the particle collection and registered signals [177].

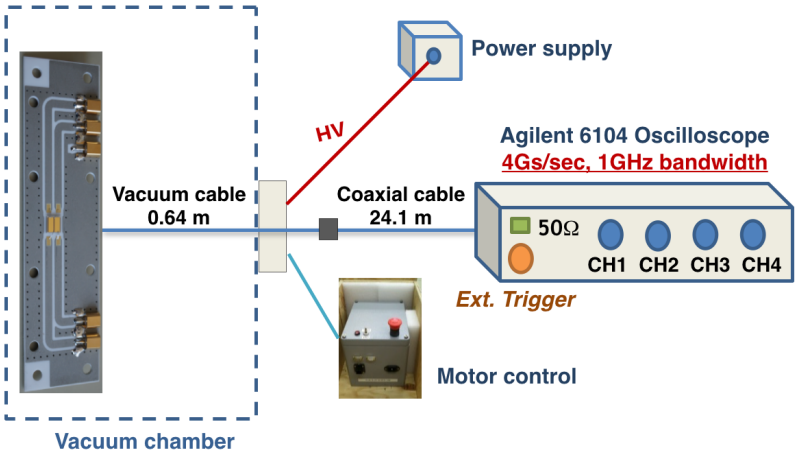

Fig. 3.1 Schematic of the DS detector at ATF2.

Distortions of the measured beam profile due to such misalignment errors are shown in Fig. 3.2 where we assumed a beam size of 2 mm and 1 mm, vertically and horizontally, respectively. Therefore, before performing the scanning either vertically or horizontally, the DS has to be carefully aligned in the direction perpendicular to the scanning. The DS has only one degree of freedom, and thus we align the beam against the DS center by moving the upstream two quadrupoles QD0 and QF1, vertically and horizontally, respectively. Correlations between the vertical and horizontal beam positions at the DS detectors and displacements of QD0 and QF1 have been determined to be

$$\begin{aligned} \Delta y_{\mathrm{DS}} &= 5.4 \times \Delta y_{\mathrm{QD0}} \\ \Delta x_{\mathrm{DS}} &= 11.0 \times \Delta x_{\mathrm{QF1}} \end{aligned} \tag{3.1}$$

where Δy_{QD0} and Δx_{QF1} are displacements of QD0 and QF1, respectively.

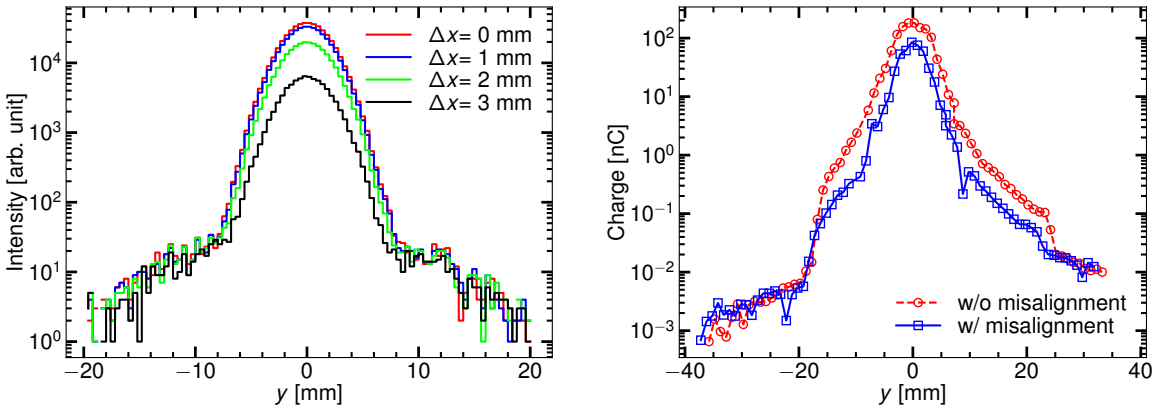

(a) (b)

Fig. 3.2 Predictions (a) and measurements (b) of the profile distortion due to the horizontal misalignment of the DS strip with respect to the beam center.

For a DS in the air, the output charge signal increases linearly with the number of the incident electrons, from a single electron to more than 10^7 [118]. The charge generated in a single crystal diamond has been estimated to be 2.88 fC per electron for a Charge Collection Efficiency (CCE) of 100 % [178]. Diamond crystal having a band gap as large as 5.5 eV, a small leakage current and a high singal-to-noise ratio (SNR) make it suitable for the detection of signals from small numbers of incident electrons. The capability for detecting single electron using the sCVD DS has been demonstrated at LAL [179] where a diamond sample was placed outside of the beam pipe of the PHoto-Injecteur at LAL (PHIL) accelerator to prevent undesired induction currents when beam passes the diamond. However, the DS strip detectors used at ATF2 and the related circuitry on the PCB were placed in the vacuum chamber, connected to the acquisition system outside via in-vacuum coaxial cables. Hence, a transverse closed circuit with a considerable size is formed around the PCB. Any sudden change of the electromagnetic field passing through this closed circuit will induce a current signal, according to Faraday's law of electromagnetic induction. In the frequency domain, the main components of this pick-up signal were found to be around 0.3 GHz, 0.7–0.9 GHz and 1.3 GHz. Using two low-pass filters (30 MHz and 80 MHz), the shape of the waveform is improved significantly, but the integrated charge signal from this pickup noise remains unchanged, as shown in Fig. 3.3. The lower limit for detecting signals in the presence of this background noise, that is, the smallest level of this pick-up signal, was measured to be around 0.3 pC, corresponding to a charge signal of about 100 incident electrons.

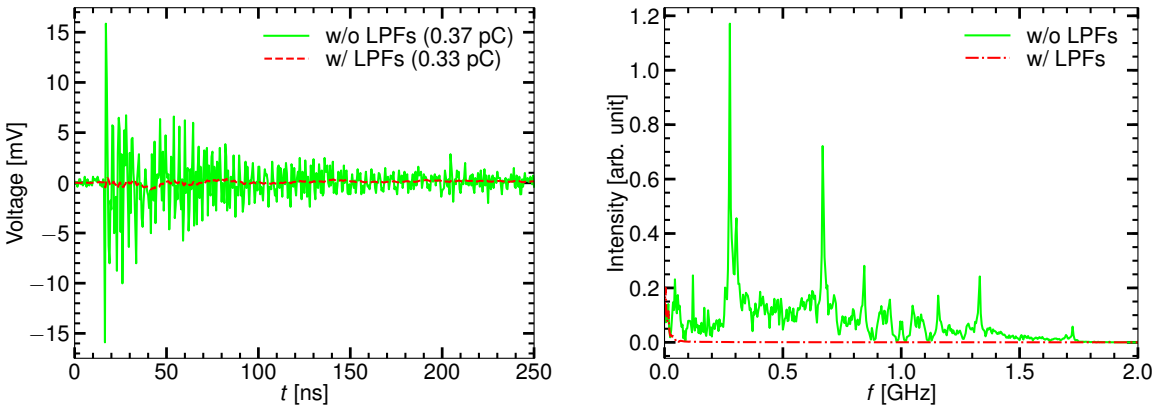

(a) (b)

Fig. 3.3 Pick-up signal in the time domain (a) and frequency domain (b).

Moreover, the jitter and the expected deformation of DS waveforms produce additional systematic errors, as shown in Fig. 3.4. Unfortunately, the physical mechanism for the waveform deformation has not been fully understood and needs further investigation. To summarize, the background noise level of the DS mainly depends on the pick-up signal, the signal jitter and the waveform deformation. As a consequence, the minimum charge signal which can be detected is estimated to be 1–2 pC, corresponding approximately to 700 incident electrons.

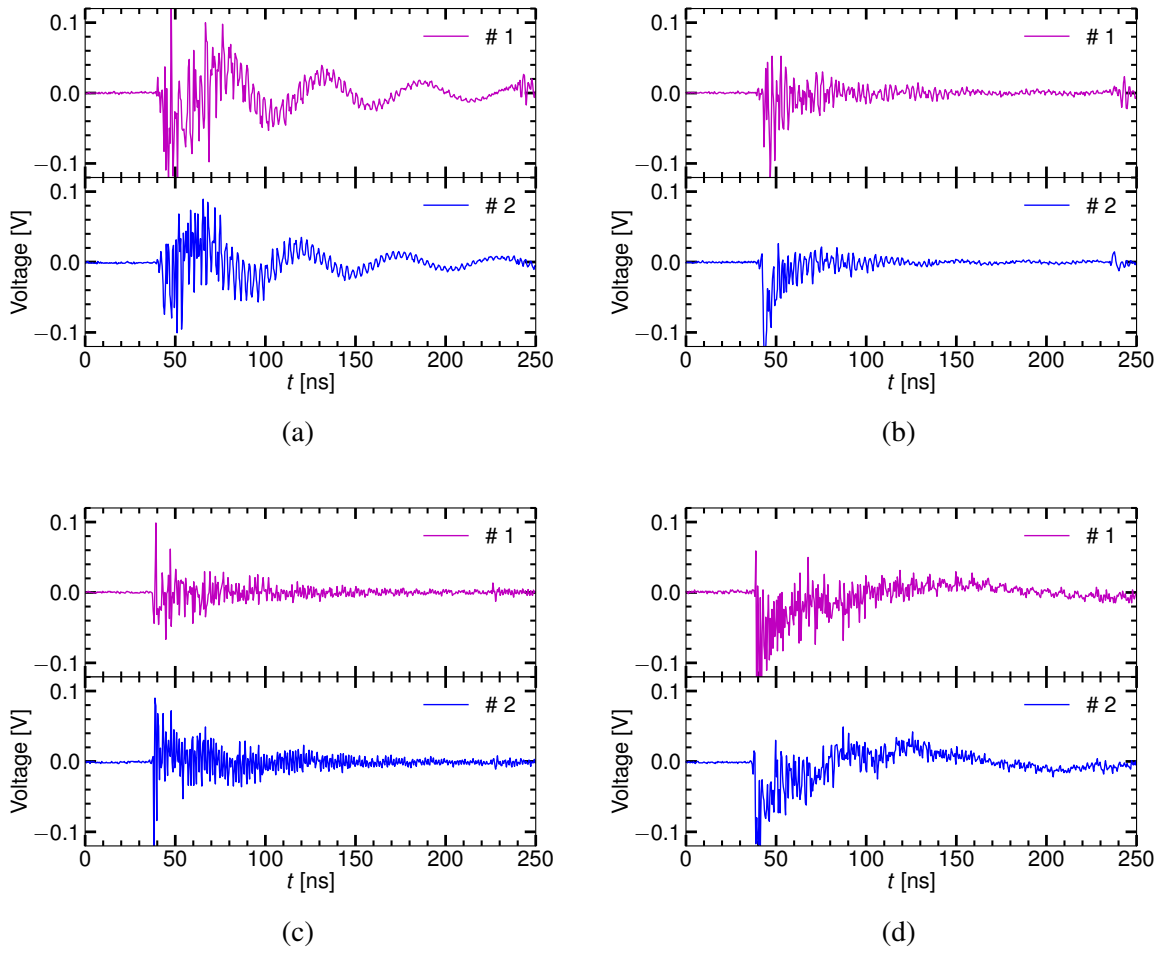

Fig. 3.4 Output signal of the vertical DS on the top (a) and bottom (b) sides, and of the horizontal DS on the left (c) and right (d) sides. The DS strip was kept in the halo region for these measurements.

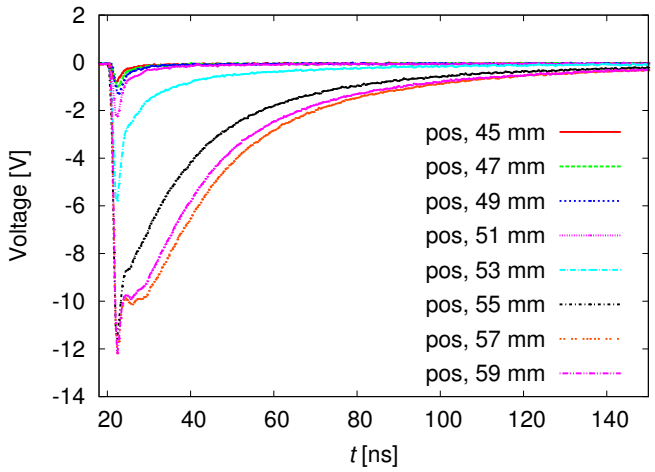

Fig. 3.5 Typical waveforms of the DS within the core region (beam center is around 57 mm).

When the DS strip moves into the core region, the total number of incident electrons reaches 10^8, and the output signal can be significantly distorted due to the space-charge effect inside the diamond crystal bulk and the instantaneous voltage drop at the 50 Ω resistor, as shown in Fig. 3.5. Due to energetic electrons penetrating the DS bulk, a large amount of electron-hole pairs are created and then move in opposite direction with a drift velocity of about 6×10^4 m/s [180] in the presence of an external electric field. Meanwhile, the space charge force, induced by carriers accumulating near the metallised surfaces of the DS crystal, will slow down the drift velocity of subsequent carriers and lead to a longer charge collection time. If the number of charge carriers is large enough, the drift velocity of later carriers can be reduced significantly and inhibit later charge collection. The drift velocity of the charge carriers in the diamond crystal can be approximated by

$$v_{\mathrm{dr}} = \frac{\mu E}{1+\mu E/v_s} \tag{3.2}$$

where μ is the mobility of electron-hole pairs, E the electric field strength, v_s the maximum drift velocity relevant to the energy loss in the crystal lattice through the emission of optical phonons and from scattering processes [181]. Furthermore, the dependence of the instantaneous current signal on the drift velocity of the carriers can be written as

$$I = \frac{\sum_i q_i v_{\mathrm{dr},i}}{d} \tag{3.3}$$

where q_i is the charge of a carrier and d is the thickness of the DS bulk. For 2×10^7 incident electrons, the maximum instantaneous current is as much as 7 A and the instantaneous voltage on the two sides of the 50 Ω resistor rapidly increases to 350 V. Then, the bias voltage on the DS strip drops to 50 V which will decrease the drift velocity of the carrier and increase the probability of carriers loss through recombination. Due to the space-charge effect and the instantaneous voltage drop, the maximum integrated charge signal is about 200 nC for 2×10^9 incident electrons, which is much less than the 5.76 μC that would be expected from simple linear scaling. The linear dynamic range of the DS was found to be around 10^4, from a minimum of 700 to about 2×10^7 electrons. To have a good SNR for the halo measurements, the lower limit of the dynamic range should be about 1000 electrons, which is the case in spite of the pick-up noise generated by the beam passage. Therefore, we have put more emphasis on how to extend the upper limit of the dynamic range. It is complicated and beyond the scope of this dissertation to quantitatively model the physical mechanisms associated with the saturation of the signal collection at high incident charge. On the other hand, a feasible and effective compensation scheme has been established to ensure sufficient dynamic range to measure both the core and halo parts.

3.1.2 Reconstruction of the measured core profile

In Ref. [182], a method to estimate the output waveform has been proposed based on a theoretical charge current model which includes the space charge limitation and the instantaneous voltage drop on the DS strip. By solving the drift-diffusion equation, the instantaneous evolution of carriers density and the instantaneous current could be predicted analytically. However, it is difficult to obtain an accurate model of charge collection which can be used for quantative comparisons with measurements, as the waveforms are affected by many other processes [181].

The charge signal integral corresponding to a given number of incident electrons has been instead determined through an experimental calibration procedure. The number of incident electrons on the DS strip can be controlled by varying the beam intensity and adjusting the DS strip against the beam center. Additionally, the beam size growth due to the strong IBS effect in the damping ring needs to be estimated in advance and taken into account. Evaluation of the expected charge signal integral is based on two assumptions: a charge generation of 2.88 fC/e and a Gaussian distribution of beam core. The saturation of the charge collection is clearly observed for a number of incident electrons larger than 10^7, and the CCE is found to be less than 15% for a number of incident electrons exceeding 2×10^8, as shown in Fig. 3.6 (a). Computing the ratio of the expected charge generation Q_{gen} and the charge signal readout Q_{read}, the vertical beam profile can be rescaled. Although such a correction can improve the profile, the resulting shape remains inconsistent with the predicted beam profile in the presence of the BGS, radiation damping and quantum excitation, as shown in Fig. 3.6 (b).

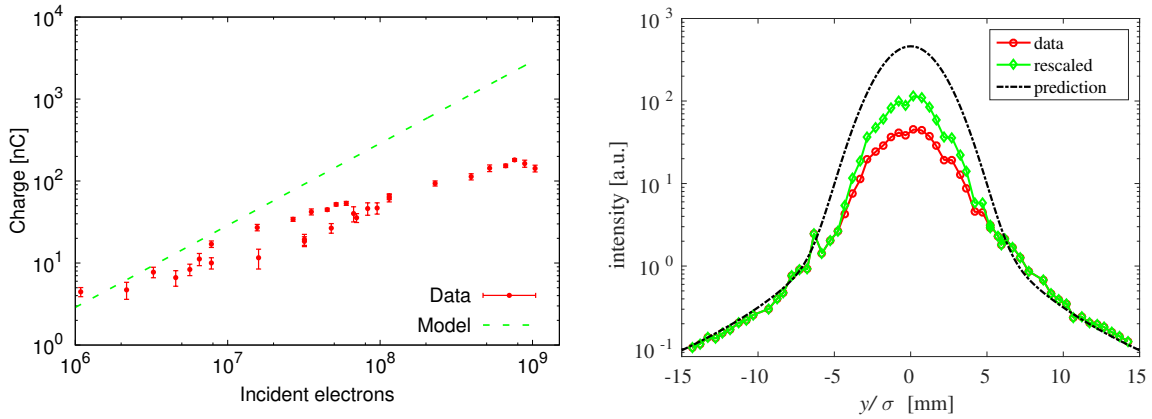

(a) (b)

Fig. 3.6 Calibration of the charge signal as a function of the number of incident electrons (a) and the rescaled beam profile based on the calibration (b).

Reliably calibrating the integrated charge of the DS output versus the number of incident electrons requires a precise alignment of the DS to beam center, and an accurate prediction of the number of incident electrons, that can be influenced by orbit jitter, beam energy jitter and the systematic errors of the beam size measured by the DS. In addition, the non-Gaussian beam

distribution results in a considerable error on the calibration. These might be reasons why the rescaled profile is different from the prediction in Fig. 3.6 (b).

An alternative "self-calibration" method was proposed and validated to more accurately correlate the integrated charge collection with the number of incident electrons. The beam core distribution was measured by the WS located 2.89 m upstream and propagated to the DS to predict the number of electrons striking each strip according to its position with respect to the beam center. Subsequently, the charge Q_{exp} which would be collected in the absence of saturation was computed based on the known electron-hole pairs generation and CCE measured at low incident charge [118]. The rescaling factor κ was then defined as the ratio of Q_{exp} to the charge signal readout and applied to rescale the DS data within beam core. After such rescaling based on "self-calibration", the linear dynamic range could be extended beyond 10^5 for the populations of collected electrons ranging from 1×10^3 to more than 5×10^8. The reconstructed beam profile appears to be in excellent agreement with the theoretical evaluation, thereby confirming the validity of the above reconstruction scheme (see Fig. 3.7).

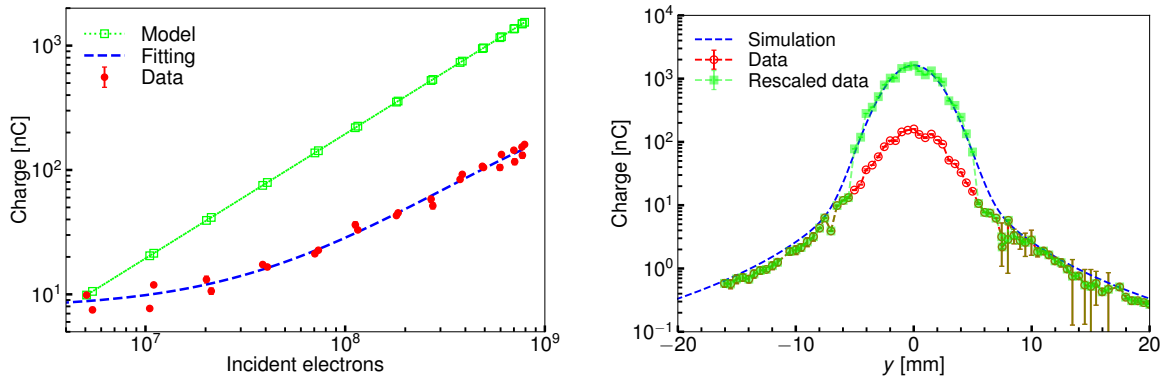

(a) (b)

Fig. 3.7 Ideal and actual charge collections on the DS strip as a function of incident electron population for the evaluation of rescaling factor (a) and a comparison of vertical beam profile before and after correction (b).

3.2 Design of a high dynamic-range YAG/OTR monitor

3.2.1 Ce:YAG scintillation and OTR

The favourable scintillating properties, mechanical rigidity and radiation hardness have made the scintillator material an excellent candidate for direct two-dimensional (2D) imaging devices, nowadays widely used for diagnostics of energetic particles and photons, especially for low-energy beams [183–186]. Previous investigations have demonstrated a high photon emission and a fast decay time for most scintillators. The photon-emission spectrum in the visible light region allows usage of conventional low-cost observation systems. Some important properties of

the most popular scintillators are presented in Tab. 3.1, where the photon yield (PhY) is defined as the number of photons emitted per MeV of energy deposition, and τ_γ, λ_{peak}, ρ and n_{eh} are the decay time constant, the dominating peak of the light emission spectrum, the density of the scintillator and the efficiency of electron-hole production, respectively.

Table 3.1 Properties of common scintillators [187]

Type	Ce:YAG	CsI(TI)	BGO	GSO	Ce:YAP
PhY [ph/MeV]	20300	51800	8200	11500	19700
τ_γ [ns]	88	900	300	43	31
λ_{peak} [nm]	550	560	480	430	380
ρ [g/cm^3]	4.55	4.51	7.13	6.70	5.35
n_{eh} [eh/MeV]	15000	39000	6150	6320	6000

To put it simply, the generation of the scintillation light inside inorganic scintillating material, for instance, Cesium (Ce) doped YAG, can be characterized by the following 3-step process:

1. Generation of electron-hole (e-h) pairs through ionization processes. Particles or high energy photons strike the scintillator and excite the valence electrons through Coulomb scattering into the conductance band, inducing electron-hole pairs;

2. Thermalization of e-h pairs, being transported and trapped at activators (Ce ions);

3. Photon emission at activators through transitions from the f to the d energy level.

For the diagnostics of beam halo, one of the most important parameters is the photon-emission efficiency, that is, the number of photons emitted per electron, which is given by [188]

$$n_{\text{ph}} = \left(\frac{E_d}{\beta_0 E_{\text{gap}}}\right) \eta_{\text{cap}} \eta_{\text{QE}} \tag{3.4}$$

where E_d is the energy deposition, β_0 a constant, E_{gap} the bandgap energy (7 eV for YAG), η_{cap} the efficiency of transferring energy from e-h pairs to activators and η_{QE} the quantum efficiency (QE) of photon emission. The yield of e-h pairs through the ionization process is a function of the energy deposited, which depends on the energy of the primary particles, the generation of secondary particles and the energy dissipation. Past studies have shown that the efficiency of the e-h pair production is about 6×10^4 eh/MeV for Ce:YAG [189, 190]. Also, the photon yield is related to the efficiency of the e-h pair generation and the energy transport/capture efficiency, which is affected by the recombination of electrons and holes at activators, the exciton-exciton annihilation and non-radiative decay [188]. Normally, the carrier capture efficiency is approximatly 1/3 [191]. The QE of the photon emission process has been evaluated to be around 100% [192]. Therefore, the photon yield of Ce:YAG is expected to be about 2×10^4 ph/MeV

and the photon-emission efficiency can be approximated as

$$n_{\mathrm{ph}} \approx \frac{6\times 10^4[\mathrm{MeV}^{-1}]}{3} E_d \tag{3.5}$$

To quantify the photon-emission efficiency, we further express the energy deposition in the scintillator through ionization and Bremsstrahlung processes by

$$E_d = \varsigma\left(\frac{dE_i}{d\varsigma} + \kappa\frac{dE_{br}}{d\varsigma}\right) \tag{3.6}$$

where ς is the scintillator thickness, $dE_i/d\varsigma$ the ionization energy deposition and κ the fraction of Bremsstrahlung radiation energy (E_{br}) stopped in the scintillator.

The scintillation light from Ce:YAG has a very fast rise time (about 5 ns) and a two-component decay with decay time constants of 88 and 300 ns, respectively. The whole time distribution spectrum can be characterized by

$$I(t) \approx -I_0\exp(-t/t_r) + I_1\exp(-t/t_f) + I_2\exp(-t/t_s) \tag{3.7}$$

where t_r is the rise time constant of the fast component, and t_f and t_s the decay time constants of the fast and slow components, respectively [187, 193]. Such a short decay time is favorable for diagnostics using short exposure time (from microsecond to millisecond) to reduce the background noise.

Both crystal and ceramic Ce:YAG are excellent host materials featuring high transmission for the scintillating light, with a peak within 525–550 nm [187, 189]. To compare the resolution of crystal and ceramic Ce:YAG screens, experiments with 50 and 100 μm thickness ceramic Ce:YAG and 50 μm thickness crystal Ce:YAG have been performed at ATF. Experimental results suggest that crystal Ce:YAG has the best resolution, although the difference between measurements using both types of 50 μm thickness YAG screens is small [195]. Considering requirements on the photon-emission efficiency and resolution for beam halo diagnostics, 0.5 mol% ceramic Ce:YAG manufactured by Konoshima Chemical Company, Ltd., Japan, has been used. The optical emission and transmission spectra near the visible-light region are represented in Fig. 3.8 (a, b). The scintillating light spectrum is centered near 525 nm with a transparency of about 80% (almost 100% for a wavelength larger than 550 nm). The decay time constants for the fast and slow components are 78 and 294 ns, respectively, as shown in Fig. 3.8 (c). The PhY of the 0.5 mol% ceramic YAG was found to be 0.37% of that of the CsI(TI) scintillator, i.e., about 2×10^4 ph/MeV, which is consistent with the nominal value. The measurements also suggest that the PhY of ceramic Ce:YAG is similar for different Ce concentrations from 0.05 mol% to 1 mol%, as shown in Fig. 3.8 (d).

For a precise and reliable diagnostic of beam halo, one of the biggest challenges for the Ce:YAG is to ensure a sufficient dynamic range while preserving a high SNR. Even though

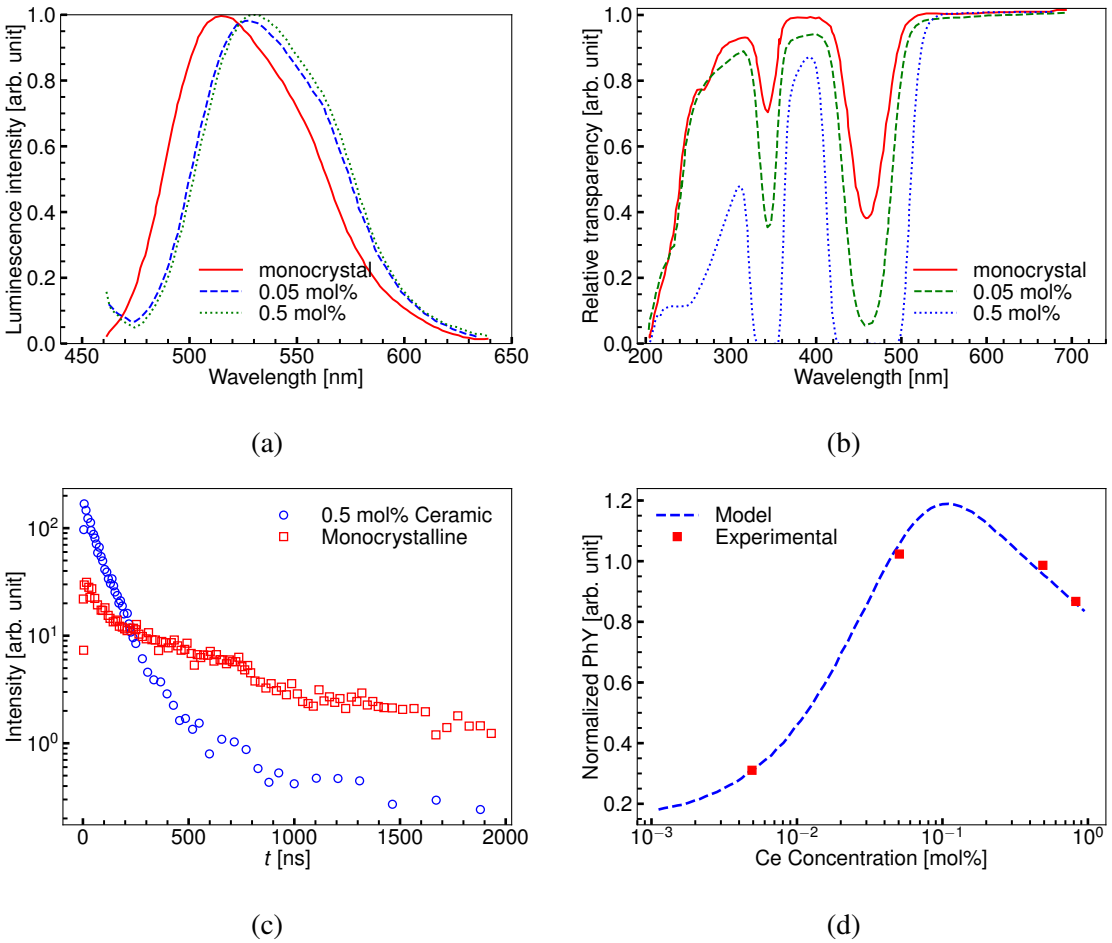

Fig. 3.8 The optical emission spectrum (a), transparency (b), time distribution of light pulse (c) and normalized PhY ability of the ceramic Ce:YAG screen (d). Reproduced from Ref. [194].

the 0.5 mol% ceramic Ce:YAG has an excellent PhY, the lower limit of the dynamic range is somehow determined by the competition between the photon-emission efficiency and the background noise level. On the other hand, the upper limit of the dynamic range is restricted by the scintillation saturation, which results in a non-linear response to beam density (the so-called saturation effect), as shown in Fig. 3.9. This saturation effect may induce undesired beam profile distortions and has to be well eliminated or compensated.

To compensate beam profile distortions due to scintillation saturation, an OTR screen has been mounted on the screen holder. This design aims at providing simultaneous and saturation-free measurements of core and halo in the presence of a high beam intensity. OTR is a kind of electromagnetic radiation emitted by charged particles passing through a boundary between two media with different dielectric constants (here the vacuum-metal interface). The mechanism of OTR emission is similar to the sudden change of charge of primary particles and mirror charge [196]. When the charged particles hit the surface of the foil, the sudden neutralization between the charge of the primary particles and its mirror charge on the surface will result in a backward radiation emission along the direction of specular reflection, as shown in Fig. 3.10 (a).

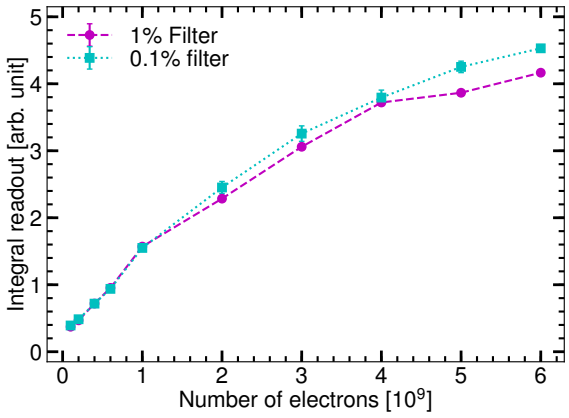

Fig. 3.9 Non-proportionality of the light yield versus the number of incident electrons.

The forward emission is produced when particles exit the material, which is analogous to the sudden appearance of primary particles charges. The direction of the forward emission is always along the beam trajectory. The angular distribution has a maximum at $\theta_{\max} = 1/\gamma$ and is symmetric in the azimuthal direction, as shown in Fig. 3.10 (b).

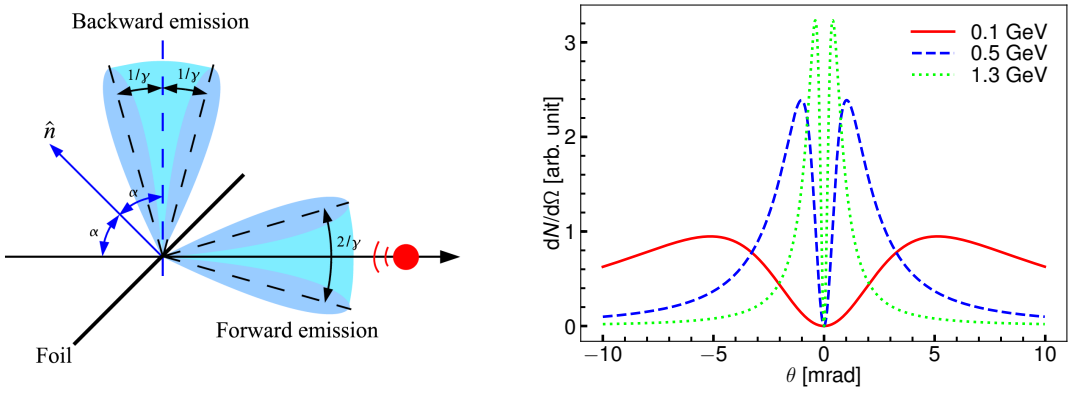

(a) (b)

Fig. 3.10 Schematic of OTR emission when a particle crosses a vacuum-metal interface (a) and the corresponding angular distribution (b). Notice that the amplitudes of the curves in (b) have been artificially matched.

In the case of a relativistic electron crossing the boundary surface between vacuum and foil, the angular distribution of OTR can be expressed as [197]

$$\frac{d^2W}{d\omega d\Omega} = \frac{e^2}{4\pi^2\varepsilon_0 c_0}\frac{\beta^2\sin^2\theta}{(1-\beta^2\cos^2\theta)^2} \tag{3.8}$$

where W is the radiated power, ω the frequency of the light, $d\Omega$ the solid angle, ε_0 the vacuum permittivity, c_0 the velocity of light in vacuum, β the relativistic velocity and θ the angle between the observation and the specular reflection directions. The angle-integrated spectral power of

OTR can be approximated by

$$\frac{dW}{d\omega} \approx \frac{e^2}{4\pi^2\varepsilon_0 c_0}(\log 4\gamma^2 - 1) \tag{3.9}$$

which indicates that the OTR has a very wide spectrum. Since the spectral response of conventional camera sensors is around the visible-light region, the number of photons in this region is more important and can be analytically estimated by

$$n(\omega_1, \omega_2) = \frac{\alpha_0}{\pi}(\log 4\gamma^2 - 1)\log\left(\frac{\omega_2}{\omega_1}\right) \tag{3.10}$$

where $\omega_{1,2}$ represent the minimum and maximum of the frequency range.

For a relativistic beam, the cone angle of OTR is normally very tight, e.g., less than 0.5 mrad for the ATF beam energy. This is smaller than the acceptance angle of typical imaging lenses, and most of the OTR can be collected and focused on the camera sensor. The fraction of the OTR photons received by an optical observation system can be derived as

$$\eta = \frac{\log[1 + 4\gamma^2 \tan^2(\theta_0/2)] + \frac{\cos\theta_0}{1+\gamma^2\sin^2\theta_0} - 1}{\log 4\gamma^2 - 1} \tag{3.11}$$

where θ_0 is the acceptance angle. In a tiny portion of the spectrum, the number of the OTR photons arriving at the camera sensor is given by

$$n_{\text{coll}}(\omega_1, \omega_2) = \eta n(\omega_1, \omega_2) \tag{3.12}$$

which amounts to about 0.011–0.014 ph/e for a beam energy of 1.3 GeV and a collection angle of 0.112 rad. The fraction of OTR collected by the observation system as a function of beam energy is illustrated in Fig. 3.11.

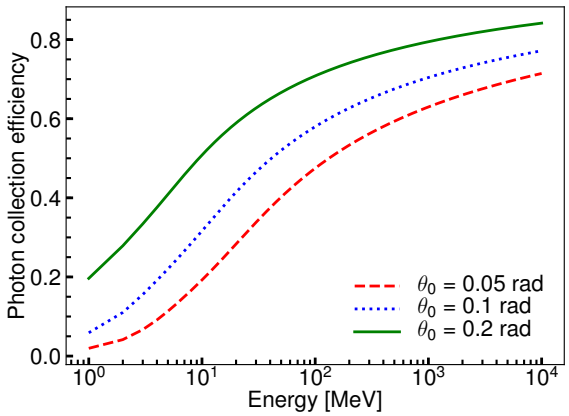

Fig. 3.11 The efficiency of OTR collection as a function of beam energy for three differential acceptance angles.

Comparing with the Ce:YAG screen, one significant advantage of the OTR is the linear response with respect to the population of incident particles, in other words, it is saturation-free. Besides, a resolution of 2 μm has been demonstrated by the existing OTR systems at the ATF2 extraction line [198]. These are reasons why an OTR screen has been considered as a complementary diagnostic for the dense beam core. Furthermore, the resolution and PhY of Ce:YAG and OTR screens have been estimated, analytically and experimentally, and are presented in the following sections.

3.2.2 Mechanical and optical design

The design of the YAG/OTR monitor has benefited from the experience accumulated on the prototype YAG monitor and the OTR monitors at ATF/ATF2. The mechanical design includes the arrangement of the YAG/OTR screens on the holder with respect to their luminescence properties, the upgrade of the automatic manipulator and the optimization of the target chamber. The optical observation system is oriented toward the 2D image of the beam, (σ_x, σ_y) $\sim$ (100 μm, >30 μm), with a good resolution (several microns) and SNR (>3).

This detector mainly consists of four YAG screens and an OTR target on a holder, a manipulator, neutral-density (ND) and band-pass (BP) filters, a microscope lens and a scientific Complementary Metal Oxide Semiconductor (sCMOS) camera, as shown in Fig. 3.12. To reduce the cost, some components were reused from discarded instrumentations at ATF.

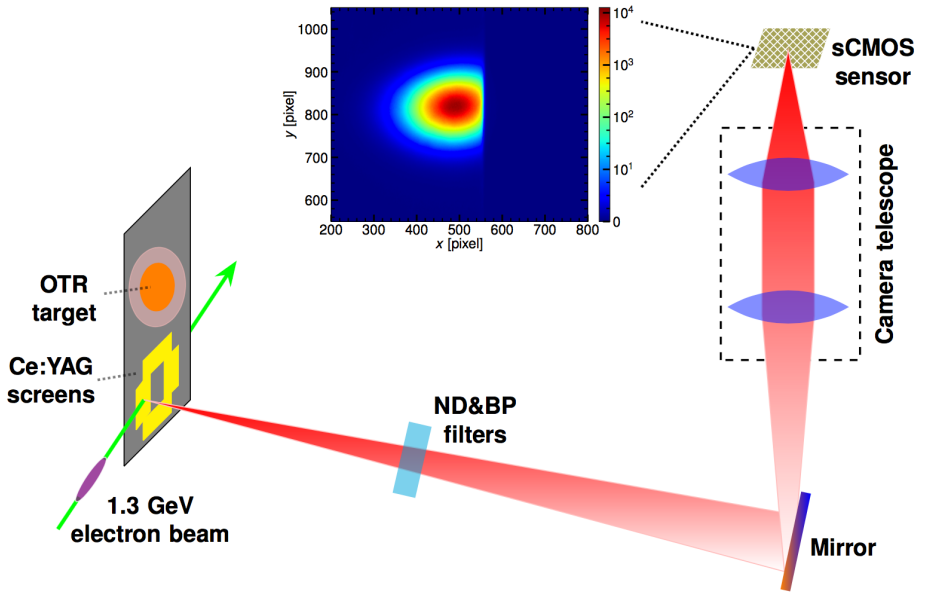

Fig. 3.12 Schematic of the YAG/OTR screen monitor.

To mitigate the "blooming" effect due to the bright core, four YAG screens were assembled on a holder with a square opening in the center (with dimensions 4×2.4 mm^2). The size of YAG pads is 4×6×0.1 mm^3. For beam halo measurements, the central opening allows core particles to

pass through without hitting the screen. Moreover, an aluminized Kapton 2 μm thick OTR target has been seated in a titanium conical receptacle with an exposed screen diameter of 7 mm. YAG screens are placed at 45° to the beam trajectory and the observation is perpendicular to them, at 135°, horizontally. To probe the backward OTR emission using the same observation system, the OTR target was placed at 67.5°. In addition, a rectangular opening that is broader than the gap between YAG screens has been drilled on the holder in order to suppress the scintillating light reflected from the holder surface (which has been found to blur the image significantly).

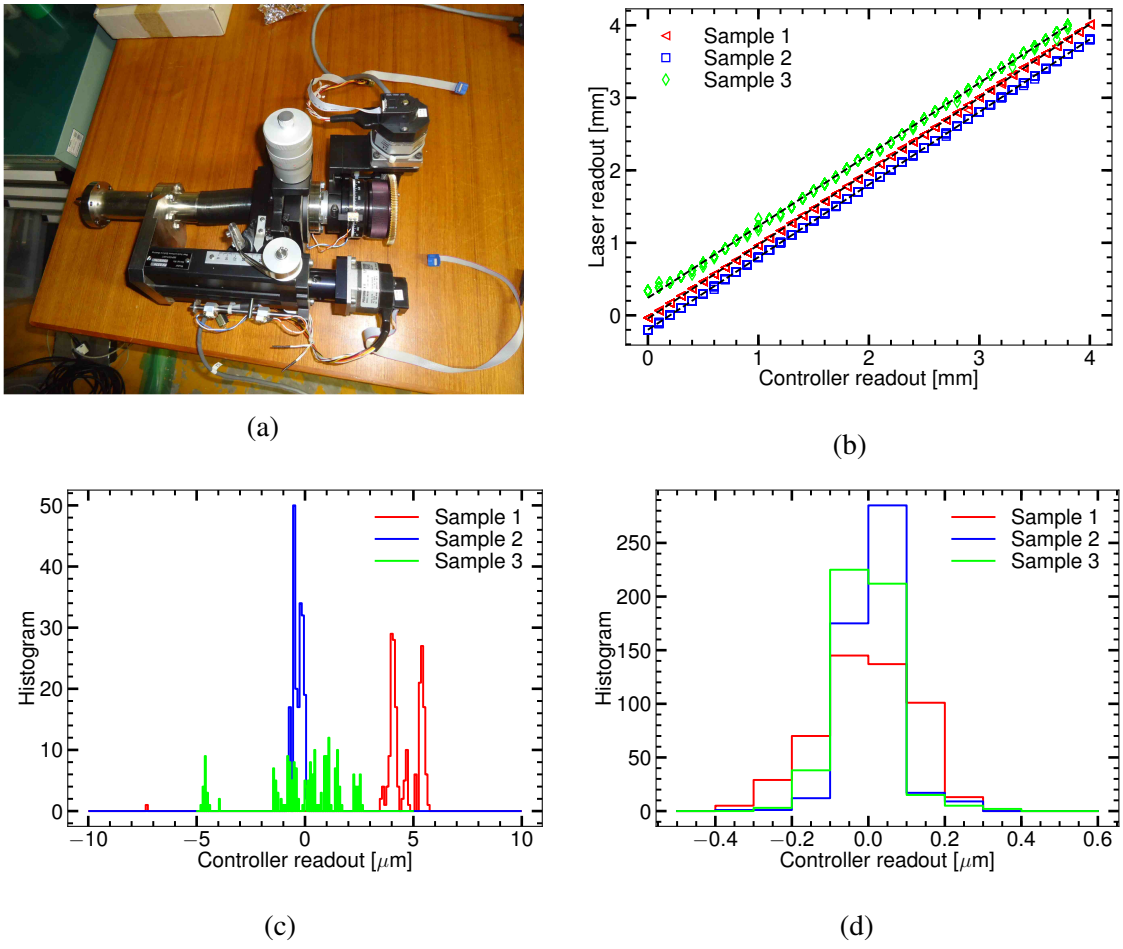

(a) (b) (c) (d)

Fig. 3.13 A picture of the manipulator (a) and measurements of the linearity (b), backlash (c) and readout error (d).

The holder to accommodate the screens is actuated by a four-dimensional ($\vec{x}$, $\vec{y}$, $\vec{s}$ and the rotation around $\vec{s}$-axis) manipulator refurbished from the one used by the Laser Wire (LW) monitor [199, 200]. The linearity of the manipulator movement has been calibrated using an additional laser. The calibration curves are presented in Fig. 3.13 (b) and indicate a good linearity. Besides, the backlash and readout accuracies of the manipulator have been studied and were found to be around 13.5 μm and less than 0.2 μm, respectively, as shown in Fig. 3.13. To control the manipulator remotely, an interface has been developed in Python and implanted in the ATF server.

The target chamber was designed taking into account the size and moving range of the holder, the aperture of the conventional beam pipe (ϕ24 mm) and flexibility for observing the light. The mechanical drawing of the chamber is represented in Fig. 3.14. Diameters of the section across the beam pipe and an extended section, between the former and the manipulator, are 22 and 35 mm, respectively. The screen holder is placed in these sections and connected to the actuator. The scintillation light and OTR are extracted through a fused silica viewport which has been machined to accept an indium seal to preserve a low vacuum pressure.

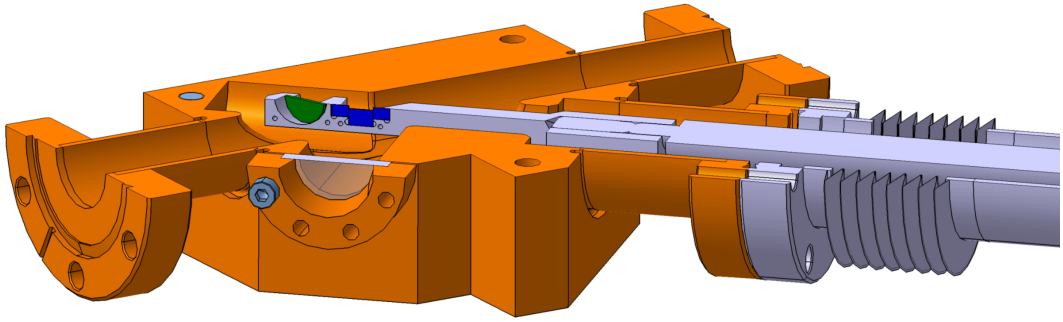

Fig. 3.14 The model of the YAG/OTR target chamber.

The observation system is composed of a set of ND filters (10%, 1% and 0.1%) and BP filters (550±10 nm), an aluminum coated plane mirror, an objective lens and a highly sensitive (QE∼70%) cooled sCMOS camera (pco.edge 4.2 L) with 6.5 μm square pixels, as sketched in Fig. 3.12.

Two commercial microscope zoom lenses with focal lengths of 132 mm and 170 mm have been used to focus the image on the sCMOS sensor. The nominal magnification factor of the microscope lens is 0.38–4 to allow either full viewing of the screens or high-resolution observation. The main parameters of the two lenses are listed in Tab. 3.2. The magnification factor is determined either by recording the position shift of the holder edge at the camera sensor as a function of the manipulator readout or by comparing the size of the YAG pad imaged on the sensor with the actual size. Typically, a magnification factor of 2.5–3.0 was used, as shown in Fig. 3.15.

Table 3.2 Summary of some parameters for the microscope lenses [201]

N/D	Magnification	WD	F number (obj.)	F number (img.)	NA (obj.)
TS-93006	0.5x–4.0x	132	19.0 – 5.9	9.5 – 24.0	0.026 – 0.084
TS-93022	0.38x–3.0x	170	25.0 – 8.9	9.5 – 26.6	0.020 – 0.056

The sCMOS camera was placed 30 mm above the beam line in order to reduce the background noise due to synchrotron radiation upstream. The camera was mounted on a movable mechanical

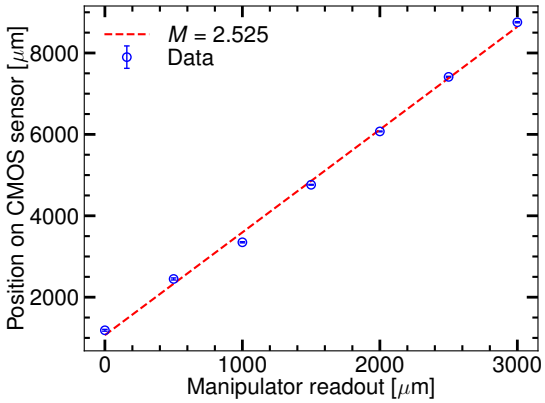

Fig. 3.15 An example of magnification factor calibration.

support, remotely and automatically controlled with a home-made software. The noise level of the sCMOS sensor is of great importance and is related to the temperature of the sensor, the exposure time and the choice of shutter mode. The temperature of the sensor is stabilized at 10 °C thanks to an accompanying cooling system. The exposure time varies from 1 ms to several seconds according to specific requirements. The camera has two shutter modes: rolling shutter mode offering an excellent low-noise performance, and global shutter mode providing a very short exposure time. The technical data sheet of this camera is presented in Tab. 3.3.

Table 3.3 Parameters of the sCMOS camera [202]

Resolution	Pixel size	Spectral range	Quantum efficiency
2048×2048	6.5 μm×6.5 μm	300–1100 nm	>70% (peak)
Readout noise	A/D conversion	DNR A/D	Frame rate
1.3_{rms} e-	0.46 e-/count	16 bit	40 fps

The measured 2D background images are shown in Fig. 3.16. They exhibit non-uniform distributions, in other words, the noise level varies for each pixel. The rms background noise level was demonstrated to be less than 1 digital count, in either rolling or global shutter mode with an exposure time of 10 ms. Evaluation of the background noise as a function of the exposure time shows only small variations in the measured background level for an exposure time of 10 ms, as shown in Fig. 3.16. From these results, we could conclude that the sCMOS camera has a low readout noise and sufficient sensitivity for relatively low light intensities.

One may notice that the readout per pixel has a constant offset which has been designed to ensure a low readout noise. To obtain the absolute count versus the number of photons, this offset has to be accurately determined and subtracted. One solution is to subtract the offset and background using a 2D background image taken under the same conditions. However, the fluctuation of the readout per pixel always exists, even for an average over 20 frames, and it is not easily possible to identify the offset level for each pixel precisely. On the other hand, we

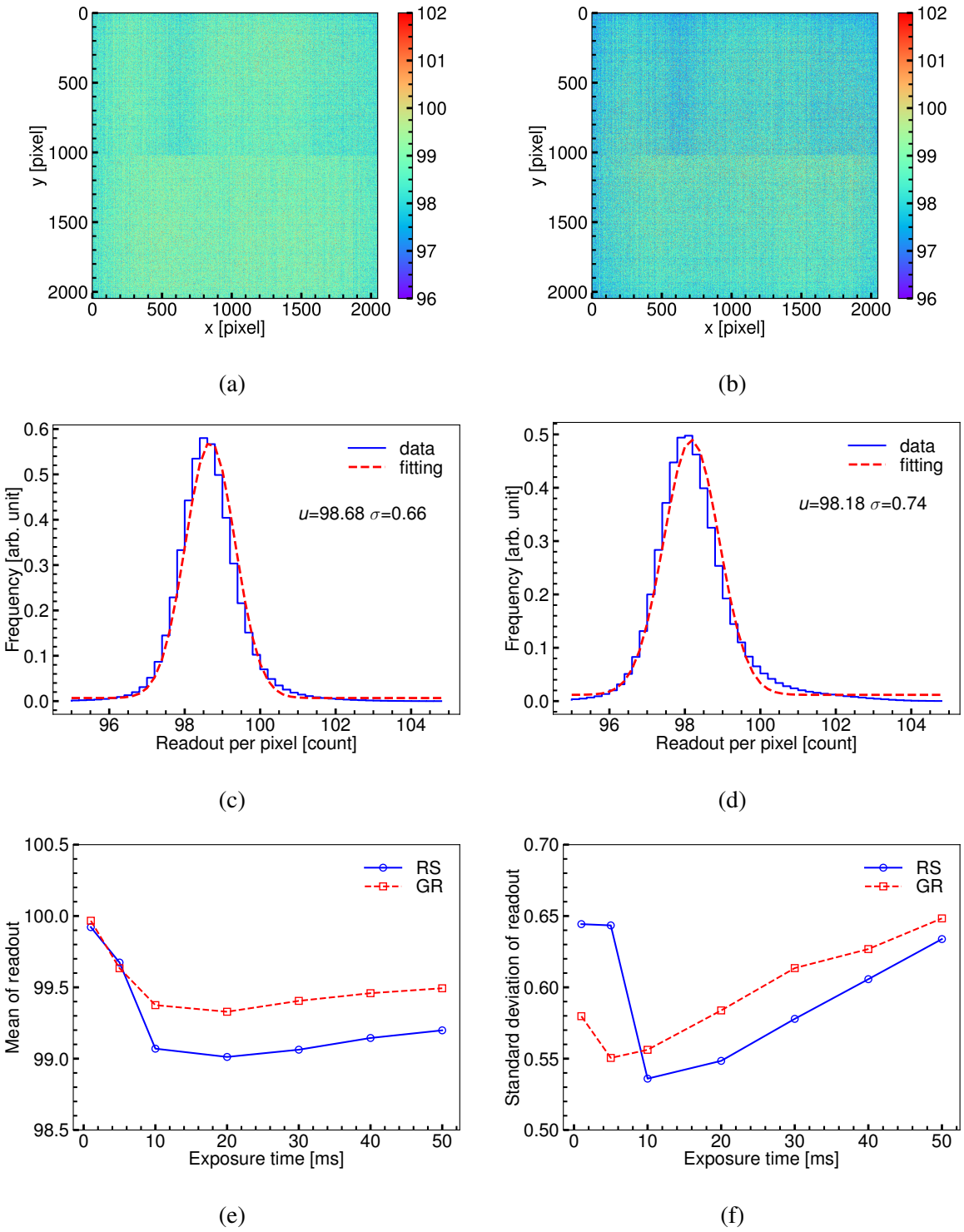

Fig. 3.16 Images of the background noise (a, b) and histograms of readout per pixels (c, d) in the rolling and the global shutter mode, respectively. Mean and standard deviation of the readout as a function of the exposure time (e, f).

use a universal readout value, for instance, the mean of readouts over all pixels, to represent the offset plus the background noise. After such subtraction, the sum of counts over row or column, e.g., 600 pixels, is typically less than 300 counts (see Fig. 3.17) which implies a residual readout error/noise of about 0.5 count/pixel.

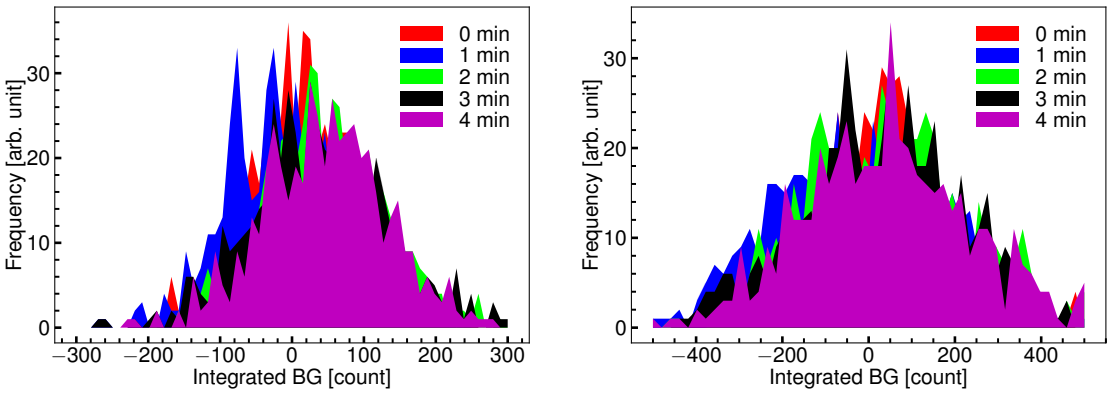

(a) (b)

Fig. 3.17 Integral of readout over row (a) and column (b) after subtracting the offset and background. Figures were taken with an interval of one minute.

3.2.3 Estimation of wakefield effects

The wakefields induced by irregular pipes, cavities and target chambers along the ATF2 beam line have been found to be a severe issue for the ultra-small beam size tuning [203, 204]. Typically, the wakefield excited by particles, for example, by the head of a bunched beam, will result in transverse kicks to the following particles and cause orbit distortions and beam size growth downstream. To quantify the wakefield induced by the YAG/OTR monitor system, detailed numerical simulations have been performed using CST PS [205] for a beam intensity of 3×10^9 e/pulse and a bunch length of 7 mm. The target chamber and holder accommodating the different screens are shown with realistic sizes in Fig. 3.14. The transverse wakefield is characterized in terms of a transverse wake potential with respect to the bunch displacement acting on a longitudinal particle distribution [206, 207]. For the sake of simplicity, the wakefield impact at the IP has been estimated analytically based on linear transfer matrix.

To describe the kick angle, we define the mean wake and the mean square wake, considering only the dipole component of the wakefield and for a small beam offset at the wakefield source [204]

$$\begin{aligned} a_w &= \int_{-\infty}^{\infty} w_p(s)\rho(s)ds/Q \\ a_{w^2} &= \int_{-\infty}^{\infty} w_p^2(s)\rho(s)ds/Q \end{aligned} \tag{3.13}$$

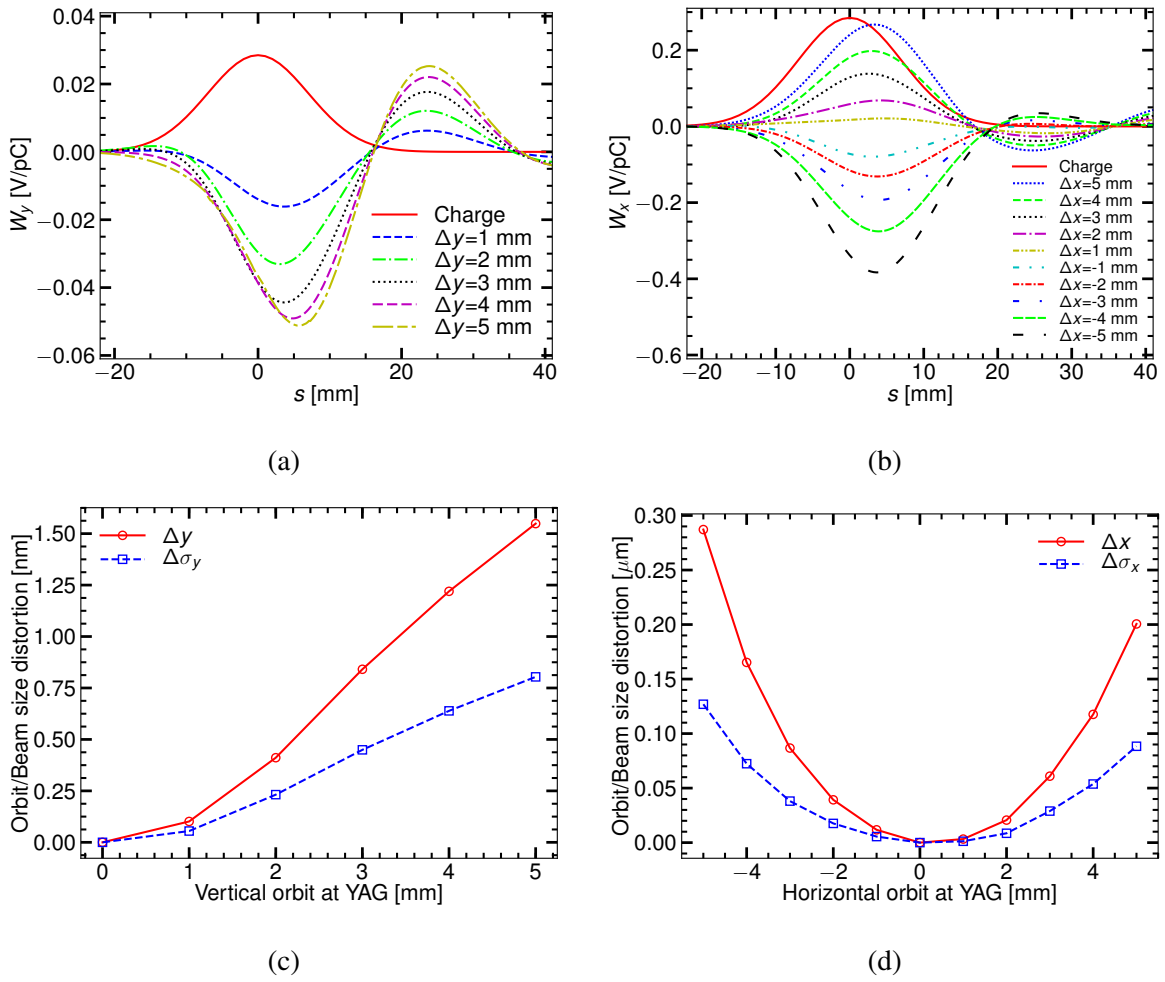

Fig. 3.18 Wake potential functions evaluated by CST PS (a, b), and the resulting orbit and beam size distortions at the IP (c, d), vertically and horizontally, respectively.

where $w_p(s)$ is the wake potential, $\rho(s)$ the longitudinal distribution function and Q the bunch charge. Then, the kick angle induced on a particle near the bunch center can be obtained as

$$\begin{aligned} a_\theta &= \frac{eQ\Delta_y}{E} a_w \\ a_{\theta^2} &= \frac{e^2Q^2\Delta_y^2}{E^2} a_{w^2} \end{aligned} \tag{3.14}$$

where E is the beam energy and Δ_y the vertical displacement at the source point. Downstream, the orbit distortion and beam size increase can be expressed as

$$\begin{aligned} \Delta\bar{y} &= R_{34}\frac{eQ\Delta_y}{E} a_w \\ \Delta\sigma_y^2 &= R_{34}^2\left(\frac{eQ\Delta_y}{E}\right)^2 \sigma_w^2 \end{aligned} \tag{3.15}$$

where R_{34} represents the linear transport from the wakefield source to the examination point and $\sigma_w^2 = a_{w^2} - a_w^2$ the rms of the wake potential.

Simulations with CTS PS plus the above analytic estimations show that: for a vertical displacement of 5 mm, the amplitude of the wake potential is less than 0.05 V/pC which can cause an orbit distortion of 0.9 nm and a growth of the vertical beam size of 0.5 nm at the IP, as shown in Fig. 3.18 (a, b); for a horizontal offset of 5 mm at the YAG chamber, the amplitude of the wake potential is smaller than 0.4 V/pC which leads to an orbit distortion of 0.29 μm and a horizontal beam size dilution of 0.13 μm at the IP, as shown in Fig. 3.18 (c, d). After implementing the orbit correction scheme, the beam offset at the YAG/OTR monitor is typically less than 1 mm and influence on the small beam size tuning is thus expected to be negligible.

3.2.4 Efficiencies of photon emission and collection

In addition to the noise level of the sCMOS sensor, the photon emission and the photon collection (PhC) efficiencies[1] of Ce:YAG also contribute to determine the lower limit of the dynamic range. The photon emission efficiency is a function of the PhY and the energy deposition (in the absence of scintillation saturation). The PhC efficiency depends also on the configuration of optical system and transparency of screens and viewport.

The PhY of the ceramic 0.5 mol% Ce:YAG has been presented at the beginning of this section. The energy deposition has been estimated both analytically, based on a standard stopping power database, e.g., the ESTAR database [208], and through a Monte Carlo simulation. Considering the collision stopping power (about 1.95 MeV·cm^2/g) and omitting the energy deposition due to Bremsstrahlung, as shown in Fig. 3.19 (a), the total energy deposition in the YAG screen is about 0.125 MeV per electron for an effective thickness of 141 μm. Monte Carlo simulation using the MCNPX code [209] gives a maximum energy deposition of 0.1 MeV per electron for a beam energy of 1.3 GeV, which is rather close (see Fig. 3.19 (b)). Hence, the photon emission efficiency of the ceramic Ce:YAG has been further evaluated as about 2000–2500 ph/e using Eq. (3.5).

For the estimation of the PhC efficiency of Ce:YAG, we first make some assumptions: A) the scintillation light is mainly concentrated in a range from 500 nm to 600 nm, as shown in Fig. 3.8 (a); B) the transparency of the ceramic 0.5 mol% Ce:YAG is 80%; C) the transmission of the scintillation light through the viewport and the optical system is about 85%. Notice that the refraction of the exiting scintillation light further reduces the PhC efficiency, as shown in Fig. 3.20. As a consequence, the effective angle aperture for the YAG scintillating light decreases from 0.112 rad to 0.062 rad for a magnification factor of 3. The scintillation light is spatially homogeneous, and the PhC efficiency is finally estimated to be about 0.32–0.4 ph/e.

[1] We define the PhC efficiency as the number of photons collected on the camera sensor per incident electron.

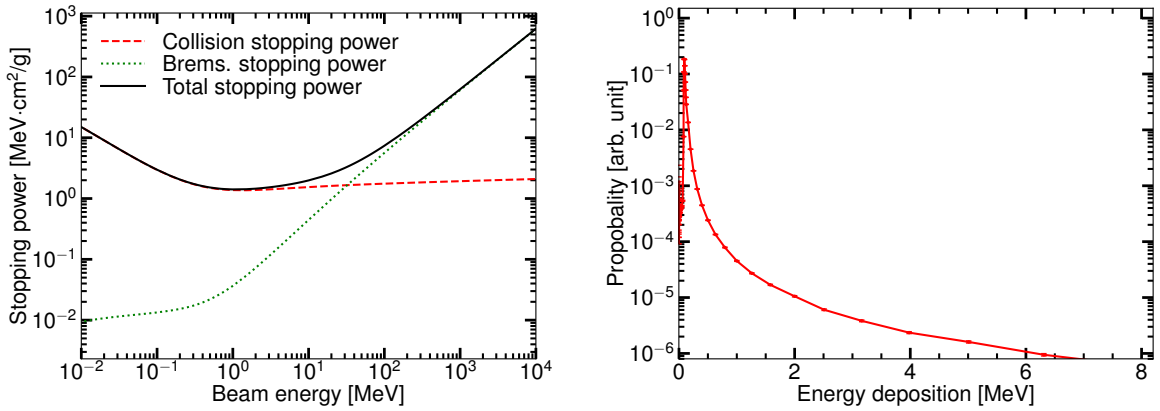

(a) (b)

Fig. 3.19 The stopping power of YAG according to the ESTAR database (a) and the energy deposition spectrum evaluated with MCNPX (b).

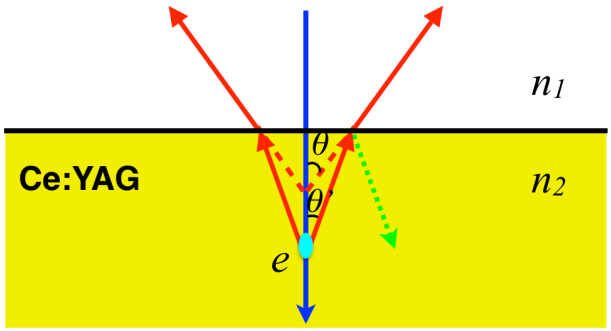

Fig. 3.20 Schematic illustrating the reduction of the observation angle due to refraction when light exits the YAG. The effective observation angle decreases to $\theta' = \arcsin(n_1/n_2 \sin\theta)$ where $n_1 = 1$ and $n_2 = 1.82$ are the refractive indexes of vacuum and YAG material, respectively.

Using the above assumptions, we have also evaluated the PhC efficiency of the OTR in the visible-light range to be around 6.3×10^{-3}–7.5×10^{-3} ph/e. It is much less than the PhC efficiency of the YAG screen, which implies that the latter is superior for halo diagnostics.

3.2.5 Dynamic range

Our measurements of the beam halo at ATF2 have used only the YAG screens and the estimation of the dynamic range is dedicated to this case. The lower limit to the dynamic range is related to the photon collection efficiency of the Ce:YAG monitor, the sensitivity and noise level of the sCMOS sensor, and the background noise from the environment. Through the above analytical evaluations, a PhC efficiency of 0.32–0.4 ph/e and a residual rms fluctuation of 0.5 count/pixel have been obtained. To ensure reliable signal detection, a SNR of more than 3 is required. As a

result, the minimum reliable readout per pixel is set as 2, which corresponds to a particle density of 4 electrons over one pixel size on the screen.

On the other hand, the upper limit of the dynamic range is determined by the scintillation saturation. The physical mechanism of scintillating saturation is very complex and beyond our consideration. In this dissertation, scintillation saturation is only evaluated analytically and then examined through experimental measurements. Assuming a transport efficiency $\beta = 1$ in the extreme conditions, the maximum particle density without saturation is determined by the concentration of Ce ions and can be estimated by

$$\rho_{e,\max} = \frac{\rho_{Ce^{3+}}}{\beta n_{eh} E_d} \tag{3.16}$$

where $\rho_{Ce^{3+}}$ is the density of the doped Ce ions (Ce^{3+} for instance), and n_{eh} is the density of the generated e-h pairs. For 0.5 mol% Ce:YAG, a top limit of the "saturation threshold" is about 100 fC/μm^2. For a magnification factor of 3, the scintillating process is saturated if the number of electrons over pixel size exceeds 2.94×10^6. These estimations indicate a maximum dynamic range of about 1×10^6, i.e., from 4 electrons to 2.94×10^6 electrons per pixel size, for the 2D images. However, the measured saturation level of Ce:YAG scintillator is typically much less than the theoretical prediction (10–100 fC/μm^2) [189, 210–212], and therefore, experimental determination will be of great importance.

To further increase the dynamic range, the combination of beam core acquired with the OTR screen and beam halo measured by YAG screens has been proposed. Some critical questions including the difference between the OTR image and the YAG measurement and how to match the images from OTR and YAG screens are still under investigation.

3.2.6 Spatial resolution

The spatial resolution of the YAG screen is mainly determined by the optical diffraction limitation, the finite thickness of the crystal, the pixel size and the saturation effect. The optical diffraction limitation to the resolution can be characterized by the Point Spread Function (PSF): the source distribution generated by a single particle and projected by the optical system on the image plane (see Fig. 3.21). In the case of a relativistic beam, the scintillating light can be treated as an ideal isotropic point source, and the PSF is

$$E(r) \propto \frac{4J_1^2(kr\theta_0)}{(kr\theta_0)^2} \tag{3.17}$$

where J_1 is the Bessel function of the first kind, k the wave number, r the transverse coordinate on the image plane from the center and θ_0 the angular acceptance. Furthermore, an approximation of the resolution from optical diffraction can be obtained through a Gaussian fitting of the PSF

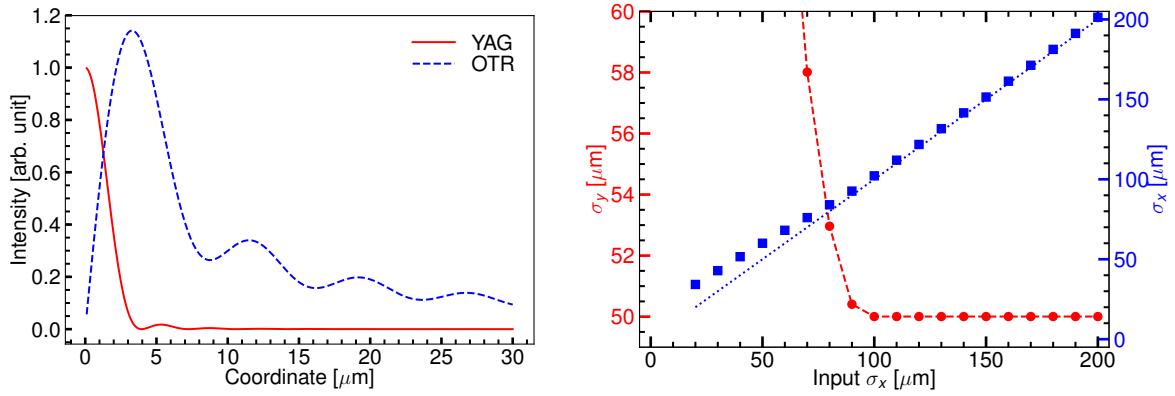

(a) (b)

Fig. 3.21 The calculated PSF of the YAG scintillation light and OTR (a), and simulations of the measured horizontal beam size as a function of actual horizontal beam size (b). Notice that the fitting of the beam size becomes inaccurate for values smaller than 100 μm.

function [213]

$$\sigma_{\text{diff}} \approx 0.61\lambda/\theta_0 \tag{3.18}$$

The resolution associated with the thickness of the scintillator can be approximated by [189]

$$\sigma_f = \frac{d}{n_2}\tan(\theta_0/2) \tag{3.19}$$

where d is the thickness of the scintillator and n_2 is the refraction index. Numerical simulations have suggested an approximation of the finite thickness associated resolution as $\sigma_f = 0.3\sigma_{\text{px}}/M$, where σ_{px} is the pixel size and M is the magnification [214]. In the absence of the saturation of the scintillation light, the resolution of vertical measurements is then

$$\sigma_{\text{res},y} \approx \sqrt{\sigma_{\text{diff}}^2 + \sigma_f^2 + \sigma_{\text{px}}^2} \tag{3.20}$$

For a magnification factor of 3, the vertical resolution has been estimated to be about 2.08 μm. However, the horizontal resolution is further degraded by the overlap of scintillation light emitted at different depth, because YAG screens are inserted horizontally at 45° to the beam trajectory. Preliminary numerical simulations have been carried out with the following assumptions: a 2D Gaussian beam distribution and a threshold for the saturation of the scintillation light of 16 fC/μm^2. For a constant vertical beam size of 50 μm, the measured horizontal beam size appears larger than it should for values less than 100 μm, as shown in Fig. 3.21 (b).

The resolution of measurements using OTR screen is generally defined as the rms of the PSF, while it is also limited by the optical system. The OTR PSF has been theoretically estimated as [213, 214]

$$E(r) = \left(\frac{1 - J_0(r\theta_0/\lambda)}{r\theta_0/\lambda}\right)^2 \tag{3.21}$$

and, the approximated diffraction limited resolution is further expressed as

$$\sigma_{\text{diff}} \approx 2.1\lambda/\theta_0 \tag{3.22}$$

The resolution for the OTR measurements in this dissertation is evaluated in the range from 5.38 μm to 8.38 μm using Eq. (3.20) and for the most commonly used observation systems. Here, we take into account the light in the 450–700 nm range with respect to the QE of the sCMOS sensor.

Preliminary analytical estimations indicate that the resolution of the YAG/OTR monitor is less than 10 μm and is sufficient to measure a beam size of (σ_y, σ_x) $\sim$ (>30 μm, 100 μm). In practice, the optical chromaticity and aberration, imperfect focusing and misalignment of the observation system may also degrade the resolution. Also, measurements of the micron size beam using YAG screens may also suffer from saturation effects, such that the practical resolution has to be demonstrated experimentally.

3.3 Performance studies of the YAG/OTR monitor with beam

3.3.1 Efficiencies of photon emission and collection

To study the PhC efficiency and saturation threshold of the 0.5 mol% Ce:YAG, the number of collected photons as a function of the transverse beam size has been measured. The standard PhC efficiency and PhY could be quantified when beam sizes are large, and the saturation threshold could be extrapolated from the maximum particle density when the photon collection begins to decrease for the case of a smaller beam size. This method can avoid both the lengthy tuning involved in working with high intensity beams and the uncertainty of the beam intensity measurements in the lower range (< 1×10^9 e/pulse).

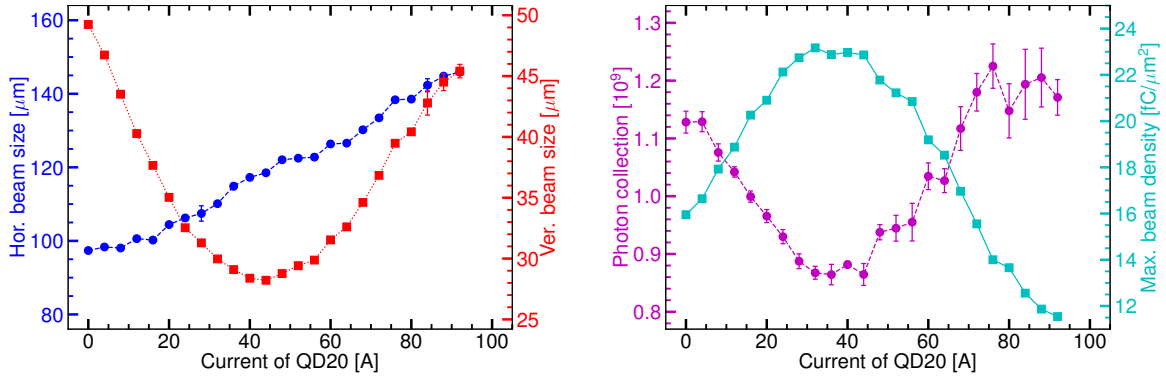

(a) (b)

Fig. 3.22 Vertical and horizontal beam sizes (a) and the number of collected photons (b) as a function of the QD20 current.

With a beam intensity of 3×10^9 e/pulse, we adjusted beam sizes at the YAG/OTR monitor using a quadrupole (QD20) upstream, as shown in Fig. 3.22 (a). The flux of YAG scintillation tends to be constant when beam sizes are large enough and the measurement is free of saturation, as shown in Fig. 3.22 (b). A maximum number of photons of about 1.2×10^9, corresponding to a PhC efficiency of 0.37–0.4 ph/e, can be clearly seen from the results. Taking into account the reduction of the observation angle and losses of light inside the YAG screen and optical lenses, the photon emission efficiency of the YAG screen was estimated to be about 2300-2500 ph/e, which is consistent with the predictions.

Besides, one may see that the photon collection significantly decreases when focusing the beam down to 40 μm vertically. The maximum charge density can approximate the threshold of scintillating saturation at the transition to saturation (for a QD20 current of 5 A or 75 A). In this way, a lower limit of the saturation threshold is found to be 16 fC/μm^2.

The PhC efficiency of OTR is sensitive to the angle between the observation and backward emission, as shown in Fig. 3.23 (a). Therefore, the OTR screen has been cautiously adjusted to maximize the number of photons on the sensor, before performing beam observations. Measurements have been carried out for varying beam intensities. The results indicate a PhC efficiency of about 8×10^{-3} ph/e in the 450–700 nm region which is slightly larger than the analytical predictions, as shown in Fig. 3.23 (b). What's more, a linear response to the number of incident electrons has been clearly observed.

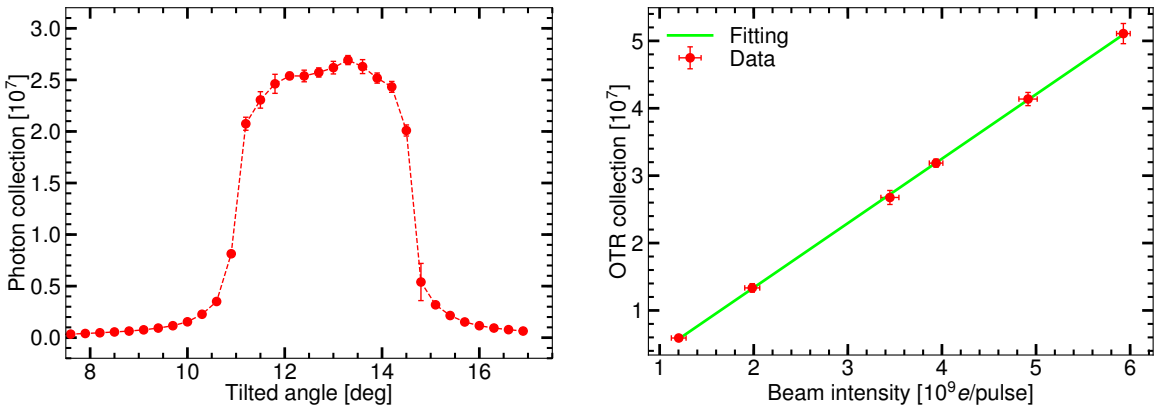

(a) (b)

Fig. 3.23 Dependence of the PhC on the rotation angle of the OTR target (a) and the beam intensity (b, the rotation angle is 12.5°).

3.3.2 Dynamic range

Rather than the foreseen combination of measured profiles from the YAG and OTR screens, which is rather complicated, we have demonstrated the feasibility of solely using the YAG screens with a satisfactory dynamic range and without saturation. After subtracting the offset

and background noise, the lower limit of the dynamic range has been estimated to be 4 electrons per pixel size on the YAG screen. The upper limit is determined by the saturation level of Ce:YAG, which has been measured as 16 fC/μm^2. Assuming a magnification factor of 2.5, the effective particle density on the YAG screen is 4–4.8$\times$10^5 e in a 2.6$\times$2.6 μm^2 area. These 2D distributions, measured by the profile scanning vertically and horizontally, exhibit a maximum pixel readout of about 2$\times$10^5 (corresponding to $\sim$ 4$\times$10^5 e), implying a dynamic range of about 1$\times$10^5, as shown in Fig. 3.24. Such a wide DNR is in a good agreement with the prediction and satisfies the requirements for beam halo diagnostics.

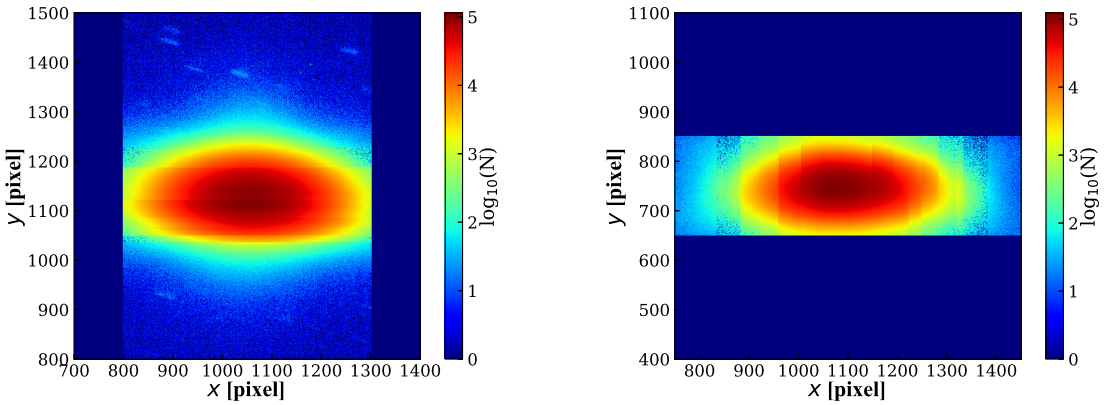

(a) (b)

Fig. 3.24 2D beam profiles measured through vertical (a) and horizontal (b) scanning. The maximum readout per pixel is above 1$\times$10^5 without saturation.

3.3.3 Spatial Resolution

To characterize the resolution of the YAG/OTR monitor, we first matched the ATF2 optics to the 10β_x^*1β_y^* at the IP, and corrected the vertical dispersion and *xy* coupling using the corresponding knobs in the extraction line. Since the vertical beam size can be reduced to several microns at the location of the YAG/OTR monitor, the corresponding resolution could be demonstrated directly by focusing the beam vertically.

Due to the different horizontal tilts of the OTR target and YAG screen, the observation system should be carefully adapted immediately after switching screens. If not, the measured beam size will be enlarged, especially for OTR measurements, as shown in Fig. 3.25.

The minimum vertical beam size has been found to be around 9.3 μm using the YAG screen, including either a 10% ND filter or the 550$\pm$10 nm BP filter, as shown in Fig. 3.26 (a, b). However, the minimum vertical beam size measured by the OTR screen is about 10.2 μm with the 550$\pm$10 nm BP filter to suppress the optical chromaticity and aberration of the observation lenses, as shown in Fig. 3.26 (c, d). The discrepancy of beam sizes measured by the two screens might be due to the optical diffraction and optical aberrations.

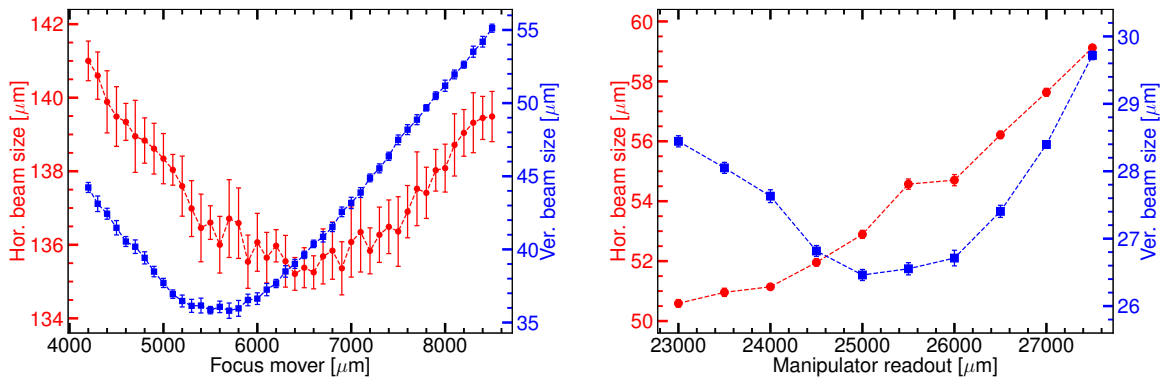

(a) (b)

Fig. 3.25 Evolution of beam sizes for OTR measurements due to the blurring effect caused by a change of the optical path (a) and horizontal translation of the holder (b).

By comparing measurements with the OTR and YAG screens, the influence of scintillation saturation on the horizontal beam size measurement can also be observed (see Fig. 3.26 (d)). Increasing the current of QD20 magnet from 35 A to 70 A, horizontal beam sizes measured by YAG screen are significantly larger than that given by OTR screen. Meanwhile, similar vertical beam sizes of less than 25 μm have been obtained using two screens. It is apparent that the scintillating process is saturated in the beam core region for such small beam sizes. The difference between observations using YAG and OTR screens is maximum when the vertical beam size reduces to the minimum value. The influence of scintillation saturation becomes insignificant when the vertical beam size is increased to more than 30 μm with the horizontal beam size remaining above 150 μm. One may see that the scintillation saturation also enlarges the observed vertical beam size and therefore the actual smallest beam size might be less than 9.3 μm. From these measurements, we conclude that the resolution of the YAG/OTR monitor is below ten microns, which accomplishes our design goals.

3.4 Halo diagnostics using the YAG/OTR monitor

The dynamic range and the resolution of the YAG/OTR monitor have been demonstrated to be more than 1×10^5 for 2D images and less than 10 μm, respectively. Thanks to such excellent performances, the YAG/OTR monitor is not only appropriate for beam halo diagnostics but also suitable for fast observations of the transverse beam profile (core) as well as for the dark current.

To reduce the systematic errors, a multi-frame imaging scheme has been implemented, requiring however excellent stability of both the beam position and beam size at the YAG/OTR monitor. For large beam sizes, the beam position and size have been recorded by capturing the beam profile images over 100 shots. Measurements indicate that the standard deviation of the beam position and core beam size fluctuations are less than 10% and 2% of the core beam size,

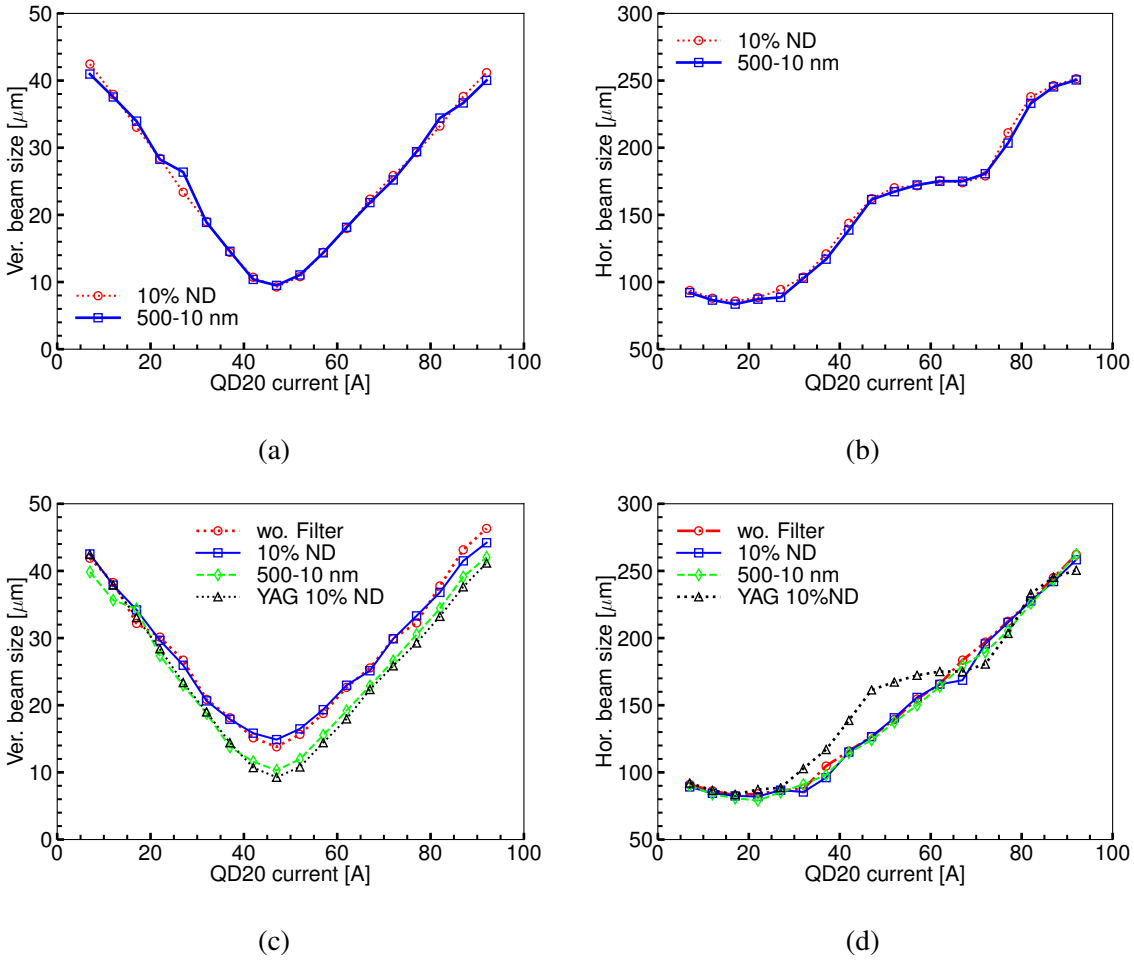

Fig. 3.26 Vertical and horizontal beam sizes as a function of the QD20 current measured by the YAG (a, b) and OTR (c, d) screens.

respectively, as shown in Fig. 3.27. Moreover, quality cuts were applied removing images with unreasonably large deviation from the expectation, e.g., a sudden drop of intensity or a large jitter.

Considering the layout of four YAG pads (top, bottom, left and right, see Fig. 3.12), measurements of the vertical or horizontal beam distributions (halo) have been performed in the following manner. In the vertical plane, for instance, the holder is first adjusted to get clear images of bottom halo particles using the bottom YAG pad. In this case, the intensity of scintillation light is weak and the blooming effect from the brilliant core region is eliminated. However, the distribution near the edge of the YAG pad is found to be strongly distorted due to the reflection on the imperfect/unpolished edge. Therefore, a "boundary" is defined about 50–100 μm below the edge (the largest slope of the horizontally projected profile), and only the part below this "boundary" is taken as an effective slice of the whole beam profile. Then, the bottom YAG pad is moved up with a small step to obtain images of more halo particles. A new "boundary" is determined following the above criteria, and the part below the new "boundary" and above the

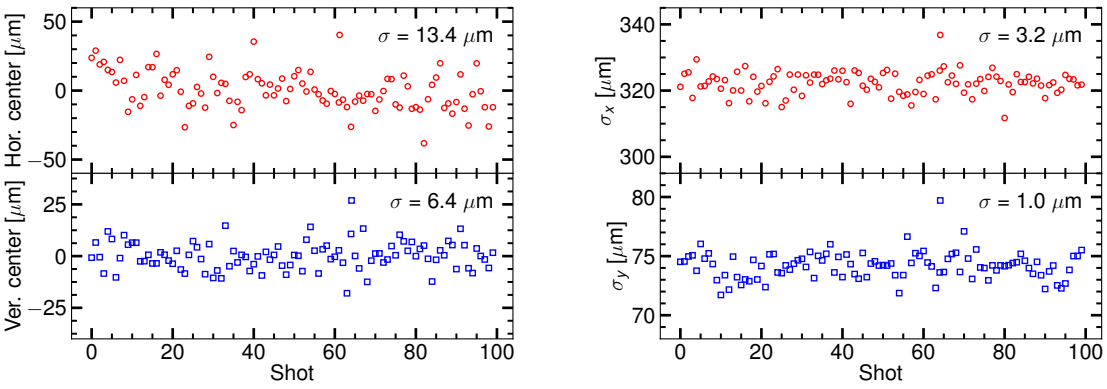

(a) (b)

Fig. 3.27 Beam position (a) and beam size (b) shot by shot fluctuations at the YAG/OTR monitor.

last "boundary" is then recorded and combined with previous slices. Such scanning is repeated until entering the core region and then one moves to the top YAG pad to acquire the upper half of the beam profile. The 10% and 1% ND filters are inserted when the intensity of the scintillation light is high (near/in the core region). Finally, the whole beam profile is assembled by combining all the sliced images with respect to the attenuations, as shown in Fig. 3.28. Applying such a horizontal/vertical scanning method, the dynamic range of the reconstructed 2D beam distribution reaches 1×10^5. However, measurements with such vertical scanning only properly reconstruct the vertical halo because the horizontal halo parts are no longer reliable when merging slices with different attenuation.

After subtracting the constant offset and background noise, 2D beam distributions are projected to the vertical or horizontal plane and then compared with theoretical predictions. Examples of the vertical and horizontal distributions are presented in Fig. 3.29. The 1D distribution was integrated over about 700 pixels, and therefore the residual noise level is about 300–400 counts (about 0.5 count/pixel). As can be seen, the effective dynamic range for 1D distributions is also about 1×10^5.

In addition, it is interesting to highlight the observation of dark current using the YAG screen thanks to its excellent PhY ability. Interrupting the beam operation by blocking the drive laser in the photo-cathode RF gun, a low-intensity image can be clearly observed on the YAG screen with a repetition rate of 3.12 Hz, as shown in Fig. 3.30. Considering the measured PhY and photon collection efficiency, the intensity of the dark current in the extraction line could be estimated as 77 fC, i.e., 4.8×10^5 electrons. Such a low-intensity bunch experiences the common acceleration, storage and extraction as an ordinary beam. As a result, evaluations of natural emittances and the energy spread from distributions of dark current could be foreseen in the near future.

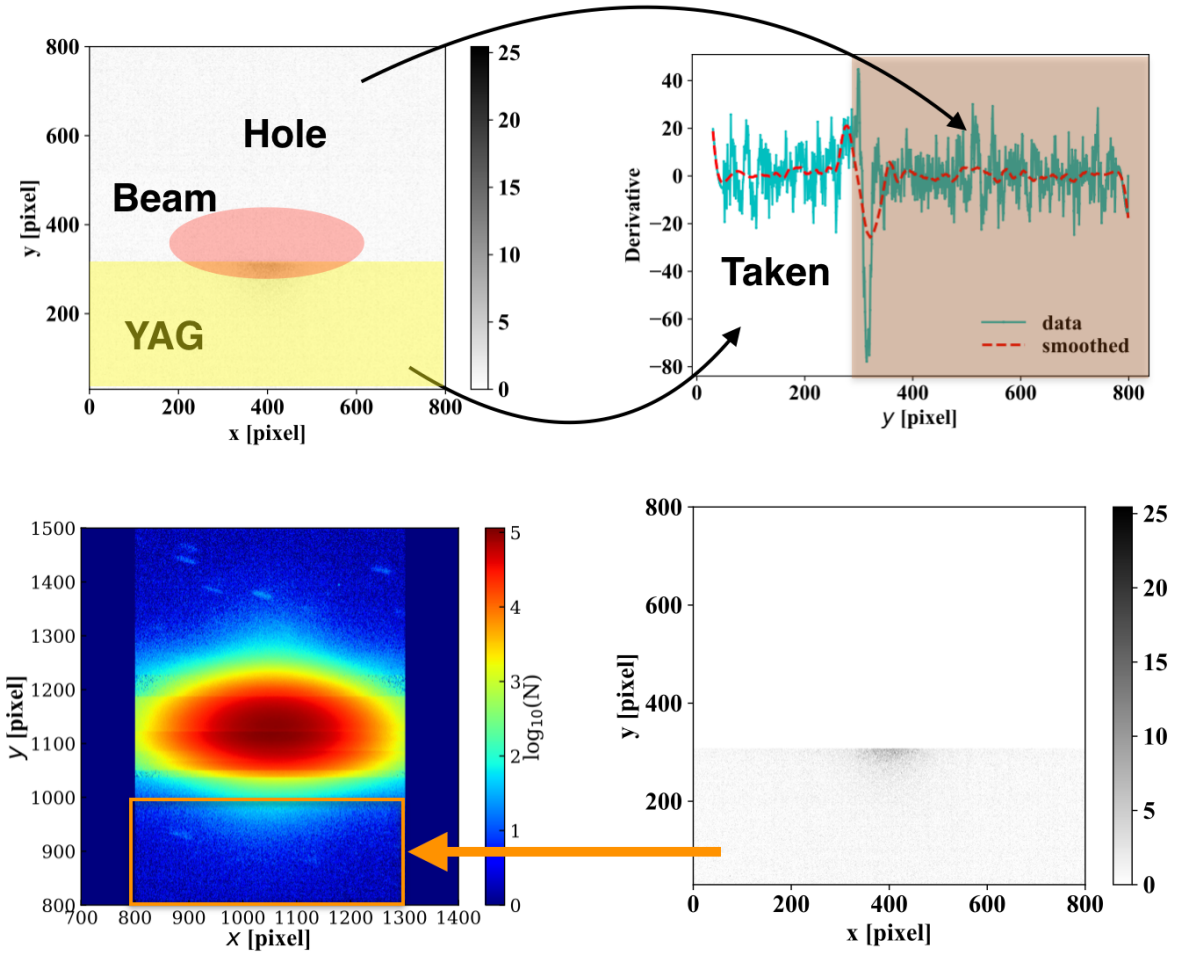

Fig. 3.28 Illustration of 2D beam profile reconstruction from sliced YAG images.

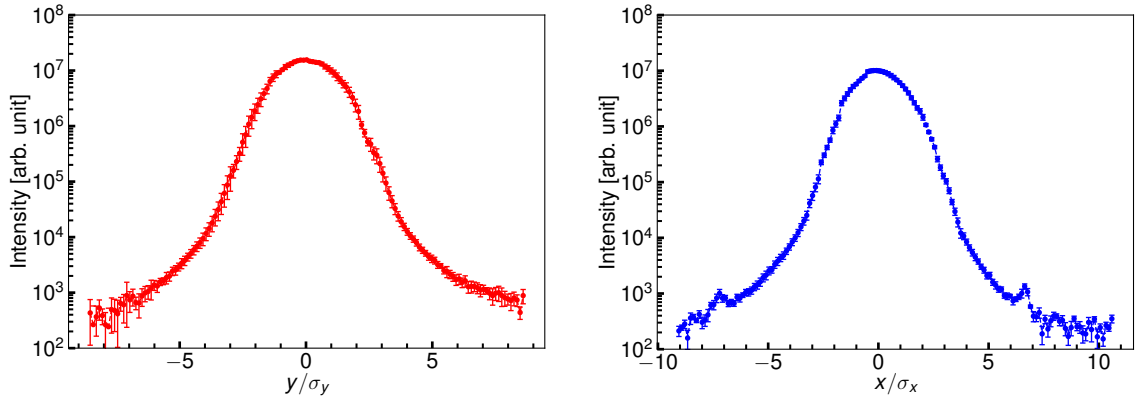

(a) (b)

Fig. 3.29 Vertical (a) and horizontal (b) profiles measured with the YAG screen.

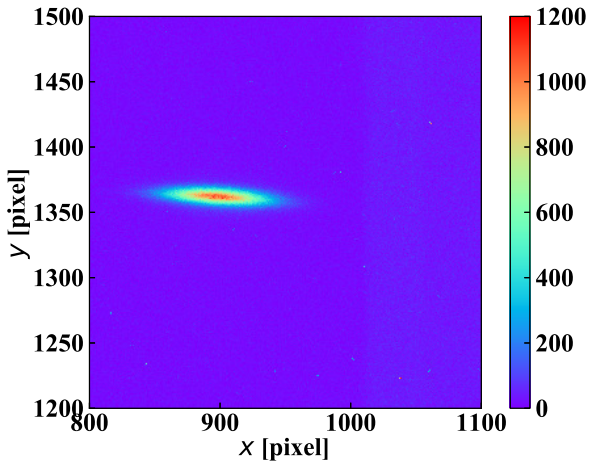

Fig. 3.30 The dark current image captured by the YAG screen.

Chapter 4

Measurements of beam halo at ATF

4.1 Beam halo from beam gas scattering

4.1.1 Halo distribution and its vacuum dependence

To probe the predictions of beam halo in the presence of elastic BGS, measurements have been carried out using both the DS detector and the YAG/OTR monitor. Beam intensity was stabilized at 3×10^9 e/pulse in order to reduce beam tuning time and influence of other effects related to beam intensity. The average vacuum pressure in the ring is calculated based on readouts of Cold Cathode Gauges (CCGs) and taking into account the distance between adjacent CCGs [215]. The vacuum pressure is about 2×10^{-7} Pa and can be increased to 1×10^{-6}–2×10^{-6} Pa by switching off Sputter Ion Pumps (SIPs), as shown in Fig. 4.1. The vertical emittance of the beam in the ring is around 12 pm by applying the standard tuning techniques [153].

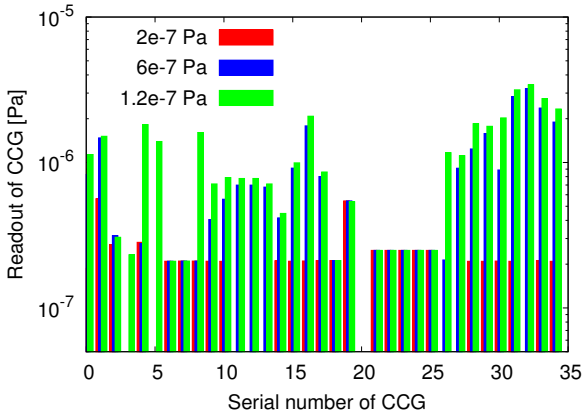

Fig. 4.1 Readouts of CCGs distributed around ATF damping ring for the gas pressures of 2×10^{-7} Pa, 6×10^{-7} Pa and 1.2×10^{-6} Pa.

Measurements using the diamond sensor (DS) detector were typically in the $10\beta_x^*1\beta_y^*$ optics for the ATF2 beam line. Before performing the measurement (scanning), the alignment of the DS strips with respect to the beam in the perpencular direction has to be executed [54]. This

process was achieved by moving QD0 or QF1 magnets transversely. To reconstruct the measured beam profiles, both the vertical and the horizontal beam sizes were measured in advance using the Wire Scanner (WS) located just after the IP.

Diagnostics using the YAG screens require a low particle density on the screen in order to avoid the scintillation saturation. Comparing with the DS scanner, the *xy* coupling at the YAG/OTR monitor can be corrected using QK1–QK4 skew quadrupoles and confirmed by the 2D images on screens.

As can seen in Fig. 4.2, vertical beam halo distributions measured by the DS detector after implementing the rescaling correction described in Chap. 3 and by the YAG/OTR monitor are in good agreement with the numerical predictions presented in Chap. 2, for different vacuum pressures in the damping ring. Moreover, the increase of the vertical halo for degraded vacuum pressures is clearly observed. This good agreement between simulations and measurements together with the clear pressure dependence indicates that the dominant mechanism for vertical halo formation is the elastic BGS process.

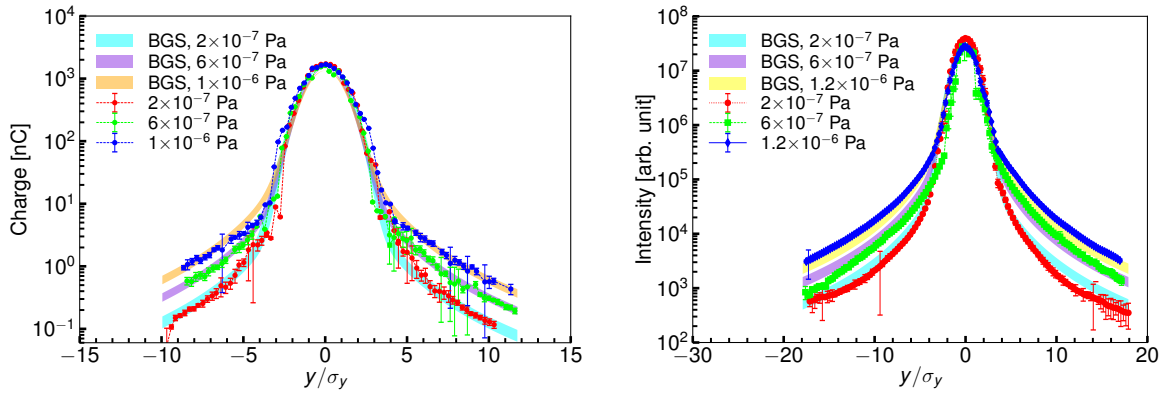

(a) (b)

Fig. 4.2 Vertical beam profiles measured by the DS detector (a) and the YAG/OTR monitor (b). The measurements were performed on different days but the beam conditions were similar. Even though the DS measurement is up to $\pm 20\sigma_y$ we reject data beyond $\pm 10\sigma_y$ because of the narrow aperture ($\sim 15\sigma_y$) of the beam pipe in the huge bending magnet behind the IP.

Horizontal beam profiles measured by the DS detector and YAG/OTR monitor suggest a higher halo level than predicted from the BGS process. This is shown in Fig. 4.3. Asymmetrical distributions are also observed with more halo particles on the right side (high-energy side). In addition, the vacuum dependence of the horizontal halo was found to be insignificant. The horizontal dispersion at the YAG/OTR monitor can be well corrected but that at the DS detector is always large (around 1 m) due to the large horizontal bending magnet upstream. A potential non-Gaussian momentum distribution may mix with the horizontal betatron distribution and complicate the horizontal halo measurement using the DS detector. These measurements indicate that the elastic BGS does not dominate the horizontal halo and that other processes must play

more important roles. They stimulate further experimental investigations of the asymmetry of the horizontal distribution and of a potential momentum tail from Touschek scattering.

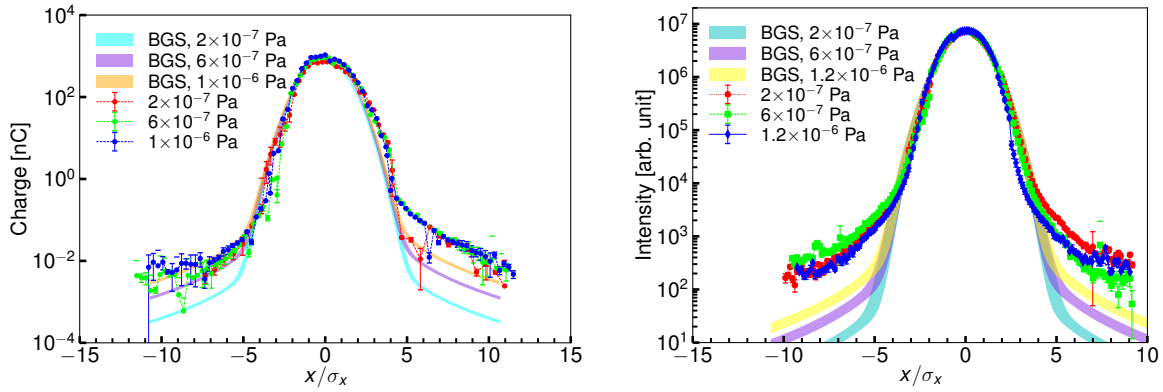

(a) (b)

Fig. 4.3 Horizontal beam profiles measured by the DS detector (a) and the YAG/OTR monitor (b). For a reasonable SNR, measurements were typically restricted within $\pm 10\sigma_x$.

4.1.2 Vertical emittance growth

In addition to the generation of beam halo, vertical emittance growth was also expected according to the numerical investigations. Presently, there are two devices to measure the vertical emittances: the X-ray Synchrotron Radiation (XSR) beam profile monitor [216] in the damping ring and the multi-OTR system in the ATF2 beam line [79]. The emittance growth in the extraction kicker region may complicate the measurements, and therefore only the XSR monitor was used in our experiments [217].

The XSR monitor receives the X-ray light radiated by the electron beam passing a bending magnet (BH1R.27) located at the exit of the western arc section. The bending radius is 5.4 m for a beam energy of 1.3 GeV, and the critical energy of the SR light is 0.816 keV. The XSR monitor contains a monochromator, two Fresnel Zone Plates (FZPs) and an X-ray 16-bit CCD camera, as shown in Fig. 4.4. The SR light is monochromatized to a photon energy of 3.225 keV (0.38 nm), and the beam image is magnified by a factor of 20 using the FZPs [218] before being collected on the CCD sensor (HAMAMATSU C4742-98-KWD). The spatial resolution of the XSR monitor has been demonstrated to be less than 1 μm which is sufficient to measure a vertical emittance around 8.6 pm with a rms deviation around 10%. A software has been developed for data acquisition and image display in real time, as shown in Fig. 4.4 (a). The vertical emittance is determined using the defining expression, $\varepsilon_y = \sigma_y^2/\beta_y$, where β_y is the β-function at the source point of the radiation, extrapolated from a fitting of β-functions at five quadrupoles around the XSR monitor, as shown in Fig. 4.4 (b). The β-functions at the quadrupoles are obtained from the

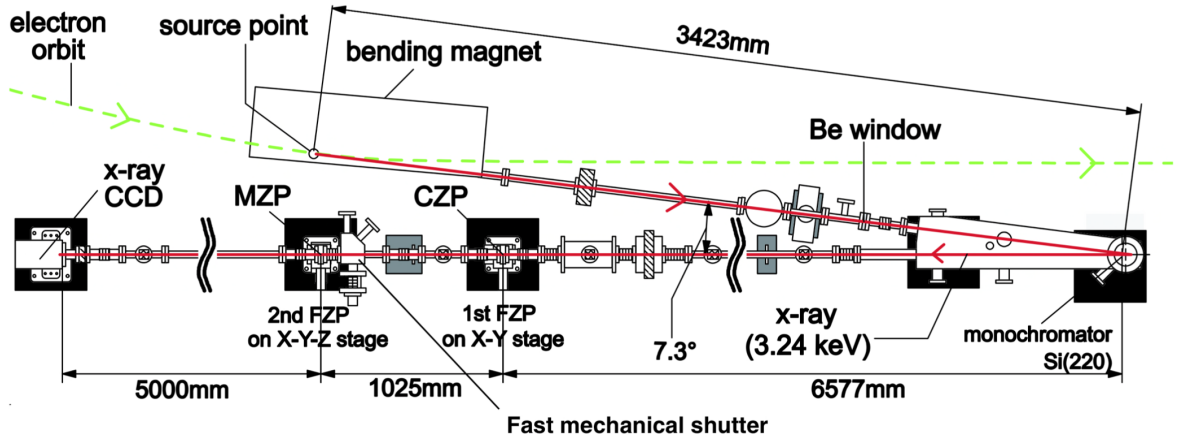

(a)

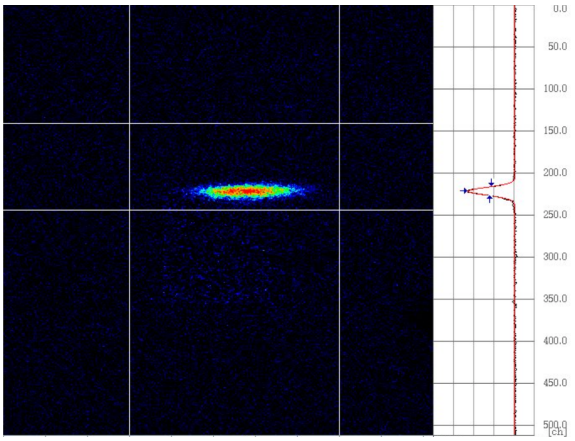

(b)

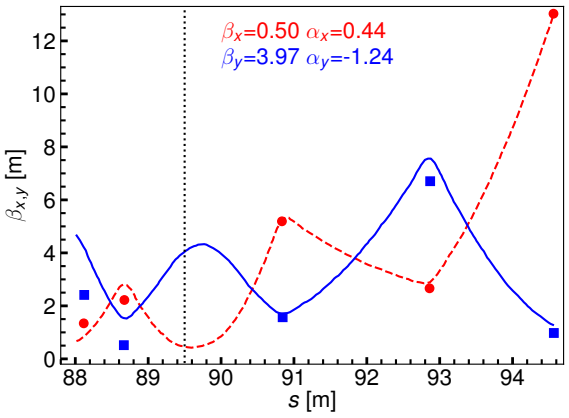

(c)

Fig. 4.4 Schematic of the XSR monitor (a), an example of XSR image (b) and the fitting of the β-function near the source point (c). Figure (a) is taken from Ref. [216].

respective strength dependencies of the betatron tune, using a script implemented in the ATF server (see Fig. 4.4 (c)).

To probe the numerical predictions of vertical emittance growth, measurements have been carried out for vacuum pressures ranging from 2.5×10^{-7} Pa to 1.75×10^{-6} Pa. The measured vertical emittance increases from 12.6±0.5 pm to 16.0±1.0 pm, which is higher than the simulation result, see Fig. 4.5 (a). This difference might be caused by the uncertainty in the vacuum pressure measurement, systematic errors in the XSR monitor or some other physical process contributing to emittance growth [219]. After resetting the SIPs, the vertical beam size monitored by the XSR reduced from 7.02 μm to 6.2 μm while the vacuum pressure decreased from 1.75×10^{-6} Pa to 2.5×10^{-7} Pa. Agreement between simulations and measurements indicates that, for typical vacuum pressures in the ATF damping ring, halo formation and emittance growth due to BGS are both measurable and significant. These aspects should be taken into account in the design of future low-emittance storage rings.

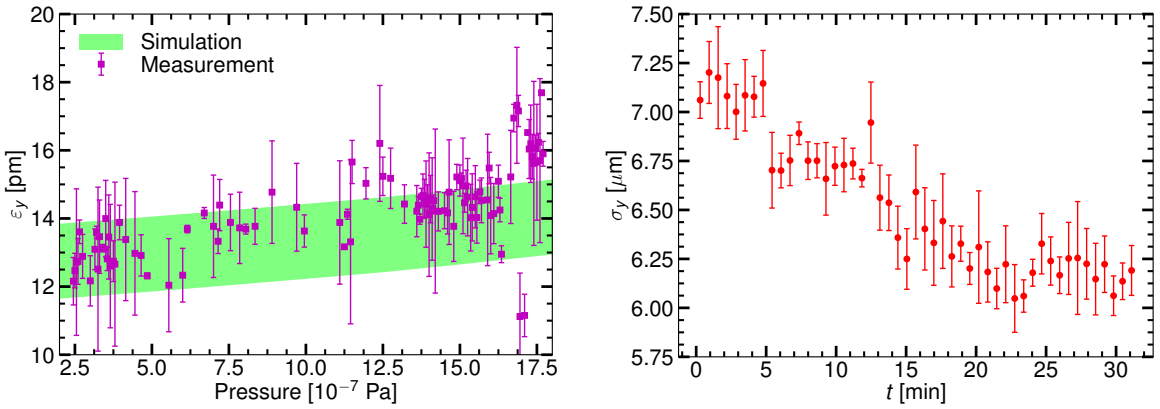

(a) (b)

Fig. 4.5 Vertical emittance growth as a function of the average vacuum pressure (a) and the time evolution of the vertical beam size measured by the XSR when all the SIPs were reset at t=0 (b). The green band showing the simulation results represents a $\pm$10% uncertainty in the vertical natural emittance.

Although the vertical beam halo has been demonstrated to be driven by the BGS process, the physical origin of the horizontal halo and the possible impact of a non-Gaussian momentum tail are still open questions.

As part of our investigation of potential sources for the horizontal beam halo, we have also estimated the possible enhancement and distortion of the horizontal halo in the ATF2 beam line.

4.2 Enhancements of beam halo along ATF2

ATF2's nominal optics is dedicated to the nanometer-scale beam size at the virtual IP, based on the local chromaticity correction scheme. The horizontal halo distributions at the Post-IP locations can on occasion be affected by the imperfections and errors in the presence of the chromaticity and aberrations, the extraction kicker field and secondary particles generated in the FF section. These effects might induce significant horizontal beam halo or have influence on the performance of diagnostics, and should be carefully evaluated.

4.2.1 Optical aberration

Residual chromaticity and aberration in the FF section could in principle induce extra beam halo at the DS. In the $10\beta_x^*1\beta_y^*$ optics, the propagation of particle distribution including tails from BGS indicates that there are more particles on the right side in the horizontal distribution, with very large amplitudes of betatron oscillation (see plot (a) in Fig. 4.6), if the physical aperture is not considered. However, once the aperture is considered, these particles are stopped in the large β_y and large η_x regions, i.e., around QM12–QD10 and BDUMP, see plot (b) of Fig. 4.6. In this

study, the distribution in the longitudinal phase-space was assumed to be Gaussian. The strengths of sextupoles in the FF were set to the realistic values representative of the beam operation.

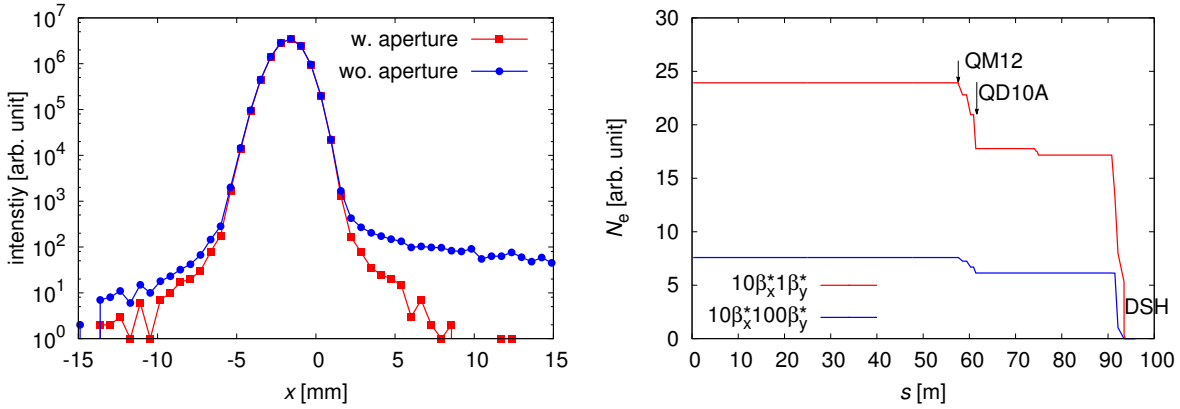

(a) (b)

Fig. 4.6 Simulated horizontal profile at the DS detector with/without physical aperture (a) and the corresponding loss map (b). Beam profiles are obtained by tracking particles, exported from the BGS simulations described in Sec. 2.4.3, to the DS detector in the $10\beta_x^* 1\beta_y^*$ optics.

To understand the asymmetry of the horizontal profile at the Post-IP, we first propagate particles in the $10\beta_x^* 100\beta_y^*$ optics in which case the vertical β-function, chromaticity and aberration in the FF section are small. As a consequence, beam loss along ATF2 is reduced by around 60% in the $100\beta_y^*$ optics (see Fig. 4.6 (b)) but the horizontal halo in the Post-IP seems changeless, as shown in Fig. 4.7 (a). These results may indicate the enhanced horizontal halo is from the upstream and not due to the chromaticity in the FF section. Concerning the initial distribution of the lost particles, we found that the vertical betatron actions of these particles are much larger than the those defining the vertical emittance, as can be seen in Fig. 4.7 (b). The particle with a large vertical betatron action presumably get lost in the high β_y region, which is consistent with the estimated loss map.

In the $10\beta_x^* 1\beta_y^*$ optics, particles with large vertical action might survive thanks to an orbit distortion in the FF section. Rather than the complex simulations with a realistic optics and orbit, we performed and compared experimental measurements in $10\beta_x^* 1\beta_y^*$ and $10\beta_x^* 100\beta_y^*$ optics. Horizontal profiles measured by the DS detector are shown in Fig. 4.8. They imply that the distribution in the $100\beta_y^*$ optics has a higher halo level than that in the $1\beta_y^*$ optics. This difference further verifies the above prediction: the influence from the chromaticity and aberration in the FF section is small, while the higher horizontal halo level with $100\beta_y^*$ optics might be due to a combination of survived particles with large amplitudes in the action-angle phase space, more incident particles on the DS strip for a smaller vertical beam size or the impact of a potential momentum tail.

The chromaticity and aberration in the FF section does not affect the beam at the YAG/OTR monitor. However, the optical aberration from the upstream extraction section may cause some distortion. Since the optical aberrations depend on the phase advance between the possible

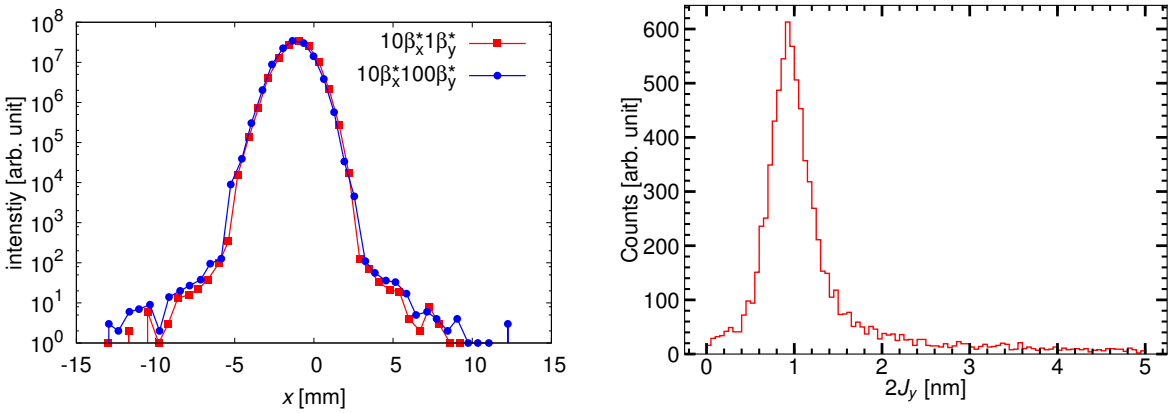

(a) (b)

Fig. 4.7 Horizontal profiles in the $10\beta_x^*1\beta_y^*$ and $10\beta_x^*100\beta_y^*$ optics (a) and a histogram of the vertical betatron action of the lost particles (b).

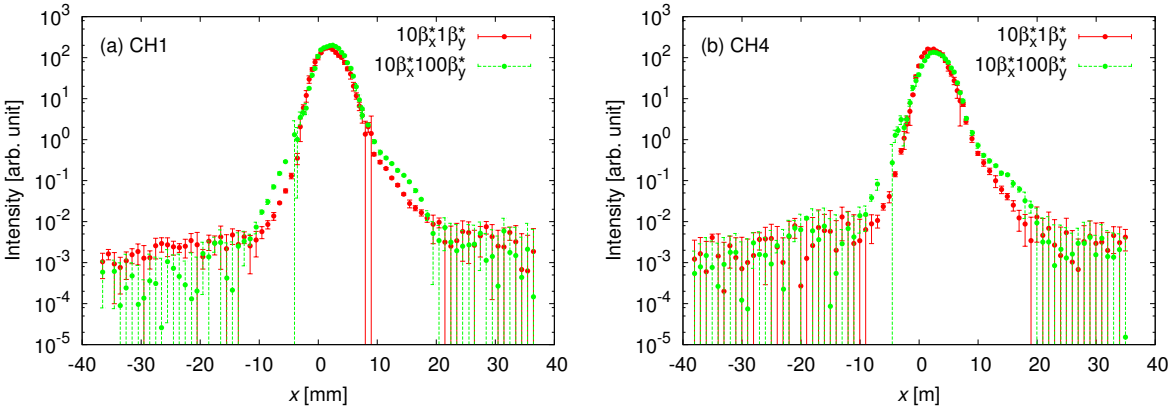

(a) (b)

Fig. 4.8 Horizontal distributions measured by two broad DS strips in the $10\beta_x^*1\beta_y^*$ and $10\beta_x^*100\beta_y^*$ optics. Notice that no rescaling corrections were applied for the beam cores.

sources and the diagnostic point, measurements of the horizontal distribution with different strengths of QF21 quadrupole have been carried out. The halo part was found to be not very sensitive to the strength of QF21, but behaviors of the left and right halos were not the same, as shown in Fig. 4.9. The observed asymmetry and the slight overall enhancement may be due to optical aberrations in the extraction section .

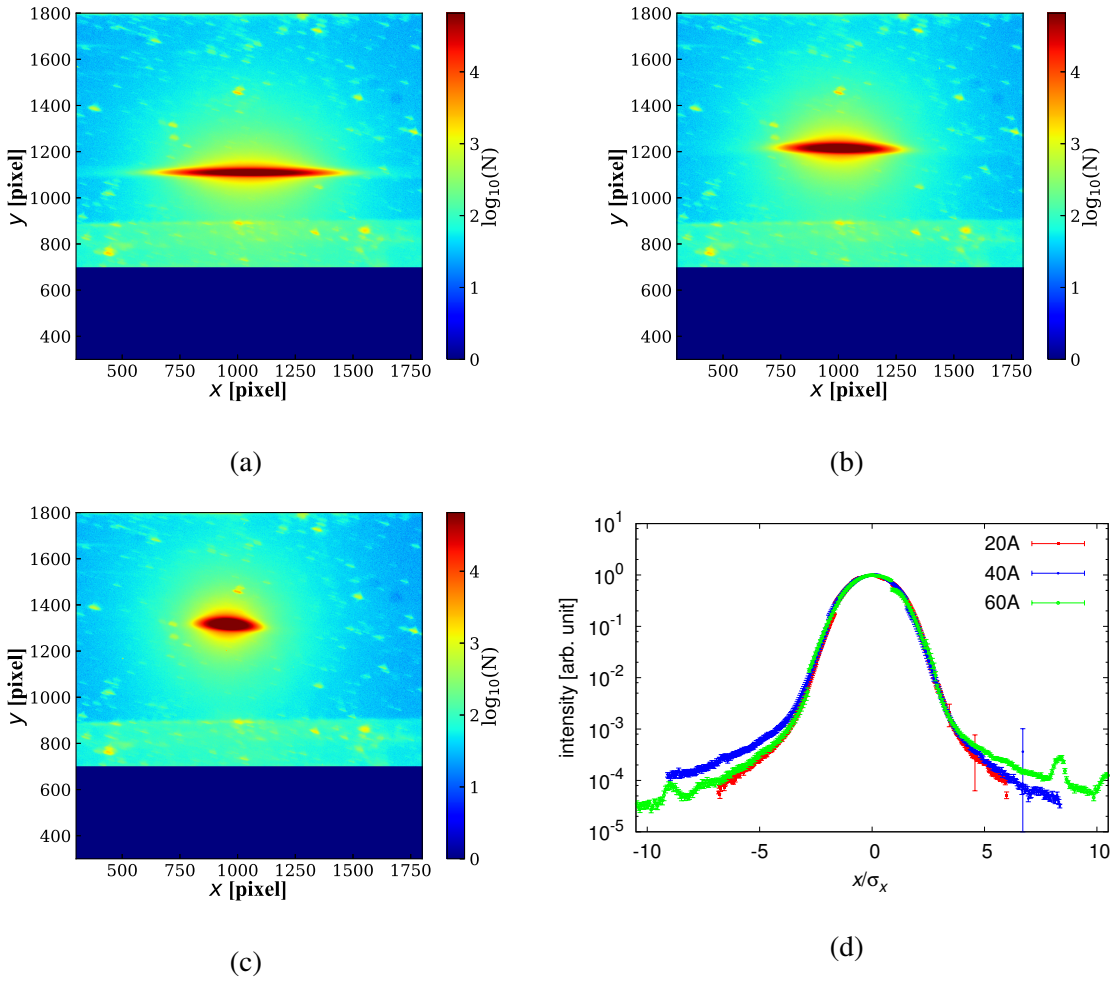

Fig. 4.9 Beam images for the QF21 currents of 20 A, 40 A and 60 A (a–c) and their projections on the horizontal plane (d).

4.2.2 Secondary emission

Not only the particles with large vertical action can result in extra horizontal halo at the DS detector, but also secondary particles generated in the FF section. To investigate this possibility, measurements with a reduced beam loss at the BDUMP controlled by a vertical collimator located in the large β_y region have been carried out.

This vertical collimator has been developed for a purpose of mitigating the undesired background in the *Shintake* monitor [85, 220] for the nanometer beam size measurement at the IP.

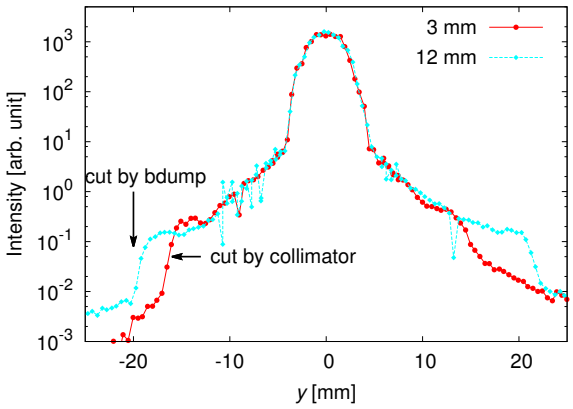

Fig. 4.10 Vertical beam profiles measured by the DS detector for collimator apertures of 12 mm and 3 mm. The cuts around $\pm 20\sigma_y$ are due to the narrow aperture around the BDUMP magnet before closing the collimator jaws.

The collimator was placed between QM11 and QD10 magnets where the β_y is large ($\approx$7000 m) and has been confirmed to be effective to collimate the vertical halo (see Fig. 4.10) and reduce the background at the Post-IP [221]. For two different half apertures of the vertical collimator, 12 mm and 3 mm, the horizontal halo was measured using the DS detector on March 11, 2016 and June 23, 2017. As shown in Fig. 4.11, the earlier measurements indicate a slight decrease of the horizontal halo when the collimator was closed, however the more recent measurements do not reproduce such a reduction, making it hard to draw very strong conclusions on the role of secondary particles to explain the observed horizontal tails.

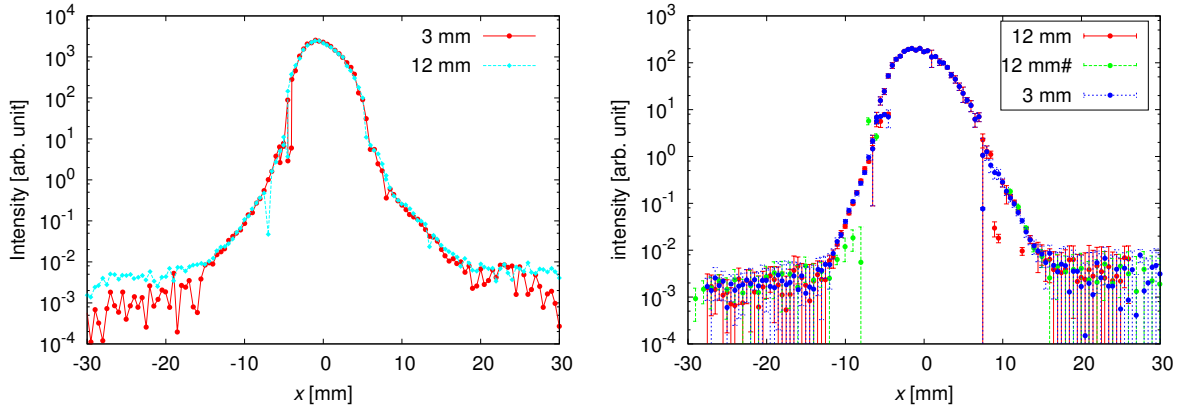

(a) (b)

Fig. 4.11 Horizontal beam profiles obtained by the DS detector when the collimator was opened and closed to 3 mm. (a): measurements performed on March 11, 2016; (b): data acquired on June 23, 2017. The latter is without the rescaling correction.

Further simulations would be needed to fully understand the potential contribution of secondary particle emission in the FF section to the horizontal halo distribution at the Post-IP. Avoiding the possible perturbation from beam loss in the FF section was one of the motiva-

tions for developing and installing the new YAG/OTR monitor in front of the matching section (QM16–QM11).

4.2.3 Imperfect Extraction

In the extraction section, the electron beam is deflected by around 4.6 mrad using a pulsed kicker magnet and then arrives in three septum magnets where it is again bent successively by 28, 75 and 235 mrad [36, 222]. Before entering the septum magnets, the kicked beam passes through two quadrupoles, QM6 and QM7, with a horizontal orbit displacement of 8 mm and 22.5 mm, respectively, as shown in Fig. 4.12. Notably, at QM7 magnet, the beam orbit is very close to the magnet bore, and the higher order component might be significant.

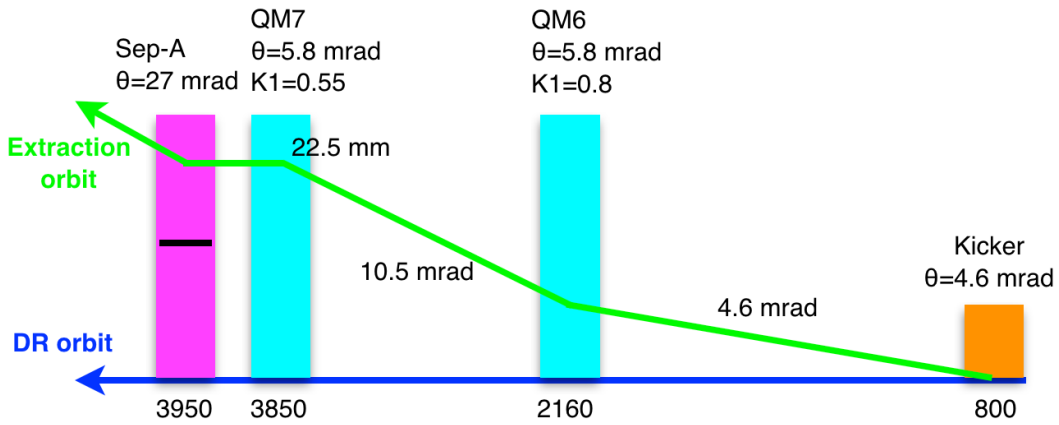

Fig. 4.12 Beam orbit in the extraction kicker region

To prevent the possible emittance growth due to the coupling from the sextupole component of the field near the magnet bore of QM7, the old QM7 magnet has been replaced by a magnet named TOKIN 3581, which has a large bore aperture. Simulations and measurements suggest that the sextupole component of the TOKIN 3581 is small, i.e., $K_2L = 1\ \mathrm{m}^{-2}$ [77, 223], for a nominal off-center orbit. Concerning the possible errors of the magnetic field, the horizontal distributions at the YAG/OTR monitor and the DS detector seem insensitive to the orbit distortion at QM7 (see Fig. 4.13).

However, the quadrupole and sextupole components of the extraction kicker pulsed magnet are not negligible [77], e.g., a sextupole component of $K_2L = -15.3\ \mathrm{m}^{-2}$ which can induce vertical emittance growth and perhaps generate additional beam halo. To check this point, particles were propagated through the extraction kicker magnet with a horizontal orbit offset and to the diagnostic points. In the $10\beta_x^* 1\beta_y^*$ optics, beam profiles at the YAG/OTR monitor were found to be insensitive to the horizontal orbit displacements at the extraction kicker while distributions at the DS detector are enlarged for a large horizontal orbit displacement, as shown in Fig. 4.14.

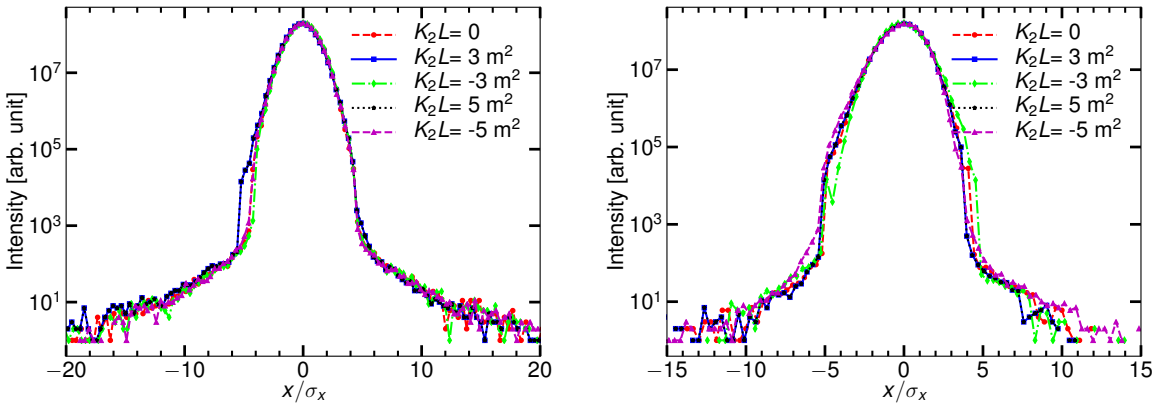

(a) (b)

Fig. 4.13 Simulated horizontal profiles at the YAG/OTR monitor (a) and the DS detector (b) with respect to the K_2 component of QM7.

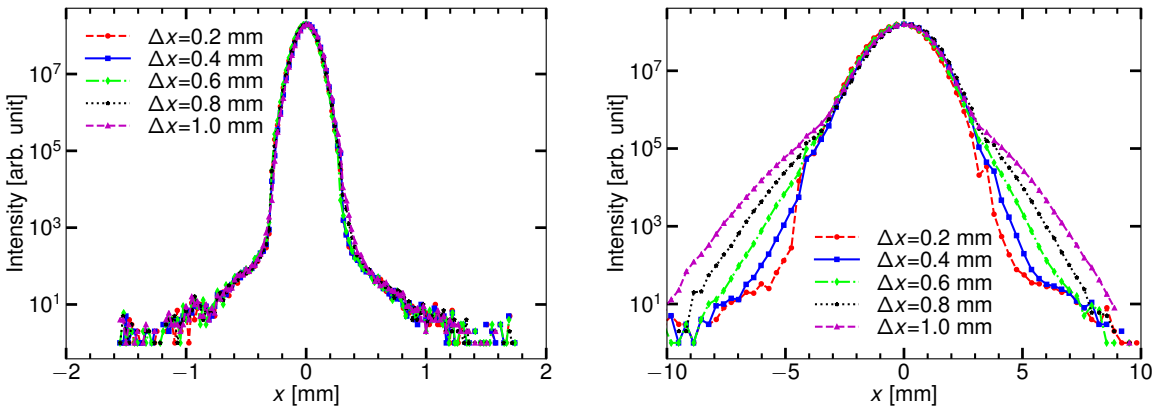

(a) (b)

Fig. 4.14 Horizontal beam profiles at the YAG/OTR monitor (a) and the DS detector (b) as a function of the horizontal displacement at the kicker pulsed magnet.

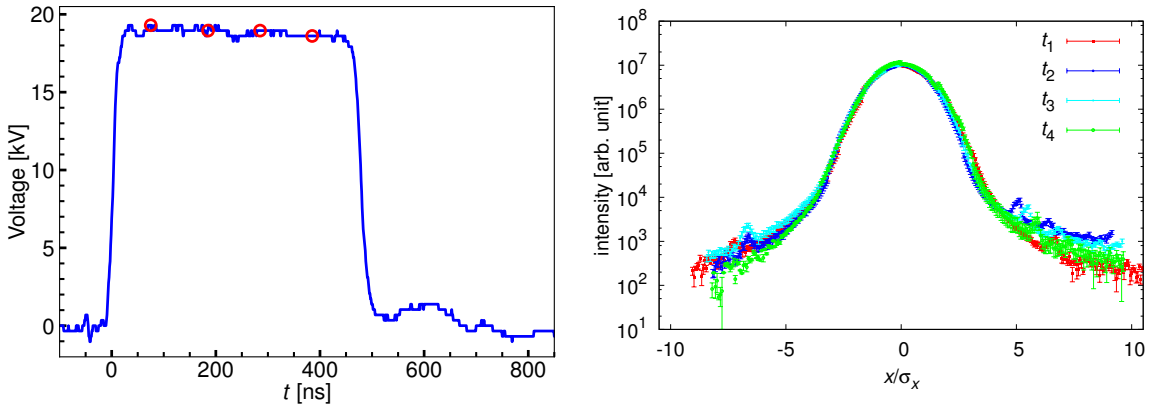

(a) (b)

Fig. 4.15 Shape of the extraction kicker pulse (a) and the corresponding horizontal beam profiles at the YAG/OTR monitor (b). The red circles indicate the moment of beam extraction.

To ensure an efficient beam extraction, the strength of the kicker pulse magnet has to be stabilized around the designed value. Beam orbit displacement at the extraction kicker was typically corrected ($\Delta x < 1$ mm). To illustrate the influence from the extraction kicker, horizontal beam distributions for different kicker timings have been measured using the YAG/OTR monitor. In this process, the change of kicker field strength is small to guarantee an efficient beam extraction, as shown in Fig. 4.15 (a). Beam halo for the different extraction timings are seen at a similar level, but asymmetric profiles were sometimes observed, as shown in Fig. 4.15 (b). These results indicate that the higher order components of the kicker magnet may also play a role in enhancing the horizontal halo and generating asymmetric horizontal distributions.

4.3 Momentum tail measurements

For an efficient diagnostic of the momentum distribution (energy spectrum), the optical dispersion at the diagnostic point has to be enlarged to dominate horizontal or vertical distribution. To characterize the resolution of the momentum visualization, a minimum distinguishable energy spread can be defined as [142]

$$\delta_{m,\mathrm{sep}} = 2\sqrt{\varepsilon_{x,y}\beta_{x,y}}/\eta_{x,y} \tag{4.1}$$

which indicates that the energy resolution can be improved by minimizing $\sqrt{\beta}/\eta$. This can be realized through rematching the optics of the extraction line. Actually, since the vertical emittance is around 1% of the horizontal emittance, measurements in the vertical plane are easier. Thanks to the two skew quadrupoles (QS1X and QS2X) in the inflector, a method to manipulate the vertical dispersion while preserving a small β-function at the diagnostic point has been proposed. With an enlarged vertical dispersion at the location of the YAG/OTR monitor, it has

been possible to isolate and measure the tails of the momentum distribution, and uncover the interplay between momentum tail and Touschek scattering.

4.3.1 Experimental design

In the design of the ATF2 beam line, the vertical dispersion in the extraction line is zero. A feasible way to generate a considerable vertical dispersion at the location of the diagnostic, i.e., the YAG/OTR monitor, has to be established. A brute force method would consist in generating the dispersion using a bending magnet, requiring presumably an extra beam line dedicated to energy spectrum measurements. It is however not feasible at ATF.

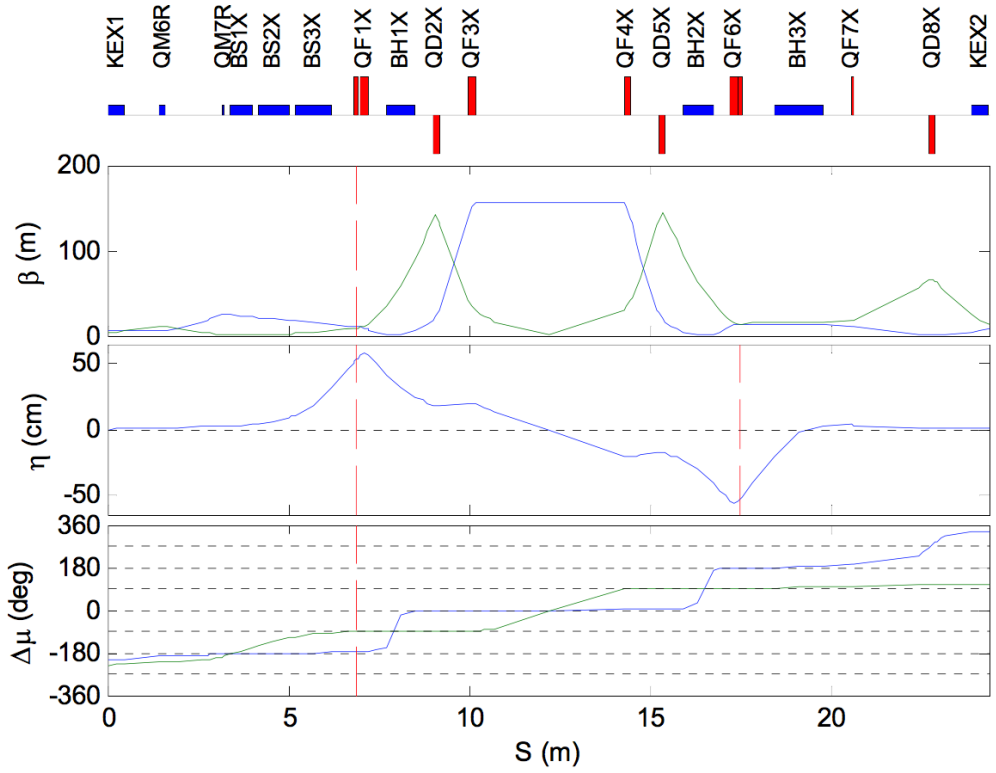

Fig. 4.16 Optical functions in the inflector. The red dashed lines indicate the locations of the QS1X and QS2X. Taken from Ref. [77].

In the inflector, the optics has been designed to be symmetric about its midpoint with the maximum horizontal dispersion around QF1X and QF6X but of opposite sign. Near these two quadrupoles, two skew quadrupoles (QS1X and QS2X) are placed with $\Delta u_x = 2\pi$ and $\Delta u_y = \pi$, as shown in Fig. 4.16. This pair of skew quadrupoles can work in the $\sum$-knob mode and the Δ-knob mode, for dispersion correction and xy coupling correction, respectively. In principle, the Δ-knob can also be used to generate the pure vertical dispersion with only very small residual xy coupling. In reality, the actual optics implemented in the inflector departs somewhat from the ideal design. Hence the $\sum$-knob might also induce undesired xy coupling and some further optimization is required. Assuming a zero vertical dispersion at the entrance of QS1X, the

propagation of a dispersion vector from QS1X to the entrance of QS2X is governed by[1]

$$\vec{\eta}_{2a} = \boldsymbol{M} \cdot \boldsymbol{R}_{1X} \cdot \vec{\eta}_{1a} + \vec{\eta}_{\Delta} \tag{4.2}$$

with

$$\boldsymbol{R}_{1X} = \begin{pmatrix} 1 & l & 0 & 0 \\ 0 & 1 & -1/f_1 & 0 \\ 0 & 0 & 1 & l \\ -1/f_1 & 0 & 0 & 1 \end{pmatrix} \tag{4.3}$$

where $\vec{\eta}$=(η_x, η'_x, η_y, η'_y)^T, $\vec{\eta}_{1a}$ and $\vec{\eta}_{2a}$ dispersion functions at the entrance of QS1X and QS2X, respectively, $\boldsymbol{M}$ the 4×4 transfer matrix from the exit of QS1X to the entrance of QS2X, $\boldsymbol{R}_{1X}$ the transfer matrix of QS1X, $\vec{\eta}_{\Delta}$ the particular solution, f_1 the focal length of QS1X and l the thickness of QS1X and QS2X. From QS1X to QS2X, $\vec{\eta}_{\Delta}$ is in the form of

$$\vec{\eta}_{\Delta} = (d, d', 0, 0)^{\mathrm{T}} \tag{4.4}$$

where d and d' are because of the horizontal bending magnets between two skew quadrupoles. Assuming the difference of the horizontal dispersions at QS1X and QS2X is small, we obtain

$$\vec{\eta}_{2a} = \begin{pmatrix} -\eta_{x0} \\ \eta'_{x,\mathrm{QS2X}} \\ -M_{34}\eta_{x0}/f_1 \\ -M_{44}\eta_{x0}/f_1 \end{pmatrix} \tag{4.5}$$

where η_{x0} is the horizontal dispersion at the entrance of QS1X, $\eta_{x0} \approx \eta_{x,\max}$. Then, the vertical dispersion downstream of QS2X is given by

$$\vec{\eta}_{s_2} = \boldsymbol{N} \cdot \boldsymbol{R}_{2X} \cdot \vec{\eta}_{2a} \tag{4.6}$$

where $\boldsymbol{N}$ represents the 4×4 transfer matrix from the exit of QS2X to a point s_2 downstream, $\boldsymbol{R}_{2X}$ the transfer matrix of QS2X, which can be expressed as

$$\boldsymbol{R}_{2X} = \begin{pmatrix} 1 & l & 0 & 0 \\ 0 & 1 & -1/f_2 & 0 \\ 0 & 0 & 1 & l \\ -1/f_2 & 0 & 0 & 1 \end{pmatrix} \tag{4.7}$$

[1]To be simple, the transformation of the dispersion function has been reduced to 4 dimensions. Meanwhile, the particular solution is represented by $\vec{\eta}_{\Delta}$.

where f_2 is the focal length of QS2X. The vertical dispersion function at s_2 can be written as

$$\vec{\eta}_{y,s_2} = \eta_{x0} \begin{pmatrix} -\frac{M_{34}N_{33}}{f_1} + \frac{N_{34}}{f_2} - \frac{M_{44}(lN_{33}+N_{34})}{f_1} \\ -\frac{M_{34}N_{43}}{f_1} + \frac{N_{44}}{f_2} - \frac{M_{44}(lN_{43}+N_{44})}{f_1} \end{pmatrix} \tag{4.8}$$

In the thin-lens approximation with $l \to 0$, we obtain

$$\vec{\eta}_{y,s_2} = \eta_{x0} \begin{pmatrix} \frac{M_{34}N_{33}}{f_1} - \frac{N_{34}}{f_2} - \frac{M_{44}N_{34}}{f_1} \\ -\frac{M_{34}N_{43}}{f_1} - \frac{N_{44}}{f_2} - \frac{M_{44}N_{44}}{f_1} \end{pmatrix} \tag{4.9}$$

The transformation of the coordinates $(x, x', y, y')^{\mathrm{T}}$ from the entrance of QS1X to s_2 can be expressed as

$$\vec{X}_{s_2} = \boldsymbol{N} \cdot \boldsymbol{R}_{2X} \cdot \boldsymbol{M} \cdot \boldsymbol{R}_{1X} \cdot \vec{X}_0 \tag{4.10}$$

where $\vec{X}_0$ and $\vec{X}_{s_2}$ represent the coordinates in the transverse phase space at the entrance of QS1X and s_2, respectively. The change of the vertical coordinate at s_2 due to QS1X and QS2X is

$$\Delta y_{s_2} = -\frac{M_{12}N_{34}}{f_2}x_0' - \Big(\frac{M_{11}N_{34}}{f_2} + \frac{M_{34}N_{33} + M_{44}N_{34}}{f_1}\Big)x_0 + \frac{M_{12}N_{34}}{f_1 f_2}y_0 \tag{4.11}$$

Typically the skew quadrupoles are weak, i.e., $f_1 f_2 \to \infty$, the above expression can thus be simplified as

$$\Delta y_{s_2} = -\frac{M_{12}N_{34}}{f_2}x_0' - \Big(\frac{M_{11}N_{34}}{f_2} + \frac{M_{34}N_{33} + M_{44}N_{34}}{f_1}\Big)x_0 \tag{4.12}$$

Assuming the phase advance between QS1X and QS2X satisfies $\Delta u_x = 2\pi$ and $\Delta u_y = \pi$, $M_{12} = M_{34} = 0$ and $M_{11} = -M_{44} = 1$, Eq. (4.9) exhibits the mathematical expression associating to the $\sum$-knob. However, the above assumptions are only a rough approximation. A ratio κ_{QS} between the strengths of QS1X and QS2X was introduced as a fudge factor to accommodate the actual optics. To generate considerable vertical dispersion with the minimum xy coupling, κ_{QS} is defined by the ratio between the enlargements of the vertical beam size at s_2 when separately driving QS1X and QS2X. For the actual optics of ATF2, κ_{QS} was found to be around 1:0.7. It was shown that using this ratio can introduce a pseudo-pure vertical dispersion and preserve a small residual xy coupling, as shown in Fig. 4.17 (a). The vertical dispersion at the YAG/OTR monitor can be increased to around 300 mm with this method, corresponding to the maximum QS1X/QS2X current of 5 A, as shown in Fig. 4.17 (b).

The dependence of the minimum distinguishable energy deviation on the vertical dispersion for different values of β_y, 5 m, 20 m and 50 m, at the diagnostic point, is illustrated in Fig. 4.18 (a). For a vertical dispersion above 160 mm, $\delta_{m,\mathrm{sep}}$ is not larger than 3×10^{-4} which is sufficient for the momentum spectrum measurements. The potential residual impact of the betatron xy coupling (from $\vec{x}$ to $\vec{y}$) was evaluated by computing its maximum fractional contribution to the vertical offset for varying vertical dispersions. For particles with initial horizontal actions of $400\varepsilon_x$, the change of the vertical coordinate at the YAG/OTR monitor is less than $0.6\sigma_{y,s_2}$, as

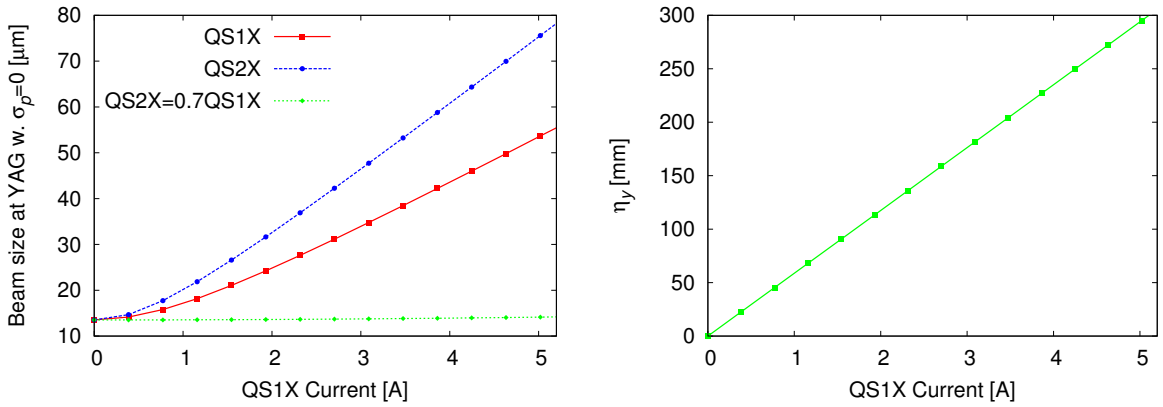

(a) (b)

Fig. 4.17 Comparison of the vertical betatron beam sizes at the YAG/OTR monitor when adjusting the vertical dispersion using only QS1X and QS2X, and both QS1X and QS2X with a ratio of 1:0.7 (a). The increase of the vertical dispersion at the YAG/OTR monitor for the available QS1X current (b), when QS2X is set simultaneously in a ratio of 1:0.7.

shown in Fig. 4.18 (b). This result implies that the accompanying *xy* coupling is small compared to the total rms beam height.

In the extraction line, the residual vertical dispersion is typically non-zero due to the misalignment of magnets and mismatch of the dispersion transfered from the damping ring. Therefore, QS1X and QS2X are typically used in $\sum$-knob mode during regular operation, i.e., the strength of QS1X/QS2X is not zero when $\eta_y \approx 0$ in the extraction line. To establish a considerable vertical dispersion, the strengths of QS1X and QS2X were decreased with a ratio of 1:0.7 and same polarity. The vertical dispersion at the YAG/OTR monitor could be increased to around 200 mm while keeping the vertical β function and *xy* coupling as small, as shown in Fig. 4.19. Dispersion at the YAG/OTR monitor is approximated by that at a BPM 30 cm downstream. Measurement of dispersion is done by recording the trajectory change in the BPMs for different beam energies (changing the frequency of the RF cavity in the damping ring). An example of the dispersion function along the whole beam line is shown in Fig. 4.20 where the propagation of dispersion is accomplished in the Flight Simulator software [224].

4.3.2 Experimental results

Thanks to the YAG/OTR monitor, vertical profiles can be easily recorded during the adjustment of the vertical dispersion. Although the large vertical dispersion has been shown to dominate the vertical beam size in simulation, the influence of the vertical betatron distribution could not be entirely excluded. Vertical profiles resulting from a mix of betatron and momentum amplitudes like that in Fig. 4.21 (a) can not be compared directly. However, since the vertical betatron halo has been proved to be driven by BGS process in the damping ring, the vertical profile in the presence of BGS can be accurately predicted at the diagnostic point with a realistic optics.

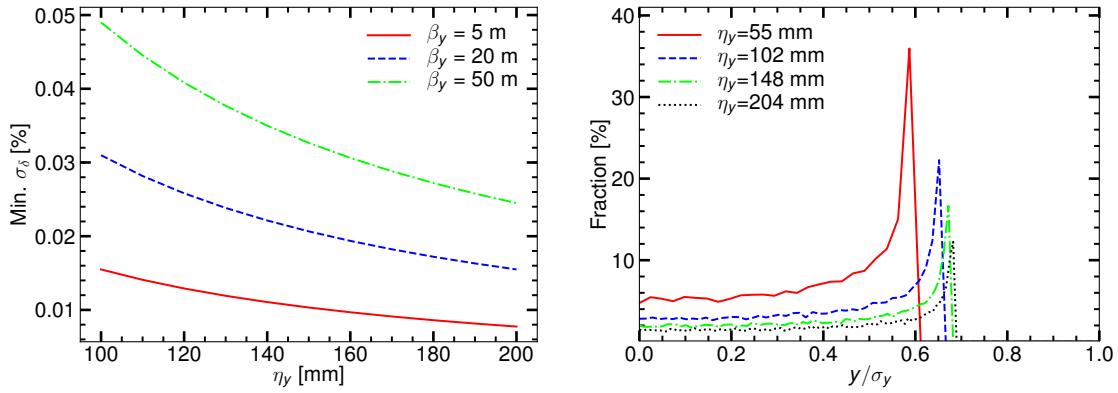

(a) (b)

Fig. 4.18 The minimum distinguishable momentum deviation as a function of the vertical dispersion for three vertical β-function values (a) and the fraction of the vertical displacement resulting from *xy* coupling (b) at the YAG/OTR monitor.

Particles generated in the presence of radiation damping, quantum excitation and BGS were used as input at the entrance of ATF2. For a large vertical dispersion at the YAG/OTR monitor, e.g., 200 mm, the vertical distribution from tracking is then compared with the measured profiles, as presented in Fig. 4.21 (b). One may see that the measured distribution has a higher tail level than the simulation by a factor around 4.

To confirm the negligible impact of the vertical betatron halo, complementary measurements have been performed. Since the vertical betatron halo is related to the vacuum pressure in the damping ring, the vacuum dependence of the vertical profiles with different magnitudes of the vertical dispersion can help to separate the influence of the betatron halo. Increasing the vertical dispersion at the diagnostic point from 50 mm to 200, the vacuum dependence becomes weak and insignificant, as shown in Fig. 4.22. Measurements indicate that it is the momentum distribution but not the vertical betatron distribution that determines the vertical profile for $\eta_{y,\mathrm{YAG}} \approx 200$ mm. Moreover, the insignificant vacuum dependence of the "vertical" profiles measured with a large vertical dispersion is also consistent with the fact that the conjectured momentum tail is not related to the BGS process in the damping ring. Notice that there is no obvious beam tilting or rotation when adjusting the vertical dispersion using QS1X/QS2X skew quadrupoles. Through the comparison of the "vertical" profiles predicted by tracking and measured by the YAG/OTR monitor, and the vacuum dependence for several vertical dispersion values, we could conclude that the "vertical" profile with a vertical dispersion of 200 mm offers a good representation of the momentum distribution.

Concerning the beam profiles shown in Fig. 4.22, the dependence of the "vertical" profile on the vertical dispersion can be presented with and without normalization to the rms beam size, as shown in Fig. 4.23. Without normalizing, the beam distribution becomes broader and tail/halo levels become higher when increasing the vertical dispersion from 50 mm to 200 mm,

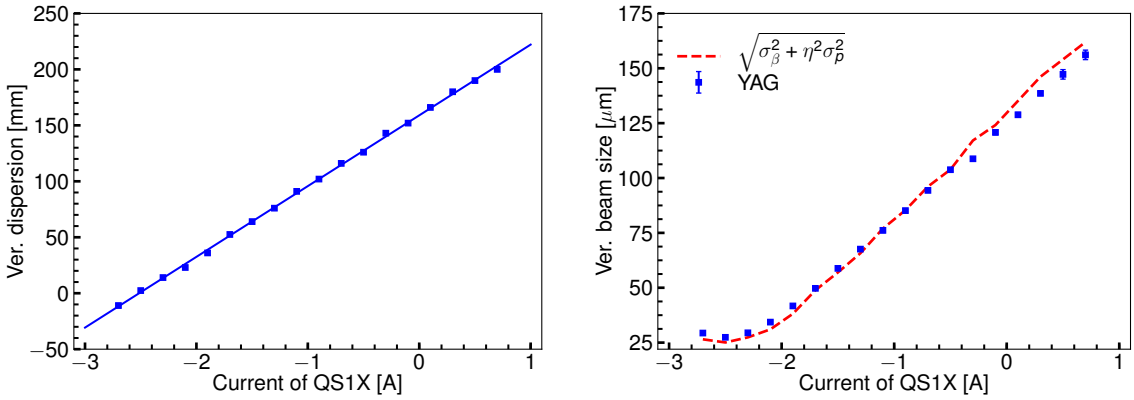

(a) (b)

Fig. 4.19 Manipulation of the vertical dispersion at the YAG/OTR monitor by increasing the current of QS1X/QS2X with a ratio of 1:0.7 (a) and the corresponding vertical beam sizes measured by the YAG screen and predicted based on the vertical betatron beam size, vertical dispersion and the rms energy spread (b). The vertical betatron beam size is assumed to be constant and equal to the minimum vertical beam size ($\eta_y = 0$). Note that the vertical dispersion in the left plot was first corrected to zero using QS1X and QS2X skew quadrupoles.

as shown in Fig. 4.23 (a, c). However, the relative tail/halo level is reduced for a larger vertical dispersion in the normalized coordinate for the vacuum pressures of 2×10^{-7} Pa and 1.2×10^{-7} Pa, as shown in Fig. 4.23 (b, d). Furthermore, the decrease of relative tail/halo level appears more significant for the worsened vacuum pressure. As can be seen in Fig. 4.23, comparing the profiles in the normalized frame for different vertical dispersion values, the momentum tail appears to be relatively lower than the vertical BGS halo in the normalized coordinate.

To uncover the correlation between the momentum distribution, especially the momentum tail, and Touschek scattering, measurements have been carried out for different beam intensities. Considering the difficulty and time to tune the beam with very high intensity (>10^{10} e/pulse), the maximum beam intensity was finally set as 7×10^9 e/pulse. To obtain an adequate SNR, the lower beam intensity was chosen as 2×10^9 e/pulse. The analytical estimations of the Touschek scattering rate have been described in Sec. 2.5.3. After normalizing to the same beam intensity, an increase of the momentum tail by a factor 2.3 for the beam intensity from 2×10^9 e/pulse to 7×10^9 e/pulse was predicted. For a vertical dispersion of 200 mm, dilution of the core part[2] and an increase of the momentum tail has been observed, as shown in Fig. 4.24. Regarding the momentum distribution for a beam intensity of 7×10^9 e/pulse, the momentum tail ranging from $3\sigma_\delta$ to $6\sigma_\delta$ is about 2–3 times larger than that for a beam intensity of 2×10^9 e/pulse[3]. Enhancement of the momentum tail is consistent with the analytical estimations of

[2]The detailed measurements of the energy spread as a function of beam intensity can be found in Ref. [73].

[3]Comparing the profiles for beam intensities of 2×10^9 e/pulse and 4×10^9 e/pulse, the momentum tail in [$3\sigma_\delta$, $6\sigma_\delta$] increases by a factor of around 1.5 which is also in good agreement with the estimations of the Touschek scattering rate.

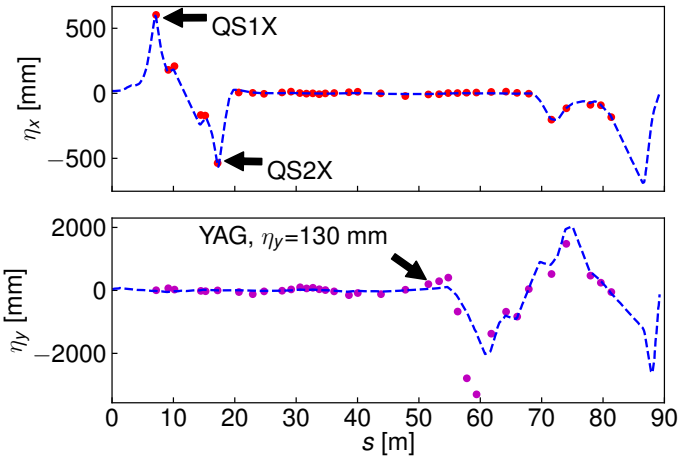

Fig. 4.20 Horizontal (a) and vertical (b) dispersion measured with the Flight Simulator software. The vertical dispersion is produced by adjusting QS1X and QS2X (see description in the text).

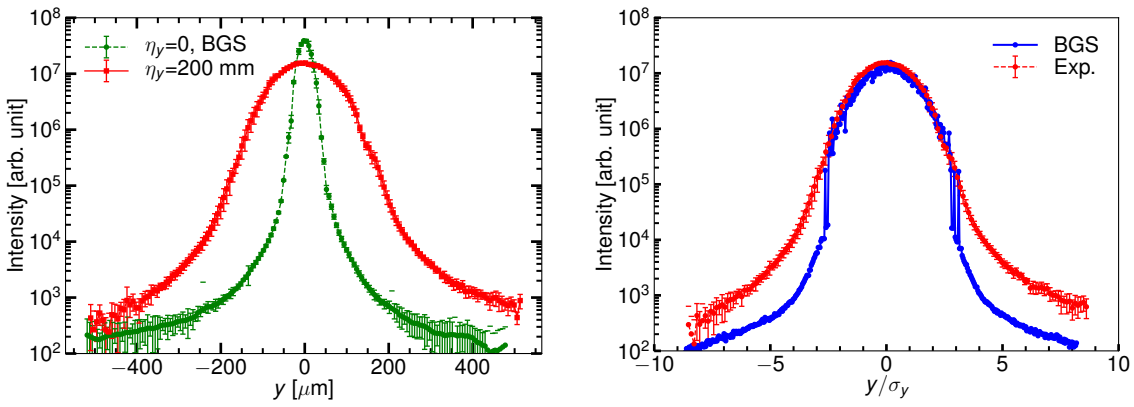

(a) (b)

Fig. 4.21 Vertical beam distribution for vertical dispersions of zero and 200 mm (a) and a comparison of the vertical profiles ($\eta_y = 200$ mm) obtained from measurement and from tracking with BGS (b).

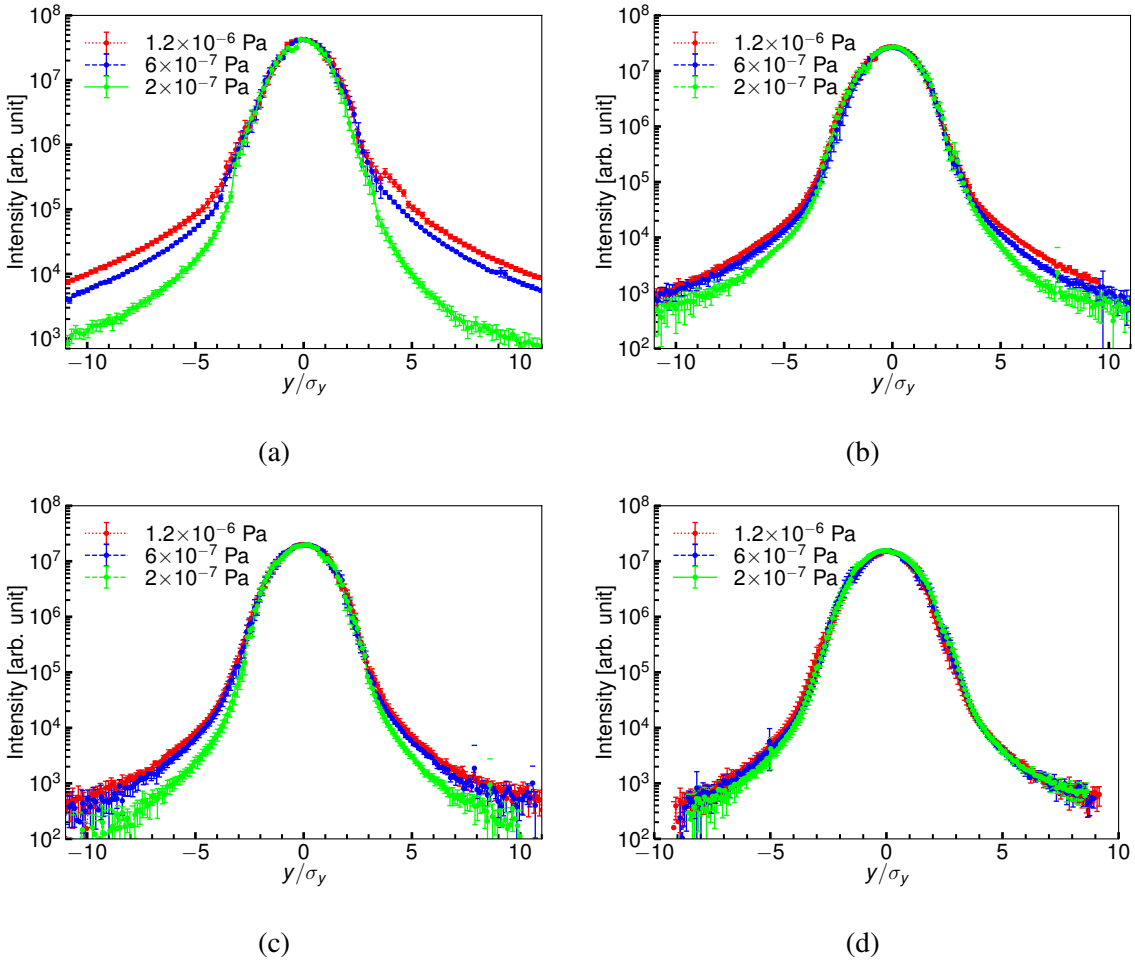

Fig. 4.22 Vertical beam profiles for the vacuum pressures of 2×10^{-7} Pa, 6×10^{-7} Pa and 1.2×10^{-6} Pa in the presence of the vertical dispersion of 50 mm, 100 mm, 150 mm and 200 mm (a-d).

the Touschek scattering rate. This evidence indicates that the strong Touschek scattering might drive a significant momentum tail. However, for a high beam intensity, other collective effects, e.g., potential well distortion, impedance and ions-cloud effects could also become stronger and might contribute to distorting the momentum distribution. Other advanced measurements with a constant beam intensity but involving different Touschek scattering rates would be needed to fully characterize the origin of the momentum tail.

According to the theory of Touschek scattering, manipulation of beam emittances will change the scattering rate at fixed beam intensity. However, as explained in Sec. 2.5.3, The Touschek scattering rate decreases by 50% when the vertical emittance is enlarged from 8 pm to 42 pm, which seems not sufficient to probe experimentally.

Alternatively, the evolution of emittances with respect to the storage time is always common for all the injected beams. Observation of the momentum tail with respect to storage time can provide a sensitive approach to probe a varyingTouschek scattering rate, but with constant beam intensity and COD in the ring. After beam injection, the evolution of emittance as a function of

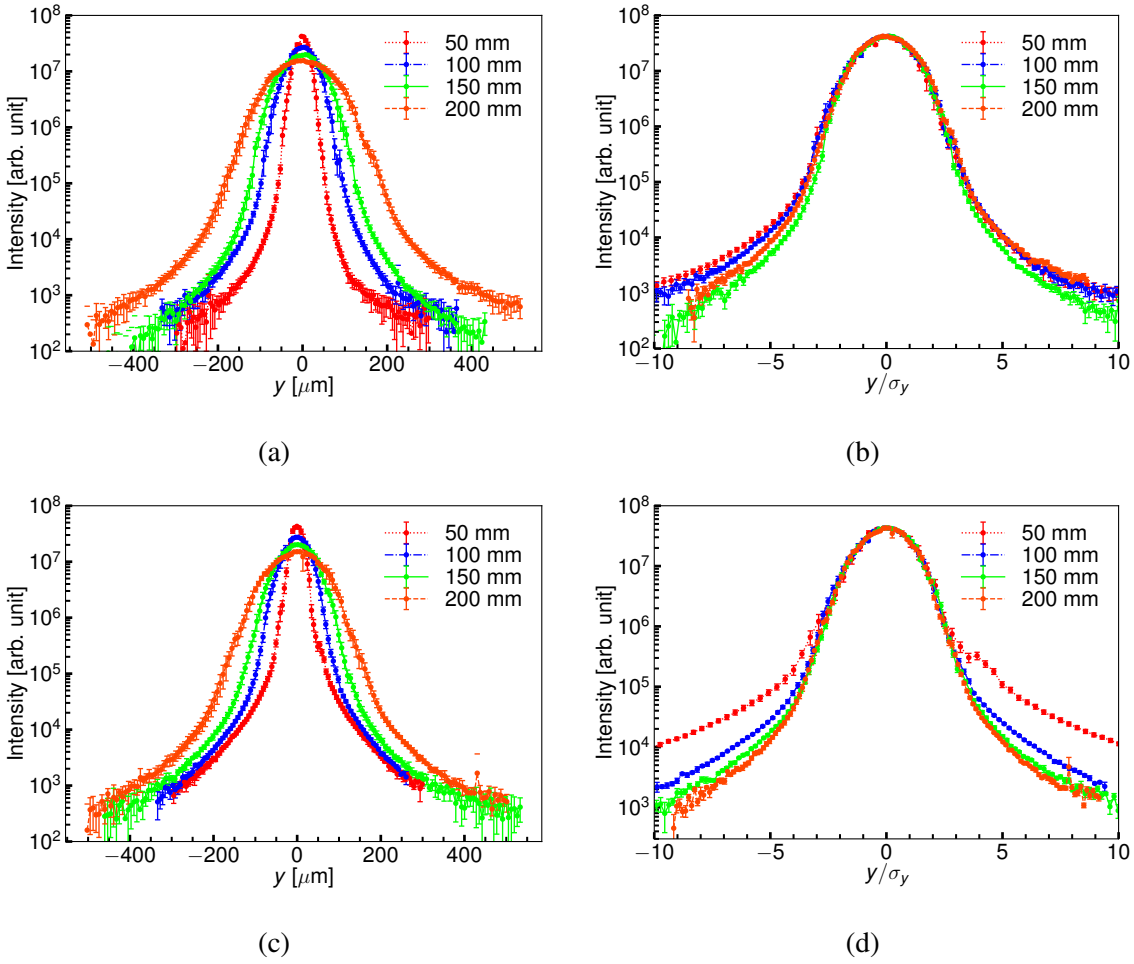

Fig. 4.23 "Vertical" beam profiles for vacuum pressures of 2×10^{-7} Pa (a, b) and 1.2×10^{-6} Pa (c, d) in the presence of the vertical dispersion of 50 mm, 100 mm, 150 mm and 200 mm.

storage time can be approximated analytically by solving the differential equation based on the BM model of IBS (see Sec. 2). The horizontal emittance and energy spread firstly reduce to the respective minimum values at around 50–70 ms, as a result of the synchrotron radiation, and then they start to increase dominated by the boosted IBS diffusion rate in the presence of the smallest horizontal and longitudinal emittances. Because the vertical damping time is longer than the horizontal and longitudinal ones, the vertical emittance keeps on decreasing until reaching the equilibrium state, as shown in Fig. 4.25. Dependence of the energy spread as a function of the storage time has been reported in Ref. [73], where good agreement between measurements and theoretical predictions has been exhibited, see Fig. 4.25 (d). To reproduce these observations, the time dependence of the energy spread in the presence of a large vertical dispersion was measured using the YAG/OTR monitor. The evolution of energy spread versus storage time is found to be similar as the prediction and previous measurement. However, the correlation between energy spread and storage time is not fullly consistent quantitatively between the two measurements, as shown in Fig. 4.25. The reason might be that the adjustment of the vertical dispersion is

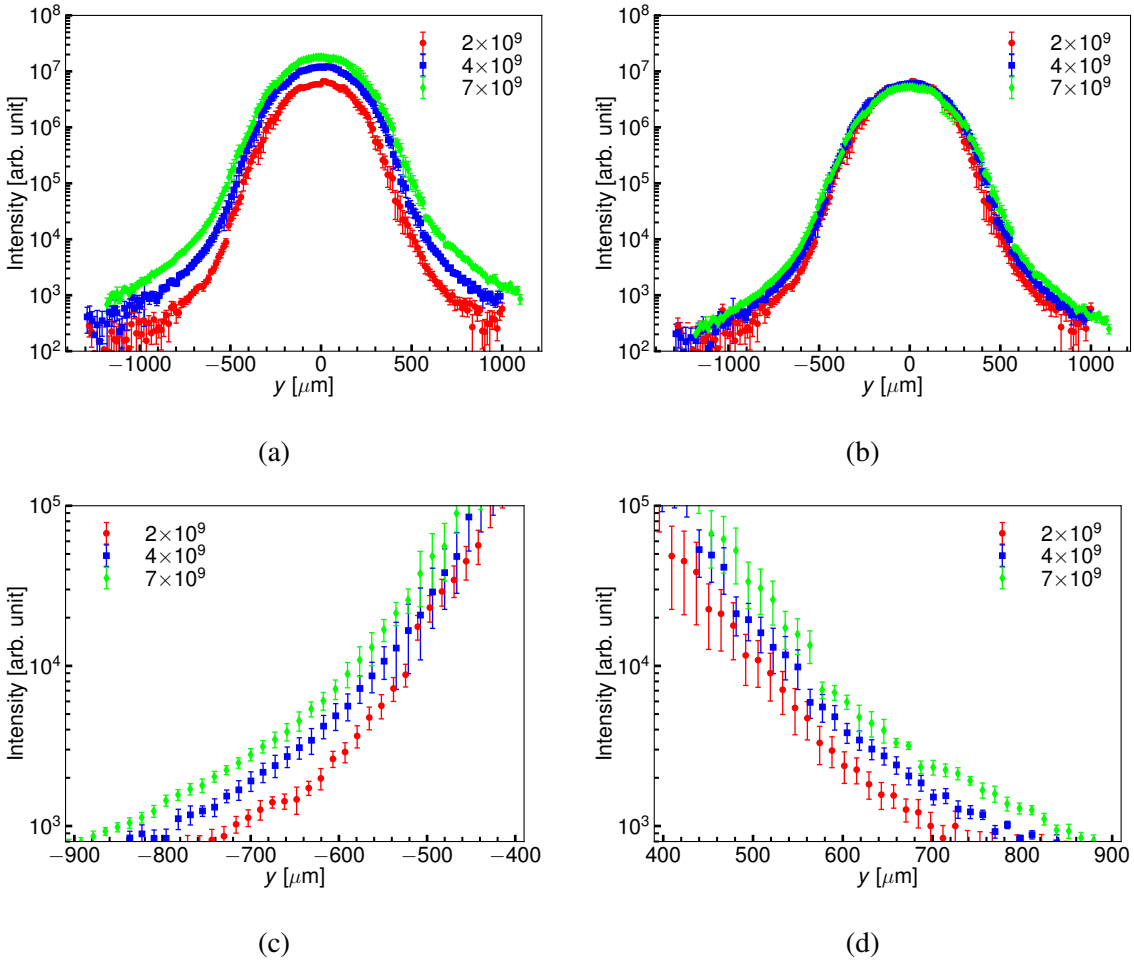

Fig. 4.24 Vertical profiles (momentum distribution) as a function of beam intensity. (a): the actual distributions; (b): normalized to the same beam intensity (2×10^9 e/pulse); (c) and (d): tail distribution on the left and right sides, respectively.

not perfect and the vertical betatron motion may still play a role in the momentum distribution measurements.

Following the preliminary estimations and measurements of energy spread (Fig. 4.25 (d)), measurements of the momentum tail at 120 ms, when the Touschek scattering rate is small, and at 200 ms and 300 ms, when the Touschek scattering rate reaches equilibrium, have been carried out. The momentum distributions at 200 ms and 300 ms are fairly consistent while the rms size (energy spread) and momentum tail at 120 ms appear to be smaller than at 200 ms and 300 ms, as shown in Fig. 4.26. These measurements are qualitatively consistent with the presence of the IBS & Touschek scattering.

Measurements of the intensity and storage time dependence of the momentum tail at ATF2 suggest the relevance of the Touschek scattering process as generating mechanism. Concerning a potential impact on the horizontal phase space distribution, some horizontal halo coupled from the longitudinal phase space can in principle be expected. Intensity dependence of the horizontal halo has been performed and is presented in Fig. 4.27. The horizontal size is enlarged

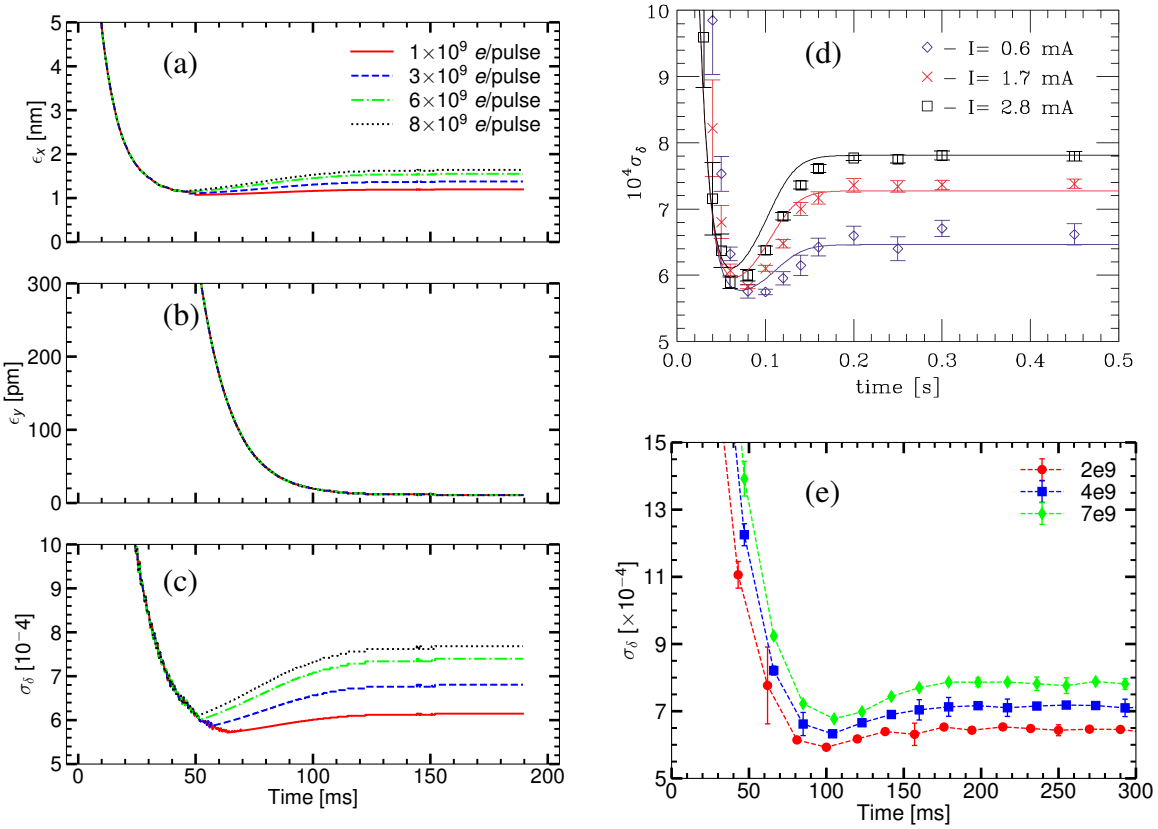

Fig. 4.25 Time dependence of transverse emittance and energy spread. (a–c): analytical approximation of the time dependence of the horizontal emittance, vertical emittance and energy spread, respectively; (d): measured energy spread with respect to the storage time, for three different beam intensities (taken from Ref. [165]); (e): recent measurements of energy spread for different beam intensities.

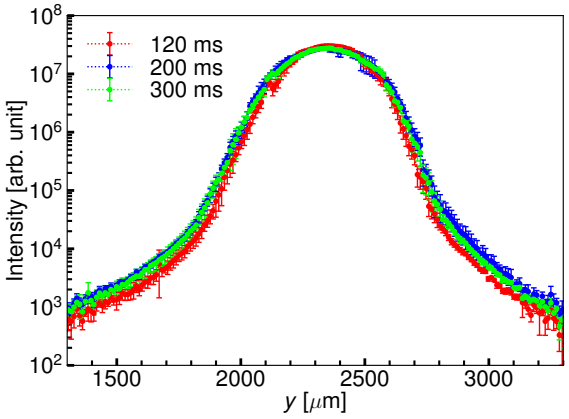

Fig. 4.26 "Vertical" profile (momentum distribution) for three different storage times, 120 ms, 200 ms and 300 ms. Notice that the beam intensity was stabilized at around 7×10^9 e/pulse.

due to the strong IBS diffusion rate and the number of halo particles significantly increases after normalizing to the same beam intensity (1×10^9 e/pulse). These results are consistent with the behaviors of the momentum distribution and further imply that the horizontal halo and the momentum tail are most likely from Touschek scattering.

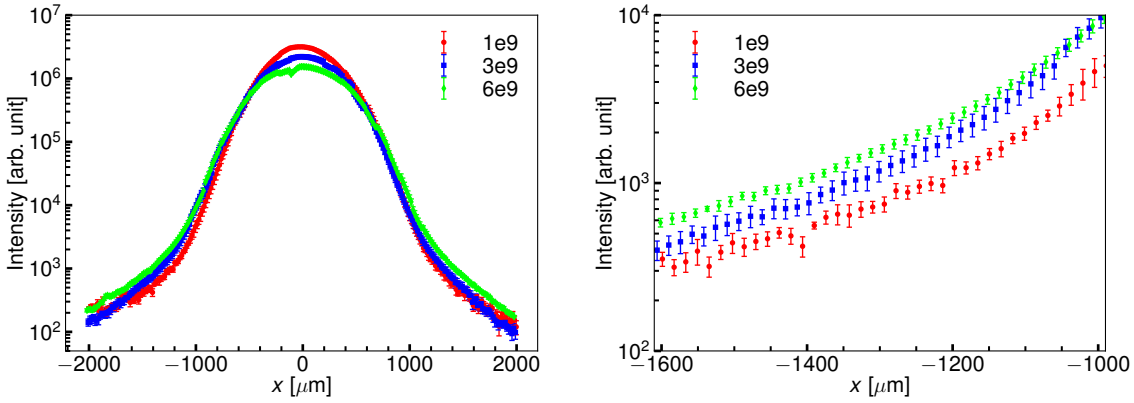

Fig. 4.27 Horizontal distributions for three different beam intensities, 1×10^9 e/pulse, 3×10^9 e/pulse and 6×10^9 e/pulse (a), and the enlarged image clearly showing the halo distributions (b).

Concluding this section, measurements of the momentum distribution have been accomplished based on a novel vertical dispersion manipulation scheme, using the skew quadrupoles located in the inflector. Through the vacuum dependence, intensity dependence and extraction time dependence, the measured momentum distributions have been demonstrated to be qualitatively consistent with the predicted presence of strong Touschek scattering in the ring. The behavior of the horizontal tail/halo, analogous to the momentum tail as a function of beam intensity, also points to Touschek scattering as a likely generating mechanism. To fully prove this, a complete Monte Carlo simulation of the momentum tail from Touschek scattering and its dependence on beam intensity, vacuum pressure and storage time needs to be considered, taking into account the realistic optics of the ring with the necessary errors and corresponding correction strategy.

Chapter 5

Conclusion and Prospects

For the future linear and circular colliders, beam halo is undoubtedly one of the critical issues limiting the performance and causing component damage and activation. Understanding halo formation and distribution is not only a crucial topic related to beam instability but also of great importance for the design of an efficient collimation system to mitigate the unwanted background induced by halo particles. As a successful test facility for the R&D of ILC, the ATF has provided an excellent opportunity to uncover the physical origins of beam halo and to demonstrate powerful diagnostics requiring extremely high dynamic range and sensitivity. In this dissertation, we have presented the theoretical investigation of the primary halo sources at the ATF, followed by the development of the necessary instrumentation for halo measurements. To validate the theoretical predictions, precise experimental measurements have been carried out, and the results have been discussed.

The first set of problems addressed in this thesis are the numerical evaluations of beam halo from beam-gas scattering and Touschek scattering. For the BGS, the analytical approximation based on the Hirata's model [124] has been established and accompanied by a Monte Carlo simulation developed in the context of the SAD program. In the simulation, the actual COD and the realistic equilibrium emittances have been approached by introducing local orbit bumps using the steering magnets of the damping ring. We have attempted to benchmark the simulation of BGS using the vacuum lifetime, which was found to be more than 80 minutes by the two numerical methods but was measured close to 16 minutes. The reasons for this discrepancy may be the presence of additional halo particles from other sources and the reduced dynamic aperture due to the non-linear magnetic fields present in the lattice. The two numerical evaluations predict a considerable population of halo particles arising from BGS and their vacuum dependence which is further used to determine whether the beam halo is dominated by BGS or not. To establish a scenario for halo generation from Touschek scattering, the dynamics of Coulomb scattering between two particles has been described. Through a Monte Carlo simulation using the modified SIRE code, emittance growth due to IBS has been predicted and found to be consistent with the analytical estimation based on the BM model (in SAD). To further explore the possibility of

momentum tail and horizontal tail/halo induced by Touschek scattering, preliminary estimations of the Touschek scattering rate have been performed. Dependences of the Touschek scattering rate on the beam intensity and the vertical emittance in the presence of emittance dilution from IBS have been compared. The results are later employed for the experimental verification of the influence of Touschek scattering on the generation of a momentum tail.

To achieve a sufficient dynamic range required for the halo measurements, a set of diamond sensor detectors have been developed and installed at ATF2 in 2015. The initial linear dynamic range was found to be around 10^4 limited by the pick-up signal, charge collection saturation in the diamond crystal and the instantaneous voltage drop at the signal collection resistor. To expand the dynamic range of this DS detector, a "self-calibration" method has been proposed and implemented to reconstruct the core profile thanks to the wire scanner located just behind the IP. After such a correction, the effective DNR is increased to beyond 10^5 which is sufficient for accurate beam halo measurements. To obtain the simultaneous diagnostics and confirm the observations given by the DS detector, a new YAG/OTR monitor has been developed in collaboration with KEK and CERN instrumentation experts and installed in the extraction section. This monitor mainly consists of 4 ceramic 0.5 mol% Ce:YAG screens with a central quadrilateral hole and an OTR target on a holder, a microscope lens, and a 16-bit sCMOS camera with a low noise level. The background level for experimental operation has been demonstrated to be less than 1 electron per pixel while the upper limit of the light signal is determined by the saturation of the scintillation for local charge densities above 16–18 fC/μm^2. The linear dynamic range for 2D beam profile imaging using only the YAG monitor has been demonstrated to be above 10^5 which can be further extended by a combination of images from YAG and OTR screens. Moreover, the spatial resolution of the YAG/OTR monitor is less than 10 μm using both YAG and OTR screens, which is fully consistent with the design goals and nominal beam size at the detector.

For the vertical beam halo, based on a satisfactory agreement between the numerical predictions in the presence of BGS and the measurements obtained by the YAG/OTR monitor and DS detector, together with a significant vacuum dependence, we have concluded that BGS dominates the vertical beam halo. The vertical emittance growth due to BGS has been observed at the ATF for the first time thanks to the XSR monitor. However, the horizontal halo was found to be higher than the predictions based on BGS. To reveal the origin of the observed horizontal halo, the influence of the chromaticity and other aberration in the final focus and extraction sections have been studied. Measurements show that the above effects can only induce some slight enhancements to the horizontal halo and asymmetry in the horizontal distribution. To study the possible presence of a momentum tail and horizontal tail/halo from Touschek scattering, a novel scheme to increase the vertical dispersion in the extraction, using two skew quadrupoles in the inflector, has been proposed and validated. For reasonable currents of the two skew quadrupoles, a vertical dispersion up to 200 mm at the YAG/OTR monitor could be achieved. Subsequently, the momentum distribution was found to be qualitatively consistent

with the presence of Touschek scattering, considering its significant intensity dependence and its evolution with respect to the storage time. Moreover, the horizontal tail/halo increases also for the higher beam intensity which indicates the possible influence from Touschek scattering. To further clarify these observations, comparisons with Monte Carlo simulations of beam distortion due to Touschek scattering are currently underway.

Further investigations of the beam halo at ATF, should include the following aspects:

1. Improvement of the performance of the diagnostics. To increase the dynamic range of the DS detector, suppressing the pick-up signal by optimizing the layout of the in-vacuum elements and applying an efficient the RF shielding, and preventing the instantaneous voltage drop at the charge collection resistor should be considered. Concerning the YAG/OTR monitor, its dynamic range for both 1D and 2D images can be further extended by combining the images from the OTR screen (core part) and YAG screen (halo part) using an efficient algorithm.

2. It is of great importance to develop an analytical estimation and a Monte Carlo simulation of the tail/halo driven by the Touschek scattering in the presence of the synchrotron radiation and IBS. The analytic approximations could consider the Fokker-Planck equation or follow the derivation of the beam distortion used to model BGS. A Monte Carlo simulation, which is currently under development, will include both IBS and Toushek scattering. Furthermore, it will be great to take into account other collective effects, for example the potential-well distortion, to quantify the scattering rate precisely.

3. Comparison of the measured momentum and horizontal distributions with the simulations will be necessary to confirm the contribution of Touschek scattering, of course after the development of the simulation described above. If it is possible, an optimized algorithm to manipulate the vertical dispersion with realistic optics and dispersion will be very interesting and useful. Further experimental investigation of the momentum tail and horizontal tail/halo to provide an accurate halo model in the three degrees of freedom is strongly recommended.

Exploring these topics will not only deepen the understanding of the beam halo formation, which is essential for the future colliders, but also expand the knowledge of IBS&Touschek scattering, which is important for the low-emittance storage rings.

References

[1] V. Abazov, B. Abbott, M. Abolins, B. Acharya, M. Adams, T. Adams, et al. Measurement of the W boson mass. *Phys. Rev. Lett.*, 103(14):141801, 2009.

[2] V. Abazov, B. Abbott, M. Abolins, B. Acharya, M. Adams, T. Adams, et al. Search for W boson resonances decaying to a top quark and a bottom quark. *Phys. Rev. Lett.*, 100(21):211803, 2008.

[3] M. Ciccolini, A. Denner, and S. Dittmaier. Strong and electroweak corrections to the production of a higgs boson+ 2 jets via weak interactions at the large hadron collider. *Phys. Rev. Lett.*, 99(16):161803, 2007.

[4] O. Brüning. *Large Hadron Collider Design Report*. European Organization for Nuclear Research, 2004.

[5] https://home.cern/fr/about/updates/2017/06/lhc-racks-records. 2017.

[6] P. Higgs. Broken Symmetries and the Masses of Gauge Bosons. *Phys. Rev. Lett.*, 13:508–509, 1964.

[7] S. Weinberg. A model of leptons. *Phys. Rev. Lett.*, 19(21):1264, 1967.

[8] M. Veltman et al. Regularization and renormalization of gauge fields. *Nuclear Physics B*, 44(1):189–213, 1972.

[9] H. Haber and G. Kane. The search for supersymmetry: probing physics beyond the standard model. *Physics Reports*, 117(2-4):75–263, 1985.

[10] G. Aad, T. Abajyan, B. Abbott, J. Abdallah, S. Khalek, A. Abdelalim, et al. Observation of a new particle in the search for the Standard Model Higgs boson with the ATLAS detector at the LHC. *Phys. Lett. B*, 716(1):1–29, 2012.

[11] V. E. Barnes, P. L. Connolly, D. J. Crennell, B. B. Culwick, W. C. Delaney, W. B. Fowler, et al. Observation of a hyperon with strangeness minus three. *Phys. Rev. Lett.*, 12:204–206, 1964.

[12] E. D. Bloom, D. H. Coward, H. DeStaebler, J. Drees, G. Miller, L. Mo, et al. High-energy inelastic e-p scattering at 6° and 10°. *Phys. Rev. Lett.*, 23:930–934, 1969.

[13] M. Breidenbach, J. I. Friedman, H. W. Kendall, E. D. Bloom, D. H. Coward, H. DeStaebler, et al. Observed behavior of highly inelastic electron-proton scattering. *Phys. Rev. Lett.*, 23:935–939, 1969.

[14] J. J. Aubert, U. Becker, P. J. Biggs, J. Burger, M. Chen, G. Everhart, et al. Experimental observation of a heavy particle j. *Phys. Rev. Lett.*, 33:1404–1406, 1974.

[15] J. E. Augustin, A. M. Boyarski, M. Breidenbach, F. Bulos, J. T. Dakin, G. J. Feldman, et al. Discovery of a Narrow Resonance in e^+e^- Annihilation. *Phys. Rev. Lett.*, 33:1406–1408, 1974.

[16] M. L. Perl, G. S. Abrams, A. M. Boyarski, M. Breidenbach, D. D. Briggs, Bulos F., et al. Evidence for Anomalous Lepton Production in $e^+ - e^-$ Annihilation. *Phys. Rev. Lett.*, 35:1489–1492, 1975.

[17] S. W. Herb, D. C. Hom, L. M. Lederman, J. C. Sens, H. D. Snyder, J. K. Yoh, et al. Observation of a Dimuon Resonance at 9.5 GeV in 400-GeV Proton-Nucleus Collisions. *Phys. Rev. Lett.*, 39:252–255, 1977.

[18] D. P. Barber, U. Becker, H. Benda, A. Boehm, J. G. Branson, Bron J., et al. Discovery of Three-Jet Events and a Test of Quantum Chromodynamics at PETRA. *Phys. Rev. Lett.*, 43:830–833, 1979.

[19] S. Abachi, B. Abbott, M. Abolins, B. S. Acharya, I. Adam, D. L. Adams, et al. Observation of the Top Quark. *Phys. Rev. Lett.*, 74:2632–2637, 1995.

[20] M. Moanmad Kassem AyoubM. *Search of the Standard Model Higgs boson decaying into two lepton taus with the Run2 data of ATLAS detector in LHC*. PhD thesis, 2016.

[21] H. Hahn, E. Forsyth, H. Foelsche, M. Harrison, J. Kewisch, Parzen, et al. The rhic design overview. *Nucl. Instrum. Methods Phys. Res., Sect. A*, 499(2-3):245–263, 2003.

[22] N. Phinney, N. Toge, and N. Walker. ILC reference design report volume 3-accelerator. *arXiv preprint arXiv:0712.2361*, 2007.

[23] M. Aicheler, P. Burrows, M. Draper, T. Garvey, P. Lebrun, K. Peach, et al. A Multi-TeV linear collider based on CLIC technology: CLIC Conceptual Design Report. Technical report, SLAC National Accelerator Lab., Menlo Park, CA (United States), 2014.

[24] M. Benedikt and F. Zimmermann. Future circular colliders. *Future Research Infrastructures: Challenges and Opportunities*, 194:73, 2016.

[25] CEPC-SPPC Study Group et al. CEPC-SPPC Preliminary Conceptual Design Report, Volume II-Accelerator. *IHEP, Beijing, China, Rep. IHEP-AC-2015-01*, 2015.

[26] Jonathan L Feng. Physics at e+e- colliders. *International Journal of Modern Physics A*, 15(16):2355–2364, 2000.

[27] T. Behnke et al. ILC TDR and DBD. *ILC-Report-2013-040. http://www. linearcollider. org/ILC/Publications/Technical-Design-Report*, 2013.

[28] M. Zobov, D. Alesini, M. Biagini, C. Biscari, A. Bocci, R. Boni, M. Boscolo, et al. Test of "Crab-Waist" Collisions at the DA Φ NE Φ Factory. *Phys. Rev. Lett.*, 104(17):174801, 2010.

[29] K. Hirata. Analysis of beam-beam interactions with a large crossing angle. *Phys. Rev. Lett.*, 74(12):2228, 1995.

[30] W. Herr and B. Muratori. Concept of luminosity. 2006.

[31] V. Shiltsev, Y. Alexahin, V. Lebedev, P. Lebrun, R. Moore, T. Sen, et al. Beam-beam effects in the Tevatron. *Phys. Rev. ST Accel. Beams*, 8(10):101001, 2005.

[32] M. Furman. Hourglass effects for asymmetric colliders. Technical report, Lawrence Berkeley Lab., CA (USA), 1991.

[33] TO. Raubenheimer and F. Zimmermann. Final-focus systems in linear colliders. *Rev. of Modern Phys.*, 72(1):95, 2000.

[34] J. Sekutowicz, K. Ko, L. Ge, L. Lee, Z. Li, C. Ng, et al. Design of a Low Loss SRF Cavity for the ILC. In *PAC2005*, pages 3342–3344. IEEE, 2005.

[35] A. Yamamoto and PM ILC-GDE. Global R&D Effort for the ILC SC Linac Technology. 2008.

[36] F. Hinode. ATF design and study report. *KEK Internal*, 1995.

[37] A. Grudiev and W. Wuensch. Design of an X-band accelerating structure for the CLIC main linac. Technical report, 2008.

[38] I. Wilson and W. Wuensch. The CLIC Main Linac Accelerating Structure. *arXiv preprint physics/0008101*, 2000.

[39] G. Geschonke and A. Ghigo. CTF3 design report. Technical report, 2002.

[40] E. Jensen. CTF3 Drive Beam Accelerating Structures. Technical report, 2002.

[41] R. Tomás, H. Braun, J. Delahaye, E. Marn, D. Schulte, F. Zimmermann, et al. ATF2 ultra-low IP betas proposal. In *PAC09*, page WE6PFP024. Triumf Vancouver, 2009.

[42] E. Marin, R. Tomás, P. Bambade, K. Kubo, T. Okugi, T. Tauchi, et al. Design and high order optimization of the Accelerator Test Facility lattices. *Phys. Rev. ST Accel. Beams*, 17(2):021002, 2014.

[43] M. Patecki and R. Tomás. Effects of quadrupole fringe fields in final focus systems for linear colliders. *Phys. Rev. ST Accel. Beams*, 17(10):101002, 2014.

[44] http://clic-study.web.cern.ch.

[45] I. Agapov, H. Burkhardt, D. Schulte, A. Latina, G. Blair, S. Malton, et al. Tracking studies of the Compact Linear Collider collimation system. *Phys. Rev. ST Accel. Beams*, 12(8):081001, 2009.

[46] R. Assmann, J. Jeanneret, R. Schmidt, J. Wenninger, G. Burtin, M. Hayes, et al. Requirements for the LHC collimation system. Technical report, 2002.

[47] J. Resta Lopez. Design and performance evaluation of nonlinear collimation systems for CLIC and LHC. Technical report, 2007.

[48] K. Bane, Leopold F., C. Adolphsen, F. Decker, P. Emma, P. Krejcik, et al. Measurement of the Effect of Collimator Generated Wakefields on the Beams in the SLC. In *PAC1995*, volume 5, pages 3031–3033. IEEE, 1995.

[49] C. Assmann. Collimators and beam absorbers for cleaning and machine protection. 2005.

[50] W. Scandale, D. Still, A. Carnera, G. Della Mea, D. De Salvador, R. Milan, et al. High-efficiency volume reflection of an ultrarelativistic proton beam with a bent silicon crystal. *Phys. Rev. Lett.*, 98(15):154801, 2007.

[51] G. Stancari et al. Collimation with hollow electron beams. *Phys. Rev. Lett.*, 107(8):084802, 2011.

[52] W. Scandale, A. Vomiero, S. Baricordi, P. Dalpiaz, M. Fiorini, V. Guidi, et al. High-efficiency deflection of high-energy protons through axial channeling in a bent crystal. *Phys. Rev. Lett.*, 101(16):164801, 2008.

[53] F. Zimmermann et al. Lecture Notes for Accelerator Physics and Technologies for Linear Colliders. *University of Chicago, Physics*, 575, 2002.

[54] R. Yang, T. Naito, S. Bai, A. Aryshev, K. Kubo, T. Okugi, et al. Evaluation of beam halo from beam-gas scattering at the KEK Accelerator Test Facility. *Phys. Rev. Accel. and Beams*, 21(5):051001, 2018.

[55] H. Burkhardt, I. Reichel, and G. Roy. Transverse beam tails due to inelastic scattering. *Phys. Rev. ST Accel. Beams*, 3(9):091001, 2000.

[56] RW. Assmann, F. Zimmermann, F. Schmidt, and M. Zorzano-Mier. Equilibrium beam distribution and halo in the LHC. Technical report, 2002.

[57] A. Fedotov. Beam halo formation in high-intensity beams. *Nucl. Instrum. Methods Phys. Res., Sect. A*, 557(1):216–219, 2006.

[58] D. Shatilov. Beam-beam simulations at large amplitudes and lifetime determination. *Part. Accel.*, 52:65–93, 1996.

[59] CK. Allen et al. Beam-halo measurements in high-current proton beams. *Phys. Rev. Lett.*, 89(21):214802, 2002.

[60] T. Wangler et al. Beam-halo in mismatched proton beams. *Nucl. Instrum. Methods Phys. Res., Sect. A*, 519(1):425–431, 2004.

[61] O. Tanaka, N. Nakamura, M. Shimada, T. Miyajima, A. Ueda, T. Obina, et al. New halo formation mechanism at the KEK compact energy recovery linac. *Phys. Rev. Accel. and Beams*, 21(2):024202, 2018.

[62] J. Qiang, P. Colestock, D. Gilpatrick, H. Smith, T. Wangler, and M. Schulze. Macroparticle simulation studies of a proton beam halo experiment. *Phys. Rev. ST Accel. Beams*, 5(12):124201, 2002.

[63] M. Ikegami, S. Machida, and T. Uesugi. Particle-core analysis of dispersion effects on beam halo formation. *Phys. Rev. ST Accel. Beams*, 2(12):124201, 1999.

[64] J. O'Connell, T. Wangler, R. Mills, and K. Crandall. Beam halo formation from space-charge dominated beams in uniform focusing channels. In *PAC1993*, pages 3657–3659. IEEE, 1993.

[65] I. Hofmann and O. Boine-Frankenheim. Space-Charge Structural Instabilities and Resonances in High-Intensity Beams. *Phys. Rev. Lett.*, 115(20):204802, 2015.

[66] P. Tenenbaum, TO. Raubenheimer, and M. Woodley. Sources of beam halo in the Next Linear Collider main linac. In *Proceedings of PAC 2001, Chicago, USA*, pages 3843–3845.

[67] A. Ignatenko. *Development of Beam Halo Monitors for the European XFEL using radiation hard sensors and demonstration of the technology at FLASH*. PhD thesis, BTU Cottbus-Senftenberg, 2015.

[68] K. Wittenburg. Beam halo and bunch purity monitoring. *CERN Accelerator School 2009-005*, page pp. 557, 2009.

[69] B. Grishanov, P. Logachev, F. Podgorny, V. Telnov, D. Angal-Kalinin, R. Appleby, et al. ATF2 proposal. 2005.

[70] K. Kubo. Beam development in ATF damping ring. 1998.

[71] A. Wolski, J. Gao, and S. Guiducci. Configuration studies and recommendations for the ILC damping rings. 2006.

[72] Y. Papaphilippou, L. Rinolfi, E. Koukovini, A. Vivoli, A. Bernhard, S. Calatroni, et al. Conceptual design of the CLIC damping rings. In *Conf. Proc.*, volume 1205201, page TUPPC086, 2012.

[73] K. Kubo et al. Extremely Low Vertical-Emittance Beam in the Accelerator Test Facility at KEK. *Phys. Rev. Lett.*, 88:194801, Apr 2002.

[74] Y. Honda et al. Achievement of ultralow emittance beam in the accelerator test facility damping ring. *Phys. Rev. Lett.*, 92(5):054802, 2004.

[75] P. Raimondi and A. Seryi. Novel final focus design for future linear colliders. *Phys. Rev. Lett.*, 86(17):3779, 2001.

[76] P. Bambade, M. Pons, J. Amann, D. Angal-Kalinin, R. Apsimon, S. Araki, et al. Present status and first results of the final focus beam line at the KEK Accelerator Test Facility. *Phys. Rev. ST Accel. Beams*, 13(4):042801, 2010.

[77] M. Woodley. ATF2 Measurement: Extraction Tuning and Matching. *ICFA Beam Dyn. Newslett.*, 61:36–49, 2013.

[78] T. Okugi et al. Linear and second order optics corrections for the KEK Accelerator Test Facility final focus beam line. *Phys. Rev. ST Accel. Beams*, 17(2):023501, 2014.

[79] A. Faus-Golfe, D. McCormick, J. Resta-López, E. Marín, C. Blanch Gutierrez, J. Alabau-Gonzalvo, et al. Upgrade and systematic measurement campaign of the ATF2 multi-OTR system. 2013.

[80] Y. Kim, R. Ainsworth, A. Aryshev, S. Boogert, G. Boorman, J. Frisch, et al. Cavity beam position monitor system for the Accelerator Test Facility 2. *Phys. Rev. ST Accel. Beams*, 15(4):042801, 2012.

[81] G. White et al. Experimental validation of a novel compact focusing scheme for future energy-frontier linear lepton colliders. *Phys. Rev. Lett.*, 112(3):034802, 2014.

[82] G. White. ATF2 Optics Design. *ICFA Beam Dyn. Newslett.*, 61:26–36, 2013.

[83] S. Kuroda, ATF2 Collaboration, et al. ATF2 for final focus test beam for future linear colliders. *Nuclear and Particle Physics Proceedings*, 273:225–230, 2016.

[84] T. Shintake. Proposal of a nanometer beam size monitor for e+ e- linear colliders. *Nucl. Instrum. Methods Phys. Res., Sect. A*, 311(3):453–464, 1992.

[85] T. Suehara, M. Oroku, T. Yamanaka, H. Yoda, T. Nakamura, Y. Kamiya, et al. A nanometer beam size monitor for ATF2. *Nucl. Instrum. Methods Phys. Res., Sect. A*, 616(1):1–8, 2010.

[86] J. Yan et al. Measurement of nanometer electron beam sizes with laser interference using Shintake Monitor. *Nucl. Instrum. Methods Phys. Res., Sect. A*, 740:131–137, 2014.

[87] N. Fuster-Martínez, T. Tauchi, F. Toral, S. Wallon, A. Faus-Golfe, N. Terunuma, et al. Commissioning and First Performance Studies of a Single Vertical Beam Halo Collimation System at ATF2. In *IPAC 2016, Busan, Korea*, 2016.

[88] P. Cameron and K. Wittenburg. Halo diagnostics summary. In *AIP Conference Proceedings*, volume 693, pages 103–107. AIP, 2003.

[89] T. Shea and P. Cameron. Halo diagnostics overview. In *AIP Conference Proceedings*, volume 693, pages 9–13. AIP, 2003.

[90] R. Valdiviez, F. Martinez, A. Rendon, T. Wright, J. Ledford, N. Patterson, et al. The Final Mechanical Design, Fabrication, and Commissioning of a Wire Scanner and Scraper Assembly for Halo-Formation Measurements in a Proton Beam. In *PAC 2001*, volume 2, pages 1324–1326. IEEE, 2001.

[91] T. Wangler, C. Allen, K. Chan, P. Colestock, K. Crandall, R. Garnett, et al. Experimental study of proton-beam halo induced by beam mismatch in LEDA. In *PAC2001*, volume 4, pages 2923–2925. IEEE, 2001.

[92] T. Mitsuhashi. Beam halo observation by coronagraph. *proceedings of DIPAC2005, Lyon, France*, 2005.

[93] C. Welsch, E. Bravin, B. Burel, T. Lefèvre, T. Chapman, and M. Pilon. Alternative techniques for beam halo measurements. *Measurement Science and Technology*, 17(7):2035, 2006.

[94] H. Zhang, R. Fiorito, A. Shkvarunets, R. Kishek, and C. Welsch. Beam halo imaging with a digital optical mask. *Phys. Rev. ST Accel. Beams*, 15(7):072803, 2012.

[95] T. Lefevre, A. Perrot, E. Bravin, H. Braun, R. Corsini, and D. Schulte. Beam halo monitoring at CTF3. Technical report, 2004.

[96] C. Welsch, E. Bravin, T. Lefèvre, T. Chapman, B. Burel, and M. Pilon. High dynamic range beam profile measurements. Technical report, 2006.

[97] H. Aoyagi, Y. Asano, T. Itoga, N. Nariyama, T. Bizen, T. Tanaka, et al. Pulse-mode measurement of electron beam halo using diamond-based detector. *Phys. Rev. ST Accel. Beams*, 15(2):022801, 2012.

[98] H. Aoyagi, Y. Asano, T. Itoga, N. Nariyama, T. Bizen, K. Fukami, et al. Electron beam halo monitor for a compact x-ray free-electron laser. *Phys. Rev. ST Accel. Beams*, 16(3):032802, 2013.

[99] P. Cameron. Tune-Based Halo Diagnostics. In *AIP Conference Proceedings*, volume 693, pages 118–121. AIP, 2003.

[100] K. Wittenburg et al. Overview of recent halo diagnosis and non-destructive beam profile monitoring. In *Proc 39th ICFA Advanced Beam Dynamics Workshop on High Intensity High Brightness Hadron Beams, HB2006*, volume 29, 2006.

[101] M. Yoshimoto, K. Okabe, M. Kinsho, and H. Harada. Beam halo measurement using a combination of a wire scanner type beam scraper and some beam loss monitors in J-PARC 3-GeV RCS. 2015.

[102] S. Liu, P. Bambade, A. Faus-Golfe, N. Fusster-Martinez, S. Bai, J. Gao, et al. Beam halo measurements using wire scanners at ATF2. In *IPAC'14*, pages 3445–3448, 2014.

[103] S. Arutunian, N. Dobrovolski, M. Mailian, I. Sinenko, and I. Vasiniuk. Vibrating wire for beam profile scanning. *Phys. Rev. ST Accel. Beams*, 2:122801, Dec 1999.

[104] S. Arutunian, N. Dobrovolski, M. Mailian, and I. Vasiniuk. Vibrating wire scanner: First experimental results on the injector beam of the Yerevan synchrotron. *Phys. Rev. ST Accel. Beams*, 6(4):042801, 2003.

[105] S. Arutunian, M. Mailian, and K. Wittenburg. Vibrating wires for beam diagnostics. *Nucl. Instrum. Methods Phys. Res., Sect. A*, 572(3):1022–1032, 2007.

[106] S. Arutunian, A. Avetisyan, M. Davtyan, G. Harutyunyan, I. Vasiniuk, M. Chung, and V. Scarpine. Large aperture vibrating wire monitor with two mechanically coupled wires for beam halo measurements. *Phys. Rev. ST Accel. Beams*, 17(3):032802, 2014.

[107] J. Gilpatrick. Wide Dynamic-Range Beam-Profile Instrumentation For A Beam-Halo Measurement: Description And Operation. In *AIP Conference Proceedings*, volume 693, pages 122–125. AIP, 2003.

[108] A. Freyberger. Large dynamic range beam profile measurements. In *PAC2003*, volume 4, pages 2565–2567. IEEE, 2003.

[109] T. Mitsuhashi, E. Bravin, O. Jones, F. Roncarolo, H. Schmickler, and G. Trad. Design of Coronagraph for the Observation of Beam Halo at LHC. In *IBIC2015*, pages 288–292. JACOW, Geneva, Switzerland, 2016.

[110] T. Mitsuhashi, G. Trad, E. Bravin, and F. Roncarolo. First Observation of the LHC Beam Halo Using a Synchrotron Radiation Coronagraph. 2017.

[111] Y. Hashimoto, H. Akino, T. Toyama, Y. Omori, T. Mitsuhashi, H. Sakai, et al. Two-dimensional and wide dynamic range profile monitor using OTR/fluorescence screens for diagnosing beam halo of intense proton beams. 2015.

[112] G. Sims and M. Denton. Characterization of a charge-injection-device camera system as a multichannel spectroscopic detector. *Optical Engineering*, 26(10):261008, 1987.

[113] T. Mitsuhashi. Coronagraph for diagnosing beam halo. In *Workshop on Beam Halo Monitoring*, 2014.

[114] H. Zhang. *Experimental study of beam halo in intense charged particle beams*. PhD thesis, University of Maryland, College Park, 2014.

[115] G. Haouat, N. Pichoff, C. Couillaud, J. Di Crescenzo, S. Joly, S. Sequin, and S. Striby. Experimental study of the ELSA electron-beam halo. In *AIP Conference Proceedings*, volume 333, pages 245–251. AIP, 1995.

[116] G. Haouat, N. Pichoff, C. Couillaud, J. De Brion, J. Di Crescenzo, S. Joly, et al. Halo of a high-brightness electron beam. In *PAC1995*, volume 5, pages 3170–3172. IEEE, 1995.

[117] L. Fernandez-Hernando, D. Chong, R. Gray, C. Ilgner, A. Macpherson, A. Oh, et al. Development of a CVD diamond beam condition monitor for CMS at the Large Hadron Collider. *Nucl. Instrum. Methods Phys. Res., Sect. A*, 552(1-2):183–188, 2005.

[118] S. Liu et al. In vacuum diamond sensor scanner for beam halo measurements in the beam line at the KEK Accelerator Test Facility. *Nucl. Instrum. Methods Phys. Res., Sect. A*, 832:231–242, 2016.

[119] K. Satou, N. Hayashi, S. Lee, and T. Toyama. A prototype of residual gas ionization profile monitor for J-PARC RCS. *Proceedings of EPAC06, Edinburgh, UK, TUPCH065*, 2006.

[120] H. Harada, K. Yamamoto, and M. Yoshimoto. Upgrade of ionization profile monitor (IPM) in the J-PARC 3-GeV RCS. *IPAC'12*, 12:840, 2012.

[121] H. Harada, S. Kato, and K. Yamamoto. Ionization Profile Monitor (IPM) of J-PARC 3-GeV RCS. 2013.

[122] C. Welsch, H. Zhang, V. Tzoganis, A. Jeff, and T. Cybulski. Non-invasive Beam Profile Monitoring. Technical report, 2015.

[123] P. Thieberger et al. Scattered electrons as possible probes for beam halo diagnostics. In *Workshop on Beam Halo Monitoring, Menlo Park, CA*, 2014.

[124] K. Hirata and K. Yokoya. Nongaussian distribution of electron beams due to incoherent stochastic processes. *Part. Accel.*, 39(KEK-PREPRINT-91-212):147–158, 1992.

[125] T.O. Raubenheimer. Emittance growth due to beam-gas scattering. *KEK-92-7*, 1992.

[126] D. Wang et al. Analytical estimation of ATF beam halo distribution. *Chin. Phys. C*, 38(12):127003, 2014.

[127] T. Suehara, M. Oroku, T. Yamanaka, H. Yoda, T. Nakamura, Y. Kamiya, et al. Design of a nanometer beam size monitor for ATF2. *arXiv preprint arXiv:0810.5467*, 2008.

[128] S. Liu, P. Bambade, F. Bogard, J-N. Cayla, H. Monard, C. Sylvia, et al. Status of diamond detector development for beam halo investigation at ATF2. In *IPAC'14*, pages 3449–3452, 2014.

[129] T. Naito and T. Mitsuhashi. Beam halo measurement utilizing YAG: Ce screen. In *Proceedings of IBIC2015, Melbourne, Australia*, pages 373–376, 2016.

[130] S. Lee. *Accelerator physics*. World Scientific Publishing Company, 2011.

[131] E. Courant and H. Snyder. Theory of the alternating-gradient synchrotron. *Annals of physics*, 281(1-2):360–408, 2000.

[132] W. Herr. Mathematical and numerical methods for non-linear beam dynamics. *arXiv preprint arXiv:1601.05411*, 2016.

[133] E. Forest et al. From Tracking Code to Analysis. *Flow, Turbulence and Combustion*, 2016.

[134] A. Wolski. Low emittance machines. In *CERN Accelerator School*, 2017.

[135] M. Reiser. *Theory and design of charged particle beams*. John Wiley & Sons, 2008.

[136] K. Oide and H. Koiso. Dynamic aperture of electron storage rings with noninterleaved sextupoles. *Phys. Rev. E*, 47(3):2010, 1993.

[137] K. Brown and S. Howry. Transport/360: A computer program for designing charged particle beam transport systems. Technical report, Stanford Linear Accelerator Center, Calif., 1970.

[138] K. Brown. SLAC Report 75, 1972.

[139] J. Le Duff. Etude de quelques phénomènes stochastiques dans les anneaux de stockage. Technical report, Paris 11. Lab. Accél. Linéaire, 1965.

[140] F. Tecker. Longitudinal dynamic. *CERN Accelerator School*, 2017.

[141] E. McMillan. The synchrotron—a proposed high energy particle accelerator. *Phys. Rev.*, 68(5-6):143, 1945.

[142] H. Wiedemann. *Particle accelerator physics*. Springer, 2015.

[143] D. Koningsberger and R. Prins. X-ray absorption: principles, applications, techniques of EXAFS, SEXAFS, and XANES. 1988.

[144] Revol, J. and Jacob, J. and Berkvens, P. and Bouteille, J. and Biasci, J. and Raimondi, P. and others. ESRF upgrade phase II status. 2014.

[145] M. Sands. The physics of electron storage rings: an introduction. In *Conf. Proc.*, volume 6906161, pages 257–411, 1970.

[146] M. Rosenblatt. A central limit theorem and a strong mixing condition. *Proceedings of the National Academy of Sciences*, 42(1):43–47, 1956.

[147] A. W. Chao. Evaluation of beam distribution parameters in an electron storage ring. *Journal of Applied Physics*, 50(2):595–598, 1979.

[148] K. Ohmi, K. Hirata, and K. Oide. From the beam-envelope matrix to synchrotron-radiation integrals. *Phys. Rev. E*, 49(1):751, 1994.

[149] J. Jackson. *Electrodynamics*. Wiley Online Library, 1975.

[150] A. Wrulich. Single-beam lifetime. 1994.

[151] S. Rice. Mathematical analysis of random noise. *Bell Labs Technical Journal*, 23(3):282–332, 1944.

[152] SAD is a computer program for accelerator design; see http://acc-physics.kek.jp/SAD/.

[153] K. Kubo. Simulation study of low emittance tuning of the Accelerator Test Facility damping ring at KEK. *Phys. Rev. ST Accel. Beams*, 6(9):092801, 2003.

[154] R. Yang et al. Numerical investigation of beam halo from beam gas scattering in KEK-ATF. *J. Phys. Conf. Ser*, 874(1):012063, 2017.

[155] Wiedemann H. *Particle Accelerator Physics (Third Edition)*.

[156] F. Zimmermann et al. Measurements and simulations of the transverse acceptance in the ATF damping ring. *SLAC-AP-113*, 1998.

[157] T. Okugi et al. Evaluation of vertical emittance in KEK-ATF by utilizing lifetime measurement. *Nucl. Instrum. Methods Phys. Res., Sect. A*, 455(1):207–212, 2000.

[158] A. Piwinski. Intra-beam-scattering. 1974.

[159] C. Bernardini, G. Corazza, G. Di Giugno, G. Ghigo, J. Haissinski, P. Marin, et al. Lifetime and beam size in a storage ring. *Phys. Rev. Lett.*, 10(9):407, 1963.

[160] A. Piwinski. The Touschek effect in strong focusing storage rings. *arXiv preprint physics/9903034*, 1999.

[161] J. Le Duff. Single and multiple Touschek effects. Technical report, CERN, 1988.

[162] J. Bjorken and S. Mtingwa. Intrabeam scattering. *Part. Accel.*, 13(FERMILAB-PUB-82-047-T):115–143, 1982.

[163] P. Zenkevich, O. Boine-Frankenheim, and A. Bolshakov. Kinetic Effects in Multiple Intra-Beam Scattering. In *AIP Conference Proceedings*, volume 773, pages 425–429. AIP, 2005.

[164] K. Kubo, S. Mtingwa, and A. Wolski. Intrabeam scattering formulas for high energy beams. *Phys. Rev. ST Accel. Beams*, 8(8):081001, 2005.

[165] K. Bane, H. Hayano, K. Kubo, T. Naito, T. Okugi, and J. Urakawa. Intrabeam scattering analysis of measurements at KEK's Accelerator Test Facility damping ring. *Phys. Rev. ST Accel. Beams*, 5(8):084403, 2002.

[166] K. Bane. A simplified model of intrabeam scattering. *arXiv preprint physics/0206002*, 2002.

[167] K. Kubo and K. Oide. Intrabeam scattering in electron storage rings. *Phys. Rev. ST Accel. Beams*, 4(12):124401, 2001.

[168] M. Martini. Intrabeam scattering: Anatomy of the theory. *CERN Yellow Reports: School Proceedings*, 3:291, 2017.

[169] M. Zisman, J. Bisognano, and S. Chattopadhyay. Zap user's manual. Technical report, 1986.

[170] P. Zenkevich, O. Boine-Frankenheim, and A. Bolshakov. A new algorithm for the kinetic analysis of intra-beam scattering in storage rings. *Nucl. Instrum. Methods Phys. Res., Sect. A*, 561(2):284–288, 2006.

[171] M. Martini, F. Antoniou, and Y. Papaphilippou. Intrabeam scattering. *ICFA Beam Dyn. Newsl.*, 69:38–59, 2016.

[172] M. Martini and A. Vivoli. Intra-beam scattering in the CLIC damping rings. 2010.

[173] T. Takizuka and H. Abe. A binary collision model for plasma simulation with a particle code. *Journal of computational physics*, 25(3):205–219, 1977.

[174] W. Heitler. *The quantum theory of radiation*. Courier Corporation, 1954.

[175] T. Okugi, T. Naito, K. Kubo, N. Terunuma, J. Urakawa, F. Zimmermann, and H. Hayano. Lifetime measurement of ATF damping ring. Number SLAC-PUB-7859, pages 1318–1320, 1998.

[176] M. Pomorski, E. Berdermann, W. De Boer, A. Furgeri, C. Sander, J. Morse, et al. Charge transport properties of single crystal CVD-diamond particle detectors. *Diamond and Related materials*, 16(4-7):1066–1069, 2007.

[177] R. Yang, P. Bambade, V. Kubytskyi, A. Faus-Golfe, T. Naito, and N. Fuster-Martínez. Modeling and experimental studies of beam halo at ATF2. 2016.

[178] L. Pan and D. Kania. *Diamond: electronic properties and applications*. Springer Science & Business Media, 2013.

[179] V. Kubytskyi, V. Krylov, P. Bambade, B. Cabouat, F. Wicek, F. Bogard, et al. Study of low multiplicity electron source LEETECH with diamond detector. *Journal of Instrumentation*, 12(02):P02011, 2017.

[180] S. Liu. *Development of diamond sensors for beam halo and compton spectrum diagnostics after the interaction point of ATF2*. PhD thesis, Universite Paris-Sud, 2015.

[181] R. Sussmann. *CVD diamond for electronic devices and sensors*, volume 26. John Wiley & Sons, 2009.

[182] V. Kubytskyi, S. Liu, and P. Bambade. Modeling/measurement comparison of signal collection in diamond sensors in extreme conditions. In *Proceedings of IPAC2015, Richmond, USA*.

[183] C. Lindstrøm, E. Adli, J. Allen, W. An, C. Beekman, C. Clarke, et al. Measurement of transverse wakefields induced by a misaligned positron bunch in a hollow channel plasma accelerator. *Phys. Rev. Lett.*, 120(12):124802, 2018.

[184] E. Stenson, U. Hergenhahn, M. Stoneking, and T. Pedersen. Positron-induced luminescence. *Phys. Rev. Lett.*, 120:147401, 2018.

[185] D. Dowell, P. Bolton, J. Clendenin, P. Emma, S. Gierman, W. Graves, C. Limborg, et al. Slice emittance measurements at the SLAC gun test facility. *Nucl. Instrum. Methods Phys. Res., Sect. A*, 507(1-2):327–330, 2003.

[186] J. Ruan, A. Johnson, A. Lumpkin, R. Thurman-Keup, H. Edwards, R. Fliller, et al. First observation of the exchange of transverse and longitudinal emittances. *Phys. Rev. Lett.*, 106(24):244801, 2011.

[187] M. Moszyński, T. Ludziejewski, D. Wolski, W. Klamra, and L. Norlin. Properties of the yag: Ce scintillator. *Nucl. Instrum. Methods Phys. Res., Sect. A*, 345(3):461–467, 1994.

[188] S. Payne, N. Cherepy, G. Hull, J. Valentine, W. Moses, and W. Choong. Nonproportionality of scintillator detectors: Theory and experiment. *IEEE Transactions on Nuclear Science*, 56(4):2506–2512, 2009.

[189] A. Murokh, J. Rosenzweig, V. Yakimenko, E. Johnson, and X. Wang. Limitations on the resolution of YAG: Ce beam profile monitor for high brightness electron beam. In *The Physics of High Brightness Beams*, pages 564–580. World Scientific, 2000.

[190] R. Bartram and A. Lempicki. Efficiency of electron-hole pair production in scintillators. *Journal of luminescence*, 68(5):225–240, 1996.

[191] T. Ludziejewski, M. Moszyński, M. Kapusta, D. Wolski, W. Klamra, and K. Moszyńska. Investigation of some scintillation properties of YAG: Ce crystals. *Nucl. Instrum. Methods Phys. Res., Sect. A*, 398(2-3):287–294, 1997.

[192] E. Zych, C. Brecher, A. Wojtowicz, and H. Lingertat. Luminescence properties of Ce-activated YAG optical ceramic scintillator materials. *Journal of luminescence*, 75(3):193–203, 1997.

[193] M. Moszyński, T. Ludziejewski, D. Wolski, W. Klamra, and VV. Avdejchikov. Timing properties of GSO, LSO and other Ce doped scintillators. *Nucl. Instrum. Methods Phys. Res., Sect. A*, 372(1-2):51–58, 1996.

[194] T. Yanagida, H. Takahashi, T. Ito, D. Kasama, T. Enoto, M. Sato, et al. Evaluation of properties of YAG (Ce) ceramic scintillators. *IEEE transactions on nuclear science*, 52(5):1836–1841, 2005.

[195] T. Naito and T. Mitsuhashi. YAG: Ce screen monitor using a gated CCD camera. In *IBIC2014, Monterey, CA, USA*, pages 14–18, 2014.

[196] E. Bravin. *CERN Accelerator School, Beam diagnostic*, chapter Transverse beam profiles, page 377. CERN-2009-005. 2009.

[197] A. Chao, K. Mess, M. Tigner, and F. Zimmermann. *Handbook of accelerator physics and engineering*. World Scientific, 1999.

[198] M. Ross, S. Anderson, J. Frisch, K. Jobe, D. McCormick, B. McKee, et al. Very High Resolution Optical Transition Radiation Beam Profile Monitor. In *AIP Conference Proceedings*, volume 648, pages 237–247. AIP, 2002.

[199] A. Aryshev, G. Blair, S. Boogert, G. Boorman, A. Bosco, L. Corner, et al. Micron size laser-wire system at the ATF extraction line, recent results and ATF-II upgrade. *Nucl. Instrum. Methods Phys. Res., Sect. A*, 623(1):564–566, 2010.

[200] S. Boogert, G. Blair, G. Boorman, A. Bosco, L. Deacon, P. Karataev, et al. Micron-scale laser-wire scanner for the KEK Accelerator Test Facility extraction line. *Phys. Rev. ST Accel. Beams*, 13(12):122801, 2010.

[201] *www.sugitoh.com*.

[202] *https://www.pco.de/scmos-cameras/pcoedge-42-lt/*.

[203] K. Kubo et al. Wakefield effects to the beam size at atf2. *Unpublished*.

[204] K. Kubo, J. Snuverink, and A. Lyapin. Wakefield issues for the linear colliders. *ICFA Beam Dyn. Newslett.*, 61:69–85, 2013.

[205] *CST:https://www.cst.com*.

[206] B. Zotter and S. Kheifets. *Impedances and wakes in high-energy particle accelerators*. World Scientific, 1998.

[207] N. Fuster-Martinez, J. Snuverink, A. Faus-Golfe, and A. Latina. Geometric wakefield regimes study of a rectangular tapered collimator for ATF2. Technical report, 2016.

[208] *ESTAR:https://physics.nist.gov/PhysRefData/Star/Text/ESTAR.html*.

[209] L. Waters et al. MCNPX user's manual. *Los Alamos National Laboratory*, 2002.

[210] A. Lumpkin. Time-resolved imaging for the APS linac beams. Technical report, Argonne National Lab., IL (US), 1998.

[211] R. Spesyvtsev and M. Staykov. *Transverse Beam Size Measurement Systems at Photo Injector Test Facility in Zeuthen*. PhD thesis, Diploma thesis, DESY/Karazin Kharkiv National University, 2006.

[212] J. Krzywinski, A. Andrejczuk, R. Bionta, T. Burian, J. Chalupskỳ, M. Jurek, et al. Saturation of a Ce:YAGscintillator response to ultra-short pulses of extreme ultraviolet soft X-ray and X-ray laser radiation. *Optical Materials Express*, 7(3):665–675, 2017.

[213] V. Lebedev. Diffraction-limited resolution of the optical transition radiation monitor. *Nucl. Instrum. Methods Phys. Res., Sect. A*, 372(3):344–348, 1996.

[214] B. Yang, J. Bailey, D. Walters, and S. Stein. Design of a high-resolution optical transition radiation imager for the linac coherent light source undulator. In *PAC2005*, pages 4209–4211. IEEE, 2005.

[215] N. Terunuma, M. Tejima, J. Urakawa, and F. Hinode. Development of the Vacuum System for ATF Damping Ring. *KEK-PROC–93-10*, 1994.

[216] T. Naito. Emittance measurement using X-ray beam profile monitor at KEK-ATF. In *Proceedings of IBIC2012, Tsukuba, Japan*, 2012.

[217] F. Zhou, J. Amann, A. Seryi, M. Woodley, C. Spencer, and S. Selestiky. Simulation studies on the Vertical Emittance Growth in the Existing ATF Extraction BeamLine. Technical report, 2007.

[218] K. Iida, N. Nakamura, H. Sakai, K. Shinoe, H. Takaki, M. Fujisawa, et al. Measurement of an electron-beam size with a beam profile monitor using Fresnel zone plates. *Nucl. Instrum. Methods Phys. Res., Sect. A*, 506(1-2):41–49, 2003.

[219] F. Zimmermann. Studies of Emittance Growth in the ATF. *SLAC-AP-107*, 1997.

[220] N. Fuster-Martínez, T. Tauchi, F. Toral, S. Wallon, A. Faus-Golfe, N. Terunuma, et al. Design study and construction of a transverse beam halo collimation system for ATF2. 2015.

[221] N. Fuster-Martinez. Beam halo collimation studies and measurements in the Accelerator Test Facility ATF2. *Unpublished*, 2018.

[222] T. Naito, S. Araki, H. Hayano, K. Kubo, S. Kuroda, N. Terunuma, et al. Multibunch beam extraction using the strip-line kicker at the KEK Accelerator Test Facility. *Phys. Rev. ST Accel. Beams*, 14(5):051002, 2011.

[223] M. Pons, A. Faus-Golfe, P. Bambade, G. Le Meur, and F. Touze. Modeling of the shared magnets of the ATF Extraction Line. *CARE/ELAN Document-2008-013*, 2009.

[224] G. White, A. Seryi, Y. Renier, R. Tomas, D. Schulte, et al. A flight simulator for ATF2: A mechanism for international collaboration in the writing and deployment of online beam dynamics algorithms. In *Conf. Proc.*, volume 806233, page TUPP016, 2008.

Titre : Mesures et caractérisation du halo du faisceau de l'accélérateur ATF au KEK

Mots clés : Halo du faisceau, diffusion du faisceau sur le gaz résiduel, diffusion « Touschek », capteur diamant, moniteur YAG/OTR, queue de distribution en énergie

Résumé : Aux futurs collisionneurs linéaires et circulaires, la présence d'un halo autour du faisceau est susceptible de fortement limiter les performances, et peut également activer, voire endommager, les composants de l'accélérateur. Le halo doit par conséquent est contrôlé par un système de collimateurs efficace. Pour évaluer l'impact sur les expériences de physique des particules ainsi que les efficacités de collimation, une bonne compréhension des mécanismes physiques générateurs de halo est essentielle, pour par exemple prédire les distributions de probabilité de manière fiable. Pour ce faire, une investigation systématique ont été menée à l'Accelerator Test Facility (ATF) du KEK dans le cadre de cette thèse, d'abord à travers une analyse théorique des principales sources de halo dans ATF, puis moyennant le développement et l'implémentation de diagnostiques dédiés aux mesures du halo, dont les résultat sont ensuite présentés et comparés aux prédictions théoriques.

Le halo produit par la diffusion des particules du faisceau sur les noyaux des molécules du gaz résiduel dans la chambre à vide (« Beam Gas Scattering » - BGS) est d'abord estimé analytiquement, avec certaines approximations, puis moyennant une simulation Monte-Carlo. Un nombre considérable de particules de halo BGS est prédit, ainsi qu'une dépendance dans la pression de gaz résiduel. Pour étudier la possible formation d'un halo par le mécanisme de diffusion intra-paquet à grand angle dit de « Touschek » en présence d'une dispersion optique résiduelle, le taux de cette diffusion a été estimé en fonction de plusieurs paramètres faisceau pertinents. Une simulation Monte-Carlo de la diffusion intra-faisceau à petit angle (IBS) et de « Touschek » est aussi en cours de développement.

Pour tester les prédictions théoriques, les performances d'un détecteur de halo déjà existant basé sur un capteur diamant ont été améliorées moyennant une technique de repondération qui a permis d'en augmenter la gamme dynamique jusqu'à 10^5. Afin de disposer d'un instrument complémentaire pour mesurer le halo, un moniteur YAG/OTR a aussi été conçu, construit et installé dans la ligne d'extraction d'ATF. Il a pu être montré que la gamme dynamique et la résolution de ce moniteur YAG-OTR sont, respectivement, autour de 10^5 et inférieure à 10 μm.

Grâce aux diagnostiques développés pour mesurer le halo du faisceau d'ATF, les distributions transverses et en énergie ont pu être étudiées. L'accord satisfaisant obtenu entre les prédictions théoriques et les mesures, ainsi qu'une dépendance importante dans la pression de gaz résiduel, ont permis de montrer que la distribution verticale du halo est dominée par le mécanisme BGS. Par contre, la distribution horizontale est bien supérieure aux prédictions BGS, et est par ailleurs asymétrique. L'asymétrie observée peut être en partie reliée à la qualité du champ de l'élément pulsé servant à l'extraction du faisceau d'ATF, ainsi qu'à certaines aberrations dans le transport optique. La distribution de probabilité du halo en fonction de l'énergie a par ailleurs pu être mesurée, grâce à une technique nouvelle d'ajustement de la dispersion optique dans le plan vertical, et a été trouvée compatible qualitativement avec le mécanisme de diffusion « Touschek ». Un scénario plausible de génération du halo dans le plan horizontal a ainsi pu être suggéré.

université PARIS-SACLAY | ÉCOLE DOCTORALE PHENIICS

Title : Diagnostics and characterization of beam halo at the KEK Accelerator Test Facility

Keywords : Keywords: Beam halo, beam gas scattering, Touschek scattering, diamond sensor detector, YAG/OTR monitor, momentum tail

Abstract : At future linear and circular colliders, beam halo can strongly limit machine performances, cause as well component damage and activation, and should, therefore, be controlled by an efficient collimation system. To evaluate the impact on particle physics experiments and collimation efficiencies, a clear understanding of beam halo formation mechanisms is essential, e.g., to predict halo distribution reliably. For this purpose, systematic investigations have been carried out at the Accelerator Test Facility (ATF) of KEK. In this dissertation, the theoretical analysis of the primary halo sources at ATF and the development of dedicated halo diagnostics are presented. Measurements of beam halo at ATF are also described and compared with the theoretical predictions.

Beam halo arising from Beam-Gas Scattering (BGS) in the damping ring was firstly estimated through analytical approximations and a Monte Carlo simulation. A considerable amount of halo particles generated by BGS and the corresponding vacuum dependence have been predicted. To explore the probability of beam halo formation from Touschek scattering in the presence of dispersion, the Touschek scattering rate was estimated with respect to relevant beam parameters. Furthermore, a Monte Carlo simulation of Intra-Beam Scattering (IBS) and Touschek scattering is under development.

To probe the theoretical predictions, the performance of an already existing diamond sensor detector was optimized via a data rescaling technique to increase the dynamic range to 10^5. For a complementary diagnostics of beam halo, a YAG/OTR monitor was also designed and installed in the extraction section of ATF2. The dynamic range and resolution of the YAG/OTR monitor have been shown to be around 10^5 and less than 10 μm, respectively.

Thanks to the halo monitors developed at ATF2, the transverse halo and momentum tail have been studied. Satisfactory agreement between numerical predictions and measurements as well as a significant vacuum dependence indicate that the BGS process dominates the vertical halo. On the other hand, the horizontal halo appeared to be higher than the prediction from BGS, and moreover asymmetric. The observed asymmetry was shown to be related to the quality of the extraction kicker field and optical aberration. Finally, the momentum tail was for the first time observed by implementing a novel scheme of vertical dispersion adjustment and was found to be qualitatively consistent with the presence of Touschek scattering. A possible scenario for horizontal beam halo formation from Touschek scattering was also suggested.